A functional and therapeutic investigation of ciliopathy proteins and ciliopathies

A thesis submitted for the degree of
Doctor of Philosophy to UCL

Jonathan Leslie Tobin

Molecular Medicine Unit
UCL Institute of Child Health
London

September 2008

Declaration

I, Jonathan Tobin, confirm that the work presented in this thesis is my own. Where information has been derived from other sources, I confirm that this has been indicated in the thesis.

Jonathan Tobin, September 2008

Abstract

This thesis aims to investigate new functions for ciliopathy proteins and identify candidates for therapeutic application. The ciliopathies form a class of genetic diseases whose aetiology lies in the primary cilium. Over 30 genes have been identified as mutant in ciliopathies and their proteins localise at the primary cilium. When mutated they can cause kidney disease, obesity, polydactyly, and retinal degeneration.

In this project, I have studied craniofacial dysmorphology related to Bardet-Biedl syndrome (BBS) in humans, mice, and zebrafish, and shown there to be consistent midfacial flattening and hypoplasia. *Bbs8*, a causative gene of BBS, has a key role in neural crest migration and possibly in cell migration in general. This accounts for the frequent observation of Hirschsprung's disease, a gut immotility disorder, in BBS. I identified new roles for BBS and other ciliopathy proteins in Sonic hedgehog (Shh) signal transduction and showed that they are important in the downstream processing of the transcription factor Gli3.

I modelled ten different ciliopathy genes in the zebrafish and identified specific ciliary phenotypes, such as laterality randomisation, otic vesicle anomalies, and kidney cysts. Administration of two drugs, Rapamycin and Roscovitine, were sufficient to rescue formation of kidney cysts and restore the filterative capacity of the kidney. This paves the way for studies in mouse models and, ultimately, in humans, where no treatment for ciliopathic renal disease exists.

I examined whether *FTO*, a gene associated with obesity in the general population, functioned in ciliary processes. I provided some evidence that its protein was involved ciliary processes and glucose homeostasis. I also showed that *fto* interacted with its neighbouring ciliary gene, *ftm*, in the zebrafish. I performed similar interaction studies to show that a non-synonomous SNP in a gene associated with lipid accumulation in *C. elegans* had deleterious effects on protein function, explaining its high degree of association in BBS patients.

Table of Contents

List of figures

List of tables

For my family and Hannah

Acknowledgements

I would like to thank my primary supervisor, Professor Phil Beales, for his support and generosity during my three years in his laboratory. Phil has given me the freedom to explore my own ideas without constraint and has backed me up in everything I have wanted to achieve. I also thank Professor Pete Scambler, my secondary supervisor, and all the members of the Molecular Medicine Unit at the Institute of Child Health. I am extremely grateful to Dr Paris Ataliotis for proofreading my thesis, as well as being an excellent running partner.

Several collaborators have assisted, both practically and conceptually, and have taught me essential skills during my PhD. Masa Tada and Masa Kai in the UCL Cell & Developmental Biology department allowed me uncompromised access to their zebrafish facilities, practical expertise, and scientific insight. Roberto Mayor and his lab taught and enthused me about neural crest migration. Alan Burns at ICH helped me perform experiments on avian embryos and I enjoyed many hours working with him. James Briscoe gave great advice and ideas about Sonic hedgehog signalling. His technician, Anita Mynett, taught me how to prepare mouse neural tubes. Professor Peter Hammond and his technician, Matt DiFranco, performed 3D facial scanning of human and mouse BBS subjects, which contributed the basis of a major part of my thesis and a significant publication.

I thank my family who have given me every possible opportunity and enabled me to pursue my interests in life. Throughout my PhD, I have been supported by Hannah's unstinting love and enthusiasm. Finally, thanks to my examiners for reading this.

“I thought of it while riding my bike.”
Albert Einstein on the theory of relativity

List of abbreviations

µg	Microgram
µM	Micromolar
µm	Micrometre
ADPKD	Autosomal dominant polycystic kidney disease
AER	Apical ectodermal ridge
ALMS	Alstom syndrome
AP	Antero-posterior
APC	Adenomatous polyposis coli
ARPKD	Autosomal recessive polycystic kidney disease
ATP	Adenosine triphosphate
BBS	Bardet-Biedl syndrome
BMI	Body mass index
BMP	Bone morphogenetic protein
BSA	Bovine serum albumin
cAMP	Cyclic adenosine monophosphate
CCHS	Congenital central hypoventilation syndrome
cDNA	Complementary DNA
CE	Convergent-extension
CNCC	Cranial neural crest cell
CNS	Central nervous system
Cos2	Costal-2
CT	Computerized tomography
ddNTP	Dideoxynucleoside triphosphate
Dhh	Desert hedgehog
DIC	Differential interference contrast
DMEM	Dulbecco's modified Eagle's medium
DMSO	Dimethylsulphoxide
dNTP	Deoxynucleoside triphosphate
dpf	Days post fertilisation
DSM	Dense surface modeling
DV	Dorso-ventral
Dvl	Dishevelled
E	Embryonic day
EDTA	Ethylenediaminetetraacetic acid
eGFP	Enhanced GFP
EMT	Epithelial-mesenchymal transition
ENS	Enteric nervous system
ENU	Ethyl-N-nitrosurea
ESRF	End-stage renal failure
EST	Expressed sequence tag
EVC	Ellis-van-Creveld syndrome
FACS	Fluorescence activated cell sorter
FBS	Fetal bovine serum
FGF	Fibroblast growth factor
FITC	Fluorescein isothiocyanate
Fu	Fused

GAPDH	Glyceraldehyde-6-phosphate dehydrogenase
GDNF	Glial-derived neurotrophic factor
GFP	Green fluorescent protein
Gli	Glioma transcription factor
Gli3A	Gli3 activator
Gli3R	Gli3 repressor
GPCR	G-protein coupled receptor
GSK3β	Glycogen synthase kinase 3β
GTP	Guanosine triphosphate
HEK	Human embryonic kidney
HPE	Holoprosencephaly
hpf	Hours post fertilisation
hpi	Hours post injection
HSCR	Hirschsprung's disease
HUVEC	Human umbilical vascular endothelial cell
IFT	Intraflagellar transport
Ihh	Indian hedgehog
IMCD3	Inner medullary collecting duct 3
IP	Immunoprecipitation
JATD	Jeune asphyxiating thoracic dystrophy
JBTS	Joubert syndrome
kDa	Kilodalton
KI	Knock-in
KV	Kupffer's vesicle
LB	Luria broth
LCA	Leber's congenital amaurosis
LH	Lateral hypothalamus
LMBBS	Laurence Moon Bardet-Biedl syndrome
MAB	Maleic acid buffer
MDCK	Madine Darby canine kidney
MKKS	McKusick-Kaufman syndrome
MKS	Meckel-Gruber syndrome
mM	Milimolar
MO	Morpholino oligonucleotide
mRNA	Messenger RNA
ms	Milisecond
mTOR	Mammalian target of Rapamycin
NC	Neural crest
NCAM	Neural cell adhesion molecule
NCC	Neural crest cell
nM	Nanomolar
NPHP	Nephronophthisis
NTD	Neural tube defect
OCT	Optimal cutting temperature
OFD	Oro-facio-digital syndrome
OMIM	Online mendelian inheritance in man
P	Postnatal day
PAGE	Polyacrylamide gel electrophoresis
PBS	Phosphate buffered saline

PC	Polycystin
PCA	Principle component analysis
PCM	Pericentriolar material
PCP	Planar cell polarity
PCR	Polymerase chain reaction
PDGF	Platelet derived growth factor
PFA	Paraformaldehyde
pg	Picogram
PKA	Protein kinase A
PKD	Polycystic kidney disease
PKD	Polycystic kidney disease
PNS	Peripheral nervous system
POMC	Pro-opio-melanocortin
Ptc	Patched
PTU	Phenolthiourea
qRT-PCR	Quantitative real-time reverse transcription PCR
QTL	Quantitative trait locus
RA	Retinoic acid
RNAi	RNA interference
RP	Retinitis pigmentosa
SDS	Sodium dodecylsulphate
Shh	Sonic hedgehog
shRNA	Short hairpin RNA
siRNA	Small interfering RNA
SLNS	Senior-Loken syndrome
Smo	Smoothened
SNP	Single nucleotide polymorphism
ss	Somite stage
Su(Fu)	Suppressor of fused
TAP	Tandem affinity purification
TEM	Transmission electron microscopy
TPR	Tetratricopeptide repeat
Tx-100	Triton X-100
V	Volt
VCFS	Velo-cardio-facial syndrome
VEGF	Vascular endothelial growth factor
VMH	Ventral medial hypothalamus
ZPA	Zone of polarising activity

Chapter 1: Introduction

History of the cilium

The word "cilium" means eyelash in Latin and its use in Biology has been attributed to the eighteenth century Danish naturalist Otto Muller. He was referring to the structure first observed by Antony Van Leeuwenhoek in 1675 using a primitive microscope, when he observed the moving flagellum of a freshwater protozoon. Leeuwenhoek went on to observe flagella beating on the mammalian spermatozoon and pondered "…how such an unbelievable motion is brought about" (Quoted in Frixione, 2000).

Ever since then the motile cilium and flagellum[1] have fascinated biologists because of their elegant structures and movement. Over the next century, cell biologists observed motile cilia lining epithelia of the oviduct, respiratory tract, brain ventricles, and on spermatozoa. Their interest in these organelles arose from the importance they attributed to the beating motion. Disorders of motile cilia can result in human diseases such as Kartagener's syndrome, in which cilia become immotile and are unable to beat. This causes in bronchiectasis (inflammation of the bronchi) because the airway epithelium is unable to clear mucus, as well as causing *situs inversus*, or reversal of organ laterality.

In contrast to the motile cilia which fascinated the early microscopists, primary cilia form a separate class of cilia and were not discovered until 1898, when Zimmerman first described them lining kidney tubules (Wheatley, 2005). Primary cilia are immotile and so their function was unknown until relatively recently. They are ancient organelles and are present, at least at some point during the life cycle, on almost all eukaryotic cells (Davis et al., 2006).

For the purposes of this thesis, I will concentrate on the biology of primary cilia, and not motile cilia, because my work concerns the ciliopathies, a group of

[1] The terms "cilium" and "flagellum" are often used interchangeably and refer to the same organelle. In multicellular organisms, cilia beat in a wavelike motion and flagella beat in a whipping motion, such as on spermatozoa.

genetic diseases caused by mutations affecting proteins which function in the primary cilium. It is first important to distinguish between the structure and function of the motile and primary (or immotile) cilia.

Motile and primary ciliary cell biology

Motile cilia tend to be concentrated in large numbers on the apical surface of cells, and beat in coordinated "Mexican" waves to clear mucus from the respiratory epithelium, drive sperm along the fallopian tube, and move cerebrospinal fluid in the brain ventricles and spinal cord. In cross section, these cilia are constructed from a "9+2" arrangement of microtubules in which nine microtubule doublets surround a central inner pair. These microtubules are stable, and not dynamic as they are in the cytoplasm. This stability is achieved by acetylation of the tubulin monomers. Figure 1 shows cross sections through motile and primary cilia (Fig. 1A and B), and scanning electron micrographs of these types of cilia *in vivo* (Fig. 1C and D).

Each microtubule doublet consists of an "A" strand which is constructed from 13 tubulin protofilaments, and a "B" strand made from 10 protofilaments (Alberts, 2008). In motile cilia, radial spokes connect the outer and inner doublets. The inner doublet is used for generating shear forces needed to bend the cilium and induce motility. Bending is achieved by dynein motor proteins shifting one microtubule doublet relative to the central pair, and is dependent on ATP hydrolysis. When this beating is coordinated amongst cells lining an epithelium, the result is a unidirectional flow of fluid.

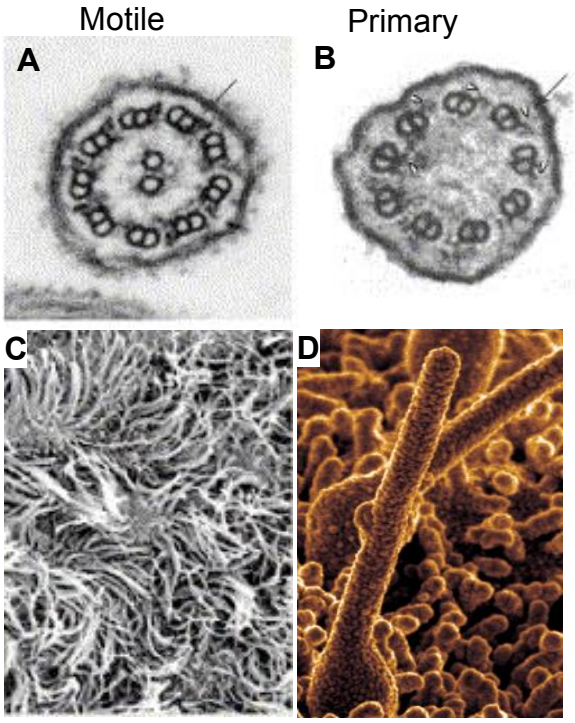

Figure 1. The structure of motile and primary cilia

Fig. 1A and 1B are TEM cross-sections through motile and primary cilia respectively. Fig. 1C shows motile cilia lining the oviduct, 1D shows primary cilia projecting from the surface of the node in a mouse embryo. Taken from (Huangfu and Anderson, 2005).

Primary cilia differ from motile cilia in their lack of the central microtubule doublet, so they are described as having a "9+0" arrangement. 9+0 cilia are immotile and do not beat, with the unusual exception of cilia covering the node (or organiser) of the mammalian embryo. These nodal cilia do beat, and have been described as a third class of cilia. The function of primary cilia, once disregarded as vestigial (Webber and Lee, 1975), is complex and variable. In some cells they function as an antenna to respond to extracellular signalling molecules, in others they act as mechanosensors and bend in response to fluid flow, and they are also crucial for certain important developmental signalling cascades. As such, primary cilia are crucial for development and maintenance of numerous organs and tissues, as will be discussed in detail later in this chapter.

The anatomy of the cilium

The ciliary axoneme (shaft) is only 0.25μm in diameter but its length can range from several microns to up to 2mm. The basal body is a cylindrical structure measuring 0.4 by 0.2μm positioned perpendicular to the cell membrane, anchoring the cilium in the cytoplasm (Lodish, 2002). It also acts as the nucleation point from which the cilium extends out from the cell. The basal body consists of nine triplets of microtubules arranged in a ring from which extend three microtubules: A, B, and C. All three fibres project from the basal body into the proximal region of the cilium known as the transition zone; this is the region from which a nascent cilium grows. Further along the cilium is the middle zone composed of nine doublets consisting of just A and B filaments. The axoneme terminates with the distal zone, comprised primarily of microtubule singlets.

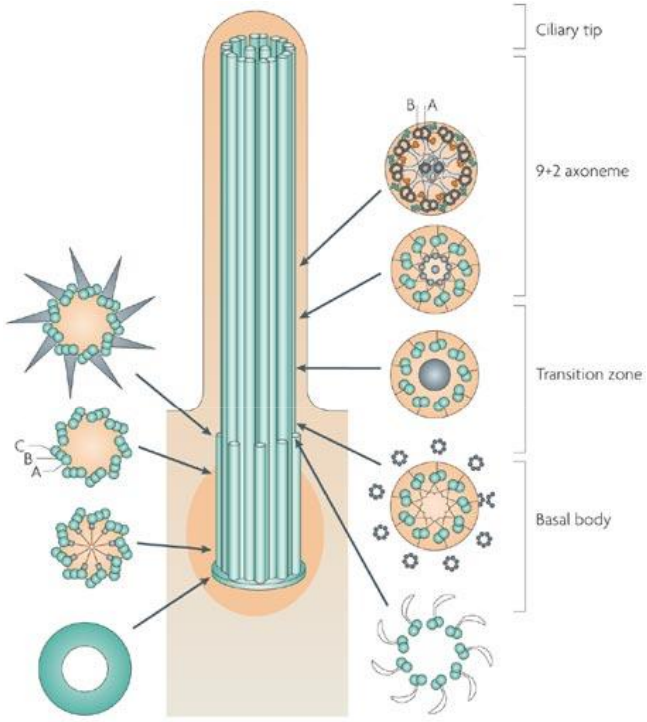

Figure 2. Longitudinal section through a cilium

At the proximal, cytoplasmic end of the cilium lies the basal body with microtubule triplets. Distal to this is the transition zone where the microtubules are arranged in doublets. The axoneme comprises the majority of the length of the cilium. Taken from (Fliegauf et al., 2007).

Intraflagellar transport

The ciliary matrix (cytoplasm) is devoid of ribosomes, meaning that any proteins needed for ciliary biogenesis or function must be transported into the cilium from the cytoplasm. A system of ferrying proteins to (anterograde) and from (retrograde) the cilium is executed by a process called intraflagellar transport (IFT). Anterograde transport involves the loading of cargo proteins bound for the cilium onto an IFT particle, which in turn is attached to a kinesin motor protein complex. The motor complex consists of the motors KIF3A and KIF3B (Rosenbaum and Witman 2002), which slide along the axoneme. The IFT particle consists of at least 17 proteins and is divided into two subcomplexes: subcomplex A with around 6 proteins, and subcomplex B with 11 proteins, outlined in Table 1 (Lucker et al., 2005). Retrograde transport back to the cytoplasm relies on the dynein motors, which also serves to recycle the kinesin motors.

Subcomplex A	Subcomplex B
IFT43	IFT20
IFT122A	IFT27
IFT122B	IFT46
IFT139	IFT52
IFT140	IFT57
IFT144	IFT72
	IFT74
	IFT80
	IFT81
	IFT88
	IFT172

Table 1. A list of IFT complex A and B proteins.

The two sub-complexes are coordinated by a bridge of accessory proteins. The precise nature of the IFT particle is not completely characterised, but it is complex and the ciliary proteome consists of some 1,000 proteins, many of which are directly involved with IFT (www.ciliaproteome.org; (Gherman et al., 2006)). No IFT particles accumulate in the distal tip of the cilium so the amount of retrograde transport always equals anterograde. In fact, the rate of IFT remains constant throughout the cycle of cilium assembly and disassembly. When the cilium is fully grown, many IFT particles enter the cilium without cargo and passage up and down the axoneme. Loading of cargo is regulated at the basal body and the complex of proteins surrounding it, the pericentriolar material (PCM). Many of

these cargoes derive from vesicles budded directly off the Golgi apparatus, so it is not surprising that the cilium usually forms apically to the trans-Golgi network (Davis et al., 2006). Figure 3 depicts the process of IFT.

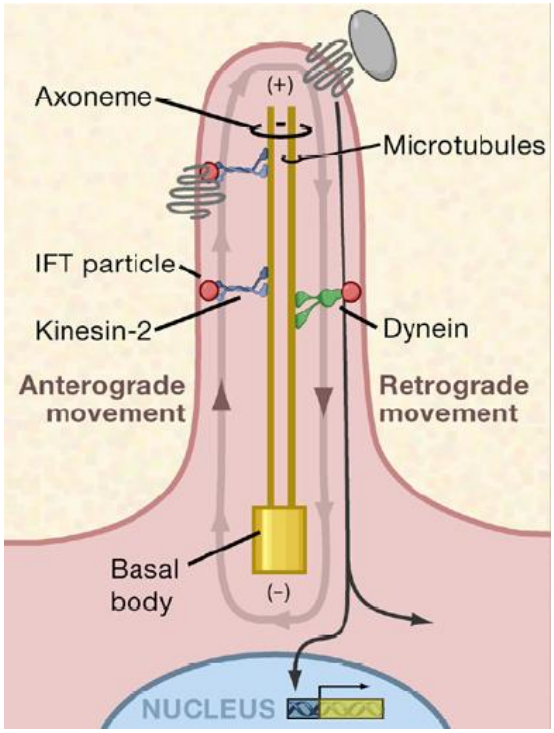

Figure 3: **The mechanism of intraflagellar transport**

Cargo bound for the cilium is loaded at the basal body and attached to an IFT particle, which is propelled distal-wards along the axoneme, by the Kinesin-2 motor complex. The Dynein motor complex powers retrograde transport back to the cytoplasm. Taken from (Scholey and Anderson, 2006).

The ciliopathies form a new class of genetic syndrome

Due to the importance of primary cilia in cell biology, physiology, and development, mutations in genes affecting proteins involved with ciliary function can have devastating effects on human development and health. Since 2003, a growing list of ciliopathies has emerged – diseases in which genes encoding components of the cilium (including the basal body) are mutated (For review see (Badano et al., 2006)). Understanding these diseases has been helped enormously by basic research into ciliated organisms, such as the unicellular alga *Chlamydomonas reinhardtii* and the nematode *Caenorhabditis elegans*, as well as

work done on vertebrate models. In return, the ciliopathies have shed a huge amount of light on the functional importance of cilia and their proteins. As such, the study of ciliopathies is a perfect example of how basic science can be transferred to understanding human disease, and vice versa.

Several other ciliary genes are mutated in human diseases, such as polycystic kidney disease, but these proteins are not involved in ciliary function *per se*, they just localise to the cilium for their function. In addition, they tend only to affect the kidney (although rarely can cause *situs inversus* too), whereas ciliopathies tend to involve multiple systems. Ciliopathy proteins tend to be involved with the intrinsic function of the cilium, and lack of any one of them often causes the cilia to be malformed or absent. Also, the ciliopathies are defined as affecting primary cilia, and the term is not extended to encapsulate motile ciliary dysfunction disorders such as heterotaxia and Kartagener's syndrome.

The ciliopathies currently include: Bardet-Biedl syndrome (BBS), Nephronophthisis (NPHP), Senior-Loken syndrome (SLNS), Alstrom syndrome (ALMS), Meckel syndrome (MKS), Joubert syndrome (JBTS), Oro-facial digital type I (OFD 1), Jeune asphyxiating thoracic dystrophy (JATD), Leber Congenital Amaurosis (LCA). The list of ciliopathies is growing, and while it stands at around ten diseases, estimates are that there may be as many as 25 (P. Beales, personal communication).

The core ciliopathies, whose ciliary origins are best studied, are NPHP, BBS, and MKS. They exist in a phenotypic spectrum, with NPHP being considered the mildest, BBS as intermediate in severity, and MKS is pre- or perinatal lethal. For each syndrome, there are many causative genes, reflecting the common underlying biological theme of the cilium uniting these diseases. The different ciliopathies are clinically distinct and diagnosis is usually made based on phenotype and confirmed by genotype.

Because of their common involvement in ciliary processes, the ciliopathies show a common denominator of clinical features. In fact, these features are so

characteristic that they can be used as a way of predicting and identifying new ciliopathy syndromes, as Beales et al did for Jeune syndrome (Beales et al., 2007). This insight can then be used to discover new ciliary proteins and further our understanding of ciliary biology. This table identifies the "hallmarks" of ciliopathy. The features are listed in order or prevalence.

Feature	NPHP	SLNS	BBS	MKS	JBTS	JATD	OFD
Kidney cysts	■	■	■	■	■	■	■
Liver disease	■	■	■	■	■	■	■
Situs inversus	■	■	■	■	■	■	
Polydactyly			■	■	■	■	■
Agenesis of corpus callosum			■	■	■	■	■
Mental retardation			■	■	■	■	■
Dandy-Walker malformation*		■	■	■	■		
Retinal degeneration		■	■	■	■		
Encephalocoele			■	■	■	■	

Table 2. Summary table showing common features of ciliopathies.

Red shading indicates the feature is present in the syndrome.

* This is a defect of the brain ventricles affecting the formation of the cerebellum. Data taken from (Badano et al., 2006) and OMIM.

From the table it is clear that cystic kidneys and liver disease are common to all ciliopathies. Second to this is *situs inversus*, reversal of organ laterality. Polydactyly, agenesis of the corpus callosum, and mental retardation are a triad of features that seem to manifest together. This possibly reflects common underlying signalling defects that will be discussed later. Retinal degeneration is common to several ciliopathies and usually culminates in blindness. Encephalocoele is a neural tube defect (NTD) in which portions of the anterior neural tube fail to close, resulting in brain protruding through the skull and is always lethal.

Table 2 also shows how NPHP has less multi-system involvement than the other diseases, and is considered phenotypically milder than BBS or MKS. It primarily involves the kidney and is a common cause of kidney failure amongst children (Hildebrandt and Zhou, 2007). When NPHP presents with retinal degeneration it

is called Senior-Loken syndrome (SLNS). BBS involves more organ systems and has become the most studied ciliopathy, partly because it is informative about the role of cilia in so many different systems. It also manifests a strong phenotype while not being lethal. Meckel (MKS) and Joubert (JBTS) syndrome are both lethal and can be distinguished because JBTS presents a molar-tooth shaped cerebellum on MRI, and MKS causes NTDs. MKS and JBTS can be considered at the extreme end of the ciliopathy phenotypic spectrum.

Other ciliopathies affect different systems while preserving hallmarks such as kidney diseases, situs inversus, and polydactyly. OFD1 and JATD both cause skeletal defects. LCA only tends to affect the retina and so blindness is the main feature. As such, it is debateable whether LCA should be considered a ciliopathy under the terms stated above.

The relevance of studying ciliopathies

Ciliopathies are rare diseases in the general population, although tend to be up to ten times more common in highly inbred populations such as in the Middle East; Pakistan; Newfoundland, Canada; and the Faroe Islands. Data on prevalence are variable and hard to estimate due to low numbers of patients. BBS is present at 1 in 100,000 in the West and about 1 in 13,000 amongst Bedouin Arabs (OMIM 209900). MKS is more common at around 1 in 9,000 (OMIM 249000).

Despite the rarity of these diseases, they are important to study for three reasons: first, they cause severe, multi-system pathology resulting in a very low quality of life and early death for most patients. Currently there are no cures and few treatments and so understanding the disease is important for developing therapies to treat patients. Second, the ciliopathies share some features common in the general population. Kidney cysts are present in about 1 in 500 adults; retinal degeneration in 1 in 3,000; and polydactyly in 1 in 500. One of the most prominent features of BBS is obesity, present in one third of adult Britons (Hyde, 2008). In BBS, this is combined with type 2 diabetes, hypertension, and cardiovascular disease, so it makes a good model for studying the poorly

understood metabolic syndrome, present in 25% of the American population (www.americanheart.org). Third, studying the ciliopathies is informative about the basic biology of cilia and their role in cell signalling and development.

The genetics of the ciliopathies

The first ciliopathy gene, *MKKS* or *BBS6*, was identified simultaneously by two independent groups in 2000 (Katsanis et al., 2000; Slavotinek et al., 2000). Since then, over 30 genes causing ciliopathy syndromes have been identified. For some of these proteins, their function is being elucidated, while others remain elusive. Table 3 summarises the known ciliopathy genes and their protein products:

Disease	Causative genes	Protein function	Reference
BBS[1,2,3,4]	*BBS1*	Cilia function	(Mykytyn et al., 2002)
	BBS2	Cilia function	(Nishimura et al., 2001)
	BBS3/ARL6	Vesicle trafficking	(Fan et al., 2004)
	BBS4	Microtubule transport	(Mykytyn et al., 2004)
	BBS5	Cilia function	(Li et al., 2004)
	BBS6/MKKS	Cilia/chaperone	(Katsanis et al., 2000)
	BBS7	Cilia function/IFT	(Badano et al., 2003)
	BBS8/TTC8	Cilia function/IFT	(Ansley et al., 2003)
	BBS9/B1	Unknown	(Nishimura et al., 2005)
	BBS10	Putative chaperone	(Stoetzel et al., 2006)
	BBS11/TRIM32	E3 ubiquitin ligase	(Chiang et al., 2006)
	BBS12	Type II chaperone	(Stoetzel et al., 2007)
Alstrom[1,3]	*ALMS1*	Ciliogenesis	(Hearn et al., 2002)
Meckel/ Joubert[2,3,4]	*MKS1*	Unknown (cilium)	(Kyttälä et al., 2006)
	MKS2	Unknown (uncloned)	
	MKS3/TMEM67	Transmembrane (cilium)	(Smith et al., 2006)
	MKS4/RPGRIP1L	Basal body function	(Arts et al., 2007)
	MKS5	Unknown (uncloned)	
	MKS6/CC2D2A	Cilium/calcium binding	(Tallila et al., 2008)
	AHI1	WD repeats	(Dixon-Salazar et al., 2004)
NPHP[2,3]	*NPHP1*	Cilium	(Hildebrandt et al., 1997)
	NPHP2/INVS	Cilium, laterality	(Otto et al., 2003)
	NPHP3	Unknown	(Olbrich et al., 2003)
	NPHP4	Cilium	(Mollet et al., 2002)
	NPHP5	IQ domain/cilium	(Otto et al., 2005)
	NPHP6/CEP290	Cilium/centrosome	(Valente et al., 2006)
	NPHP7/GLIS2	Transcription factor	(Attanasio et al., 2007)
	NPHP8/NEK8	Nemo-like kinase	(Otto et al., 2008)
OFD Type I[2,4,5]	*OFD1*	Unknown	(Ferrante et al., 2001)
Jeune[2,3,4,5]	*IFT80*	IFT subcomplex B	(Beales et al., 2007)
Ellis van Creveld[2,4,5]	*EVC1*	Cilium	(Ruiz-Perez et al., 2000)
	EVC2	Unknown	(Galdzicka et al., 2002)

Phenotypic subgroups: 1) obesity as primary feature. 2) kidney disease. 3) retinal degeneration. 4) polydactyly. 5) skeletal dysplasia

Table 3. Table summarising the genes and their proteins mutated in human ciliopathies.

This classification shows how, even within the ciliopathies, the diseases can be subcategorised contingent on the biological role of the protein involved. I have classified ciliopathy features into five subgroups above. Excluding kidney disease as a discriminator due to its ubiquity, this classification defines two groups: ciliopathies with skeletal involvement (JATD, OFD1, EVC), and those no skeletal involvement (BBS, NPHP, MKS/JBTS, ALMS).

Most ciliopathies are autosomal recessive, with the exception of OFD1, which is X-linked dominant. However, the inheritance pattern of some ciliopathies is more complex and sometimes involves more than one locus. In 2001, it was suggested that BBS requires triallelic inheritance, consisting of homozygous mutations at one locus and a heterozygous change in a third allele at a different locus (Katsanis et al., 2001). Evidence for this came from homozygous mutations in *BBS2* not causing disease in one individual, but when present with a third mutation in a *BBS6* allele, BBS features manifested (*ibid.*). Since then, it has been reported that *BBS4* and *BBS1* may display triallelic inheritance (Beales et al., 2003). Hoefele (2007) screened NPHP patients and found third alleles mutated in second NPHP loci, adding evidence that oligogenic, or triallelic, inheritance exists in other ciliopathies (Hoefele et al., 2007). Meanwhile, several studies have performed mutation screening on large cohorts of BBS patients and found no evidence for triallelism (Hichri et al., 2005; Laurier et al., 2006; Nakane and Biesecker, 2005; Smaoui et al., 2006).

Leitch et al (2008) found *MKS1*, *MKS3*, and *CEP290* (*NPHP6*) mutations in BBS patients with mutations in BBS genes (Leitch et al., 2008). The presentation of seizures in these patients suggested that this extra mutational load modified the phenotype to make it more severe. Furthermore, mutations in ciliopathy genes have been shown to cause diseases not previously associated with that gene. For example, mutations in *CEP290* can cause NPHP, SLNS, or JBTS (Baala et al., 2007; Helou et al., 2007); *RPGRIP1L* can cause MKS or JBTS (Delous et al.,

2007), and *AHI1* mutations can cause NPHP or JBTS (Wolf et al., 2007). These findings suggest that the ciliopathies exist as a phenotypic spectrum modulated by the type, number, and position of underlying mutations. Understanding these genotype-phenotype correlations is of importance in understanding the diseases.

Furthermore, our thinking that all ciliopathies are caused by mutations in ciliary genes is being challenged. In 2008, Attanasio et al identified mutations in the transcription factor gene *GLIS2* in NPHP patients and recapitulated the phenotype in mouse (Attanasio et al., 2007). Ciliary proteins have also been localised to the Golgi apparatus and to microtubules outside of the cilium (Follit et al., 2006); H. May-Simera, thesis). Our study of ciliopathies may need to extend beyond the cilium and basal body to fully understand the mechanisms of disease.

Bardet-Biedl syndrome as a "model" ciliopathy

Basal body dysfunction was identified as a probable cause of BBS in 2003 (Ansley et al., 2003). The clue came from a patient with *situs inversus* who was then shown to have mutations in *BBS8*, whose protein localised to the basal body. Since then, almost all the BBS proteins have been localised to the primary cilium or basal body (for review see (Tobin and Beales, 2007)) (BBS11 localisation has not been reported yet). BBS patients have all the common features of ciliopathies: polydactyly, cystic kidneys, retinitis pigmentosa, and *situs inversus*. Nearly all BBS patients are obese, the precise reason being unclear, but thought to be linked to a defect in the satiety centre of the hypothalamus, whose neurons are ciliated (Berbari et al., 2008a; Berbari et al., 2008b).

BBS patients are usually born with post-axial polydactyly (extra little finger or toe) of some or all limbs, and hypogenitalism. In the first few years of life, they begin to put on weight and become obese. By the age of eight, night blindness manifests proceeding to complete blindness by around fifteen years. Kidney cysts usually appear in childhood and most patients require dialysis or transplantation to survive. End-stage renal failure is the most common cause of premature death from BBS and is estimated to kill around 30% of patients (OMIM). Most patients

survive until the third decade of life, but some patients have been known to live into their seventh decade (P. Beales, personal communication). Complications often arise from overweight, including hypertension and type 2 diabetes. Many patients also have congenital cardiovascular disease.

The origin of most of these features relates to primary cilium dysfunction. Rod-cone dystrophy, or retinitis pigmentosa, is caused because the outer segment of the rod cell, which contains the photoreceptor pigments, is a modified cilium. This connecting cilium transports vesicles containing rhodopsin and structural proteins from the cell body to the outer segment via IFT, at a rate of 2,000 vesicles per second (Sung and Tai, 2000). The dysfunction of BBS proteins in this transport causes progressive degeneration of the outer segment, first resulting in night-blindness and then complete loss of vision.

Post-axial polydactyly may be related to the fact that the apical ectodermal ridge (AER) of the developing embryonic limb bud is ciliated. The AER is where the digits are patterned, and it receives the Sonic hedgehog (Shh) signal secreted from the zone of polarising activity (ZPA) in the posterior margin of the limb bud. Misinterpretation of the Shh signal can result in polydactyly, which might be the case in BBS. Because the development of the external genitalia relies on similar signalling mechanisms to the limb extremities, it is thought that Shh signalling deficiencies could also result in the small genitalia seen in BBS patients. However, this has not yet been proven.

Table 4 shows the primary and secondary features of BBS and their incidence rates.

Primary features	**% Prevalence** (after Beales et al 1999)	**Comment**
Rod-cone dystrophy	93%	Other ocular defects included: astigmatism, strabismus, cataracts, colour blindness, macular oedema and degeneration, and optic atrophy
Post-axial polydactyly	69%	Present on all four limbs in 21% of patients, only hands in 9% and only feet in 21%. Brachydactyly present in 46% and syndactyly in 9% of patients
Truncal obesity	72%	Mean BMI in males was 31.5kg/m^2, in females it was 36.6kg/m^2
Hypogonadism	98%	Males had micropenis and 8% had maldescended testes. Most women reported irregular menstrual cycles and genital abnormalities e.g. hydrometrocolpos
Renal anomalies	24% (only 52% of patients had undergone renal exam)	Renal parenchymal cysts (10%), calyceal clubbing (10%), fetal lobulation (12%), scarring (12%), dysplastic kidneys (5%), unilateral agenesis (4%), renal calculi (2%), vesicoureteric reflux (9%), bladder obstruction (4%), hydronephrosis (4%), horseshoe kidney (2%), ectopic kidney (2%)
Secondary features		
Speech disorder/delay	54%	
Developmental delay	50%	52% showed delay in walking of up to one year, speech delayed by up to two years in 47%, delay in pubescence in 31% (all males)
Behaviour	33%	Emotional immaturity, outbursts, disinhibition, depression and lack of social dominance, obsessive compulsive behaviour
Ataxia/imbalance	40%	Abnormal gait reported in 33% of patients
Diabetes mellitus	6%	
Congenital heart defects	7%	Included: aortic stenosis, patent ductus arteriosis, cardiomyopathy
Liver disease		
Hearing loss (Conductive and sensorineural)	21%	
Facial features	variable	Deep-set eyes, hypertelorism, long philtrum, thin upper lip, anteverted nares, prominent forehead with male early-onset balding
Situs inversus	unknown	
Hirschsprung disease	~10%	
Polyuria/polydipsia		May be present in the absence of renal abnormality
Dental crowding		Also includes: high arched palate, hypodontia, small roots
Anosmia	~60%	See Kulaga et al. 2004

Table 4. Primary and secondary features of BBS.

The importance of cilia in kidney development is well known. Cilia project into the lumen of the tubules in the kidney and act as flow sensors (Yoder, 2007). Dysfunction of the cilia here results in aberrant kidney development and cyst formation. Figure 4 shows primary cilia in tissues whose development is defective in ciliopathy patients.

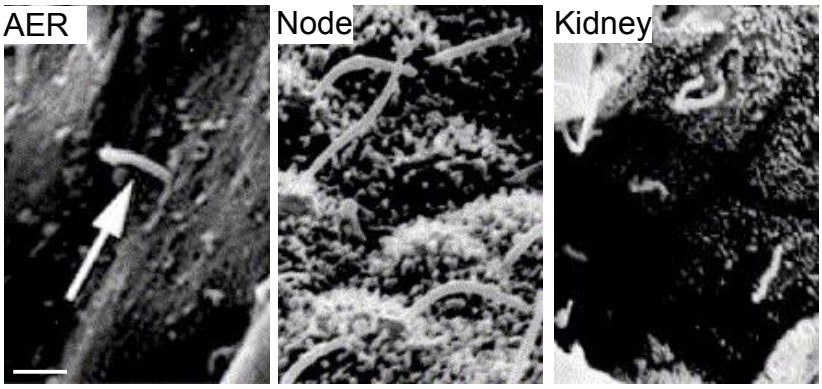

Figure 4. Primary cilia in ciliopathy contexts.

Alterations to AER cilia can cause polydactyly; nodal cilia cause heterotaxia; and kidney luminal cilia, cystic kidneys. Taken from (Marshall and Nonaka, 2006). Scale bar 5μm.

Diabetes in BBS patients may be secondary to obesity. However, non-obese BBS patients who have had calorie-controlled diets are still hyperinsulinemic (P. Beales, personal communication). This suggests that BBS proteins may have a primary role in glucose homeostasis. This is a possibility in light of the fact that pancreatic β-cells, which secrete insulin, are ciliated, which may be important for reception of signals to secrete insulin (Ait-Lounis et al., 2007).

BBS proteins are expressed in hair cells of the ear (H. May-Simera, thesis), which extend stereociliary bundles. These bend in response to acoustic vibration and open ion channels that set off action potentials to the auditory nerve. Early in development, the neat order of the stereociliary bundles is controlled by the kinocilium, a modified primary cilium. BBS protein dysfunction may affect the function of the kinocilium, resulting in disordered hair cells and resultant hearing deficits. Similarly, olfactory hair cells in the nose are ciliated and these are

required for detecting odours. As such, over half of BBS patients are completely anosmic (unable to detect smells) (Kulaga et al., 2004).

Functions of ciliopathy proteins

Many ciliopathy proteins localise exclusively to the primary cilium (including the basal body) and/or the centriole, and so it is assumed that they function in ciliary processes. However, the primary cilium is complex and is the location of many cellular processes. These include, amongst others: loading and unloading of cargo on to IFT particles at the basal body, anterograde and retrograde transport along the axoneme, ciliogenesis, localising receptors and signalling molecules to the cilium, function of signalling pathways reliant on the cilium, positioning of the cilium on the cell surface, and control of the cell cycle. Therefore, while ciliary localisation is a good clue as to ciliary function, it does not delineate what that function is. This is harder to establish and so the precise function of many ciliopathy proteins at the molecular level remains unknown.

Many ciliary genes have an X-box motif in their promoter sequence to which binds the transcription factor RFX3, which activates the transcription of many ciliary genes (Efimenko et al., 2005). In addition, several ciliopathy proteins contain domains that give clues about their function by homology to other proteins. A few examples are given below:

MKS1: contains a B9 domain of unknown function. In *C. elegans* there are three B9-containing proteins with mammalian homologues: MKS-1, TZA-1, and TZA-2 (Williams et al., 2008). These form a trimeric complex at the cilium and only affect cilium formation when combined with mutations in *nphp1* or *nphp4*. As such, the B9 domain may be an effective bait for identifying new candidate ciliopathy proteins.

MKS3: also known as Meckelin, this protein contains 7 transmembrane domains, a signal peptide, 4 N-linked glycosylation sites, and 2 cysteine-rich repeats (Smith et al., 2006). This protein is structurally similar to the Frizzled receptor involved in PCP signalling. It is not yet proven, but MKS3 could play an essential, direct role in transduction of the non-canonical Wnt signal.

BBS4 and BBS8: these proteins both contain tetratricopeptide repeats (TPRs), and the alternative name for these proteins are TTC10 and TTC8 respectively (Ansley et al., 2003; Mykytyn et al., 2001). TPRs are 34 amino acid motifs involved in protein-protein interactions. In addition, BBS8 contains a predicted pilF domain present in proteins involved in bacterial flagellar motility and pilus formation. This was used by Ansley et al (2003) to predict its role in cilia, flagellar, or pseudopodia function.

BBS6, BBS10, and BBS12: these proteins make up a novel family of type II chaperonin proteins involved in protein folding. Unlike any other BBS genes, they are specific to vertebrates, rapidly evolving, and may function redundantly (Stoetzel et al., 2006; Stoetzel et al., 2007). It is unknown what the function of these chaperonins is, but they are not included in the interacting complex of BBS proteins, the BBSome (see Nachury et al. 2007), but may be involved in aiding the folding of other BBS or IFT proteins.

No structural data from crystallographic studies has been obtained, largely owing to the fact that BBS proteins are insoluble. However, function is better characterised for BBS4, BBS7, BBS8, IFT80, and NEK8, from which inferences about other ciliopathy protein functions have been made. I will outline four studies that have illuminated functions of the BBS proteins.

The first clues about function came from studies of BBS-7 and BBS-8 in *C. elegans*. Blacque et al (2004) first showed that these two proteins localise to the base of the cilium in ciliated neurons, and GFP-tagged proteins could be observed participating in IFT (Blacque et al., 2004). The average rate of anterograde movement was approximately $0.7\mu ms^{-1}$, while retrograde was roughly $1.1\mu ms^{-1}$; rates comparable with IFT motor proteins such as OSM-3 kinesin. The authors found animals mutant for these two genes were defective in taxis towards two chemical attractants whose detection relies upon ciliated neurons. They then showed that cilia structure was abnormal in these mutants, determined by the inability to uptake DiI. GFP-tagged IFT proteins failed to localise and move properly along the cilium in *bbs-7* and *bbs-8* mutants. The authors suggested that

these proteins facilitate the incorporation of the IFT particle onto the motor protein complex, and are selective for particular cargoes.

Ou et al used the same *C. elegans* mutants to show that BBS-7 and BBS-8 coordinate the movement of IFT subcomplexes A and B (Ou et al., 2005). In the absence of these proteins, the subcomplexes moved separately, at different rates, because a different type of kinesin motor moves each subcomplex. The authors proposed a model whereby BBS-7 and BBS-8 act as a bridge between the two IFT subcomplexes. In the absence of these proteins, the two subcomplexes move independently and are unstable. As such, IFT is not completely abolished in *bbs* mutants, but it becomes unstable and slow. This explains why BBS phenotypes are less severe than complete IFT knockouts, and are not lethal. Figure 5 shows how BBS-7 and -8 act together to coordinate IFT in *C. elegans*.

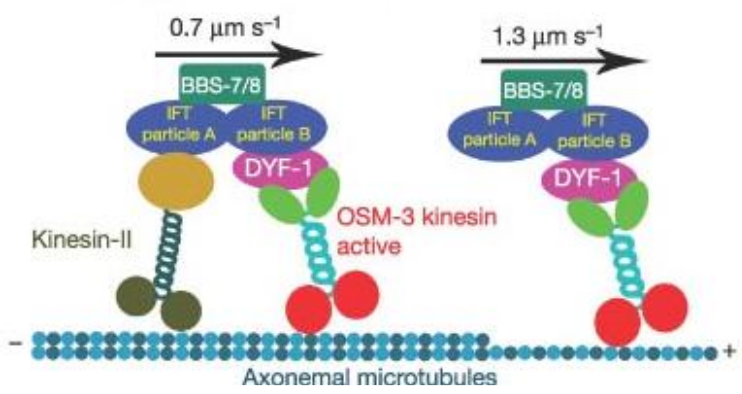

Figure 5. IFT functions of BBS-7 and BBS-8.

BBS-7 and -8 act as a bridge to coordinate IFT subcomplexes A and B to stabilise microtubule transport. In the distal zone where microtubules are monomers, speed of transport is higher than in the central portion of the axoneme. Taken from Ou et al (2005).

Kim et al performed a yeast two-hybrid screen to identify p150 and PCM1 (pericentriolar material 1) as interactors of BBS4. Silencing of *Bbs4* resulted in abrogation of recruitment of PCM1 to the pericentriolar satellites, and a deanchoring of microtubules from the centrosome. Figure 6 illustrates how BBS4 aids retrograde IFT.

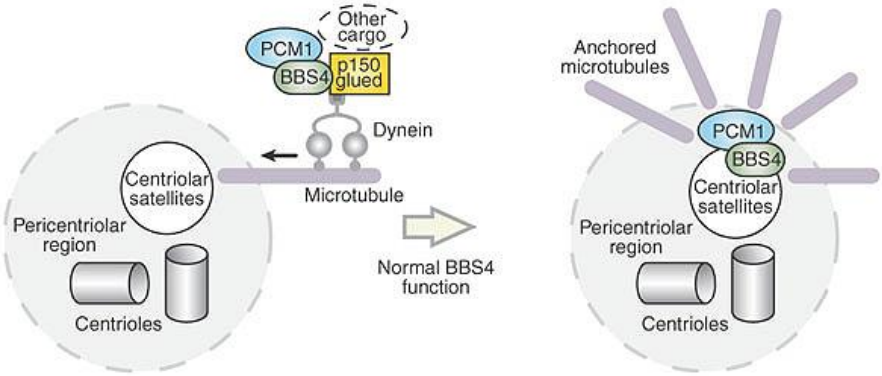

Figure 6. Function of BBS4

BBS4 interacts with PCM1 and p150glued, part of the dynein retrograde motor complex. It is thought to assist retrograde IFT and stabilise microtubules at the centrosome through its association with PCM1. Taken from Kim et al (2004).

Nachury et al provided the best insight to date as to how BBS proteins behave at the molecular level (Nachury et al., 2007). They used tandem affinity purification (TAP) to isolate a complex of BBS proteins they termed the "BBSome". This 438kDa complex consisted of stoichiometric ratios of BBS1, 2, 4, 5, 7, 8, and 9, with BBS9 acting as the central organiser, as it interacted with all other subunits. They found the most marked defects of ciliogenesis when cells were depleted of BBS1 and 5. They conjectured that the BBSome is transported to the basal body by the centriolar satellites and it associates with the ciliary membrane. They showed the BBSome to interact with Rabin8, a guanosyl exchange factor for Rab8, a small GTPase that regulates vesicle trafficking from post-Golgi vesicles. Rab8 enters the ciliary membrane and promotes ciliogenesis. They proposed that pathogenesis in BBS might be caused by defects in vesicular transport to the cilium. Figure 7 suggests how the BBSome is involved with vesicular transport to the cilium.

In light of these studies, it seems there are two general, non-exclusive models for how BBS proteins might function. One suggests that at least BBS4, 7 and 8 are necessary for microtubule-based transport along the cilium. The other theory implies that BBS proteins function as a complex mediating vesicle transport from the cytoplasm to the cilium. As such, no one clear model for the function of BBS proteins has been described and the proteins may function in numerous roles, including cytoplasmic transport.

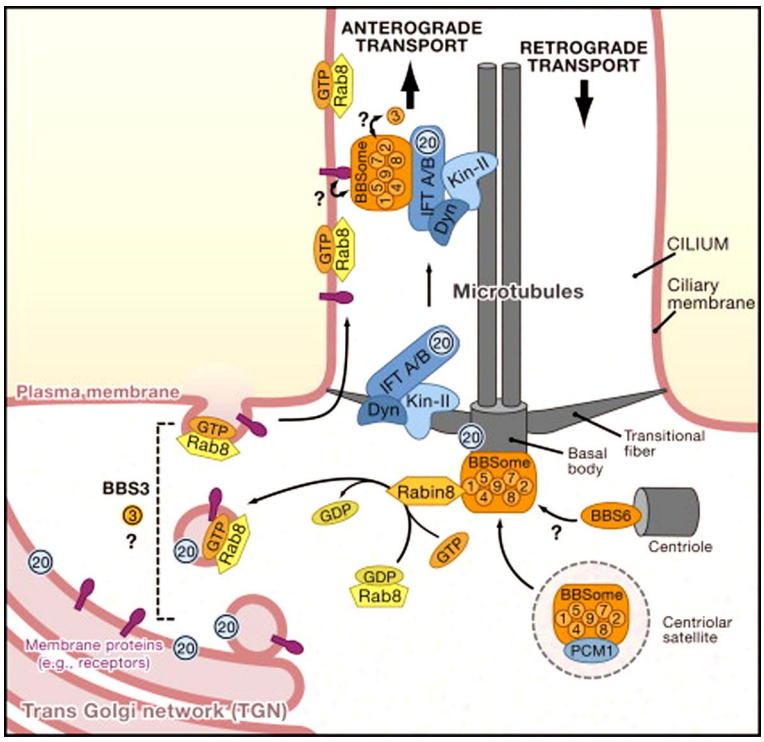

Figure 7. Proposed function of the BBSome.

The BBSome associates with Rabin8, a small GTPase involved in vesicle transport from the trans-Golgi network. Nachury et al proposed that the BBSome interacts with this to transport vesicles to the basal body and onto the IFT complex. Taken from (Leroux, 2007).

Situs inversus in ciliopathies

Situs inversus is a complete reversal of organ laterality, such that the positions of the heart, liver, stomach, and other internal organs are totally inverted – *situs inversus totalis*. Often, only some of the body's organs are inverted and this is referred to as *situs ambiguous*. These laterality defects are defined under the umbrella of "heterotaxia". Heterotaxia occurs at a rate of 1 in 10,000 in the general population, but is frequently observed (precise figures unavailable, but thought to be <10%) in ciliopathy patients.

Situs inversus in a patient with *BBS8* mutations was responsible for identifying ciliary origins of the disease due to the canonical role for the cilium in breaking of embryonic symmetry early in development. In the mouse embryo, the node appears during gastrulation at the anterior end of the primitive streak. The centre of the node is covered in motile cilia, which beat in a clockwise direction and

establish the "nodal flow", a current across the node (McGrath and Brueckner, 2003; McGrath et al., 2003). Nodal flow was shown to be sufficient for deciding laterality by the classic experiment by Nonaka et al, where he showed that reversing the flow over a cultured mouse node reversed embryo laterality (Nonaka et al., 2002).

There are two, non-exclusive, hypotheses about how nodal flow establishes asymmetry. In the first, the motile nodal cilia are surrounded by a second class of peripheral immotile cilia which sense flow by bending in response to leftward flow and initiate calcium transients (McGrath and Brueckner, 2003). In the second, nodal flow establishes a concentration gradient of morphogens including Shh, RA, and FGFs. This is thought to happen by the asymmetric distribution of vesicles containing these molecules. Tanaka et al (2005) fluorescently labelled these vesicles and showed them being absorbed by cells on the left side of the node in real time (Tanaka et al., 2005). They named these vesicles "nodal vesicular parcels".

McGrath et al (2003) showed how Shh, RA, and FGFs were necessary to establish the left-sided accumulation of calcium ions. This activates the nodal pathway on the left side of the embryo, driving expression of transcription factors such as *Lefty2* and *Pitx2*. This laterality information is then transmitted to the left-sided paraxial mesoderm, which develops left-sided character. The mechanism of transmission is unclear, but is known to involve the Notch, Wnt, and FGF pathways.

Situs inversus, or heterotaxia, are common amongst the ciliopathies compared to the general population but the incidence is still low (<10% *situs inversus*) compared to motile ciliary disorders where body *situs* is completely randomised (50% *situs inversus*). *NPHP2* was originally identified from the *invs* mouse, in which the gene encoding Inversin is mutated, so called because of the inverted laterality phenotype (Otto et al, 2003). This protein functions at the node, where it is important for nodal flow (Watanabe et al., 2003). Other ciliopathy proteins have also been localised to the node, including IFT80 (unpublished data,

molecular medicine unit, ICH). It is not clear which class of 9+0 nodal cilia (motile or immotile) the ciliopathy proteins function at, but since they perturb flow, it is likely they affect both classes.

The study of laterality is being facilitated by the zebrafish, in which asymmetry is established by a ciliated organ similar to the mammalian node, called Kupffer's vesicle (KV). This forms after gastrulation at the posterior end of the embryo and contains beating cilia, which drive fluid in a clockwise direction to establish left-right identity in the paraxial mesoderm.

Oishi et al (2006) identified a gene, *duboraya* (*dub*), essential for ciliogenesis and fluid flow in KV, with resultant randomisation of laterality in *dub* deficient embryos (Oishi et al., 2006). They showed that its function was dependent on Frizzled-2 mediated phosphorylation, linking *dub* to the non-canonical Wnt pathway. Several other ciliary mutants also show laterality defects observed by aberrant sidedness of expression of left sided markers such as *southpaw* (*spaw*) or *lefty*, or morphological phenotypes such as mis-sided heart or gut looping. These studies show that establishment of asymmetry in fish and mammals is a homologous process reliant on the same molecules and cellular processes. They also clearly link ciliary and ciliopathy proteins to asymmetry defects.

The mechanism of Sonic hedgehog signalling

The sonic hedgehog pathway is a widely deployed signalling pathway in development and its importance continues into adulthood. As such, perturbations to the pathway, either genetic or teratogenic, cause congenital malformations and, in adults, can lead to cancer. Shh has a role in the development of many organs, but I will restrict my discussion here to its canonical roles in dorso-ventral patterning of the neural tube, antero-posterior patterning of the digits of the limb, and control of midline development in the brain and face. In the last five years, a growing body of evidence has shown that cilia and IFT are essential for Shh activity, which may help explain many of the ciliopathy phenotypes we observe.

The Shh pathway relies on a diffusible ligand, Sonic hedgehog (Shh), initially a 45kDa protein that is cleaved into a 20kDa N-terminal isoform called Shh-N. The C-terminal fragment has no known function. Shh-N is then modified by addition of cholesterol moieties at the C-terminus that are thought to aid in secretion, trafficking, and receptor interaction. Lastly, the molecule is palmitoylated which has been shown to increase its diffusion by 30-fold relative to unpalmitoylated forms (Pepinsky et al., 1998).

The ligand is then secreted and is thought to be able to diffuse around 30 cell diameters *in vivo* (Zeng et al., 2001). It binds to its membrane-bound receptor, Patched-1, on a nearby cell. In the absence of Shh ligand, Patched-1 inhibits another membrane-bound protein, Smoothened (Smo), related to the G-protein coupled receptor family. Patched is thought to do this by pumping oxysterols out of the cell, which inhibit Smo activity (Javitt, 2008). When Shh binds Patched-1 (Ptc), its sterol pumping function is inhibited, enabling Smo to accumulate sterols thought to be important for its membrane localisation. Smo transduces the signal downstream.

Several proteins are involved in the downstream transduction of the Shh signal, which ultimately results in the transcriptional activation of target genes by the Gli3 transcription factor. Rab23 is a small GTPase involved in the endocytosis or targeting of vesicles containing Shh, Ptc, or Smo (Eggenschwiler et al., 2006). Downstream of Smo is a tetrameric complex made up of Fused (Fu), which positively regulates the pathway; Suppressor of Fused (Su(Fu)), a negative regulator of the pathway; Costal-2 (Cos2), a microtubule-associated kinesin-like protein; and Gli3, a transcription factor. When the pathway is activated by intermediate levels of Shh, Fused phosphorylates Costal-2, causing the dissociation of the tetramer from the microtubules to which they were bound (Fukumoto et al., 2001). Su(Fu) is a negative regulator of the pathway, as it binds to Gli transcription factors and inhibits their nuclear localisation (Ding et al., 1999). The interaction with Gli proteins is inhibited by high levels of Shh signal, enabling Gli proteins to enter the nucleus and activate downstream genes.

In the absence of Shh, promoted by Costal-2, PKA phosphorylates Gli3 and brings about its proteolytic cleavage from its full length, 190kDa transcriptionally active isoform (Gli3A) into an 83kDa transcriptional repressor (Gli3R). Shh stimulation breaks up the tetramer in which Costal-2 functions, thereby stopping it from activating PKA and preventing the breakdown of Gli3A. Gli3A enters the nucleus and activates downstream target genes. Patched-1 is upregulated by the pathway to spatially restrict the spread of Shh far beyond its producing cells

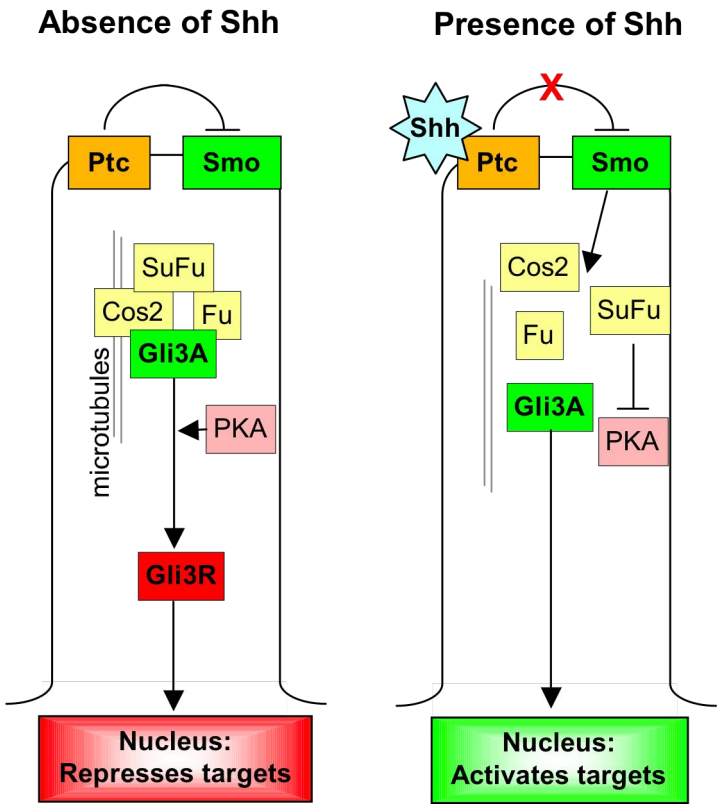

Figure 8. Mechanism of Shh transduction.

In the absence of Shh, Ptc inhibits Smo. In the cytoplasm, the tetrameric complex of Su(Fu), Costal2, Fused, and Gli3 associates with microtubules and Gli3 is cleaved into its repressor form by PKA. In the presence of Shh, the inhibition of Smo by Ptc is relieved. Smo acts to disassemble the tetrameric complex, preventing the action of PKA and leaving active Gli3 free to enter the nucleus.

(Dessaud et al., 2007). Many cell cycle genes are regulated by Shh, which is why over-activity of the pathway can result in tumour formation. Figure 8 outlines the major players in the Shh transduction pathway.

Many genes respond to particular concentrations of Shh, and as such, it acts as a morphogen inducing a graded response. This response is thought to be encoded by a gradient of Gli transcriptional activity, which is an intracellular correlate with Shh concentration (Stamataki et al., 2005). In this way, different cell fates are induced depending on the level of Shh signalling they are exposed to, which in turn depends on their distance from the source of Shh secretion.

In addition to Shh, there are two other Hedgehog pathway ligands in vertebrates: Desert hedgehog (Dhh) and Indian hedgehog (Ihh). Dhh is expressed in the testis and is thought to be involved in spermatogenesis. Ihh is expressed in developing bones and signals to the growth plate to induce cell division essential for bone growth. Mutations in *IHH* in humans causes bone growth defects such as brachydactyly (short fingers) and dysplasia of the long bones such as the femur (Hellemans et al., 2003). Downstream components of the pathway are the same in Dhh and Ihh signalling pathways, but the post-translational modifications of Dhh and Ihh differ from Shh, so their diffusion kinetics are not the same.

In the developing neural tube, Shh is secreted from the notochord and diffuses dorsally. The ventral-most cells are exposed to the highest concentration of Shh, and activate *Nkx2.2* to become motor neurons (Briscoe et al., 1999). In the middle of the neural tube, lower levels of Shh activate genes such as *Nkx6.1* and *Pax7*; these cells become interneurons. In the absence of Shh signal in the dorsal neural tube, cells differentiate into sensory neurons (Briscoe and Ericson, 2001). In *Shh* mouse mutants, ventral neuronal cell types are not specified, and the neural tube becomes dorsalised. In contrast, *Patched* mutants have an overactivation of the pathway due to constituent relief of Smo repression (Pazzaglia et al., 2006). These embryos have expanded ventral cell types.

In the skull, Shh signalling is essential for normal craniofacial development (Hu and Helms, 1999). Mutations in *Shh* in mice and humans cause holoprosencephaly (HPE), in which the lobes of the forebrain fail to split, leading to a single central eye (cyclopia) and the absence of a nose. Shh is essential for development of the frontonasal and maxillary processes of the upper and midface.

The lower face is much less severely affected. Shh is secreted from the anterior neural tube and oral ectoderm, where it organises the patterned migration of cranial neural crest cells about the midline (Eberhart et al., 2006). These cells form the bony features of the face. Craniofacial dysmorphology is a notable feature of BBS and this may rely, in part, on Shh signalling.

Ciliary involvement in Shh transduction

In an ethyl-nitrosurea (ENU) based mutagenesis screen for embryonic patterning mutants, Huangfu et al identified two IFT genes: *Ift172* and *Ift88* (Huangfu et al., 2003). While these mouse embryos expressed Shh normally, *Ptc1* expression level was markedly downregulated, a sign of reduced Shh pathway activity. In the neural tube, ventral cell types were absent, while dorsal cell types, usually repressed by Shh, were expanded. This indicated a loss of responsiveness to Shh stimulation.

Liu et al generated a hypomorphic *Ift88* allele and used it to study limb development, as the *Ift88* null died at E10.5 before the limb bud is patterned (Liu et al., 2005). These hypomorphs were polydactylous and the expression domain of *Gli3* was expanded in the limb buds. In wild types, the majority of Gli3 protein in the limb bud is proteolytically cleaved, giving a low ratio of Gli3A to Gli3R. In the hypomorphs, this ratio was increased, indicating less cleavage of Gli3 and an accumulation of the active isoform, which may induce the growth of extra digits in the limb. This effect on Gli3 explains why embryos show loss of Shh phenotypes in the neural tube but not in the limb bud, where the Gli transcription factors are deployed differently.

Corbit et al then showed that Smo localised to the cilium in response to stimulation by Shh, and that its ciliary localisation was essential for downstream signalling activity (Corbit et al., 2005). Rohatgi et al localised Patched-1 to the cilium and showed this localisation to be antagonistic to Smo ciliary localisation in the absence of Shh (Rohatgi et al., 2007). May et al showed that IFT was essential for Smo's ciliary localisation (May et al., 2005). Haycraft et al (2005)

then localised Su(Fu), Gli2, and Gli3 to the cilium, and showed this localisation to be abrogated in IFT mutants (Haycraft et al., 2005). This supported a direct role for the cilium in Gli processesing and transport. Several other ciliary proteins have since been shown to be essential for Shh signalling, including THM1 and RPGRIP1L, a causative gene of MKS (Tran et al., 2008; Vierkotten et al., 2007).

The role of ciliary proteins in Shh signalling supports some of the clinical phenotypes observed in ciliopathy patients, including postaxial polydactyly, external genitalia anomalies, and craniofacial defects. These are outlined below.

Polydactyly

A similar morphogen gradient to that in the neural tube exists in the developing limb bud. Here, Shh is secreted from the posterior margin of the bud in the zone of polarising activity (ZPA). This forms an antero-posterior gradient in the limb bud. Loss of function mutations to *SHH* cause a loss of digits, while mutations in *GLI3* cause a gain of digits resulting in polydactyly. Polydactyly is present in at least 70% of BBS patients yet none of the mouse BBS mutants produced to date show any extra digits.

Understanding why BBS patients develop polydactyly, and why it is always post-axial (extra little finger or toe), will add to our knowledge of the role of ciliary proteins in Shh transduction, if indeed this is the cause of the polydactyly. While some ciliary and IFT proteins are crucial for Shh transduction, there are 1,000 proteins in the ciliary proteome, and these are not all involved with the pathway. Understanding which genes are involved, and which aren't, will help delineate the precise role of ciliary components in the Shh pathway.

Genital abnormalities

98% of BBS patients have malformed external genitalia (Beales et al., 1999). In males, this includes micropenis, small and undescended testes, and hypospadias (mispositioning of the urethral meatus). *Shh* null mice fail to outgrow a genital

tubicle, the precursor to the penis (Haraguchi et al., 2001). Perriton et al showed that transplanting the urethral epithelium to the limb bud in chick induced mirror-image duplication of the digits, implying that Shh acts as a morphogen in genital development too (Perriton et al., 2002). Also, it shows how Shh signalling in genital development is analogous to that of the limb. The genital and limb phenotypes seen in ciliopathies such as BBS and MKS might have a shared aetiology in aberrant Shh signalling. Evidence for this speculation comes from comparing BBS and Alstrom syndrome (ALMS). ALMS is often misdiagnosed as BBS because the patients show obesity, blindness, deafness, and kidney disease. However, ALMS patients tend not to develop polydactyly, genital anomalies, or mental retardation; the three features likely attributable, at least in part, to faulty Shh signalling.

Ciliary involvement in Wnt signalling

In addition to Shh signalling and platelet derived growth factor (PDGF – not described here) signalling, the cilium is also important for both canonical and non-canonical Wnt signalling. The canonical Wnt pathway, like Shh, is involved in many contexts and employs secreted ligands which regulate cell fate and patterning during development, and can cause cancer in adulthood when overactivated. The non-canonical Wnt, or planar cell polarity (PCP) pathway, is less well understood in vertebrates, but is important for patterning cells throughout an epithelial plane, such as in the lumen of the kidney tubule or hair cells in the inner ear.

In the canonical Wnt pathway, extracellular Wnt ligands bind to the membrane receptor Frizzled, activating cytoplasmic Dishevelled (Dvl) protein. Activated Dvl inhibits the β-catenin destruction apparatus, consisting of Axin, GSK3β, and APC. β-catenin is then able to enter the nucleus where it binds its transcriptional co-factors TCF and LEF to induce transcription of downstream target genes (Widelitz, 2005). These targets are often associated with cell proliferation, maintenance of stem-cell characteristics, and survival.

Non-canonical Wnt, or PCP, signalling relies on a slightly different mechanism, despite many shared pathway components. While the canonical pathway is well characterised and mapped out in a linear pattern, PCP is much less clear-cut, and different pathway components are important in different tissue and developmental contexts. Vertebrate PCP signalling also requires Wnt ligands, but uses different members of the family (e.g. canonical Wnt ligands include Wnt4, 6, and 8; while PCP ligands include Wnt5a, Wnt9, and Wnt11). Dvl localises to the plasma membrane in PCP signalling via its DEP domain, where it is activated by Frizzled combined with a co-receptor, Knypek (Wong et al., 2003; Wong et al., 2000). Dvl then activates GTPases such as RhoA, which reorientate the cytoskeleton (Habas et al., 2003). It can also activate the JNK pathway which can induce expression of downstream genes associated with cell polarity (Yamanaka et al., 2002). Figure 9 outlines the main steps in canonical Wnt and PCP pathways.

PCP signalling has been well characterised in *Drosophila*, where it polarises the growth of bristles and hairs, as well as photoreceptors in the eye, throughout the plane of epithelia. Its importance in vertebrates has only been considered more recently. It plays a key role in the gastrulation movements of the early embryo, where it is essential for the convergent-extension movement of cells (Jessen et al., 2002). This involves mediolateral intercalation of mesodermal cells, which converge at the midline and then elongate along the anteroposterior (AP) axis.

PCP signalling is involved in other areas of organogenesis where cells are polarised in the epithelial plane. Examples include: alignment of the stereociliary bundles on the hair cells in the cochlea; closure of the neural tube, and orientation of the mitotic spindles of renal tubular cells (Fischer et al., 2006). Saburi et al (2008) created a mouse mutant of the PCP gene *Fat4*, which developed cystic kidneys as a result of disoriented cell divisions and tubule elongation (Saburi et al., 2008).

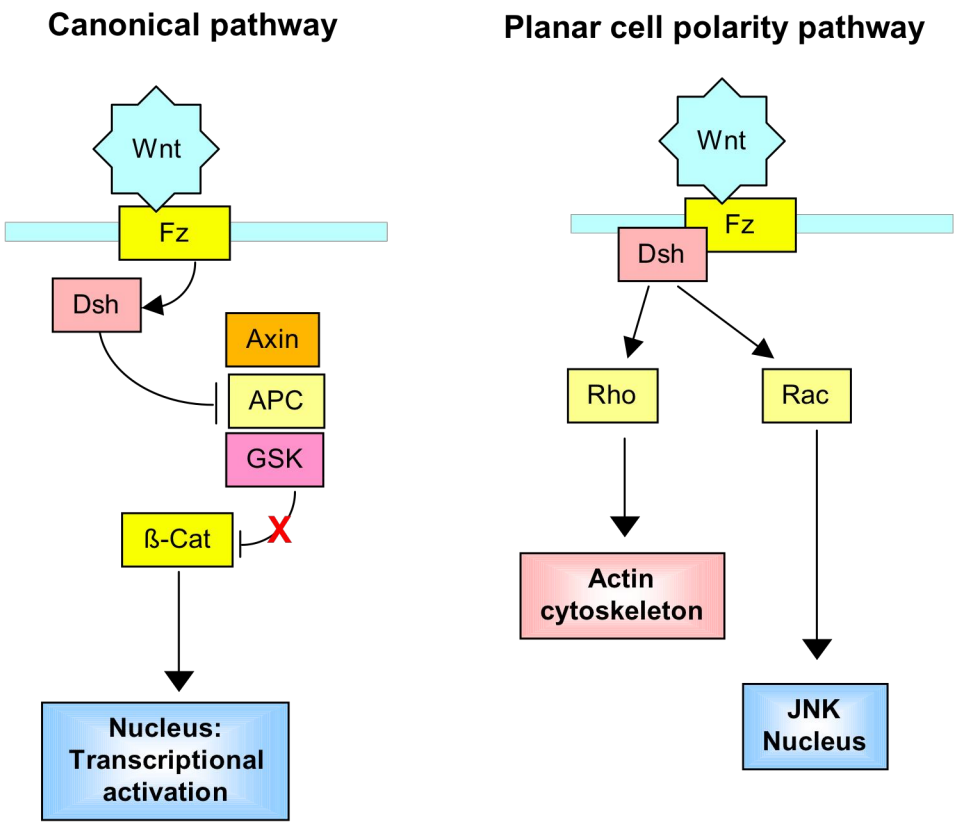

Figure 9. Wnt signalling pathways

In the canonical pathway, Wnt binds to its receptor Frizzled (Fz) that activates cytoplasmic Dishevelled. This inhibits the destruction complex consisting of Axin, APC, and GSK3β, preventing the destruction of cytoplasmic β-catenin. β-catenin then enters the nucleus and activates transcriptional targets by association with TCF and LEF. In the PCP pathway, Wnt binds to Fz, which recruits Dvl to the plasma membrane. This then activates RhoA, which remodels the cytoskeleton, polarising the cell; or Dvl activates Rac1, which can activate JNK, which enters the nucleus and activates downstream targets associated with cellular differentiation.

Mouse PCP pathway mutants, such as *circle tail*, *loop tail*, and *Dvl1* and *2* knockouts, display neural tube defects (NTDs) such as spina bifida (failure of the posterior neural tube to close), craniorachischisis (failure of the entire neural tube to close), and exencephaly (failure of the anterior neural tube to close). These null mutants tend to be embryonic or perinatal lethal. In humans, mis-sense mutations in *VANGL1*, a PCP gene related to *VANGL2*, whose homologue in mouse is mutated in *loop tail*, causes NTDs such as spina bifida (Kibar et al., 2007).

Konig and Hausen (1993) were the first to implicate cilia in planar polarity when they showed that the polarity of *Xenopus* epithelial cells aligned with the direction

of ciliary beating, although they did not know at the time that this involved PCP signalling (König and Hausen, 1993). Cano et al showed that the subcellular localisation of β-catenin was altered in *Ift88* mutant mice, and that this affected tissue organisation in the pancreas (Cano et al., 2004).

Simons et al (2005) showed that Inversin (NPHP2) localised to the cilium and acted as a molecular switch between the canonical and PCP pathways (Simons et al., 2005). Inversin inhibits canonical Wnt signalling by facilitating the degradation of cytoplasmic Dishevelled (Dvl). They showed that fluid flow in renal cells increased the level of Inversin in cultured kidney cells. They speculated that urine flow in the developing renal tubule terminates canonical Wnt signalling in favour of PCP signalling, which then patterns the tubule to give it its filterative capacity. In ciliopathy mutants, unopposed canonical Wnt signalling may suppress terminal differentiation of tubular cells, leading to cyst formation.

Ross et al (2005) showed that BBS proteins were involved in PCP signalling (Ross et al., 2005). A proportion of *Bbs4* null mice phenocopied PCP mutants such as *loop tail* (*Vangl2*, PCP receptor, mutant). These *Bbs4* mutant mice had open eyelids at birth, exencephaly, and misorientated stereociliary bundles. Compound $Bbs4^{+/-}$;$Ltap^{+/-}$ heterozygotes recapitulated these phenotypes, whereas either single heterozygote was not phenotypic, implying a genetic interaction between the two genes. They also showed that Vangl2, a membrane-bound receptor involved in PCP signalling, localises to the cilium. Park et al extended this by finding that mutations in two PCP genes, *inturned* and *fuzzy*, abrogated PCP signalling, as well as causing Shh-deficient phenotypes, which they attributed to a ciliogenesis defect (Park et al., 2006).

Two papers have directly linked canonical Wnt signalling to the primary cilium. Gerdes et al showed that suppression of *bbs1*, *bbs4*, *bbs6*, and *Kif3a* resulted in stabilisation of β-catenin and upregulation of TCF-mediated transcriptional activity, indicative of over-active canonical Wnt signalling (Gerdes et al., 2007). Corbit et al showed that canonical pathway components β-catenin and APC localised to the cilium (Corbit et al., 2008). They showed that *Ofd1* null cells

were stimulated by exogenous Wnt ligand five times more than wild type cells. They attributed this to the absence of cilia in these cells, and proposed that the cilium acts to inhibit canonical Wnt signalling, in contrast to its role in Shh signalling. This suggests that knocking out ciliary proteins relieves this brake, causing excess canonical Wnt pathway activity.

Mechanosensory functions in the kidney

In the developing kidney, cells divide rapidly to produce the branched tubules required for filtration. As the embryo develops, urine begins to flow through the tubules as the kidneys begin to function as organs of excretion and osmoregulation. The onset of flow is thought to reduce cell proliferation and begin to induce terminal differentiation of tubular cells. This change of fate coincides with a shifting emphasis from canonical to non-canonical Wnt signalling (Simons and Walz, 2006). Primary cilia projecting from tubular epithelial cells into the lumen bend as fluid flows over them (Yoder, 2007). This bending opens calcium channels in the membrane and causes a flux of intracellular calcium as cytoplasmic stores of calcium are released by calcium-induced calcium release.

Li et al placed IMCD3 (inner medullary collecting duct) cells in a flow chamber and passed a fluid flow over the cells (Li et al., 2007a). They found that cells expressing siRNA against *ALMS1*, the causative gene for Alstrom syndrome (blindness, deafness, obesity, diabetes, renal cysts), failed to produce a calcium spike, whereas calcium was released in control cells. The kidneys of knockout mice were cystic, and had increased levels of proliferation and apoptosis, which resulted in impaired function, evidenced by proteinurea.

Kidney disease is one of the most prevalent features of ciliopathies and is the most common cause of morbidity and mortality. A fuller discussion of the aetiology of kidney disease is presented in Chapter 6, but I will briefly introduce the topic here. Polycystic kidney disease (PKD) affects between 1 in 500 and 1 in 1,000 people and results in the growth of large cystic lesions, mainly in the loop of

Henle, which impair the ability of the kidney to filter the blood. This can result in chronic renal failure resulting in uraemia (accumulation of toxic waste products in the bloodstream), which poisons the brain and can result in coma and death. Currently, the only treatments are dialysis, which is time consuming, invasive, and expensive; and transplantation, but with a limited supply of organs and the risk of rejection, this is not an ideal treatment either. Several drugs inhibiting cystogenesis are in preclinical and clinical development. These are in Chapter 6. Figure 10 illustrates cystic kidneys in a foetus with MKS.

Figure 10. Cystic kidneys in an MKS foetus.

MRI scan showing cystic kidneys (bracket) and encephalocele (arrow) in a foetus with MKS. Taken from (Gupta and Jain, 2008).

Obesity

Obesity is one of the primary features of two ciliopathies whose diagnosis is often confused: BBS and Alstrom syndrome (ALMS). The frequency of overweight in BBS varies by study from 72% (Beales et al., 1999) to 91% (Green et al., 1989). The differences likely reflect different criteria classifying obesity. Beales et al found 52% of patients had a BMI (body mass index) of over 30 (classified as obese) and 16% had a BMI greater than 40 (morbidly obese). Fat tended to be distributed around the trunk and hips. Childhood obesity is present in 95% of

ALMS patients (Joy et al., 2007). Therefore, obesity is a common thread amongst certain ciliopathies, but its precise cause is not clear.

The causes of obesity in BBS are thought to arise from hyperphagia (overeating). This may stem from a defect in the satiety centre of the hypothalamus, in which ciliated neurons regulate the feeling of satiety and hunger, and control feeding behaviour accordingly (Davenport et al., 2007). Anecdotal reports claim that BBS patients rarely feel full, even after a large meal, and so cannot avoid overeating. Strict caloric restriction is required to prevent morbid obesity ensuing.

Grace et al found no difference in energy metabolism between BBS patients and controls matched for BMI, although patients tended to be much less physically active, likely contributing to their overweight (Grace et al., 2003). Studies of mouse models of BBS have indicated that they consistently eat more than their wild-type littermates and develop obesity progressively from an early onset. Rahmouni et al found *BBS2*, *4*, and *6* null mice to have low locomotor activity and increased levels of circulating leptin, a hormone that regulates satiety (Rahmouni et al., 2008). Adding exogenous leptin to wild type mice reduced bodyweight by around 10% in a 4-day period, but it had no effect on BBS mutant mice, regardless of underlying mutation. This suggested that BBS mice were leptin-resistant and the hypothalamic neurons were not responding to the signal, resulting in uncontrolled appetite and a persistent feeling of hunger. They also showed that this leptin resistance contributed to hypertension in the mutant mice, another feature of BBS.

A naturally occurring mouse mutant of *Alms1* exists known as *Fat aussie* (*Foz*) (Arsov et al., 2006). This mouse also had hyperphagia and obesity, as well as insulin insensitivity resulting in type 2 diabetes. In addition, the sperm of males were aflagellate, causing infertility, as is the case for BBS null mice. The subcellular localisation of Alms1 reveals that it has a ciliary and basal body distribution, although fibroblasts from affected individuals show no defects in cilia formation or the cytoskeleton (Hearn et al., 2005).

Berbari et al found that G-protein coupled receptors failed to localise to primary cilia in BBS mutant mice (Berbari et al., 2008b). This included melanin concentrating hormone receptor 1, a protein involved in the regulation of feeding behaviour. They suggested that this could result in hyperphagia-induced obesity.

Romano et al found that *Alms1* was expressed at highest levels in preadipocytes, but treating adipocytes with adipogenic factors had no effect on the gene expression of *Alms1*. This suggested that Alms1 might have a role in the transition from preadipocytes to adipocytes. Forti et al (2007) showed that *BBS1-9* and *BBS11* were expressed in adipocytes, and that transcript levels increased 2- to 4-fold during differentiation of adipocytes (Forti et al., 2007).

Davenport et al provided the first potential cell biological insight into the mechanism of ciliopathic obesity. They knocked out *Kif3a*, thereby completely ablating cilia, specifically in hypothalamic neurons expressing POMC (pro-opiomelanocortin), a type of neuron negatively regulating appetite (Davenport et al., 2007). They found that these mice had one specific phenotype: uncontrolled eating leading to obesity. While BBS knockout does not have as dramatic an effect on ciliogenesis as *Kif3a*, it is clear that cilia are important in this class of neuron for appetite regulation, and suggests a potential role for BBS and ALMS proteins in these neurons. Currently, no conditional mouse models exist for BBS in which this can be tested.

There seem to be potential roles for BBS proteins in appetite sensation and fat storage. The data supporting a role for the proteins in the hypothalamus are more extensive and convincing, and fit with the observation of overeating.

Other features of ciliopathies

Skeletal dysplasia

Earlier, I classified the ciliopathies with skeletal involvement into their own category, consisting of JATD, EVC, and OFD1. JATD and EVC show similar skeletal and extra-skeletal features, as does short-rib polydactyly syndrome,

although the gene for this has not yet been identified. JATD patients have a small rib cage and narrow chest, which obstructs the lungs and can cause death by asphyxiation in infancy. In addition, the long bones, such as the femur, are short, as are the bones of the hands and feet. EVC patients also have short limbs and short ribs, and have dental and craniofacial abnormalities.

Ruiz-Perez et al showed that Indian hedgehog (Ihh) was expressed normally in the growth plates of developing bones, where it signals to induce prechondrocyte proliferation (Ruiz-Perez et al, 2007). However, *Patched1* and *Gli1* were downregulated in the bones. Similarly, Beales et al showed that these target genes were downregulated in zebrafish morphants for *ift80*, a gene mutated in JATD (Beales et al., 2007).

The importance of cilia in Ihh signalling during bone development was confirmed by Koyama et al, who conditionally ablated *Kif3a* expression in cartilage (Koyama et al., 2007). They showed mutant growth plates lacked proliferating cells seen in controls, and lacked expression of important downstream genes such as collagen X, VEGF, and matrix metalloproteinase (MMP). Haycraft et al ablated *Ift88* in the limb mesenchyme, which resulted in polydactyly and shortened limbs (Haycraft et al., 2007). They showed that the polydactyly was due to Shh pathway disruption, while Ihh affected the extent of limb outgrowth. These data conclude that IFT is essential for normal skeletal development. The fact that some ciliopathies affect bone growth more than others might reflect different expression patterns of these genes.

Sensory deficits

Retinitis pigmentosa (RP) involves progressive loss of vision, first manifesting as night blindness, then tunnel vision, before progressing to complete loss of sight. It is a primary feature of several ciliopathies, including BBS, ALMS, and SNLS. The average age of complete blindness in BBS patients is fifteen (Beales et al 1999). The connecting cilium in the rod cells carries rhodopsin molecules into the

outer segment of the rod cell. Defects in ciliary transport cause these cells to die by apoptosis resulting in progressive loss of vision.

Abd-El-Barr et al showed that rhodopsin is not transported from the cell body to the outer segment in *Bbs4* null mice, and that these cells subsequently die (Abd-El-Barr et al., 2007). In addition, they noticed defects in synaptic transmission from the photoreceptors to the visual neurons.

Bainbridge et al provided the first evidence of effective gene therapy for retinal degeneration caused by a ciliopathy – LCA (Bainbridge et al., 2008). The underlying mutation was in *RPE65*, which encodes a ciliary protein expressed in the retina. They were able to reconstitute the sight of three patients by injecting an adenoviral vector underneath the retina of the patients. This raises the possibility of treating the sight of BBS patients using gene therapy.

Deafness is also present in several of the ciliopathies, most notably Alstrom syndrome. Most patients develop sensorineural hearing loss and about 10% become profoundly deaf (Marshall et al., 2007). Ross et al found that half the *Mkks* null mice tested failed to respond to auditory stimuli, compared to none of the controls (Ross et al., 2005). They found that BBS patients could not detect high frequency sounds, and adolescent patients had a hearing age of elderly individuals.

Anosmia is another sensory deficit of BBS patients, reported by two separate groups (Kulaga et al., 2004; Nishimura et al., 2004). Kulaga et al showed that BBS patients had partial or complete anosmia, with 50% being unable to detect odours at all. *Bbs4* null mice had a reduced ciliated border of the olfactory epithelium, which resulted in the trapping of olfactory receptor molecules in the cell bodies of olfactory receptors.

Hirschsprung's disease

Hirschsprung's disease (HSCR) has been reported in up to 45% of BBS patients (de Pontual et al., 2007), but a more realistic estimate of prevalence is 5-10% (unpublished observations of P. Beales). This incidence is extremely high compared to the general population where it only affects 1 in 5,000 children (0.02%).

HSCR arises when neurons fail to colonise the intestine, usually the colon, resulting in a lack of peristaltic activity and blockage of the gut, leading to chronic constipation and megacolon at birth and during infancy. The only treatment is surgical resection of the aganglionic segment, or colostomy. Stem cell therapies to reintroduce neurons into the gut are underway in mouse models, but their efficacy is uncertain and translation to humans is a long way off (Gershon, 2007).

Craniofacial dysmorphology and ciliopathies

Craniofacial dysmorphology is variable and can manifest as obvious and extreme, or subtle and hard to distinguish. OFD1 is an X-linked dominant lethal ciliopathy, meaning all patients are heterozygous females. Patients present with severe craniofacial involvement, including cleft palate and a shortened, hypoplastic midfacial region. Ferrante et al produced an *Ofd1* mouse knock-out with severe cleft-palate and a disorganised brain, in addition to polydactyly, renal cysts, and randomised laterality.

Abnormal craniofacial features have been reported in BBS patients by several independent investigators, as well as anecdotally by family members (Beales et al., 1999; Lorda-Sanchez et al., 2001). In contrast to OFD1, the features are variable and subtle, and it often takes a trained dysmorphologist to accurately describe the face, even though there is often an obvious gestalt, or overall appearance. Beales et al described the facies of BBS patients as having: "deep-set eyes, hypertelorism, downward slanting palpebral fissures, a flat nasal bridge with anteverted nares… a long philtrum and thin upper lip". Lorda-Sanchez et al came to similar conclusions with their analysis of the BBS face and added small mouth,

malar hypoplasia (small cheek bones) and retrognathia to the facial characteristics. Figure 11 shows some photographs of adults and children with BBS.

Figure 11. BBS patient faces.

Four children (top row) and adults (bottom row) with BBS. In addition to the excess fatty tissue, the patients have deep-set eyes, a small nasal bridge, retrognathia, thin lips, and a small jaw. Taken from Beales et al (1999) and the LMBBS society pamphlet.

The zebrafish as a model for studying human disease

The zebrafish is a small (3-4cm long as adult), striped fish originally derived from freshwater lakes of the Himalayan foothills. It has come to prominence in biology because of its embryos; each female can lay hundreds of eggs in a single spawning. The embryos are optically clear and so development can be observed in real time, and because they develop *ex vivo*, it is possible to manipulate the embryo as it grows. Development is rapid and all the major organ primordia have formed by 30 hours post fertilisation (hpf). The embryo hatches from its chorion and becomes free-swimming at about 2.5 days post-fertilisation (dpf). Until 5 dpf, the embryo feeds on its yolk supply, after which it begins to feed on exogenous sources. Figure 12 shows some stages of zebrafish development.

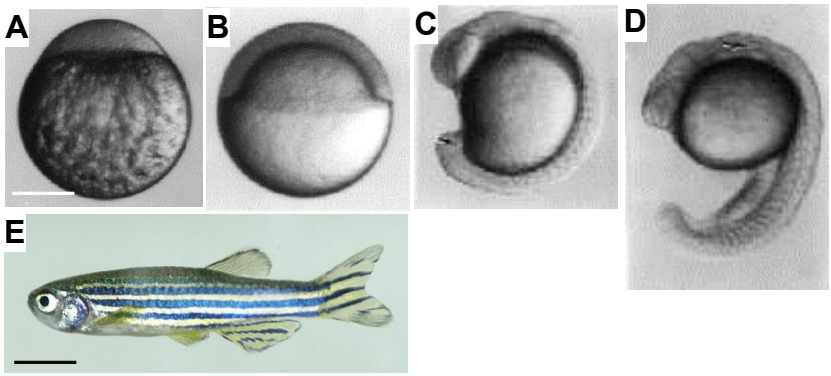

Figure 12. Stages in zebrafish embryogenesis.

A. fertilised 1-cell stage; **B.** dome stage (5hpf); **C.** 12 somites (15 hours); **D.** 20 somites (19 hours); **E.** adult zebrafish. Taken from http://www.zfin.org (July 2008) and http://www.bio.umass.edu/biology/kunkel/fish/zebra/devstages.html. Scale bars: A-D = 200μm; E = 0.5cm.

Genetic knockdowns can easily be made by injecting an antisense morpholino oligonucleotide (MO) against the gene of interest into the developing embryo at the 1 to 2-cell stage. This oligo is inherited by each daughter cell and can provide efficient knockdown of expression for around 3 days. Instead of ribose, the MO contains a 6-carbon morpholine ring in the oligonucleotide backbone. This prevents it eliciting an exonucleolytic response by the host, and allows the MO to persist in the embryo to provide longer lasting knockdown than conventional RNAi. MOs can be targeted to block translation by binding at, or just upstream of, the start AUG sequence of the mRNA. Alternatively, they can block splicing by binding across a splice donor or acceptor site at an intron-exon boundary. This produces a mature mRNA, either without an exon, or with a translated intron, both of which can lead to frameshifts resulting in a non-functional protein product.

Zebrafish morphants have been used to model several human genetic diseases, including BBS. Mouse models only exist for certain BBS genes and our lab only has access to *Bbs4* and *Bbs6* mutants, of which only *Bbs4* nulls show any embryonic phenotypes. These mutants breed very poorly and so reliably obtaining null embryos is difficult. The zebrafish can generate knockout models of any gene quickly, and with the right control experiments, it is reliable. The

physiology of all the major organ systems is homologous to mammals, and the same signalling pathways are present and function in similar roles.

There are several disadvantages to using zebrafish. First, it is harder to extrapolate findings to humans. Second, its rapid development means perturbations to the genetic program early on can have more devastating effects than in mammalian embryos, as there is less time for compensation by other genes or pathways. Third, zebrafish lack limbs so studies of polydactyly cannot be performed. Fourth, a lack of genetic mutants means only studies on embryonic, and not adult, phenotypes can be carried out.

Zebrafish ciliary phenotypes

Several zebrafish genetic mutants from mutagenesis screens have been identified in which the genes were subsequently found to encode ciliary proteins (Drummond et al., 1998; Zhao and Malicki, 2007). Disruption to ciliary genes in zebrafish gives stereotypical morphological phenotypes, including a down-curved body axis, shortened and flattened somites (the segmented blocks of muscle in the body axis), kidney cysts, and randomised left-right asymmetry (heterotaxia). As a group, these phenotypes are specific and can be used as a diagnostic toolkit if a gene has suspected ciliary involvement. Figure 13 shows some of these phenotypes in ciliary mutants.

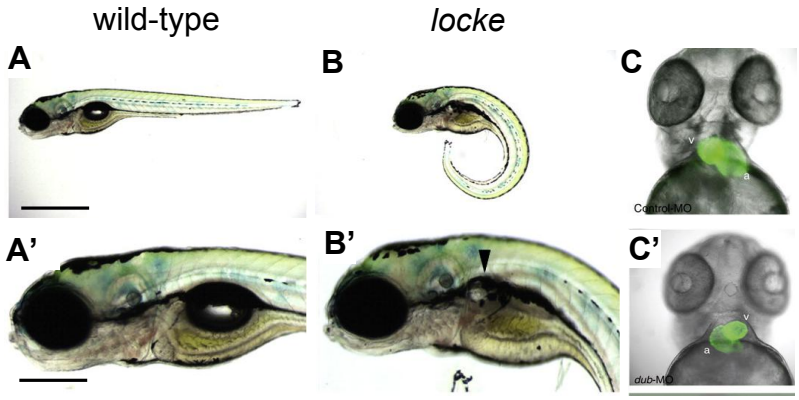

Figure 13. Zebrafish ciliary mutant embryonic phenotypes.

A and **A'**: wild-type zebrafish larva at 5dpf. **B**: *locke* mutant showing down-curved body axis and, **B'**: kidney cyst (arrowhead). **C**: control zebrafish showing right-sided ventricle and left-sided atrium in the heart. **C'** *dub* morphant with reversed heart looping compared to control (C). Taken from Sullivan-Brown et al (2007) and Oishi et al (2007). Scale bars: A,B = 1mm; A',B' = 500μm.

Objectives of this project

The study of ciliopathies has intensified since discovering the aetiology of BBS in 2003. Many new ciliopathy genes have been identified since then, but their functions are, at best, poorly understood, and mostly completely unknown. My investigations had the following objectives to discover some more about ciliopathy protein function, centering around the use of the zebrafish as a model system:

1) **To uncover the cellular and molecular basis for craniofacial dysmorphology in BBS patients**. In collaboration with Professor Peter Hammond, then at the UCL Eastman Dental Institute, I analysed data from facial scans of BBS patients and controls, and BBS null mice. I then modelled these defects using the zebrafish.

2) **To examine the novel role of BBS proteins in neural crest migration**. I took the results from the facial data in humans, mice, and fish to investigate a potential new role of BBS proteins in neural crest cell development. This led me to uncover an important role for BBS8 in cell migration.

3) **To establish the molecular basis of these migration and patterning defects.** I investigated the role of Bbs8 in two important signalling pathways: Shh and PCP.

4) **To use the zebrafish to develop a system for studying the kidney disease common to all ciliopathies and use this model to test candidate drugs**.

5) **To use the zebrafish to investigate several genetic interactions of ciliopathy and non-ciliopathy proteins, and to test the function of putative ciliary proteins**.

Chapter 2: Materials and methods

Materials

Reagents

20x SSC	3M NaCl, 0.3M sodium citrate (pH 7.0)
DNA ladder	0.1μg/μl DNA ladder (Invitrogen), 20% loading buffer in water
dNTP mix (10x)	2mM each: dATP, dCTP, dTTP, dGTP
Fish block	10% goat serum, 1% DMSO, 0.5% Triton X100, PBST
Fish water	UV illuminated, filtered through activated charcoal, 60μg/ml Instant Ocean salt mix
Hyb solution	Prehyb solution plus 5mg/ml yeast T-RNA, 50mg/ml heparin (pH 6.0)
Hybridisation buffer	50% formamide, 5x SSC, 0.1% Tween 20, 5mg/ml yeast RNA, 50mg/ml heparin, pH 6.0
LB agar	2% agar, LB broth
LB broth	1% bactotryptone, 0.5% bactoyeast, 1% NaCl
Loading buffer	20% glycerol, 0.25% bromophenol blue
Maleic acid buffer	150mM NaCl, 100mM maleic acid (pH 7.5)
PCR buffer (10x)	100mM Tris-HCl, 400mM NaCl, 15mM $MgCl_2$, 2.5mM spermidine
Prehyb solution	50% formamide, 5x SSC, 0.1% Tween-20 (pH 6.0)
RIPA buffer	25mM Tris-HCl (pH 7.6), 150mM NaCl, 1% NP-40, 1% sodium deoxycholate, 0.1% SDS, protease inhibitor cocktail (Roche)
Tail lysis buffer	100mM Tris (pH 8.5), 5mM EDTA, 0.2% SDS, 200mM NaCl, 100μg/ml Proteinase K
TE buffer	10mM Tris-HCl, 1mM EDTA (pH 8.0)

Tissue culture

Cell lines used and culture conditions

For Shh responsiveness assays NIH3T3 (immortalised mouse embryonic fibroblast) cells were used. Some experiments were also performed on two primary fibroblast lines taken from two adult patients with null mutations in *BBS8*. Cells were maintained in 75cm^2 tissue culture flasks with 20ml of DMEM supplemented with 10% BCS and 1% Penicillin and Streptomycin. Once every 3 days cells were washed with PBS and detached from the flask using trypsin and EDTA. Cells were replated at a dilution of 1:10. For luciferase assays cells were cultured in 48 well plates at a seeding density of 50,000 cells per well. For Gli3-processing assays, cells were grown in six well plates.

To check that *Bbs8* was knocked out in both primary and stably transfected cells, I performed quantitative real-time reverse transcriptase PCR (qRT-PCR). This showed that *BBS8* mRNA (normalised to *GAPDH*) was present at 5% of the wild type level in primary fibroblasts, and at 8% of the endogenous level in control stably transfected cells.

For Smoothened immunolocalisation, IMCD3 (mouse inner medullary collecting duct immortalised cells) and HEK (human embryonic kidney) cells were used. IMCD3 cells were grown in DMEM:F12 1:1 media (Invitrogen). MDCK cells were grown in DMEM. 10% FBS was used to supplement both media.

shRNA silencing of gene expression

In order to silence expression of *Bbs* genes in tissue culture cells we purchased constructs from Open Biosystems against *BBS2,3,4,5,6,7,* and *8*, and *IFT80*, designed to target both human and mouse homologues of these genes. These constructs use a modified form of the microRNA, *mir-30*, whose sequence-specific binding region has been replaced with the sequence specific to the gene of interest. This degrades mRNA by the Dicer/RISC pathway leading to effective knockdown of protein expression of around 90% (www.openbiosystems.com). The shRNA sequence is contained within the pSM2 plasmid and is under the control of the U6 upstream promoter and the plasmid contains Kanamycin and Chloramphenicol bacterial selectable markers, as well as a neomycin cassette to select stably transfected eukaryotic cells.

In order to monitor the efficiency of shRNA uptake in transiently transfected cells the 110bp fragment containing the shRNA sequence and flanking regions was cloned into the LMP vector, a micro-RNA adapted retroviral vector. This has the advantage of being integrated into the host genome and co-expressing GFP to monitor transgene expression levels. See the "Cloning" section for details of how this was achieved.

The expression levels of the shRNAs were tested by the intensity of GFP fluorescence. This was slightly variable between constructs but the constructs used extensively – *Bbs8* and *Ift80* – were both expressed at high levels in around 90% of cells transiently transfected. In order to assess functional efficacy of the shRNAs the constructs were transiently transfected into IMCD3 cells and immunostained for PCM1. This protein normally localises to the basal body in cells but has been shown to be dispersed when BBS4 is knocked down (Kim et al 2004). This was expected to be the case for other BBS knockdowns. Unfortunately, this assay did not work and gave inconclusive results, even in untransfected cells.

To validate the efficiency of knockdown in *Bbs8* shRNA treated cells, RNA was extracted from the cells and used to generate cDNA using Trizol (Invitrogen) according to the manufacturer's protocol. cDNA was reverse-transcribed from total mRNA using SuperScript reverse-transcriptase (Invitrogen) primed with random hexamers (Invitrogen). Quantitative RT-PCR was then performed using an ABI Prism 7000 (Applied Biosystems) to measure the level of *Bbs8* transcript in cells. Although this is not a direct assay, as the microRNA construct is thought to work partially by blocking translation and partly by causing RNA degradation, the results showed around 90% knockdown of Bbs8 transcript. The Bbs8 antibody is too unreliable to quantify knockdown by Western Blot but would be the best way to reliably measure shRNA efficacy.

Transient transfection of cell lines

Cell lines growing in 75cm^2 flasks were trypsinised and plated onto 6, 24, or 48 well plates. If cells were to be immunostained, they were grown on glass coverslips. HEK cells were grown on coverslips coated in 0.1% poly-L-lysine (Sigma) in PBS. Cells were grown to 95% confluence and then transfected with plasmids using Lipofectamine 2000 reagent (Invitrogen) according to the manufacturer's protocol. After transfection, cells were kept in serum-free medium for 5 hours before replacing with normal media. Cells transfected with

GFP-expressing constructs were visualised with an inverted fluorescence microscope 24 hours after transfected to monitor transfection efficiency.

Production of stable cell lines

In order to generate a cell line in which every cell constitutively expressed shRNA against *Bbs8* and *Ift80*, I created stably transfected cell lines in both 3T3 and MDCK (Madin-Darby Canine Kidney) cell lines, both of which are ciliated. Cells were transiently transfected with the shRNA construct in the LMP vector in 100mm dishes. Five days after transfection, the selectable marker Neomycin was used to select cells in which the shRNA cassette had inserted into the genome. Antibiotic selection continued for two weeks to ensure all transiently transfected cells were eliminated. Neomycin was used at 2ng/ml for 3T3 cells and 2.5ng/ml for MDCK cells.

Because the LMP vector expresses GFP linked to the expression of the shRNA, the intensity of GFP fluorescence is directly proportional to the amount of shRNA expressed. Cells were then sorted using a Coulter Altra FACS machine into low-GFP expressing and high-GFP expressing populations. Cells expressing extremely high levels of GFP were discarded because of potential toxicity from over-expression of foreign DNA. A single positive cell was sorted into each well of two 96-well plates for all samples.

These cells were then incubated in 96 well plates until a sizeable colony had grown from the single sorted cell. Viability after sorting was around 80% for both cell types. Once colonies had established in the 96 well plates, the cells were trypsinised and replated in six well plates. Twelve clones for each sample were grown and assessed for GFP fluorescence. 100% of these cells uniformly expressed GFP and so two clones for each sample (BBS8 GFP low and GFP high, IFT80 GFP low and GFP high, in both 3T3 and MDCK cell lines) were plated in 75cm^2 flasks and used for subsequent experiments. High GFP expressing cell lines were used for most assays. These cell lines will be referred to as: *Bbs8* shRNA and *Ift80* shRNA.

Scratch wound healing assays

3T3 cells stably transfected with either control or *Bbs8* suppressing shRNA, or primary human fibroblasts taken from unaffected or *BBS8* null patients were seeded on 16mm glass coverslips in 12 well plates. Cells were grown to confluence and then starved overnight in medium supplemented with 0.5% serum. This was to prevent further cell proliferation, which could confound cell migration.

After starvation, a scratch was made in a straight line through the cells using a sterile P20 pipette tip. The cells were washed carefully once in PBS to remove detached cells and then re-immersed in low-serum growth medium. Cells were fixed at 0, 6, 24, 48, and 72 hours post-scratching in 4% PFA for 15 minutes at room temperature. Cells were blocked with 1% BSA in 0.1% TX-100 for 30 minutes at room temperature before incubation in Phalloidin-594 (Invitrogen) for 1 hour at room temperature to reveal the actin cytoskeleton.

To measure the degree of cell migration, cells were imaged at low power (10x objective) and the distance between opposing cells was measured using Zeiss AxioImager 4.5 software. An average of 10 measurements was taken and the width of the gap calculated at each time point for all cell types. The differences in gap width between control and *bbs8* mutant cells were analysed by t-test (Microsoft Excel).

Shh agonists

Three different agonists were used: 1) recombinant Shh peptide (R&D Systems) dissolved at 50μg/ml in PBS with 1% BSA. This gave a strong transcriptional response but was too expensive to use for repeated experiments. 2) Shh-conditioned media: this was made by transfecting COS-7 cells with a Shh-expressing plasmid. The cells then secrete the recombinant Shh into the overlying media, which, after five days, is removed and filtered. The presence of Shh

peptide in the aspirated medium was confirmed by Western blot with an anti-Shh antibody (1:200, Santa Cruz Biotechnology, CA, USA) shown in Figure 14. Shh protein was not present in untransfected COS-7 cells. 3) Purmorphamine is a synthetic molecule that binds directly to Smoothened (Smo) to activate downstream components of the cascade. This method gave the most consistent and reliable results, and its concentration could be most easily regulated and reproduced, so it was more commonly used in subsequent assays.

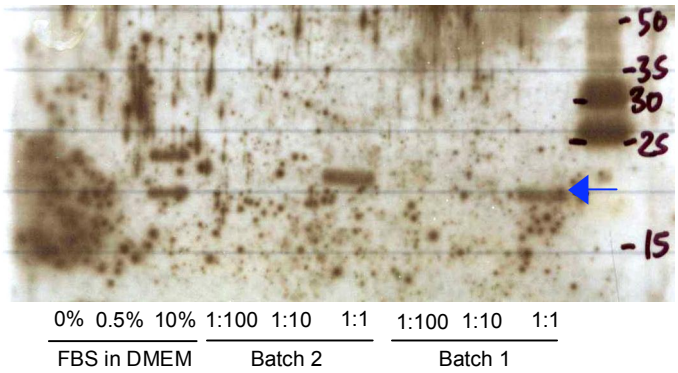

Figure 14. Recombinant Shh western blot

The arrow shows the position of the band corresponding to Shh protein (21kDa) in two independent batches of conditioned medium. 10µl of conditioned medium was taken from COS-7 aspirate (total medium produced was 10ml per batch) and mixed with an equal amount of 2x sample buffer.

A dose-response curve to differing amounts of purmorphamine (dissolved in 1% DMSO) and Shh-conditioned media was performed by adding 0, 0.1, 0.2, 0.5, 1, 2, or 5µM of purmorphamine, or 1:200, 1:50, 1:20, or 1:10 dilutions of Shh conditioned media to Shh-Light II 3T3 cells (see below) and performing a luciferase assay to assay Gli transcriptional activation. These results are shown in chapter 5.

From these results, it was ascertained that purmorphamine should be used at 0.5µM and Shh-conditioned media at a 1:20 dilution. This correlates with previously published work using these Shh pathway stimulants (Wu et al., 2004).

Luciferase reporter assays

For this assay, cells used were either transiently transfected with the luciferase reporter and an shRNA construct specifically knocking-down *Bbs8* (or a control shRNA), or stably transfected cells were used, which constitutively express shRNA against *Bbs8* (or control shRNA). In addition, the assay was tried with Shh-Light II cells (gift of James Briscoe, NIMR). These cells are stably transfected with the Gli-luciferase reporter and Renilla luciferase. Most of the results presented here used the cells stably transfected with the *Bbs8*-shRNA construct and transiently transfected with the luciferase and Renilla constructs, unless stated otherwise. This situation gave the most reliable results, as all the cells were deficient in Bbs8. If the shRNA was to be transiently transfected, there would still be some cells (around 20%) not expressing *Bbs8*-shRNA which would confound the results.

For the Gli activation luciferase assays, 50,000 cells were seeded on 48-well tissue culture plates to give 95% confluence 16 hours later. At this point, cells were transfected with 0.8μg of the Gli luciferase reporter. This construct consists of six Gli binding sites fused to the luciferase gene. When the Sonic Hedgehog pathway is activated, Gli1 binds to these sites to initiate transcription of luciferase. 25ng hCMV Renilla luciferase was co-transfected with the reporter to act as an internal transfection control.

For transfections, the plasmids were mixed with Lipofectamine 2000 reagent (Invitrogen) according to manufacturer's instructions. Cells were then incubated in serum-free media for 5 hours to uptake the plasmids. Serum-supplemented media was then added and the cells incubated overnight. The next day, when the cells had grown to confluence, they were starved in serum-free media for 24 hours to induce the growth of primary cilia. After this, the Shh-agonist was added to stimulate the Shh pathway. Non-confluent, or non-starved cells that fail to ciliate, do not respond to Shh stimulation (Ocbina and Anderson 2008).

Twenty-four hours later, the luciferase assay was performed using the Dual Luciferase assay kit (Promega, USA). Cells were lysed in their wells by adding

50µl of lysis buffer with shaking for 15 minutes. 20µl of lysate was added to each luminometer tube containing 100µl of luciferase reporter substrate. This substrate contains the luciferin that releases light in the presence of active luciferase enzyme. The intensity of this light is measured by the luminometer and correlates with the level of transcriptional activation. After the luciferase reading was taken, 100µl of Stop And Glow reagent was added to quench the firefly luciferase reaction and allow the luminometer to measure the activity of the Renilla luciferase.

The ratio of firefly luciferase activity to Renilla luciferase was then used to calculate the relative amount of transcriptional activity for each cell, controlling for differences in transfection level. Each experimental condition was performed in triplicate and each experiment was performed three times. The average of all runs was used and the standard deviation calculated.

Western blotting

Western blotting was performed on both cultured cells and embryo extracts. For embryo extracts, the tissue was first treated with 0.25% trypsin-EDTA for around 15 minutes to loosen cell contacts. It was then triturated with progressively narrower fine gauge needles to dissociate the cells. The trypsin was then inactivated by adding medium containing serum and the tissue was pelleted by centrifuging. 100µl of 2x Laemmli SDS-PAGE sample buffer containing 5% β-mercaptoethanol was added and heated at 95°C for 5 minutes to denature the proteins. For cultured cells, cells grown in 6 well plates were washed once in PBS and 100µl of 2x Sample Buffer heated to 100°C was added to each well. The cells were dislodged using a rubber stopper and decanted into 1.5ml eppendorf tubes. These were then heated at 95°C for a further 5 minutes to denature proteins.

The following protocol was the same for both embryo extracts and cultured cells. Samples were spun at 13,000 rpm for 5 minutes to pellet cell debris. 20µl of each sample was then loaded onto a 1mm thick 7.5% polyacrylamide SDS gel using

Rainbow molecular weight markers (Sigma). Gels were run for 1 hour at 200V. The proteins were then transferred to a nitrocellulose membrane (GE Healthcare) using 200mA of current for 2 hours in the cold room. The success of the Western transfer was assessed by staining with Ponceau Red solution. The membranes were then blocked for 3 hours in 5% skimmed milk powder in TBST. Primary antibody was diluted in block solution and the membranes were wrapped in plastic bagging and incubated overnight with rocking. Primary antibodies used were: anti-Gli3 H180 (Santa Cruz, detects both long and short isoforms of Gli3, used at 1:200), anti-Gli3 C20 (Santa Cruz, detects C-terminal isoform only, used at 1:200 – could not get any specific signal), anti-Shh (Santa Cruz, used at 1:1,000), anti-α-tubulin (Sigma, used at 1:5,000), anti-mTOR (Cell Signalling Technology, used at 1:1,000), anti-phospho-mTOR (CST, used at 1:1,000), anti-S6K (CST, used at 1:1,000).

Co-immunoprecipitation

IMCD3 and 3T3 cells were plated at a density of $5x10^5$ cells per well in six well plates. Cells were transfected with N- or C-terminally GFP-tagged BBS8 constructs using Lipofectamine 2000 reagent according to the manufacturer's protocol. Forty-eight hours later, cells were lysed in 1ml ice-cold RIPA buffer for 15 minutes on ice before dislodging with a rubber syringe plunger. Cells were transferred to an Eppendorf tube and spun at 13,000rpm for 5 minutes. 100µl of supernatant was removed to an Eppendorf. This sample served as the pre-IP lysate. 900µl of supernatant was transferred to a second tube. 1.5µg of anti-Gli3 antibody (Santa Cruz Biotechnology) was added to this tube and also to a separate tube containing buffer only. 20µl of protein A/G beads was added to these two tubes, which were then incubated overnight at 4°C on a roller.

The next day samples were spun down and the supernatant discarded. Pelleted beads were washed three times for one minute; vortexing, centrifuging and discarding the supernatant between each wash. The final pellet was resuspended in 50µl of 2x protein loading buffer. 20µl of each sample was loaded onto a 7.5% SDS-PAGE gel with their corresponding lysate. The membrane was probed with

an anti-GFP antibody to detect BBS8-GFP. If a band was present, BBS8 must have been immunoprecipitated with Gli3.

Immunocytochemistry

For immunocytochemistry on cultured cells; cells were fixed in either 4% PFA in PBS for 15 minutes or cold methanol for 5 minutes. Cells were blocked with 1% BSA in PBS with 0.1% Tx100 for 30 minutes before incubating with primary antibody in blocking solution for 1 hour at room temperature. Secondary antibodies used were anti-goat, rabbit, mouse, and rat IgGs conjugated to 488, 568, or 594nm fluorophores (all Invitrogen Alexa secondary antibodies).

For immunohistochemistry on wholemount zebrafish, dechorionated embryos were fixed in 4% PFA overnight at 4°C before blocking in 1% BSA, 2% sheep serum, 1% DMSO, and 0.5% Tx-100 for 1 hour at room temperature. Embryos were incubated in primary antibody overnight at 4°C, washed three times for 10 minutes in 0.5% Tx100 and then incubated in fluorescent secondary antibody for 1 hour at room temperature. Primary antibodies used were: anti-acetylated tubulin (Sigma, 1:1,000), anti-gamma tubulin (Sigma, 1:1,000), anti HuC/D (Invitrogen, 1:200), anti-GFP (Clontech, 1:500), anti-phosphohistone H3B (Millipore, 1:200).

Polymerase Chain Reaction (PCR)

PCR reactions were carried out in 96 well plates or tube strips. For most reactions the following mixture was used:

5-50ng DNA

1x PCR buffer

200μM dNTP mixture

5pmol of each primer

0.2μl Taq polymerase (Bioline)

Make up to 25μl in sterile water

Most PCR programs were carried out using a touch down program. Samples were denatured for 5 minutes at 95°C followed by ten cycles of amplification consisting of a denaturation step at 95°C for 30 seconds and an annealing step for 30 seconds starting at 65°C and decreasing by 1°C per cycle. This was followed by a 1 minute 72°C elongation step and a further 25 cycles with the annealing temperature at 55°C. Finally, a 10-minute elongation step at 72°C.

PCR products were checked on an agarose gel by electrophoresis. For most gels, 1% agarose was used dissolved in 1x TAE buffer by heating in a microwave followed by the addition of 0.5μg/ml ethidium bromide. Samples mixed with 6x loading buffer were loaded onto the hardened gel and a size marker was run alongside the DNA samples. DNA was visualised on a UV transilluminator.

Cloning

Cloning procedure

Primers with intrinsic restriction sites designed to fit into the vector of interest were designed to amplify the full-length coding region of the gene of interest. The PCR product was checked on an agarose gel, cleaned up using a Qiagel QIAquick gel extraction kit, and eluted in 30μl of water. This was then subject to restriction digestion to produce sticky ends. The vector was cut using the same enzymes and treated with 1μl of calf intestinal alkaline phosphatase for 30 minutes at 37°C to prevent recircularisation of the plasmid. Enzyme activity was quenched by denaturing at 65°C for 15 minutes. The insert and vector were then mixed in a 3:1 ratio and ligated for 3 hours at 14°C using T4 DNA ligase (Invitrogen).

2μl of the ligation product was used to transform JM109 chemically competent *E. coli* cells. For ligation products that would not transform with chemically competent cells, electrocompetent cells were used and electroporated. Transformations were left on ice for 10 minutes before heat shocking at 42°C for 40 seconds, left to recover on ice for 2 minutes and then mixed with 1ml LB

broth. This mixture was shaken at 37°C for 1 hour and then 50µl was spread onto antibiotic-containing LB agar plates.

Ten colonies were then picked at random and minipreps generated. Miniprep DNA was tested by restriction digest to check it had the gene of interest. This miniprep culture was then used to inoculate a maxiprep culture from which up to 500µg of plasmid DNA was recovered. This was dissolved in sterile water to yield a final DNA concentration of 1µg/µl.

Vectors used

pBS2 This was used to clone ESTs to make antisense riboprobes for *in situ* hybridisation.

pCS2+ This vector is designed for over-expressing genes in vertebrate embryos. It has a simian CMV promoter driving expression of the gene and a 3' polyA sequence.

pSM2 This vector expresses antisense shRNA under the control of a viral promoter.

LMP This vector is like pSM2 but contains a GFP cassette to identify transfected cells.

Sequencing

To check that plasmids contained the correct insert, and that it was in frame after PCR and cloning, the plasmids were sequenced. 200ng of plasmid DNA in 3µl of water was mixed with 5pmol of the forward or reverse sequencing primer, 1µl of BigDye premix containing the ddNTPs and polymerase, 2µl dilution buffer, and distilled water to 10µl. The tubes were placed in a thermocycler for 35 cycles of a sequencing program consisting of a 95°C denaturing step for 2 minutes followed by a cycle of denaturing from 20 seconds, annealing at 50°C for 10 seconds, and extension at 60°C for 3 minutes. The reaction mixture was topped up with sterile water to 20µl after PCR and desalted using a sephadex plate. Samples were then

sequenced on a MegaBACE capillary sequencer and the sequences analysed using Sequencher software.

Producing capped mRNA for injection

For over-expressing constructs in the zebrafish, the full-length cDNA was obtained either from Gene Service (Cambridge, UK), or by PCR amplification of the full open reading frame from a zebrafish cDNA library made from fifty 24hpf zebrafish embryos. PCR primers were designed to have restriction sites compatible for directional cloning into the pCS2+ expression vector. PCR products were digested for 2 hours at 37°C with the appropriate enzymes and then purified using a Qiagen PCR clean-up column to remove enzymes. The pCS2+ vector was cut with the same enzymes and purified with the same technique. A 3:1 molar ratio of insert to vector was ligated together using T4 DNA ligase (Promega) overnight at 14°C.

The recombinant pCS2+ vector was then linearised with NotI downstream of the 5' end of the gene. 5μg of purified DNA was transcribed using SP6 RNA polymerase at 37°C for 2 hours. A 5'methyl Guanine capping analogue (New England Biolabs) was added to the reaction mixture to add a 5' cap to the RNA to make it more stable *in vivo* and enhance translation efficiency. Free RNA nucleotides were removed at the end using a ProbeQuant G50 kit (GE Healthcare). RNA in this eluate was precipitated using phenol-chloroform followed by ammonium acetate with ethanol at -20°C for 1 hour. This was spun at 13,000rpm for 20 minutes and the resulting RNA pellet washed once in 70% ethanol. This was spun for a further 5 minutes and the RNA was redissolved at 1μg/μl in nuclease-free water. RNA was injected at 50-100ng/μl into 1-2 cell stage zebrafish embryos.

Semi-quantitative RT-PCR

In order to monitor relative expression of genes involved in Shh pathway signalling, I used semi-quantitative reverse-transcription PCR. RNA was extracted from dissociated chick embryonic limb buds or cell cultures using Trizol reagent (Invitrogen). The tissue was triturated and RNA extracted according to the manufacturer's protocol. Total RNA was resuspended in water and its concentration measured on a spectrophotometer. Equal amounts of RNA were used to synthesise first-strand cDNA with random primers and the Superscript Reverse Transcriptase enzyme (Invitrogen). PCR was performed on the cDNA using primers for *Patched1* and *Gli3*, and *Gapdh* was used as a standard by which to compare expression of the genes in question.

Quantitative real-time RT-PCR

RNA was extracted from cultured cells or from pooled groups of fifty 24 hpf or ten 5dpf zebrafish embryos using Trizol. cDNA was synthesised from the total RNA as above. All experiments were performed in triplicate using three PCR reactions per sample to get an average of each gene expression. 5ng of cDNA was added to each reaction along with 2x SYBR Green reagent, which contains nucleotides, polymerase, buffer, and a fluorescent dye that glows when double stranded DNA is produced as a result of PCR amplification.

The samples were run on an ABI7000 Prism real-time PCR machine. Levels were normalised to a baseline and the ΔΔCt method was used to calculate gene expression for each gene relative to the control gene (*Gapdh* for cultured cells, *β-actin* for zebrafish).

Mouse husbandry

Embryo collection

Bbs4 and *Bbs6* mutant mice were used for experiments on mouse embryos. All mice were on a C57/Black 6 background. To obtain embryos, heterozygotes for

both genotypes were crossed and the time when a vaginal plug was observed scored as E0.5. On the day at which embryos were required, the pregnant female was sacrificed by cervical dislocation and the uterus removed from the abdomen. Embryos were dissected out of their deciduas into cold PBS using forceps and their yolk sacs were placed in a separate eppendorf tube for retrospective genotyping. Embryos were fixed in 4% PFA at 4°C for 2 hours on rollers to ensure even fixation. All mouse experiments were performed in accordance with Home Office guidelines on animal welfare.

Mouse genotyping

To determine the genotypes of mutant mouse embryos, the yolk sac was used for embryos and tail tips for P8-P10 juvenile mice. The tissue was dissolved in 100μg/ml Proteinase K solution in tail lysis buffer (100mM Tris-HCl, pH8.8; 5mM EDTA, pH8.0; 0.2%SDS; 200mM NaCl) overnight at 55°C. Remaining hard tissue was pelleted by centrifugation and the DNA precipitated by the phenol:chloroform method. Approximately 50ng of genomic DNA was amplified by PCR using primers specific to either *Bbs4* or *Bbs6* gene traps.

Mouse embryo cryosectioning

In order to examine the expression of markers of Sonic Hedgehog activity in the neural tube, E10.5 mouse embryos were fixed in 4% PFA for 2 hours at 4°C on a nutator. Embryos were equilibrated in 20% sucrose as a cryoprotectant overnight at 4°C before cutting the embryos transversely into three sections so that sections could be taken orthogonal to the neural tube at all axial levels. Each embryo segment was embedded in OCT compound and frozen on a bed of dry ice. Frozen blocks were stored overnight at -80°C before sectioning on a Leica cryostat at 10μm thickness. The tissue was then dried on a slide warmer and slides were stored at -80°C. Excess OCT was washed off the slides with PBS before immunohistochemistry.

Mouse skull preparation

For wholemount scanning of mouse skulls using a desktop laser scanner, the skulls had first to be defleshed. Adult *Bbs4*$^{-/-}$, *Bbs6*$^{-/-}$, and wild-type mice were sacrificed and their weights and lengths measured to control for differences in weight. These are presented below.

The heads were removed and the skin cut away with forceps and scissors. Major muscles were removed with forceps before fixing and dehydrating the head in 95% ethanol overnight. After fixation, the skulls were placed in a 2% potassium hydroxide solution for a week on a shaker. The solution was refreshed every day and as the soft tissue dissolved away, it was removed with fine forceps, taking care not to damage the delicate zygomatic arch. The skulls were then dehydrated again for 48 hours in 95% ethanol and left to air-dry overnight. The dried skulls were then ready for laser scanning, which was performed by Matthew DiFranco at the Eastman Dental Institute's Biomedical Informatics department. Images of the scanned skulls were used to construct a three-dimensional model of the mean shape of control and *Bbs* mutant skulls.

Chick culture

Pluronic gel treatment

Whilst the polydactyly phenotype is highly penetrant in human cases of BBS, to date polydactyly has not been reported in any of the five published BBS mouse models (*Bbs1*, *Bbs1* M390R KI, *Bbs2*, *Bbs4*, *Bbs6*). This could be due to the specific strain the mouse models are bred into or differences in the embryology of the mouse and human limb.

To try to investigate the pathophysiology of polydactyly in the limb we tried to knock down *Bbs8* in the developing chicken limb. *Bbs8* morpholino oligonucleotide (MO) specific to the chick *Bbs8* orthologue (also called *Ttc8*) was dissolved in water to 1mM. This solution was mixed with an equal amount of 30% pluronic gel solution. When cooled, pluronic gel liquefies and solidifies on

return to room temperature. I tried to apply the gel to the chick limb bud at E2.5 by making a hole in the vitelline membrane overlying the embryo with fine forceps. Pluronic gel was cooled on ice and 5µl of gel was applied to the limb bud using a P20 pipette whose tips had been previously chilled on ice.

Despite trying this experiment several times, it was extremely difficult to get consistent uptake of the gel into limb bud, evidenced by fluorescence in the limb bud 24 hours after application due to a fluoroscein label on the morpholino. Most of the time this was due to the gel diffusing away from the site of application, coming unstuck from the ectoderm of the embryo, or only a limited amount of morpholino diffusing into the tissue. As such, no convincing results were yielded with this strategy.

In ovo electroporation

To try to knockdown expression of *Bbs8* in neural crest cells populating the gut, I electroporated the *Bbs8* MO into chick embryos. Hamburger-Hamilton stage 10-12 chicken embryos were windowed using fine scissors after withdrawing 3ml of albumin with a syringe. A 1.0mM solution of *Bbs8* morpholino mixed with phenol red for visualisation was injected into the anterior neural tube with a fine needle and microinjector. Platinum electrodes were then placed either side of the embryo at the axial level around the third somite. This was to target vagal neural crest cells migrating away from the neural tube between the first and seventh somites into the foregut. Five 50ms pulses of 12V were applied to the embryo before it was covered in tape and incubated for 24 or 48 hours at 37°C.

Dissection and fixation of chick embryos

Electroporated embryos incubated for either 24 or 48 hours after electroporation were dissected out of their egg by cutting around the blastoderm surrounding the embryo with fine scissors. A square of blastoderm was cut out and pinned at each corner onto a silgard plate. This was then bathed in 4% PFA for around 20 minutes to fix the embryo *in situ*. After this, the embryo was rigid and kept its

shape when the remaining blastoderm was cut off with fine scissors and the embryo fixed for a further two hours at room temperature.

Immunohistochemistry of chick embryos

Fixed chick embryos were equilibrated in a 15% solution of sucrose in PBS. The embryos were then embedded in a mixture of 15% gelatin, 15% sucrose and PBS prewarmed to 37°C in a water bath. Embryos were orientated in this embedding solution using forceps and left to harden on ice. Blocks were then stored at -80°C to solidify fully. Frozen blocks were sectioned transversely on a Leica cryostat making 15μm sections.

The slides were blocked with 1% BSA in PBS for 30 minutes at room temperature before incubation with the primary antibody for one hour at room temperature (mouse anti-HNK1 (1:500) or mouse anti-p75 (1:1,000)) which both detect neural crest cells. Following three washes in PBS, the secondary antibody was applied (anti-mouse IgG 594). An anti-FITC antibody (Abcam, 1:1,000) was used to enhance the green fluorescence of the fluoroscein tag on the morpholino. Images of the sections were taken on a Zeiss AxioImager microscope.

Quail embryo explant culture

As a quantitative measure of the effect of gene knockdown on neural crest migration, an ex-vivo quail assay was performed. E1.5 quail embryos were electroporated with the chick *Bbs8* MO using the same protocol as for the chicks. One hour after electroporation the embryos were dissected out of their eggs and the neural tube liberated using protease enzymes and fine forceps. The dissected neural tubes were plated onto glass coverslips coated with 0.1% fibronectin and 0.1% poly-L-lysine. These were allowed to adhere before bathing in DMEM culture medium supplemented with 10% FBS and antibiotics. The neural tubes were left overnight for the neural crest cells to migrate away. Neural tubes were then examined under an inverted microscope and imaged. The maximum distance the green fluorescent cells (morpholino-positive) had migrated away from the

neural tube was compared to the maximum distance migrated by the unelectrporated neural crest cells.

Zebrafish husbandry

Strains used

Wild type Tubingen zebrafish were used for most zebrafish experiments. Other strains used were:

- *Sox10::eGFP*. This line expresses eGFP in the neural crest cells and otic vesicle and so can be used to track migrating cells. Two separate lines were used: one with 7.2Kb of the upstream *Sox10* promoter sequence driving GFP expression, and one with 4.9Kb of promoter sequence. Both lines gave exactly the same expression domains and levels of the transgene.
- *Pax2.*1*::eGFP*. This line expresses GFP in a subset of neurons, the optic nerve, and in the pronephros. This was used to examine the development of the kidney.
- *Islet1::eGFP*. This expresses GFP in developing neurons and Rohon-Beard (RB) cells. This was used to determine localisation of RB cells in morphant embryos.

Zebrafish morpholino injection

Design of morpholino oligonucleotides

Morpholino oligonucleotides were designed to knockdown the expression of genes in the developing zebrafish embryo. For most genes studied, at least two different MO sequences were used for each gene to ensure specificity. Usually one sequence blocking translation of the mRNA was used (ATG-blocking MO) and one blocking the splicing of one of the internal introns (splice-blocking MO).

For each gene studied, the genomic sequence was obtained from the Ensembl zebrafish genome database. A region of DNA sequence ranging from 75bp

upstream of the start ATG to 25bp downstream was used to design an ATG-blocking MO. For the splice blocking MO an intron-exon boundary (or an exon-intron boundary) was selected which, when skipped, would yield an out-of-frame mRNA. 25bp either side of the boundary was used to design this MO, which would sterically hinder the activity of the spliceosome, yielding a dysfunctional protein product. All MOs were manufactured by Gene Tools (Philomath, Oregon). For some genes (*ift80*, *bbs4*, *bbs8*), control MO sequences were ordered consisting of the original MO for the gene with five mis-paired residues. This was to exclude off-target effects of the MO.

mRNA rescue experiments

In order to validate the specificity of the MOs in question, full-length mRNA was injected alongside the MO to try to rescue the phenotype caused by the MO. Rescue of the phenotype indicates specificity of the MO sequence, and that the phenotypes were not caused by toxicity or non-sequence-specific effects of the MO.

For ATG MOs the full-length cDNA of the human or mouse orthologue of the gene was obtained from Gene Service (Cambridge, UK). The cDNA was cloned into the zebrafish expression vector pCS2+ from which mRNA was synthesised using SP6 RNA polymerase. mRNA was injected into 1-cell embryos alongside its corresponding MO.

For over-expression studies, a range of mRNA concentrations was injected alone into embryos to examine gain-of-function phenotypes. Typically, 20, 50, 100, 200, and 500pg of RNA were injected into the embryos. For rescue experiments, if over-expression caused a phenotype, a dose below the threshold causing the phenotype was injected alongside the MO. This is the case with many IFT proteins, which function in stoichiometric complexes, therefore, both over-expression and loss-of-function lead to abnormalities.

In-situ hybridisation

Probes used

The following antisense probes were used for zebrafish embryos: *pax2.1*, *pax6*, *nkx6.1*, *nkx2.2*, *pax3*, *dlx2*, *dlx5*, *sox10*, *phox2b*, *foxd3*, *crestin*, *southpaw*, *sonic hedgehog*, *patched-1*, *gli1*, *gli3*, *ihha*, *wt1a*, *wt1b* (gift of Wolfgang Driever, Freiburg), *bbs8*.

The *bbs8* probe was synthesised from a *bbs8* expressed sequence tag (EST) obtained from Gene Tools. It was cloned into the pBS2 KS+ cloning vector and antisense and sense (from control) mRNA strands were synthesised with T7 and T3 RNA polymerases respectively. All probes were synthesised using Digoxigenin-labelled UTP residues in the *in vitro* transcription reaction.

Wholemount *in situ hybridisation*

Zebrafish embryos were fixed in 4% PFA in PBS overnight at 4°C. Embryos to be used at stages later than 24hpf were treated with 0.03% PTU to inhibit melanogenesis at 24hpf. This enabled clear visualisation of the *in situ* marker. Fixed embryos were washed in PBT (PBS with 0.1% Tween 20) and dehydrated in 100% methanol for 2 hours at -20°C. Embryos were then rehydrated in a series of methanol/PBS dilutions before treatment with 2μg/ml Proteinase K (PK) solution. The time of digestion in PK depended on the stage of the embryos. Embryos were washed and refixed in PFA for 20 minutes before incubation in prehybridisation solution for 2 hours at 65°C. The probe was then diluted in hybridisation solution (prehybridisation solution plus heparin and yeast tRNA) at 1ng/μl and the embryos were incubated in this overnight at 65°C.

The following day the probe was removed and recycled for future reuse. Embryos were washed once in prehybridisation solution for 5 minutes, once in 25% prehybridisation solution mixed with 75% 2xSSC, once in 2X SSC, and then three times in 0.2x SSC for 30 minutes each. Embryos were then equilibrated in maleic

acid buffer (MAB) and blocked in MABI blocking reagent (MAB with 2% blocking reagent (Roche)) for at least 2 hours at room temperature. Embryos were then incubated in horseradish-peroxidase conjugated anti-Digoxigenin antibody (Roche, 1:6,000) overnight at 4°C. The following day embryos were washed 5 times in MAB to remove the primary antibody followed by two washes in Tris-HCl pH 9.5. This was then replaced with BM Purple, used to develop the colour of the probe. The reaction was stopped just before the emergence of background staining and washed 3x in PBS pH5.5 followed by re-fixing in PFA for 20 minutes. The embryos were then mounted in 75% glycerol for imaging on a Zeiss Lumar stereomicroscope.

Alcian blue staining

Chondrocranial measurements

Alcian blue (AB) was used to reveal the cartilage of larval zebrafish. Zebrafish were injected with MO (*bbs4*, *bbs6*, *bbs8*, *ift80*, *mks1*, *mks3*, *ofd1*) and treated with PTU at 24hpf. At 5dpf, embryos were fixed in 4% PFA overnight at 4°C and then bleached in 10% hydrogen peroxide in PBS for 1 hour on ice. Embryos were washed and a 0.1% solution of Alcian Blue (Sigma, UK) in acidic alcohol (5% concentrated hydrochloric acid, 70% ethanol) was added to the embryos overnight. Embryos were washed for at least 4 hours on a shaking platform with frequent changes of acidic alcohol to remove excess stain.

For wholemounts, embryos were then mounted in 75% glycerol and imaged. For flatmounts, the embryos were treated with 1% trypsin in a 35% sodium borate solution to loosen the tissues around the cranial cartilages. The head was separated from the body with fine forceps and the notochord severed. Head tissues were dissected away from the neurocranium carefully using sharpened tungsten needles. Neurocrania were then flatmounted onto glass slides and covered with coverslips before imaging on a Zeiss AxioImager with phase contrast illumination.

Imaging neural crest migration

Live imaging of NCC migration

To track the migration of cranial neural crest cells in the zebrafish head, *Sox10:eGFP* transgenic zebrafish were injected with *bbs8* or control MO. At the 12-somite stage, which is the time of the onset of migration of CNCCs into the head, embryos were selected for strong green fluorescence on a dissecting microscope. Embryos were dechorionated, anaesthetised in 0.003% tricaine, and mounted in 1% low-melting point agarose and oriented with a mounted needle. Once the agarose had set, the embryos were bathed in embryo medium and mounted on a confocal microscope stage. The Leica SP2 confocal microscope was used to create a time-lapse movie of the migrating CNCCs over a 4-hour period, capturing frames once a minute. The total distance migrated during this time was measured by comparing the position of the migration front of the cells at 12ss and 20ss, at the end of the time period.

Imaging peristalsis in the zebrafish gut

To visualise the peristaltic movements of the zebrafish gut, 5dpf control and *bbs8* MO-injected embryos were immobilised in 1% low-melting point agarose and their foreguts imaged on a Zeiss AxioImager with DIC optics. Five-minute movies were captured at one frame per second. The number of peristaltic pulses in the gut was quantified in five control and morphant embryos each and compared.

Zebrafish cell transplants

Transplantation involves grafting cells from a host embryo to a donor and tracking the migration of these cells to see if they behave differently in a non-native tissue environment to see if the function of the gene of interest is cell autonomous or not. Around 100 *sox10::eGFP* embryos were co-injected with 3ng *bbs8* MO and a 0.5% dilution of 10kDa rhodamine dextran (Invitrogen) at the 1-2 cell stage.

These were the donors. Another batch of 100 control host embryos were untreated and incubated at the same time.

After incubation at 28.5°C for 5 hours, the donor and host embryos were dechorionated on an agarose coated dish and mounted individually on a 1% agarose mould to hold each embryo in place for micromanipulation. Around 20 donor cells were aspirated into a fine-tipped glass micropipette. To maximise the likelihood of targeting presumptive neural crest, the needle was positioned at an angle of 45° to the germ band. These aspirated cells were then carefully reinjected into the host embryos at a roughly equivalent position on the embryo. About 60 transplants could be performed in one sitting before the donor and host embryos became too developed, and my patience too tried! Transplanted embryos were then left to recover for 1 hour at room temperature before reincubating overnight at 22.5°C. Incubating at this lower temperature meant the embryos were at the stage of the onset of NCC migration (10-12ss) at around 9am the following morning.

Successful transplants were scored by the presence of GFP-positive cells in the host embryo. This meant the engrafted cells had integrated into the neural crest and therefore the expression of *Sox10* had been activated, driving GFP expression. Embryos in which the engrafted *Sox10::eGFP*-positive cells were surrounded by red-fluorescent cells were discarded as this meant the transplanted cells were surrounded by donor cells, and not host cells, which is the purpose of the experiment. The success rate of transplants integrating into the neural crest was around 20%, however after screening for contamination with excessive donor cells, only around 5% of embryos were suitable for imaging.

The successful embryos were carefully mounted in low melting point agarose to expose the lateral surface. An image was taken at the onset of CNCC migration (12ss) showing the position of the engrafted NCC, this was called t=0. Images were taken on a Leica compound microscope using a z-stack depth of about 30μm and maximum projection to get the whole image of the embryo's head in focus. Images were taken in the DIC, FITC, and rhodamine channels. Embryos were re-

imaged 2 and 4 hours after, by which time the majority of CNCC migration into the head was complete. The distance migrated by each individual NCC cell was calculated by comparing its positions at t=0, 2, and 4 hours.

Drug treatment of embryos

Drugs used in this study were: Rapamycin (Sigma), Roscovitine (Sigma), Mevenolin (Sigma), Paclitaxel (Sigma). Compounds were dissolved in 1% DMSO in zebrafish water at the following concentration ranges based on previous studies and empirical trials: Rapamycin 2nM-100nM, optimum 10nM; Roscovitine 0.1μM-100μM, optimum 10μM; Mevenolin 25μM; Paclitaxel 10μM (only partially soluble, even when dissolved in DMSO). Drugs were tested by dissolving in 5ml of fish water and adding to a group of 10 embryos in wells of a 6 well plate at either 4hpf or 24hpf. All subsequent experiments were performed adding drugs at 24hpf as it eliminated off-target effects. For controls, embryos were treated with 1% DMSO alone.

Embryos were incubated until 5dpf whereupon morphology was documented by immobilisation in 2.5% methylcellulose and imaged on a Zeiss Lumar stereo dissecting microscope. The size of kidney oedema was measured by drawing a polygon around the swelling and calculating the surface area in microns squared using Zeiss AxioImager 4.5.

Assessment of compounds on kidney function

To functionally assess the effect of treating zebrafish morphants and controls with drugs, I adapted the protocol of Hentschel et al. Zebrafish embryos were injected with MO at the 1-2 cell stage. At 24hpf, PTU was added to prevent pigmentation forming and embryos were dechorionated at 48hpf. At 96hpf embryos were anaesthetised in 0.003% Tricaine and immobilised by mounting ventral-side up in 2.5% methylcellulose to expose the heart. Using a fine-tipped glass needle and microinjector, 1nl of 10kDa rhodamine dextran (Invitrogen) was injected into the pericardium using a long pulse (800-1,000ms) of the microinjector. This ensured

a smooth and even delivery of the dye into the heart, and enables a very fine needle to be used to puncture the heart cleanly, causing least trauma or damage to the embryo.

Ten to 12 embryos were injected for each treatment and incubated in individual wells of a 24 well plate at 28.5°C. Images of the amount of red fluorescence in the pericardium, as well as in the systemic circulation, were recorded using a Zeiss Lumar fluorescent stereomicroscope. Images were recorded immediately after injection, 3 hours later, and 24 hours later. The decrease in fluorescent intensity correlates with efficiency of renal filtration as the dye is selectively removed from the blood and excreted by the glomerulus. The relative amount of fluorescence remaining in the embryo's hearts after 24 hours was calculated by measuring the fluorescent intensity of the hearts using ImageJ. A region 100x100 pixels was drawn around the heart and the average intensity recorded. An average and standard deviation of intensities was recorded for at least 10 embryos for each treatment. Statistical analyses were performed using the paired T-test in Microsoft Excel.

Single-cell dissociation of zebrafish embryos

Approximately 200 control MO injected or *bbs8* MO injected zebrafish embryos were incubated until the 14, 16, or 20 somite stage. They were then washed in calcium-free Ringer's solution (116mM NaCl, 2.9mM KCl, 5mM HEPES pH 7.2) for 15 minutes followed by trituration to remove yolks with a P200 Gilson pipette tip in which the end had been cut off. These embryos were then transferred to a solution of 0.25% Trypsin in 1mM EDTA pH 8.0 for 30 minutes, triturating with a glass Pasteur pipette every 10 minutes. Dissociation was monitored using an inverted microscope and when only single cells remained, the protease reaction was ceased by adding 5% FCS and 1mM $CaCl_2$. The cells were pelleted in a 15ml Falcon tube by spinning at 300*g* for 3 minutes. The supernatant was removed and the cells were washed with L15 media (Sigma) containing 1mM $CaCl_2$ and spun down again. The supernatant was removed again; cells were resuspended in 1ml of L15 and placed in 5ml FACS tubes.

Flow sorting GFP-positive cells from transgenic embryos

Dissociated cells from *bbs8* or control MO-injected *Sox10::eGFP* zebrafish embryos were sorted using a Beckman Coulter FACS machine, or, more recently, a MoFlo XDP. A wild-type GFP-negative batch of embryos was used as a negative control to define the parameters of the GFP-positive cells. Dead cells were excluded using the dye 7AAD. Dead cells accounted for around 0.9% of total cells in both control and morphant embryos. Cells accounted for 80-90% of total particulate matter entering the FACS machine. Around 50,000 GFP-negative cells were analysed to set the gating position for the GFP-positive cells. The Sox10:GFP positive cells were then fed into the machine and GFP-positive cells were collected in an eppendorf tube containing 0.5ml of RNAlater reagent (Ambion). This stabilised the RNA inside the cells and prevented degradation prior to extraction. Approximately 80,000 to 100,000 NCCs were obtained from 100 16ss zebrafish embryos, giving around 800 to 1,000 NCCs per embryo. This number was equivalent in controls and morphants. Roughly 4% of the total cell count of the embryos was NCCs.

Chapter 3: Modelling craniofacial defects in Bardet-Biedl syndrome

Introduction

Anecdotal reports of facial dysmorphism

In addition to the well-characterised primary features of BBS (obesity, retinitis pigmentosa, kidney disease, polydactyly, mental retardation, and hypogonadism), parents of patients have anecdotally reported being able to spot another BBS patient "from a mile away" (P. Beales, personal communication; and reports from LMBBS Society meeting). Historically, BBS was often misdiagnosed as Down's syndrome due to a similar facial gestalt and mental impairment. Whilst there are similarities between a typical BBS "face" and a Down's "face", such as small palpebral fissures, there are also numerous subtle differences that an experienced individual can identify.

Published findings of craniofacial dysmorphology

Beales et al (1999) was the first study to undertake a systematic analysis of the facies of BBS patients. By examining the photographs of 76 patients they identified:

"Considerable, inconsistent dysmorphism… a subgroup of patients showed facial similarities comprising deep set eyes, hypertelorism with downward slanting palpebral fissures, a flat nasal bridge with anteverted nares and prominent nasolabial folds, a long philtrum, and a thin upper lip."

This study was followed up by a paper in 2001 by Lorda-Sanchez et al entitled, "Does Bardet-Biedl Syndrome have a characteristic face?" They examined a further 18 BBS patients' faces and concluded similarly to Beales et al:

"…Patients share a characteristic face with a wide forehead, mild downward slanting palpebral fissures owing to mild malar hypoplasia, a large nose, and a small mouth with a thin upper lip and slight everted lower lip. The mandible looks prominent on front view, but shows clear retrognathia on lateral view."

In summary, the typical features associated with a BBS face are the following:

Feature	Frequency (As reported by Beales et al 1999, n=76)
Short palpebral fissures (the size of the eyelid opening, normally 10mm high and 30mm in a healthy adult)	92%
Brachycephaly (flattened head)	92%
Frontal balding	92%
Long philtrum (space between upper lip and nose)	82%
Thin upper lip	54%
Ptosis (closing of the eyelid)	29%
Enophthalmia (deep-set eyes)	No data but frequently observed

Table 5. Facial features and frequencies in BBS patients.

The BBS "face" is dysmorphic, attributed by parents' ability to recognise other patients with the disease from their faces, and published reports by clinicians. However, it is more subtle and variable than other canonical dysmorphic syndromes such as Down's, Treacher Collins, Williams, and Noonan syndromes. This has led to some clinicians ignoring it as a feature of the syndrome, and has made formal characterisation confusing, although some descriptive attempts have been made.

New technology in the form of 3D facial scanning has taken much of the subjectivity out of characterisation of facial dysmorphology. Its use in the past was evaluated to see if it could be applied to BBS patients.

Previous uses of 3D facial scanning

Facial scanning involves using a laser scanner or 3D photogrammatic device to capture a three dimensional image of the face, whose surface is then populated with up to 100,000 3D points. These points are used to reconstruct a wire mesh model of the face. By combining many patients' images together, the relative positions of the points of the face corresponding to specific facial landmarks can be used to construct a mean model of the face (Hammond, 2007). By combining sufficient numbers of faces to obtain statistical power (usually n>50),

comparisons can be made between syndromic faces, and age, gender, and race-matched controls. Table 6 documents previous uses of 3D facial scanning for dysmorphology and Figure 15 shows previous uses of DSM modelling on four distinct dysmorphology syndromes.

Syndrome	Resolving power	Conclusion	Reference
Autistic Spectrum Disorder	Low	Identified right-sided protrusion causing face asymmetry	(Hammond et al., 2008)
Fragile X syndrome		Faces are longer than controls	(Hammond, 2007)
Cornelia de Lange syndrome		Able to discriminate between affected and unaffected	(Bhuiyan et al., 2006)
Fabry disease	85% for males, 67% for females versus controls	Abnormalities in peri-orbital region but low distinguishing power	(Cox-Brinkman et al., 2007)
Williams-Beuren syndrome			(Hammond et al., 2005)
Noonan syndrome	94% between affected and controls		(Hammond et al., 2005)
Velo-cardio-facial syndrome	95% between affected and controls and between VCFS and NS	Could distinguish between the two syndromes	(Hammond et al., 2004)
Binder syndrome	Noses of patients are 15-17mm retracted relative to contros	Confirmed extent of nasal deficiencies	(Kau et al., 2007)

Table 6. Published uses of 3D facial scanning to resolve dysmorphology.

Using principle component analysis (PCA), the specific parameters by which the groups of faces differ can be defined. For example, distance between the eyes, length to width ratio of the face, size of the nose, thickness of lips, and so on. These components can be partitioned to accurately differentiate between two groups of individuals and discern whether an individual has the syndrome or not, based on that parameter. This technique overcomes the problems of subjectivity and the lack of expert dysmorphologists for any given syndrome. Due to such rarity of many syndromes, it takes many years for a particular physician to see sufficient patients to recognise that syndrome's gestalt.

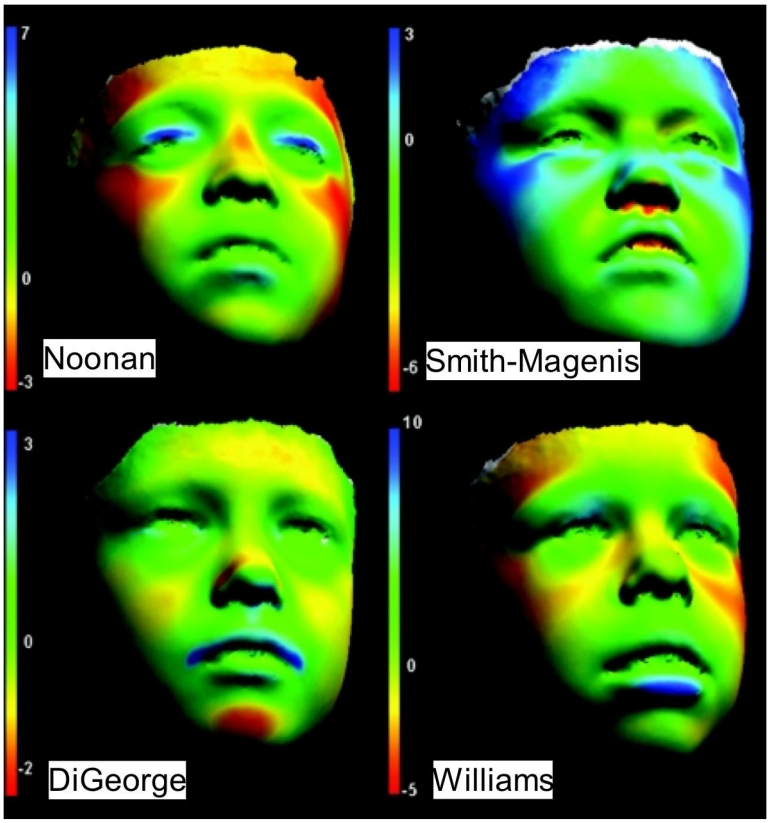

Figure 15. Discrimination between four dysmorphic syndromes by 3D DSM.
Red shows relative decrease in inter-landmark distance relative to controls while blue shows an increase in distance. Taken from Hammond et al (2005).

Professor Peter Hammond has pioneered the use of this technique to study the facies of many genetic syndromes, as well as psychiatric disorders (autism), and fetal alcohol syndrome. The first published use of this technique was in 2004 where it was used to characterise the faces of 60 adults and children with Noonan syndrome and 90 with Velo-Cardio-Facial syndrome (Hammond et al 2004).

Since then, this technique has been deployed for Cornelia de Lange syndrome, a growth deficiency where it characterised the faces of 20 patients. It has been used to study the faces of human and mouse mutants of GFTIRD1. Patients showed faces strikingly similar to those of Williams-Beuren syndrome and so identified this gene as a new candidate (Tassabehji et al., 2005). More recently, it has uncovered hitherto unrecognised asymmetry in the faces of autism sufferers, underlying possible changes in forebrain structure.

Hammond et al (2005) showed the technology to be able to discriminate accurately between four dysmorphology syndromes (DiGeorge, Noonan, Williams, and Smith-Magenis). In children, its accuracy at discriminating between individuals with each syndrome versus controls, or discriminating between any of the four syndromes, ranged from 90-98%. Using only one of three facial features; the eyes, mouth, or nose, up to 96% accuracy could be achieved. Accuracy was even higher for adults: 100% for adults with Williams syndrome versus controls.

Whilst these results suggest the technique can be used for diagnosis, it is only discriminating between four syndromes, and not the hundreds that exist, some presenting subtly. At present, it cannot be used to diagnose, *de novo*, a syndrome based purely on face alone. However, it may be a useful training aid to expedite the dysmorphologist's recognition of particular facies.

Application of 3D facial scanning to BBS

All the syndromes studied to date have had very pronounced dysmorphic features, well characterised and easily identifiable by clinicians. The BBS face is subtle and there is no statistical proof that such a characteristic "face" exists, or whether it is simply a result of excessive fat around the face. However, as there are numerous anecdotal and published identifications of the BBS face, and given the power of 3D scanning in resolving differences in facial morphology, BBS makes a good, albeit challenging candidate for the technology. The ability to accurately identify BBS facies would be a quantum step forward in the application of the technology, as it would pave the way to study many more of the subtler dysmorphism syndromes.

The aims of this study

The first aim was to analyse the results of the scanning of BBS and control faces and characterise the identity of the BBS face performed by Peter Hammond. This would give an idea about the parts of the face affected in BBS. This could then be validated experimentally by analysing the faces of BBS mutant mice, and

furthermore, zebrafish. The ultimate aim is to create a robust model system for craniofacial dysmorphology in BBS from which the biological basis of the phenotype could be determined.

Results

Characterising the facial gestalt with 3D photography

Peter Hammond scanned 83 BBS patients, irrespective of underlying mutations at two of the annual Bardet-Biedl syndrome patient conferences in Northampton, UK, and also at a patient convention in Holland. In addition, 230 controls were scanned. All subjects were Caucasian and matched roughly for age with controls. Separate analyses were performed for subjects under 20 years old to control for the variability caused by growth of the face in children. Peter Hammond and Matt DiFranco carried out analysis and statistics on the acquired images.

From the 3D photographs, a dense-surface model (DSM) was constructed for each face. Facial scans were annotated with landmarks according to Figure 16. The distances between several landmarks were measured and compared between control and BBS faces. Firstly, the n-gn to n-sn ratio was greater in BBS patients. This means the nose was relatively short compared to the face. Secondly, the t-t to n-sn ratio was lower in BBS patients. This means the face was relatively wide for the length of the nose. Thirdly, the n-gn to t-t ratio was not significantly different in BBS children compared to controls.

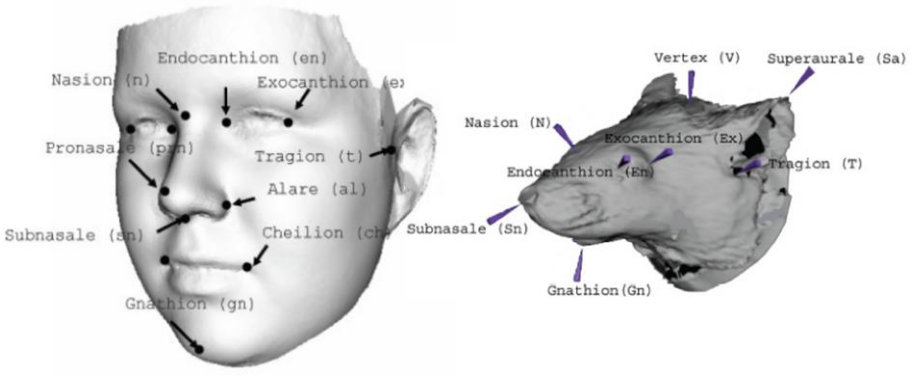

Figure 16. Facial landmarks annotated on human and mouse faces.

However, the problem with these two-dimensional analyses of interlandmark distance are three-fold: first is the arbitrary positioning of the landmarks, as they are input by the operator; second is that only 13 out of the possible c.25,000 datapoints are used for each face; and third, most importantly, is that the excessive soft tissue on patient faces obscured an accurate analysis.

To overcome these problems, Peter Hammond performed analysis on colour-distance-coded mean morphologies. Here, the mean difference in position of the points on the DSM between control and BBS faces was colour-coded. This analysis was performed in several orientations, but the most interesting differences were noticed when comparing the dorsal-ventral aspect of the face. Here, portions of the face sunken relative to the control face were rendered red, and protruding parts blue.

In the first instance, analysis was performed on the nose alone, as this is the region of the face least covered in fat. The DSM showed that in both children and adults the bridge and tip of the nose were relatively depressed in BBS patients compared to controls. This indicates hypoplasia at the nasal bridge and nasal shortening. A movie showing a dynamic morph between a control and BBS nose demonstrates differences in the nasal alae (edge of the nostrils) and columella (portion between the nostrils) (Figure 17A and B). Using a pattern recognition algorithm known as "support vector machines", a BBS nose could be distinguished from a control nose 91% of the time in children and 84% in adults, highlighting the degree of difference, which would otherwise go unrecognised (Tobin et al, 2008).

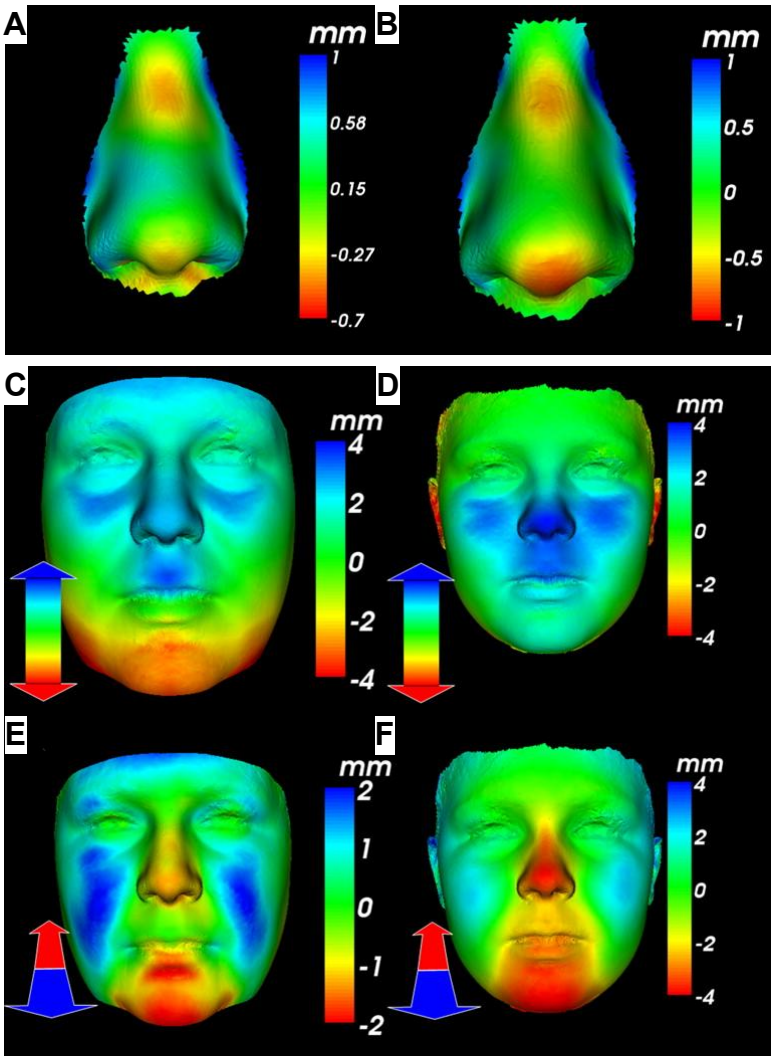

Figure 17. Craniofacial dysmorphology revealed in man and mouse.

A,B: comparison of noses of children (A) and adults (B) shows depression of the nasal tip and bony nasal bridge in patients. **C,D**: rostro-caudal comparison between control and BBS adults (C) and children (D) shows a small lower jaw and upward displacement of the upper lip and nose. **E,F**: dorso-ventral comparison shows relative flattening of the midface, consisting of a smaller chin, upper jaw, and nasal region than controls.

Next, the full face was analysed. Performing comparisons in the rostro-caudal axis, in both adults (Fig. 17C) and children (Fig. 17D), there was a relative upward displacement of the nose and upper lip (indicated by blue rendering) and reduced mandibular size (red rendering). By performing comparisons in the dorsal-ventral axis, there was clear mid-facial hypoplasia in BBS adults (Fig. 17E) and children (Fig. 17F). This consisted of a small chin, retrognathia (recession of

the mandible causing overbite), and a smaller maxilla and nose. Midfacial flattening and facial flatness was used to differentiate clearly between control and BBS faces of children in 76% of cases (n=31), based solely on one measurement from the software. Controlling for age produced a summary face with greater width, mid-facial flatness and retrognathia, and showed the technique can distinguish features unclear even to the trained dysmorphologist.

Examination of *Bbs* mutant mouse faces reveals analogous facial defects

We next investigated whether mouse BBS mutants displayed analogous craniofacial malformations. This would show if the defect was conserved and therefore likely to have a consistent biological aetiology, rather than be a secondary effect due to excess fat, or particular to human BBS patients. This work was performed mainly by Erica Eichers in James Lupski's laboratory at Baylor College in Houston, Texas.

Bbs4$^{-/-}$ (n=31), heterozygous (n=30), and wild-type (n=20) mice of the same strain (C57/black 6) were anaesthetised and their heads painted in cornstarch to improve the contrast with the background. Heads were scanned using a 3D laser scanner. Although the craniofacial anatomy of mice and humans differs, there were significant similarities in key ratios for both *Bbs4* and *Bbs6* null mice, including a larger mid-face width to height ratio (P<0.01), and a shorter snout (P<0.01). No landmark differences were seen in heterozygous mice (Tobin et al., 2008).

3D laser scanning of *Bbs* mutant skulls determines bony origins of dysmorphology

Next, we wanted to find out if the flattening of the midface had its origins in soft or hard tissue. This was done in collaboration with Matt DiFranco, then at the UCL Eastman Dental Institute in London. Heads were removed from *Bbs6*$^{-/-}$ (n=9) and wild-type (n=15) mice of C57/black 6 mice. Skin and soft tissue were stripped from the heads and they were defleshed by immersion in potassium hydroxide for up to one week. Cleaned and dried skulls were subjected to 3D

laser scanning on a desktop scanner. Colour coded representations of the skulls were generated in a similar manner to the human faces.

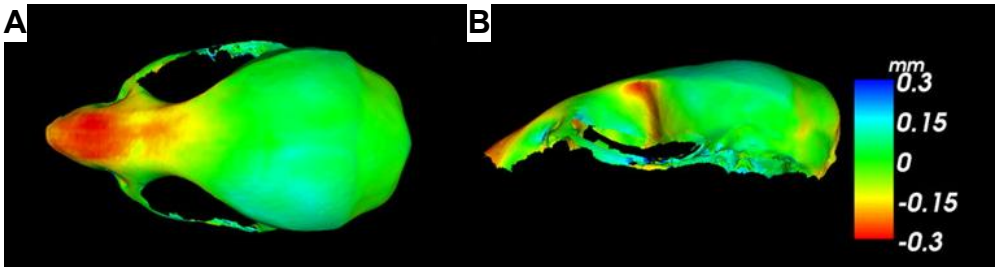

Figure 18. 3D scans of mouse skulls.

A: dorsal view of BBS mutant skulls relative to controls showing hypoplasia of the snout (revealed in blue). **B**: lateral view of the skull comparison.

When viewed from the dorsal aspect (Fig. 18A), the colour-coded representations of the mean skull models showed shortening of the snout, specifically attributed to a hypoplastic pre-maxilla and maxilla (red shading). The lateral view shows a higher cranial vault and depressed orbits, as well as the shortened snout (Fig. 18B). Enophthalmia, or sunken eyes, is a common feature noted in BBS. The bones affected in these mice are homologous to the bones of the human upper jaw and nose, and so reduced size in humans will give rise to the gross phenotype observed. This established that the defect in the human faces is most likely due to hypoplasia of the craniofacial bones contributing to the midface. As these bones are entirely derived from the embryonic neural crest, this is an obvious cell type to examine in BBS models.

Generation of *bbs* morphant zebrafish

Because of the ease of making genetic models in the zebrafish using morpholinos (MOs), the relative homology of its craniofacial development with mammals, and its utility in studying neural crest cell migration, I decided to utilise this model. In the first instance, I designed and injected ATG- and splice-blocking MOs against *bbs4*, *bbs6*, and *bbs8*. *bbs4* and *bbs6* were chosen as these were the mouse models tested, and Bbs8 protein function is best understood, mostly from studies in *C. elegans* and is thought to serve as an adaptor protein for IFT.

In situ hybridisation shows that *bbs8* is ubiquitously expressed at low level, with particularly strong expression in the eye and brain (Figure 19). Because BBS proteins are present at very low copy number in cells due to their confinement to the basal body, they are often difficult to detect by wholemount *in situ*.

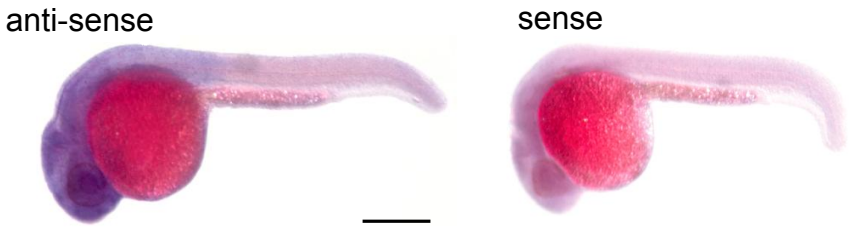

Figure 19. *In situ* hybridisation of *bbs8* in zebrafish embryos.

Anti-sense riboprobe shows that the *bbs8* transcript is ubiquitously expressed in the 24hpf zebrafish but is enriched in the eye and brain. Scale bar = 500μm.

MOs were titrated over a range of doses. It was found empirically that 4ng of *bbs4* and *bbs6* MOs gave a consistent, reproducible phenotype consisting of a convergent extension defect and kidney cysts by 3dpf. The *bbs8* MO gave a stronger phenotype, which was equally as penetrant, with 100% of embryos affected. 4ng of *bbs8* MO gave a very severe phenotype and most embryos died before 5dpf. As such, most experiments were performed with 2 or 3ng of *bbs8* MO that induced more moderate phenotypes without lethality.

At the 8-somite stage (ss), all BBS MOs induce a mild gastrulation defect evidenced by shortening of the body axis and compressed, widened somites indicative of defects in the planar cell polarity (PCP) pathway. This phenotype has been reported for all ciliopathy morphant models published to date (e.g. Gerdes et al., 2007, Ross et al., 2005). *bbs8* morphants consistently showed the most severe phenotypes. At 24hpf, embryos showed U-shaped somites, similar to those of the Sonic Hedgehog mutants *sonic you* and *smoothened you* (so-called after the U-shape somites). Morphants of all three genes had a down-turned body axis, most marked at 72hpf, a feature characteristic of other ciliopathy morphants and mutants reported previously (Drummond et al., 1998). A detailed analysis of the specific phenotypes observed appears in Chapter 6.

To test for toxicity of the specific MO sequences, I injected 5-base mispair MOs into wild type zebrafish embryos (see Appendix 2 for all MO sequences). These oligos are similar to the gene of interest but are mispaired at 5 bases, sufficient to abrogate binding to the target, but with sufficient similarity to mimic any toxicity due to the chemical nature of the MO, and the surgical manipulation during its injection. Mismatched MOs for both *bbs4* and *bbs6* conferred no visible phenotypes at 24hpf, nor later by 5dpf.

To test the specificity of the *bbs8* MO, I injected 100pg of full-length human *BBS8* RNA (76% protein sequence identity) alongside 3ng of *bbs8* MO. Human mRNA was used as its 5' sequence differed from the fish sequence sufficiently to render it incompatible with MO-mediated silencing. By 24hpf, the convergent extension (CE) defect was greatly reduced, and the somites and notochord were straightened. By 5dpf, embryos injected with MO alone had renal and cardiac oedema, a down turned body-axis, otolith defects, absence of pigmentation, and craniofacial anomalies. Co-injection of 100pg of human *BBS8* mRNA was sufficient to fully rescue the craniofacial, renal, pigmentation, and otolith defects.

Craniofacial dysmorphology in *bbs* morphants

Considering the conservation of craniofacial defects in humans and mice, and given the reproducible ciliopathic phenotypes in the zebrafish, making it a valid model of the human disease, I next investigated craniofacial morphology in the zebrafish. Despite the size and shape differences between fish and mammalian skulls, many of the same signalling molecules are deployed, and its embryological ontology and anatomical organisation are well conserved higher up the chordate phylum.

Cranial cartilages of control, *bbs4*, *bbs6*, *bbs8*, and *bbs8*-rescued embryos were visualised at 5dpf by staining with Alcian Blue. Despite a severe convergent-extension defect leading to pronounced curvature of the body axis at 5dpf, *bbs4* morphants had grossly normal craniofacial morphology, although the mandible

was wider and shorter (Fig. 20B,G). The pharyngeal apparatus was intact with all branchial arches present. Flatmount preparations of the neurocranium, which later develops into the skull, show no significant perturbations relative to controls (Fig. 20K,L).

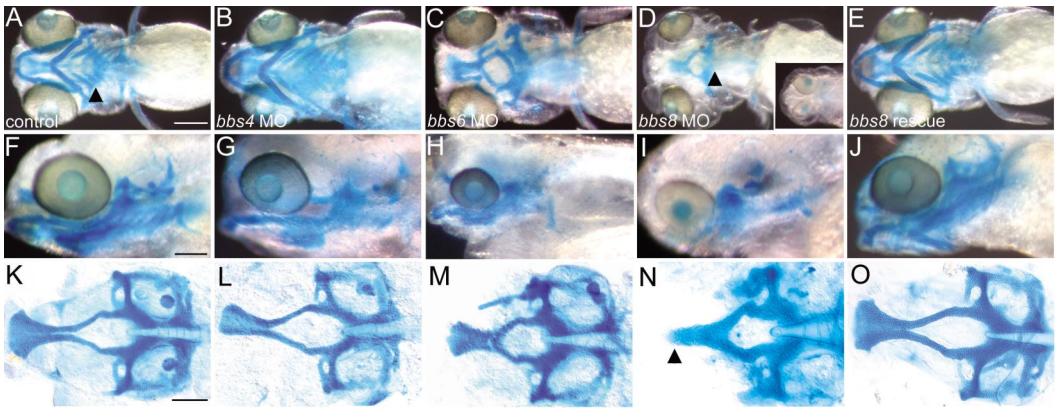

Figure 20. Craniofacial morphology of BBS morphant zebrafish.

A: control larva at 5dpf showing jaws and branchial arches (arrowhead) in dorsal view. **B**: *bbs4* morphant. **C**: *bbs6* morphant with disorganised and hypoplastic cartilages. **D**: *bbs8* morphant lacking branchial arches (arrowhead), and with cyclopia (inset). **E**: complete rescue of *bbs8* morphant craniofacial phenotype by co-injection of 100pg of human mRNA. **F-J**: lateral views of alcian blue stained wholemounts. **K**: control embryo chondrocranial flatmount. **L**: *bbs4* morphants have almost normal chondrocrania, but with a reduced ethmoid plate. **M**: trabeculae of *bbs6* morphants are shortened. **N**: *bbs8* moprhant trabeculae are fused at the midline. **O**: rescue of trabecular defect with human mRNA. Scale bars: A-J = 200μm; K-L = 100μm.

Because of the shortened body axis resulting from the convergent extension defect, the ratio of jaw length to body length is slightly higher in *bbs4* morphants than controls (Figure 21). However, the neurocranial length to width ratio is slightly lower in these morphants (1.2 MO vs 1.3 control, $P<0.05$), mirroring the broadened face in human and mouse BBS mutants.

bbs6 morphants showed a similar gross phenotype to *bbs4* morphants, with renal and cardiac oedema, a down turned body axis and convergent extension defects, but their craniofacial dysmorphology was more pronounced. Viewed ventrally, there was hypoplasia of the branchial arches; in some cases, arches were absent altogether (Fig. 20C). The mandible was severely dysplastic, small and displaced, causing retrognathia, another feature observed in human patients (Fig. 20H). Flatmounts of the neurocrania show a similar gross morphology to *bbs4*

morphants and controls, but the trabeculae, which connect the chondrocranium to the ethmoid plate, homologous to the premaxilla and maxilla in mammals, were much shorter in *bbs6* morphants (160μm MO vs 260μm control, $P<0.001$) (Fig. 20M). The shape of the ethmoid plate was not affected but it was smaller than that of *bbs4* morphants or controls. The jaw (mandible) length to body length ratio was lower than controls (0.04 MO vs 0.05 controls, $P<0.01$) (Figure 21). This means that, even controlling for a shorter body axis, the jaws are still smaller. Furthermore, the neurocranial length to width ratio was much lower than controls (0.95 MO vs 1.3 controls, $P<0.01$), correlating with the widened face seen in patients.

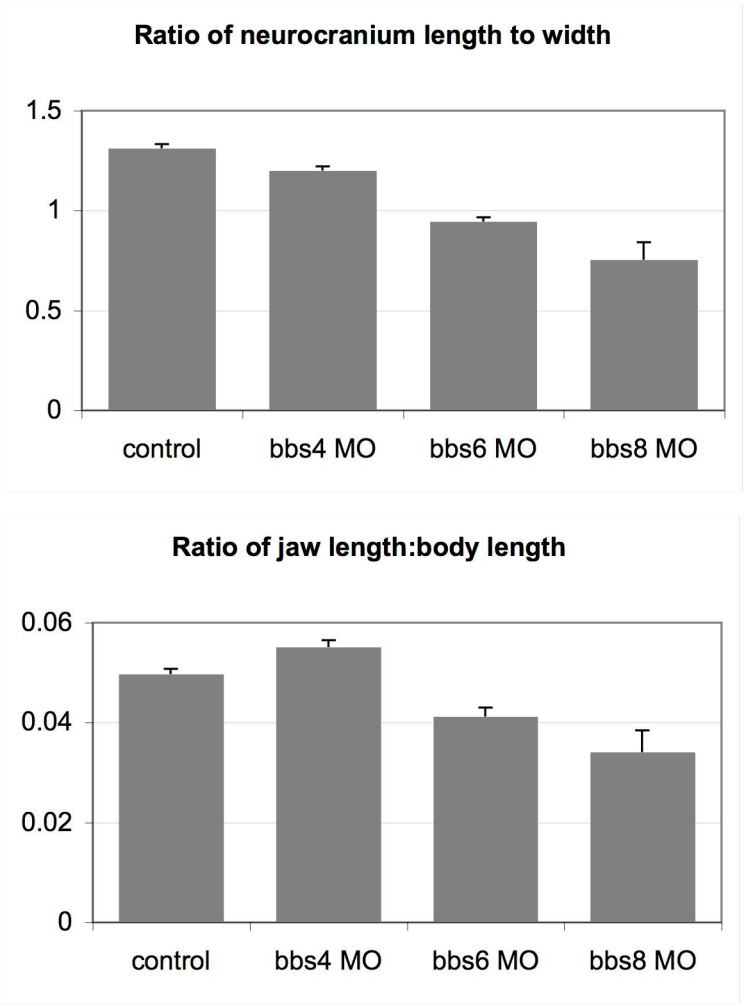

Figure 21. Quantification of morphant crania.

A: the ratio of neurocranial length to width in controls is 1.3. This ratio decreases in *bbs4*, *6*, and *8* morphants respectively, showing that the skull becomes relatively wider and shorter. **B**: the ratio of jaw length (from the tip of the ethmoid plate to the base of the chondrocranium) controls for the CE defect in BBS morphants. This shows that despite body length being reduced, particularly in *bbs6* and *8* morphants, the jaw length is still

relatively shorter, implying that reduced body length is not responsible for the shortened chondrocranium.

Bbs8 morphants consistently had the strongest phenotype, both in general and in the craniofacial skeleton, even with lower doses of MO than used for other BBS genes. Mandibles were absent in almost all cases, as were branchial arches (Fig. 20D,I). In 20% of cases, the embryos exhibited synophthalmia; in some cases, incomplete cyclopia was observed (Fig. 20D inset). In these embryos, craniofacial cartilage was often lacking altogether. This tended to coincide with reduced cartilage condensation in the fin buds too. Examination of the flatmounts revealed that the neurocranium was greatly reduced in size and the ethmoid plate failed to form normally (Fig. 20N). In about 25% of embryos, the trabeculae fused at the midline resulting in a pointed ANC instead of the trabeculae terminating in the widened ethmoid plate. Like *bbs6* morphants, the jaw length to body length ratio and the neurocranium length to width ratio are decreased, albeit to a greater extent (Fig. 21).

The fusion of the trabeculae at the midline of the skull bears striking resemblance to mutants of Sonic Hedgehog transduction, or embryos treated early in development with cyclopamine, an inhibitor of Shh signal transduction (Figure 22). This observation, coupled with the presence of other Shh-related phenotypes commonly observed in BBS patients, led to suspicions of disrupted Shh signalling in morphants and became the subject of further study, detailed in chapter 5.

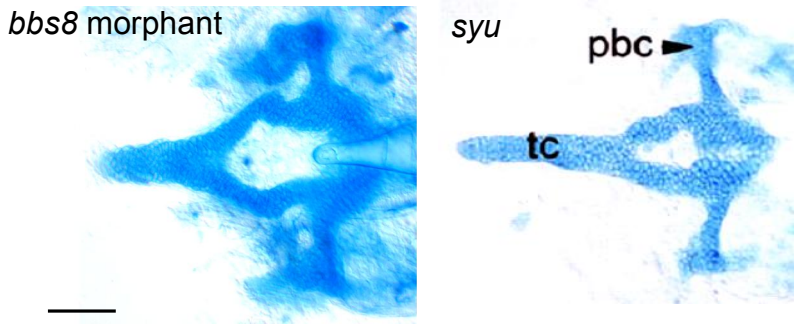

Figure 22. Comparison of *bbs8* morphant and *syu* crania.

In both cases, the trabeculae are fused at the midline, a defect idiosyncratic to *shh* mutants. tc = trabeculae, pbc = parabranchial. *syu* image taken from Wada et al (2005). Scale bar = 100μm.

Discussion

Validation of 3D scanning for subtle phenotypes

Prior to this study, the technique of 3D scanning had been used for several conditions with obvious facial phenotypes, such as DiGeorge syndrome, Noonan syndrome, and Fragile X syndrome (Hammond et al., 2005). It was unknown whether a syndrome with such variable and subtle phenotypes would register reproducible and significant differences in facial regions using this technique. However, BBS has proven to be a syndrome which computer modelling can identify as having a discrete and distinct set of distinct facial features. This has confirmed the intuitive assessment of BBS faces by parents of patients and dysmorphologists experienced in the syndrome.

Correlation of phenotypes in the mouse model

The fact that the human facial patterns were reproducible in the mouse models, both *bbs4* and *bbs6* nulls, suggests a common biological aetiology. Because the mouse skulls had shortened snouts, it was likely that these homologous bones in humans were disrupted. However, it is unethical to expose humans to X-rays to perform non-essential scans, particularly it would involve many patients and CT scans would be the only way to get accurate 3D reconstructions.

The mouse is a useful way to get an idea of what bony regions are affected. Considering the similarities in craniofacial embryogenesis and the signalling molecules employed in humans and rodents, the mouse model gives clues as to what might be awry in the human situation.

The use of the zebrafish to model analogous defects

Surprisingly, there is little published literature using animal models to study human craniofacial malformations. This is partly due to lack of technology in 3D scanning of mice, and the fact that most groups are using zebrafish to study basic

developmental biology. There is an increasing use of the zebrafish to investigate human genetic disease given its acceptance as a valid model organism, particularly for experiments inaccessible in the mouse.

I showed here that regions of the presumptive zebrafish skull are shortened, similar to the human and mouse condition. In some cases, elements such as the mandible and branchial arches are hypoplastic or altogether missing. In the case of a proportion of *bbs8* morphants, the trabeculae are fused at the midline. This is a specific feature of Sonic Hedgehog pathway mutants and so provides clues for further experiments elucidating a possible connection between BBS proteins and the Shh pathway.

It is often the case that gene knockdown in the zebrafish causes more severe effects than in mammalian models. One possible reason for this could be the rapid development of the zebrafish; all major anatomical features have developed by only 36hpf. This means any perturbation to genes expressed in early embryogenesis will be more pronounced than in mammals. Following on from this, there is very little time for other genes or other mechanisms to compensate for early loss of a gene's product. Furthermore, *ex vivo* development means the embryo is more exposed to environmental pressures such as microbes in the water. If loss of a gene even mildly affects embryonic hardiness by affecting, for example, the circulatory system, it might predispose the embryo to more environmental insults than in a mammalian embryo where the embryo is protected *in utero*.

Whilst caution must be taken in interpreting extreme phenotypes in the zebrafish, as long as appropriate controls are made, such as RNA rescue, they are reliable. The phenotypes here serve as a useful method of revealing new roles for proteins which might otherwise be left uncovered as their mammalian phenotypes are too subtle to detect.

Determining the biological processes involved

The majority of the head skeleton derives from the cranial neural crest (CNCC), from which cells migrate to the branchial arches and the frontonasal process where they form facial structures and eventually condense into cartilage and bone. The cells of the ANC, mandibles and branchial arches, which are hypoplastic or absent in Bbs morphants, are derived from neural crest cells that have migrated from the anterior neural tube.

As such, the observation of shortened trabeculae, malformed ethmoid plate, hypoplastic mandibles, and reduced branchial arches points to a dysfunction of neural crest migration. The possibility that BBS proteins are involved in NCC migration gave rise to a new set of questions. Without performing the human, and subsequently mouse, craniofacial analysis, we would not have thought to examine the craniofacial region of the fish. As such, examining facial dysmorphism in humans and then mapping these analyses to the zebrafish may provide an avenue by which to investigate the biological or molecular aetiology of the phenotype, and concurrently uncover new biological processes in which the protein takes part.

The zebrafish has become a tool for studying embryological development, including that of the craniofacial region. It is becoming increasingly acceptable as a model for human disease, given its versatility and the limitation of mouse models for performing functional studies, particularly involving cell migration. There is surprisingly little published work describing the use of the zebrafish in modelling craniofacial dysmorphology syndromes. One study of a causative gene of Noonan syndrome, *Shp2*, (Jopling et al., 2007) showed craniofacial abnormalities which phenocopied those of the Wnt5 morphant, suggesting involvement of the non-canonical Wnt pathway.

Li et al added 2% ethanol to the embryo medium of developing zebrafish to model craniofacial defects present in fetal alcohol syndrome (Li et al., 2007b). They used the fish to show that the phenotype phenocopied that of Shh mutants, similar albeit more severe than the *bbs8* morphants described here. In addition, adding

cholesterol alongside the ethanol was capable of rescuing the alcohol-induced phenotype, implying that alcohol interferes with the cholesterol modification of the Shh ligand.

These studies indicate the utility of the zebrafish in giving clues about the underlying biological basis of a human disease. From this information, further functional experiments can be designed to tease out the precise role of the protein in question.

Several zebrafish mutants have idiosyncratic cranial dysmorphologies associated with them. A large-scale mutagenesis screen identified 48 mutations in 34 loci that caused a variety of craniofacial defects (Neuhauss et al., 1996). Kimmel et al classified these into mutants with affected patterning at the midline, and those with defective antero-posterior patterning (Kimmel et al., 2001). The midline group comprised genes involved in three separate signalling pathways: Sonic hedgehog, nodal, and non-canonical Wnt.

These pathways raise some interesting questions in light of the phenotypes observed with *bbs8* morphants. Midline fusion of the trabeculae is reminiscent of Sonic hedgehog mutant zebrafish (*syu*), or embryos treated with cyclopamine early in development (Wada et al., 2005). This observation became the basis for further analysis of the Hedgehog pathway and is covered in chapter 5. BBS is also associated with polydactyly, another Sonic Hedgehog pathway phenotype. Nodal signalling controls laterality, a feature frequently perturbed in ciliopathy patients. Finally, there are published associations between BBS, the cilium, and the non-canonical Wnt pathway (Ross et al., 2005, Park et al., 2006).

Chapter 4: Neural crest migration defects underlie craniofacial dysmorphology and Hirschsprung's disease in BBS

Introduction

The neural crest in embryonic development

The neural crest is an embryonic tissue which gives rise to a plethora of cell types, amongst which are included the bones of the face. NCCs are multipotent migratory stem cells, whose fate depends upon where they migrate and where they settle, and the molecular cues they are exposed to en route and at their destination. Their progeny include, amongst others: peripheral neurons, glia, enteric neurons, melanocytes, and craniofacial bones. NCCs are responsible for some of the key anatomical features that have enabled vertebrates to become such successful predators, including a large cranium and paired sensory organs. Because of this, Peter Thorogood once famously quoted: "the only interesting thing about vertebrates is the neural crest".

Development of the neural crest can be broken down into four key steps: induction and maintenance, epithelial to mesenchymal transition (EMT), emigration from the neural tube, and differentiation. NCCs migrate dorsally away from the neural tube, as shown in Figure 23. There are four neural crest domains, which migrate in stereotypical patterns to give rise to specific cell types; these are outlined in Table 7.

Neural crest domain	Cell types formed
Cranial neural crest	Facial structures: cartilage, bone, cranial nerves, glia, connective tissue of the face Pharyngeal arches: thymus, odontoblasts of teeth, bones of middle ear and jaw
Trunk neural crest	Early migratory pathway: dorsal root ganglia, sensory neurons, sympathetic ganglia, adrenal medulla, aortic nerves Late migratory pathway: melanocytes
Vagal and sacral neural crest	Enteric (parasympathetic) ganglia of the gut
Cardiac neural crest	Melanocytes, neurons, cartilage, connective tissue of the large arteries

Table 7. Domains of neural crest and their progeny.

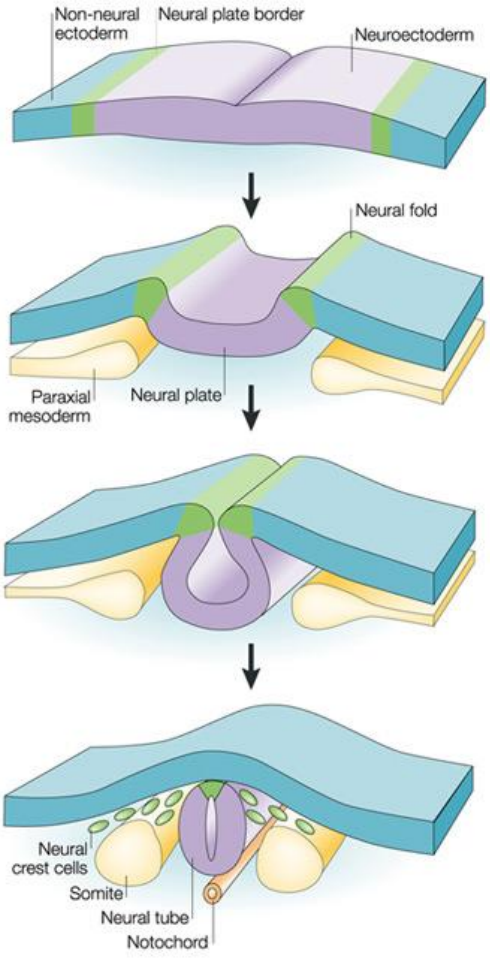

Figure 23. Embryonic origins of the neural crest.

The neural crest is specified at the border between the neuroectoderm and non-neural ectoderm during neurulation in the vertebrate embryo. The neural plate invaginates and then detaches from the overlying ectoderm. The cells formed at this hinge point become neural crest. After the neural tube has fully formed, the NCCs delaminate from the epithelium and migrate away. Taken from (Gammill and Bronner-Fraser, 2003).

Induction and maintenance of the neural crest

The neural crest is a transient population of cells that forms at the border between the non-neural ectoderm and the neuroectoderm during neurulation (see Figure 23). NCC specification relies on a gene regulatory network inducing cells where a combinatorial code of signals coalesce (Sauka-Spengler and Bronner-Fraser, 2008). These conditions exist at the border between the non-neural ectoderm and the neural plate, where high levels of neuroectodermally derived BMPs (bone morphogenetic proteins) meet high levels of ectodermal Wnt6 (Le Douarin and Dupin, 2003). These proteins induce expression of Snail and FoxD3, which together specify the NCCs (LaBonne, 2002; LaBonne and Bronner-Fraser, 1999). In fact, expression of Wnt ligands is both necessary and sufficient to induce ectopic neural crest in *Xenopus laevis* (Saint-Jeannet et al., 1997).

This cell population is then confined as differentiated from the neighbouring cells by Delta-Notch signalling (Endo et al., 2002). These cells are maintained in this specified state by the intermediate concentration of BMP ligand until they receive a cue to migrate. NCC survival is ensured by the expression of a cocktail of transcription factors, including: *AP-2*, *c-Myc*, *Snail1* and *Snail2*, *Sox9*, *Foxd3* and *Id*. Expression of these genes marks the NCCs for EMT, the next step in neural crest development.

Epithelial to mesenchymal transition

EMT is essential before the NCCs can delaminate from the basement membrane to which they are tethered after they are specified. The process of EMT involves several crucial steps: rearrangement of the cytoskeleton, loosening of cell junctions, and reduction of adhesion to the extracellular matrix (ECM).

Firstly, the apical-basal polarity of the premigratory NCCs is lost and the tight junctions joining neighbouring cells are dissolved by breaking down structural proteins such as occludins, which hold cells together (Thiery and Sleeman, 2006). Secondly, cell adhesions are broken down by transcriptional repression of E-cadherin, N-cadherin, and NCAM (neural cell adhesion molecule) (Nieto, 2001).

Repression of E-cadherin is mediated directly by Snail protein (Batlle et al., 2000). Thirdly, major changes in cytoskeletal organisation are brought about through the small GTPases RhoA and Rac1 (Alberts et al).

Many of the same molecules are involved in NCC EMT as function in tumour metastasis, when the cancerous cells detach from their epithelium and become migratory, invading neighbouring tissues, or blood and lymphatic vessels, and spreading to distant sites. NCCs, like tumor cells, are remarkable in the distances over which they can migrate, and they do this by crawling. The NCCs require ECM over which to migrate and rely on interactions between laminin, integrins, and fibronectin. Like invasive tumour cells, NCCs secrete, or express on their membranes, matrix metalloproteases (MMPs) to break down ECM as they move (Egeblad and Werb, 2002). These MMPs, such as members of the ADAM family, are important in premigratory cells to break down their ECM attachments, and in migratory cells to destroy ECM in the path of travel.

NCC migration

Once fully delaminated, migrating NCCs extend protrusions in the direction of migration by polymerising actin microfilaments in a two-dimensional orthogonal mesh with most of the filaments parallel to the substratum in the direction of migration. These lamellipodia then form focal contacts containing integrins, which adhere to the substratum, in this case the ECM. Forward movement is accomplished by actin treadmilling, whereby actin is polymerised at the leading edge of the cell and depolymerised at the trailing edge. This gives the illusion that the actin filaments are stationary as the cell moves.

NCCs migrate in streams following stereotypical pathways, coordinated by diffusible and non-diffusible guidance cues. Migration happens in a polarised manner and the centrosome often localises between the nucleus and leading edge of the cell to polarise the microtubules to assist persistent movement in a particular direction. The positioning of the centrosome seems to reinforce the

strength of cell polarity established by the actin cytoskeleton, albeit by a poorly understood mechanism.

The role of non-canonical Wnt signalling in NC migration

Two papers by Roberto Mayor's lab have demonstrated important roles for non-canonical Wnt, or planar cell polarity (PCP) signalling in neural crest migration (De Calisto et al., 2005; Matthews et al., 2008). The first paper used specific Dvl mutant constructs which either activated or repressed canonical Wnt signalling to show that, in *Xenopus*, canonical Wnt signalling is required for NCC induction, and non-canonical Wnt signalling is essential for NCC migration. The requirement for non-canonical Wnt signalling was cell autonomous and depended on the Wnt11 ligand. The second paper from Mayor's lab showed that an ECM-interacting protein, Syndecan-4, played a role in the PCP pathway and that PCP controlled the direction of cell migration by regulating the position of cell protrusion formation. This was accomplished by activation of RhoA.

Ross et al's work of 2005 showed that BBS proteins play a role in the PCP pathway, suggesting PCP signalling via the primary cilium. Subsequent work has confirmed this, particularly that of Park et al. Park et al showed that *Xenopus* lacking expression of two PCP genes, either *inturned* or *fuzzy*, had ciliogenesis defects (Park et al., 2006). Therefore, PCP seems to rely on cilium formation, while at the same time being important, in some contexts, for the formation of the cilium itself.

The fact that BBS proteins and cilia are important for non-canonical Wnt signalling, which in turn is involved in NCC migration, forms the basis for a hypothesis whereby absence of BBS proteins affects NCC migration by inhibiting non-canonical Wnt signalling. This can be put in the context of the neural crest origin of all the craniofacial bones disrupted in the human, mouse, and zebrafish BBS knockouts. The craniofacial patterning of the human cases, recapitulated in mouse and fish, shows a mid-facial depression of these crest-derived features. Because these cells migrate rostrally to populate the frontonasal prominence, it is

feasible that these cells have failed to migrate as far in the absence of BBS proteins, thereby producing a shorter snout.

The cranial neural crest

Cranial neural crest cells (CNCCs) contribute to the majority of the structures of the vertebrate head. These cells made possible some of the innovations that vertebrates have uniquely evolved, including the skull, which has allowed the vertebrate brain to expand. CNCCs are unique amongst the four neural crest domains in being able to form cartilage and bone. Fate mapping experiments by Noden et al showed that the majority of the vertebrate facial bones are NCC derived (reviewed in Hall, 1988).

CNCCs migrate out of the brain in three streams (Graham, 2003). The trigeminal crest arising from the midbrain and rhombomeres 1 and 2 contributes to the majority of the face. These cells form the frontonasal prominence, which forms the forehead, middle of the nose, philtrum of the upper lip, and the primary palate (Helms and Schneider, 2003). The ventral region of the first pharyngeal arch gives rise to the lower face: the mandibles, maxilla, and temporal bones. The second stream of migrating cells, the hyoid crest, gives rise to neurons and the hyoid skeleton, while the third stream, the post-otic, forms the pharyngeal bones. Figure 24 shows how CNCCs contribute to the majority of facial structures in vertebrates.

These streams derive their identity from the antero-posterior (AP) restricted pattern of Hox gene expression, which is in turn established by an AP gradient of retinoic acid (RA). Later on in facial morphogenesis, dorso-ventral (DV) patterning is established by Dlx homeobox transcription factors, which give the pharyngeal arches their identities.

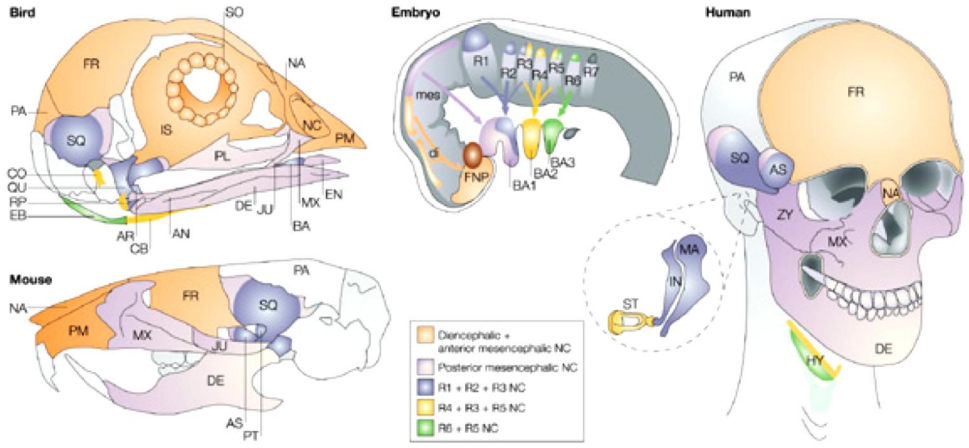

Figure 24. CNCC contributions to the amniote skull.

In birds, mice, and humans the CNCC migrating from the hind- and midbrains contribute to homologous structures: the lower and upper jaws, the nose, and structures around the upper face including the eye and forehead. The back of the skull is primarily mesodermal in origin. Taken from (Santagati and Rijli, 2003).

These NCCs have an intrinsic, species-specific set of gene expression characteristics that give each species its stereotyped countenance. Experiments by Schneider and Helms (2003) showed that transplanting frontonasal neural crest cells between quail and duck embryos resulted in a host with the beak of the donor. This and further work showed that these cells do respond to cues from the local cellular environment, but the extent to which they do depends on the size of the cell population. Therefore, it seems CNCCs have an intrinsic program of migration but they also respond to cues from the overlying ectoderm.

Several different signalling pathways interact in a complex manner to pattern the face. FGF8 is key for CNCC survival and patterning, particularly of the teeth and oral features. FGF8 expression is inhibited by BMP4, which serves to spatially restrict FGF8 (Haworth et al., 2004). FGF3 is important for pharyngeal arch polarity (David et al., 2002). Endothelin-1 concentration, together with Hand2, control cartilage and bone differentiation (Thomas et al., 1998). Sonic Hedgehog (Shh) is indispensable for frontonasal outgrowth (Hu and Helms, 1999).

The interactions of these molecules and tissues in three dimensions make the morphogenesis of the face extremely complex. Defects in initial NCC migration

and/or the molecules coordinating migration and differentiation, results in craniofacial dysmorphology associated with many genetic syndromes. This includes Bardet-Biedl syndrome, so it is important to assess whether BBS proteins play a role in this elaborate process.

Neural crest defects and craniofacial anomalies

Craniofacial anomalies comprise roughly one third of all congenital malformations. In some cases, defects are restricted to the head, in others; other parts of the body are affected too. Some defects are genetic while others are caused by fetal exposure to teratogens, the most common being alcohol. Because of the tight linkage between the development of the face and the forebrain, many craniofacial defects are associated with brain abnormalities, often causing mental retardation.

Severe craniofacial malformations can result from anomalous anterior neural tube closure or gross mispatterning of the brain and face. Table 8 summarises some of these extreme malformations and their causes:

Malformation	**Features**	**Syndromes/cause**
Holoprosencephaly (HPE)	Failure of the forebrain to divide causing cyclopia, absence of olfactory bulbs at most extreme; agenesis of corpus callosum, single central incisor when mild	Mutations in Shh or pathway components such as *Patched* and *Gli2* Or teratogens such as alcohol or retinoic acid
Anencephaly	Opening of the anterior neural tube leading to absence of the cerebral hemispheres and bones of the face	Meckel syndrome, Acrocallosal syndrome, short-rib polydactyly syndrome
Encephalocele	Gap in the neural tube causing an opening in the skull	Meckel syndrome, Joubert syndrome
Craniosynostosis	Premature fusion of cranial bones	Mutations in FGF receptors, Msx2, Twist, and others

Table 8. Craniofacial deformations associated with neural tube defects.

Although extreme, several of these malformations are features of ciliopathies. Exencephaly is a phenotype observed in some *bbs4* null mice. Encephalocele, a milder form of exencephaly, is a common feature of Meckel and Joubert syndromes. Defects at the mildest end of the HPE spectrum (single central

incisor, agenesis of the corpus callosum) have been observed in BBS patients (P. Beales, personal communication).

Genetic syndromes specifically affecting neural crest development, the "neurocristopathies", cause more subtle craniofacial dysmorphology, usually arising from aberrant specification or migration of CNCCs (Figure 25). Table 9 lists several of these syndromes and demonstrates the ubiquity of craniofacial dysmorphology.

Neurocristopathy	**Gene mutated**	**Features**	**Reference**
Waardenburg-Shah	*SOX10* (transcription factor)	Hirschsprung's, frontonasal dysplasia, cleft lip and palate, piebaldism	(Pingault et al., 1998)
DiGeorge	Deletion 22q11 (*TBX1* – transcription factor)	Craniofacial, dental, parathyroid, cardiac defects, schizophrenia	(Merscher et al., 2001)
Treacher-Collins	*TCOF1* (nucleolar phosphoprotein)	Craniofacial, hearing loss	(Wise et al., 1997)
Congenital Central Hypoventilation syndrome	*PHOX2B* (transcription factor)	Neuroblastoma, hypoventilation, facial dysmorphism, Hirschsprung's. Caused by failure of NCC to innervate the lung	(Amiel et al., 2003)
Mowat-Wilson	*ZEB2* (transcription factor)	Microcephaly, facial gestalt, Hirschsprung's, mental retardation	(Zweier et al., 2002)

Table 9. Features of neurocristopathies showing the ubiquity of craniofacial defects.

Figure 25. Facial features of some neurocristopathies.

Photographs showing craniofacial defects in three neurocristopathies: Treacher-Collins, Waardenburg-Shah, and Mowat-Wilson syndromes. Taken from http://www.emedicine.org; (Zweier et al., 2005); and (Read and Newton, 1997).

The enteric nervous system and Hirschsprung's disease

The enteric nervous system (ENS) is part of the peripheral nervous system (PNS) (Heanue and Pachnis, 2007). The ENS is highly complex and comprises a wide diversity of neurons and associated neurotransmitters. ENS function is largely independent of CNS input, and the ENS makes autonomous decisions about stimulating targets. The ENS innervates the smooth muscle lining the gut, thereby controlling the mixing and peristalsis of digested food in the intestines. Additionally, the ENS regulates intestinal secretions of enzymes, water, and electrolytes, as well as the blood flow to the gut.

Enteric neurons are organised in two layers in the gut (see Figure 26). The outermost layer consists of myenteric plexi sandwiched in between the outer longitudinal muscle and inner circular muscle layers. These neurons control muscle contraction. The inner layer of neurons lies in the submucosa and innervates the secretory cells and vasculature.

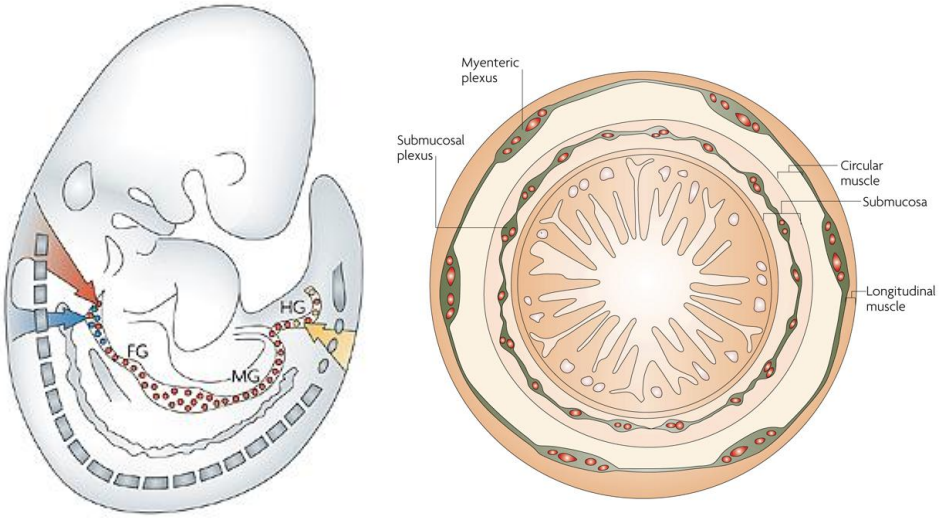

Figure 26. Organisation of the ENS.

The left-hand image shows streams of NCCs emigrating from the vagal region of the hindbrain through the branchial arches and into the foregut, where they migrate along the length of the gut to colonise it. There is a minor contribution of cells to the hindgut from sacral NCCs derived from the posterior end of the neural tube. The right-hand image shows a transverse section through the fully developed gut showing the two rings of ENS neurons: the outer myenteric plexus and the inner submucosal plexus. Taken from Heanue and Pachnis (2007).

Like the PNS, the ENS is neural crest derived. It originates from the vagal NCC, which forms caudal to the hindbrain at the level of somites 1 to 7. Cells from different axial levels of this region populate particular regions of the gut. These cells delaminate and migrate into the gut, whereupon they are called enteric neural crest-derived cells (ENCCs), and have the potential to differentiate into mature neurons. The ENCCs migrate in a rostral to caudal direction and colonise the gut in this order: foregut (oesophagus, stomach, duodenum); midgut (small intestine, caecum, ascending and transverse colon); hindgut (descending colon, sigmoid, and rectum). In humans, this migration takes place between 4 and 7 weeks gestation.

For the adult gut to function, the gut must be fully colonised from foregut to hindgut and contain the requisite number of neurons. As such, three events are required: 1) complete migration of the ENCCs to the distal-most portion of the hindgut; 2) sufficient proliferation of ENCCs to ensure sufficient neuronal mass;

3) appropriate differentiation of particular ENCCs into the correct neuronal subtype.

Failure of the enteric neurons to fully colonise the gut results in Hirschsprung's disease (HSCR), a congenital malformation with a frequency of 1 in 5,000 live births. In HSCR, there is an absence of neurons in the hindgut, causing tonic contraction of the circular muscles leading to obstruction of the gut lumen, causing megacolon, a massive enlargement of the colon. It also means stools cannot pass through the gut, leading to chronic constipation and the risk of bowel rupture. Standard treatment involves surgical resection of the affected segment of bowel, but several investigations involving the use of stem cells are underway as a potential alternative.

Most cases of HSCR are sporadic, but in the few inherited cases, it is non-Mendelian, suggesting a complex inheritance involving multiple loci. In 70% of HSCR cases, incidence is isolated and there are no extra-intestinal manifestations. However, 30% of cases are syndromic and include involvement of other organs. Many of these syndromic cases are neurocristopathies such as Waardenburg-Shah, Mowat-Wilson, and Congenital central hyperventilation syndromes. Amongst these syndromic cases, Down's syndrome accounts for 10%.

About 75% of all cases of HSCR are caused by mutations in *RET*, which encodes the receptor for glial derived neurotrophic factor (GDNF). Other genes which can cause HSCR when mutated include the neurocristopthy genes: *EDNRB* (also causes piebaldism, or melanocyte defects), *SOX10*, *PHOX2B*, and *ZFHX1B* (See Table 9 for references). Also, mutations in *Sonic Hedgehog* results in aganglionic colons in mice (Ramalho-Santos et al., 2000).

While HSCR is present at 1 in 5,000 in the population at large, several investigators have noted a high frequency of the disease in BBS patients. Maeda et al (1984) first noticed the association of BBS with HSCR. This was followed by reports by six independent observations of the same phenomenon (Alter et al., 2001; Beales et al., 1999; de Pontual et al., 2007; Işlek et al., 1996; Lorda-

Sanchez et al., 2000; Radetti et al., 1988). Cherian et al reported HSCR in two siblings with BBS (Cherian et al., 2008). In one case, the whole ileum and colon was aganglionic and in the other, only the colon. The fact that both siblings had HSCR and BBS suggests that the BBS mutation was responsible for the HSCR. de Pontual et al (2007) found that 45% (n=51) of BBS patients in their cohort, irrespective of underlying mutation, had HSCR. This is an over-representation of over 2,000-fold relative to the general population, and therefore unlikely to be due to chance ($p<0.001$). The incidence of HSCR in our BBS patient cohort is around 10% (P. Beales, personal communication).

de Pontual et al found that an allele of the *RET* gene predisposing to HSCR (TT) was present at higher frequency in patients with syndromic HSCR (including BBS, Mowat-Wilson, Waardenburg-Shah, Down Syndrome, and CCHS) versus those without (34.9% with HSCR vs 21% without, n=195 and 198 respectively). For BBS in particular the frequency of this TT allele increased from to 4% to 34% (n=23 and 28 respectively) for patients also manifesting HSCR.

The frequency of this allele is estimated at 25% in the Caucasian population. The authors suggest that the presence of the TT allele predisposes the patient to get HSCR. However, the frequency of the SNP in BBS patients with HSCR is 34% compared to a wild type frequency of 25%. This 9% increase cannot explain a 2,000-fold increase in the frequency of HSCR and so does not serve to explain the clinical phenotype.

The authors proposed that the disruption to PCP signalling caused by BBS mutation affected NCC migration which, in conjunction with a hypomorphic *RET* allele, leads to HSCR. However, this is an oversimplified model, because 66% of BBS patients have HSCR, but lack the TT allele in *RET*, and 13% of BBS patients do not have HSCR but have the TT allele. They also noted the expression of BBS genes in vagal NCCs in human embryos.

Zebrafish are a powerful means of investigating neural crest migration

Current understanding of neural crest development comes from the study of the classical embryological models: mouse, chick, frog, and now fish (Halloran and Berndt, 2003). Each model organism has its particular advantages: the mouse is most similar to humans, so is most relevant for study of disease; the chick is useful for grafting experiments, particularly transplants with quail tissue; the frog embryo is easy to manipulate, genes can easily be knocked-down or overexpressed, and fate mapping experiments can be performed.

In the last ten years, the advantages of the zebrafish for studying neural crest development have become realised. Firstly, the optical clarity means cell migration can be studied in real time in living embryos. Secondly, the high fecundity and low cost of maintenance enables forward genetic screens that are impossible in other vertebrate species. The mutants enable functional characterisation of genes involved in NCC development. Third, the availability of transgenic lines expressing GFP in particular tissues enables precise and quantitative mapping of individual cell behaviour *in vivo*. The latter point has been exemplified by the generation of the *sox10::eGFP* transgenic line that expresses GFP exclusively in the neural crest (Wada et al., 2005). I have taken advantage of this for several experiments in this thesis.

Several recent studies highlight the utility and power of the zebrafish in studies of neural crest migration. However, the zebrafish still remains a tool largely used to answer fundamental questions about embryonic development and is only just emerging as a valid system in which to model human disease processes. Nevertheless, the ability to create knockout models in zebrafish that are not readily available in mouse, and the subsequent phenotypic and functional experiments possible, make the zebrafish a perfect model for investigating NCC migration in BBS models.

Development of the neural crest in zebrafish

Zebrafish neural crest development is remarkably similar to higher vertebrates, although there are obvious anatomical differences between fish and mammals. In both fish and mammals, trunk NCCs migrate in two pathways: the medial pathway between the neural tube and the somite, where cells form peripheral neurons and glia; and the later migrating lateral pathway between the somite and the ectodermal epithelium, where cells differentiate into melanocytes. Similarly, the cranial neural crest consists of two main migratory streams. Streams of NCCs migrating from the hindbrain form the pharyngeal skeleton, while more anterior-derived cells form the braincase, or neurocranium (Lumsden and Guthrie, 1991).

In the zebrafish embryo, the head skeleton forms from CNCCs migrating rostrally from the hindbrain to populate the head and face. The pharyngeal skeleton is entirely neural crest derived and consists of seven branchial arches (Schilling et al., 1996). The anteriormost two become the mandible and ceratohyal respectively and form the lower jaws of the animal. The posterior five arches form the branchial skeleton from which the gills derive and hence the fish's breathing apparatus.

The neurocranium comprises of the broad basal plate from which protrude the long, paired trabeculae which fuse at the anterior end into a condensation called the ethmoid plate. Fate mapping experiments by Wada et al (2005) showed the trabeculae originate from dorsally-derived cells, while the ethmoid plate derives from more anterior positioned precursors (Wada et al., 2005). This is shown in Figure 27.

The fish skull is analogous to the mammalian skull and all the equivalent features are present. The migration of the CNCCs in fish responds to the same signalling cues as the mammal. Because of the complex three-dimensional geometry of the cranial skeleton, several signalling systems are deployed. Kimmel et al (2001) studied the available data and concluded there was a separate signalling pathway for each of the three main axes: anteroposterior, dorso-ventral, and medio-lateral.

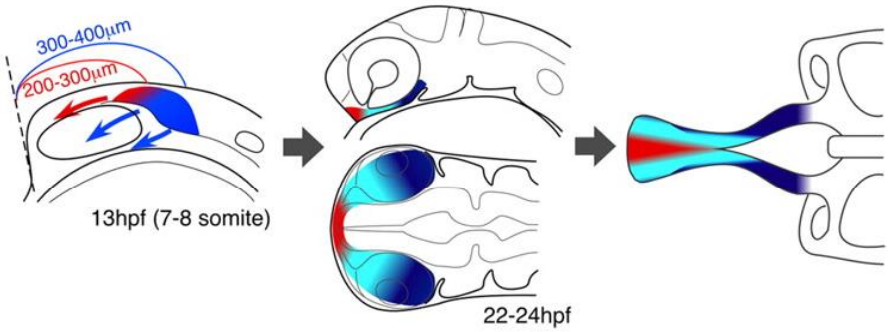

Figure 27. CNCC migration in the zebrafish embryo.

Posterior-derived CNCCs migrate dorsally around the eye and contribute to the trabeculae. Anterior-derived CNCCs migrate on a ventral pathway and give rise to the ethmoid plate. Taken from Wada et al (2005).

The anteroposterior axis is the best understood, and is produced as CNCCs emerging from different axial levels in the neural tube migrate to stereotyped destinations to pattern the AP axis. This regulates the order of the pharyngeal arches. Nested expression of different Hox genes in the rhombomeres of the hindbrain specifies the axial level of these emigrating cells.

Mutations in genes controlling dorsoventral polarity such as *Dlx5* and *Dlx6* result in rearrangements such as the homeotic transformation of lower jaw into upper jaw (Depew et al., 2002). Furthauer et al showed that Fgf8 was also required for dorsoventral patterning in the zebrafish and ectopic Fgf8 expression leads to expansion of dorsal tissues at the expense of ventral ones (Fürthauer et al., 2004). They also concluded that Fgf8 had organiser-like properties in the developing head.

The skull and pharyngeal skeleton also have a mediolateral polarity, with bones arranged in a symmetrical pattern about a midline (de Beer, 1937). Details of the development of this axis are emerging from a group of "midline mutants" in which the mediolateral axis of the skull is anomalous. The best understood molecule regulating midline polarity in the head is Sonic Hedgehog.

This ligand is secreted from the midline of the prechordal plate and anterior neural tube (Strähle et al., 2004). It also signals from the oral ectoderm to direct the polarised movement of cells at the midline of the embryo (Hu and Helms, 1999;

Marcucio et al., 2005). Shh acts to keep streams of migrating crest cells separated at the midline. Therefore, ablation of Shh or its downstream pathway components results in a fusion of the trabeculae, absence of the ethmoid plate, and synophthalmia, in which the eyes are closely spaced.

The zebrafish enteric nervous system

Just like the mammalian ENS, the zebrafish ENS derives from the vagal neural crest, whose cells migrate progressively along the gut to colonise the foregut, midgut, and hindgut. The fish gut is much less convoluted than the mammalian and, like many fish, lacks a stomach (Wallace et al., 2005). The anterior intestine, the intestinal bulb, has a wider bore than the posterior and is thought to act as a stomach-like reservoir for food. The adult gut only has two kinks; one midway through the foregut, and one at the boundary between the foregut and midgut. The ENS controls the peristaltic activity of the smooth muscle lining the gut lumen as well as the secretory and vascular supply, just as in mammals.

In mouse, the development of the ENS begins at around E9.5 and continues until around E14.5. In zebrafish, this process happens much more rapidly: NCCs begin to migrate out from the vagal region at 36hpf and have begun to colonise the foregut by 48hpf. By 72hpf, they have extended all the way along the distal portion of the gut to colonise the mid- and hindgut. By 96hpf, these cells have already differentiated into mature neurons and are functional. This can be observed by the coordinated peristaltic contractions in the gut, visible by time-lapse DIC imaging of 96hpf embryos.

The conservation of ENS developmental mechanisms, combined with the architectural simplicity of the gut make the fish a good model system for studying ENS development. Kuhlman and Eisen performed an ENU-based mutagenesis screen to identify genes involved in ENS development. They screened the phenotype by immunostaining with an anti-HuC/D-ElaV antibody, which identifies all differentiated neurons (Kuhlman and Eisen, 2007). They identified 13 mutant lines, four of which affected solely the enteric neurons, while the other

9 had pleiotropic effects. These included: small head, neural tube defects, melanogenesis defects, mislocalised dorsal root ganglia, and rounded somites. Many of these phenotypes are reminiscent of neurocristopathy and it is likely that many of these loci are involved in NCC development, but are yet to be cloned.

These authors then made time-lapse movies of the peristaltic contractions in 5.5dpf wild type and mutant embryos. They showed that the rostral to caudal peristaltic waves correlated perfectly with the degree of gut innervation. This shows that the fish can be used to test the physiological, functional effects on the gut as well as the cellular effect. As such, the fish makes a good model for studying the potential causes, both molecular, cellular, and physiological, for the high incidence of Hirschsprung's disease in BBS patients. This is valid since gut aganglionosis and immotility is what causes the symptoms of megacolon and chronic constipation in human patients.

The aims of this investigation

The human and mouse craniofacial defects discussed in the previous chapter were modelled in the zebrafish. This revealed that while craniofacial deformities were common to all BBS morphants, the most striking phenotypes were consistently seen when *bbs8* was knocked down. Given the neural crest contribution to all the affected cranial regions: the mandible, maxilla, nasal bones, and pharyngeal skeleton, I aimed to determine whether BBS proteins, in particular Bbs8, had a role in NCC development. Because NCC development comprises four main events (see above), I aimed to test these to see what role the proteins have in particular. Because the *sox10::eGFP* transgenic zebrafish allows real-time imaging of NCCs *in vivo*, I aimed to take advantage of this facility in uncovering potential effects on NCC development. In particular, I wanted to study how the contribution of the neural crest to the craniofacial skeleton was affected in *bbs8* morphants to see if craniofacial dysmorphology could be directly attributed to inhibition of migration.

In addition, I aimed to determine the effect of *bbs8* knockdown on other crest-derived cell types, in particular the melanocytes and enteric neurons. While no BBS patients have been observed with piebaldism or albinism (splotchy or absence altogether of skin pigmentation), I have already discussed the prevalence of Hirschsprung's disease. Because these are both NCC derived cell lineages I also wanted to examine these cells in *bbs8* knockdowns.

Given the availability of primary cells taken from human patients with *BBS8* null mutations, I also designed experiments to look at cell migration *in vitro* in fibroblasts to extend the study from NCCs. Additionally, I tested the molecular basis for the NCC defect by manipulating the non-canonical Wnt signalling pathway in presence and absence of Bbs8 protein to see if Bbs8 was mediating migration via this mechanism.

Finally, I wanted to further the study by examining the craniofacial morphology of other ciliopathy morphants such as *mks3* and *ofd1* to see if other ciliopathy proteins were potentially involved in NCC development. This could raise the exciting possibility that the cilium, or IFT, in general, is important for NCC migration.

Results

Induction and maintenance of neural crest cells are unaffected in morphants

The craniofacial regions disrupted in BBS mutants and morphants derive from the neural crest. These cells form at the edges of the neural plate and the dorsal aspect of the neural tube. There are several stages in neural crest development and disruption in any of them could potentially lead to the phenotypes observed in the *bbs8* morphants.

A reduction in the neural crest derived structures of the craniofacial region could be due to one of several factors: 1) neural crest are not being specified correctly; 2) the NCCs are not being maintained before migration; 3) NCCs are not migrating properly; 4) NCCs are differentiating inappropriately either along the course of migration or once they have reached their target sites.

To begin with, I tested the first two hypotheses to see if NC induction or maintenance were affected. To test NCC induction, I performed *in situ* hybridisation on 5ss embryos to examine *foxd3* and *Sox10* gene expression. These are two of the earliest markers expressed specifically in NCCs and so can be used to assess the extent of NCC induction in the neural tube. *Foxd3* expression in controls and *bbs8* morphants was comparable, suggesting that NCC induction is normal and a regular number of NCCs are being specified (Figure 28).

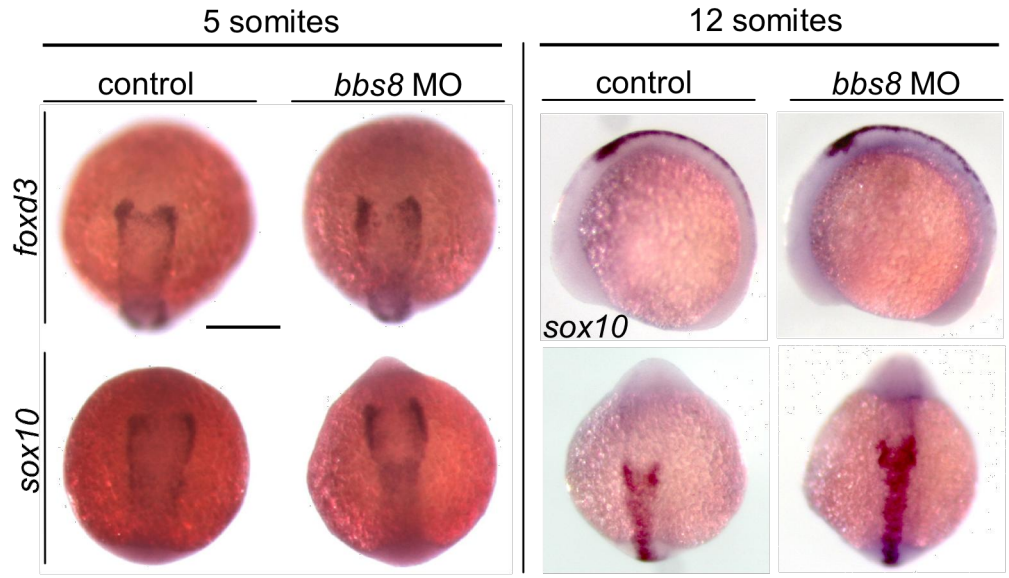

Figure 28. Induction and maintenance of NCCs.

At 5ss expression of two NCC-specific markers, *foxd3* and *sox10*, are equivalent in controls and *bbs8* morphants, suggesting normal NCC induction. At 12ss, immediately prior to migration, expression of *sox10* shows a similar pattern in controls and morphants, suggesting that NCCs in the neural tube have been maintained and proliferated normally. Scale bar = 500μm.

I next tried to determine whether NCC maintenance was affected in morphants. After specification, which occurs at the 5ss, there is a delay until the 12ss before the NCCs begin to migrate. During this four-hour period, NCCs must be maintained before they emigrate from the neural tube, anteriorly into the head and dorsally into the trunk. Embryos at 12ss were stained by *in situ* hybridisation for the marker *Sox10*, a pan-neural crest marker. Again, there was no difference in the maintenance of NCCs, as the domain size and intensity of *sox10* expression was unaffected in *bbs8* controls (Figure 28). It is possible that there may even be more pre-migratory NCCs in *bbs8* morphants.

The number and proliferation of neural crest cells is unaffected in morphants

Given that induction and maintenance of NCCs is unaffected, as an extra control I tested whether the number and proliferation of NCCs was affected in *bbs8* morphants. It may be that migrating NCCs either fail to proliferate, or die en

route during migration, which could potentially give rise to the craniofacial phenotypes observed.

First, I examined the number of NCCs in zebrafish embryos during NCC migration at 16ss. *Sox10::eGFP* embryos that express GFP specifically in the NCCs were injected with either control or *bbs8* MO and 100 embryos of each type were dissociated into single cells. These cells were sorted for GFP expression using wild-type embryos as GFP-negative controls to calibrate the cell sorter. The number of NCCs in control and *bbs8* morphants was not significantly different and in both cases ranged from around 800 cells for 14ss embryos to 1,200 for 20ss embryos. This suggested that the number of NCCs was the same during the course of migration (Fig. 29A-D).

Next, I tested whether proliferation of NCCs was affected. To do this, I performed immunohistochemistry on wholemount *Sox::10eGFP* transgenic embryos at 24hpf and 72hpf using an anti-phosphohistone antibody. At 24hpf, there was more cell proliferation in the brains of control embryos than morphants, particularly in the eye (Fig. 30A,B). However, there was no difference in the number of proliferating NCCs. In morphants, the NCCs had failed to populate the anterior portion of the head by 24hpf, whereas in controls the NCCs had migrated around the eye. At 72hpf, there was greater proliferation in the brain regions of the morphants compared to controls, but again, there was no difference in the amount of proliferation in the NCCs themselves (Fig. 30C,D).

Sox10:eGFP expression revealed a distinct lack of NCCs forming branchial arches in morphants, explaining why the arches were hypoplastic or missing. Examination of the expression of Sox10:eGFP in the trunk revealed a distinct lack of streams of migrating NCCs from the neural tube (Fig. 30E,F). HuC/D is a neuronal marker and its expression was not increased in the *bbs8* morphant NCCs trapped in the neural tube, suggesting that these cells were not inappropriately differentiating and that premature differentiation was not responsible for the observed migration defect (fig. 30G,H).

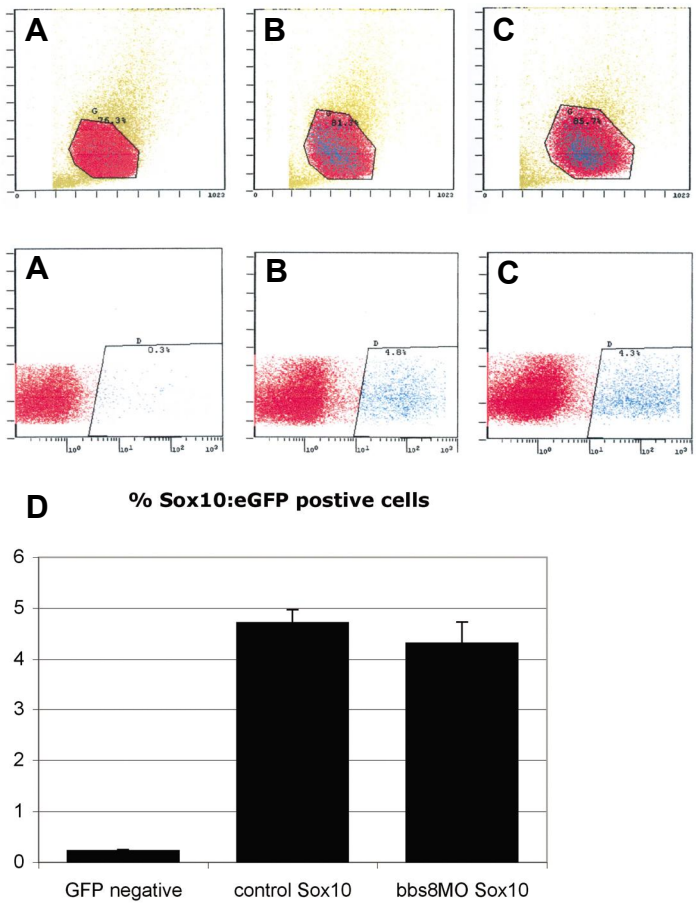

Figure 29. FACS data on NCC abundance.

A-C: FACS plots showing the proportion of events in control GFP-negative, uninjected s*ox10:eGFP*, and morphant embryos is the same. In each case around 80% of events are processed as cells. **A'**: in GFP-negative embryos, only 0.3% of cells were sorted (non-zero value likely due to autofluorescence). **B' and C'**: in uninjected and *bbs8* morphant embryos, around 4.5% of cells were fluorescent. **D**: quantification showing no significant difference between the percentage of NCCs as a total of all body cells in control and morphant transgenics, suggesting a similar amount of NCC proliferation.

Neural crest migration is inhibited in *bbs* morphants

In light of these results, I tested the extent of migration in the NCCs of morphants. In the first instance, wholemount *in situ* hybridisation was performed to examine the expression of *crestin*, a marker of neural crest cells. This was performed at the 20ss when NCCs migrate in streams ventrally away from the neural tube into the trunk, with one stream per somite. A crude quantitative measure of NCC migration is to count the number of migrating streams in each treatment. In controls, there were an average of 13 streams of crest compared to about 9 for

bbs4 morphants, 3.5 for *bbs6*, and 1 for *bbs8* (Fig. 31A-D). The effect was almost completely rescued by co-injecting human *bbs8* mRNA with the *bbs8* MO (9 streams), suggesting that the effect is specific to the MO (Fig. 31E).

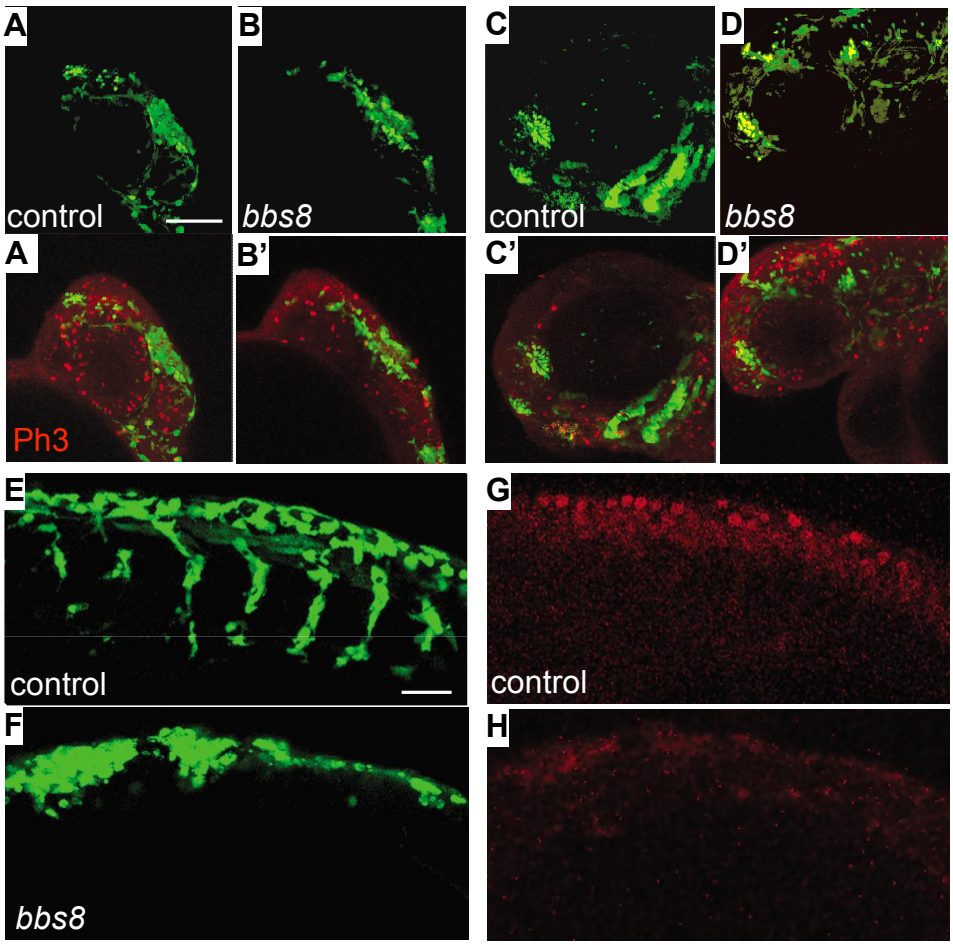

Figure 30. Examination of NCC proliferation and migration *in vivo*.

A-B': expression of Sox10:eGFP (green) shows an inhibition of migration in *bbs8* morphants. While there are more proliferating cells in the head of controls (red staining), the amount of proliferation in NCCs themselves is not changed in morphants. **C-D'**: expression of Sox10:eGFP at 72hpf reveals a lack of branchial arch formation by NCCs in morphants. It again shows no difference in proliferation of the Sox10-positive CNCCs in morphants. **E,F**: examination of the trunk of 24hpf embryos reveals a lack of migrating streams of NCCs in morphants. **G,H**: expression of the pan-neuronal marker, HuC/D, is not increased in morphant neural tubes, suggesting that the observed migration defect is not due to premature proliferation into mature neurons. Scale bars: A-D' = 100μm; E-H = 50μm.

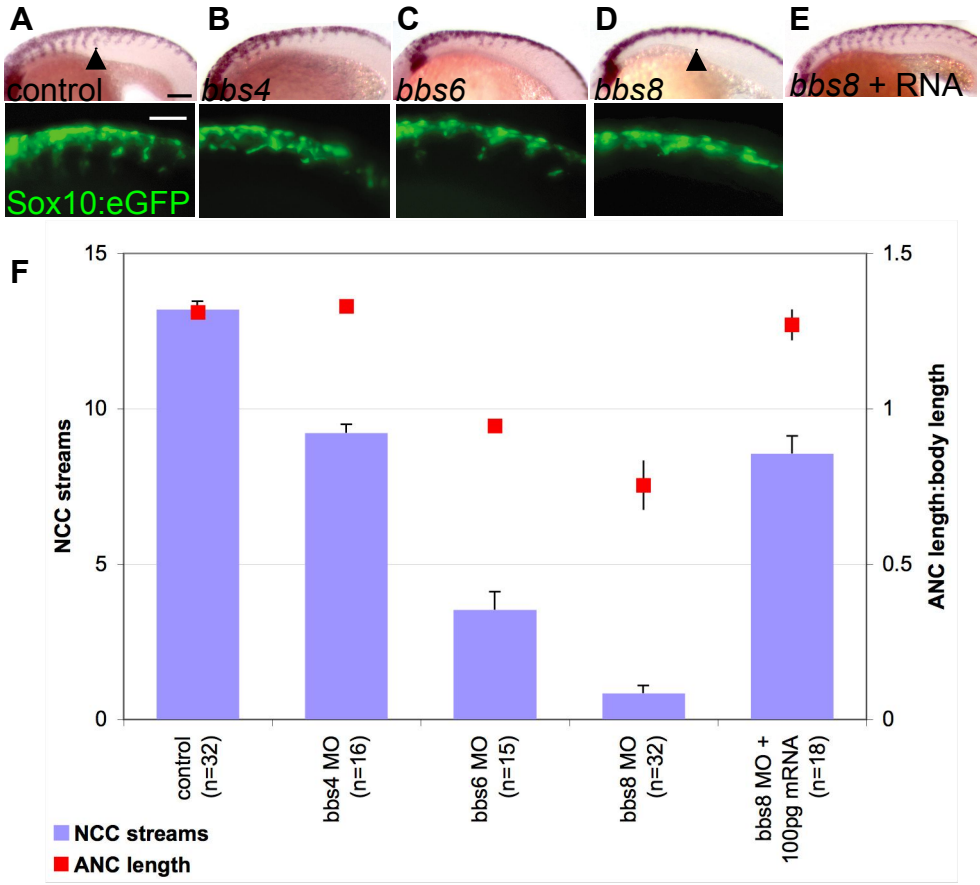

Figure 31. Quantifying the extent of NCC migration in BBS morphants.

A: control embryos at 20ss have around 13 streams of *crestin*-positive NCCs migrating ventrally from the neural tube into the trunk (also shown by expression of Sox10:eGFP). **B-D**: the number of streams of migrating NCCs is reduced in BBS morphants, most drastically in *bbs8*. **E**: the number of streams of NCCs is almost completely rescued by mRNA co-injection. **F**: the number of streams of migrating NCCs (bars) correlates with the reduction in ANC length to body length ratio. This suggests the extent to which NCC migration is reduced is responsible for the severity of craniofacial deformity. Scale bars: A-E = 100μm.

This result shows that there is either a delay or severe inhibition of NC migration in the morphants, with *bbs8* being the most severe. The degree of migrational inhibition appears to correlate with the severity of skull defect. This can be seen by comparing the graphs for skull length to width ratio, and body length to skull length ratio, with the number of streams of migrating crest cells in the morphants (Fig. 31F).

To exclude the possibility that the reduced number of streams of migrating crest was due to possible transcriptional inactivation of *crestin* in the migrating trunk

NCCs, and to validate the previous results, I made use of the *Sox10::eGFP* transgenic zebrafish, which expresses GFP in NCCs. I examined GFP expression at the 20ss and saw the same pattern of expression as the *crestin in situ* (Figure 32). This confirmed the observation of reduced trunk NCC migration. I ensured that NCC migration itself was not affected by the *sox10::eGFP* transgene by performing an *in situ* hybridisation for *crestin* on uninjected *sox10::eGFP* transgenics. This showed normal NCC migration.

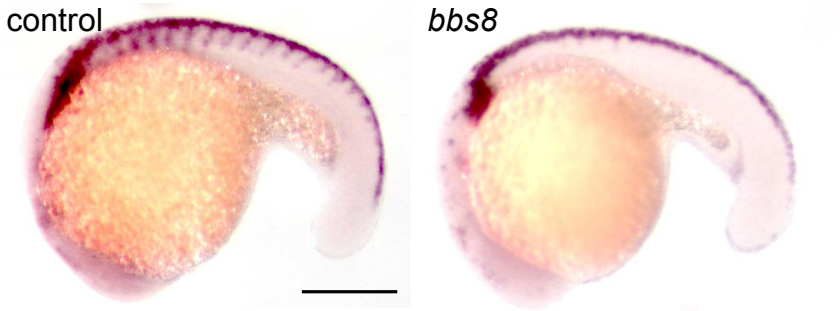

Figure 32. *crestin* expression in *sox10:eGFP* embryos.

Expression of *crestin* shows a lack of trunk streams in morphants while neural tube expression is unaffected in morphants. This suggests that NCCs populating the neural tube have failed to emigrate. It also shows in the control situation that NCC migration is not affected by the presence of the transgene in the *sox10:eGFP* transgenic zebrafish. Scale bar = 500μm.

Pigmentation is lacking in *bbs8* morphants

The most striking phenotype of *bbs8* morphants is their almost complete lack of pigmentation, mirroring published neural crest genetic zebrafish mutants such as *colourless* (*sox10* null mutant). Because melanocytes are derived from the trunk neural crest, which was observed not to migrate in *bbs8* morphants, I next examined the expression of *dopachrome tautomerase* (*dct*), a marker of melanocyte precursors at 25hpf, about 5 hours before the appearance of pigmentation in the embryo. The spotted pattern of expression in controls reveals where presumptive pigment will appear. There is a complete lack of *dct* expression in the morphants, implying that the NCCs have persisted in the trunk and failed to migrate out to differentiate into melanocytes (Figure 33).

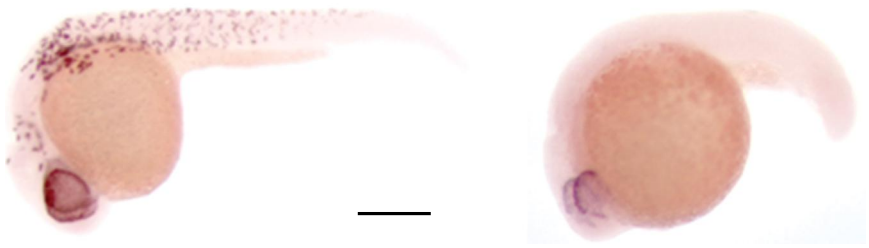

Figure 33. *dct* expression in *bbs8* morphants

There is a complete absence of *dct* expression, a pre-melanocyte marker, in morphants. Melanocytes derive from trunk NCCs and so their absence suggests a failure of these cells to reach their targets, as it is known that trunk NCCs fail to migrate in *bbs8* morphants. This likely explains the lack of pigmentation in older *bbs8* morphants. Scale bar = 500μm.

Time-lapse imaging of migrating cranial and trunk neural crest cells

Evidence suggests that trunk neural crest fails to migrate in morphants and therefore does not give rise to differentiated cell types. Because the cranial cartilages are NC-derived, I next tested whether the migration of the cranial NCCs was disrupted. To do this, I mounted *Sox10::eGFP* control and morphant transgenic zebrafish in agarose and imaged the anterior portion of the embryo to visualise CNCC migration at timepoints between the 12 and 20ss (timepoints: 12, 14, 16, 18, 20ss), a period of 4 hours during which cells migrate rostrally from the neural tube into the head.

In control embryos, cells migrated rostrally in dorsal and ventral pathways around the eye to populate the whole head by 20ss (Fig. 34A and B). In morphants, cells had not advanced as rostrally as controls by 12ss, and by 20ss, the cells had only reached the equivalent position in controls at 12ss (Fig. 34C and D). Developmental delay was controlled for by counting the number of somites in embryos before imaging. The distance migrated by the CNCCs was calculated by comparing the position of the anterior-most cell at 12ss and 20ss. In controls, these cells migrated, on average, 250μm compared to 80μm for morphants. This result was confirmed by creating time-lapse confocal movies which showed inhibited migration of both the cranial and trunk NCC in morphants.

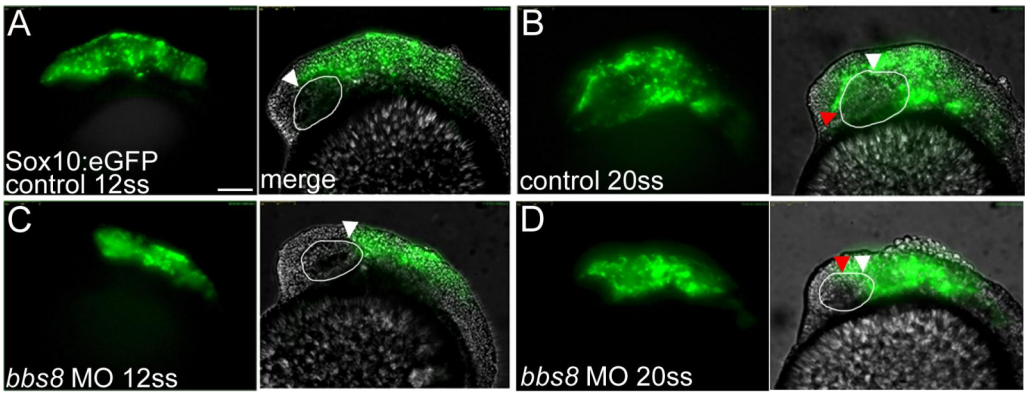

Figure 34. CNCC migration in *sox10:eGFP* control and morphant embryos.

A: at 12ss CNCCs in control embryos have begun to migrate around the eye and are about midway through the eye (arrowhead). **B**: by 20ss CNCCs have colonised the anterior part of the head and have migrated in a stream around the dorsal aspect of the eye. The white and red arrowheads show the relative positions of the migratory front at 12 and 20ss respectively. **C**: at 12ss morphant CNCCs have only migrated about a quarter of the way through the eye. **D**: at 20ss these cells have reached the same position controls cells had at 12ss. Scale bar = 100μm.

Lack of neural crest cells in the ANC after 48 hours in morphants

CNCCs migrating into the head converge at the midline and form the trabeculae, which terminate in a flattened condensation of cells called the ethmoid plate. Imaging the expression of Sox10 in transgenic zebrafish at 48hpf revealed the formation of the two trabeculae in controls, their convergence at the midline, and divergence into the ethmoid plate. In morphants, the trabeculae failed to extend and the presumptive ethmoid plate was absent (Figure 35).

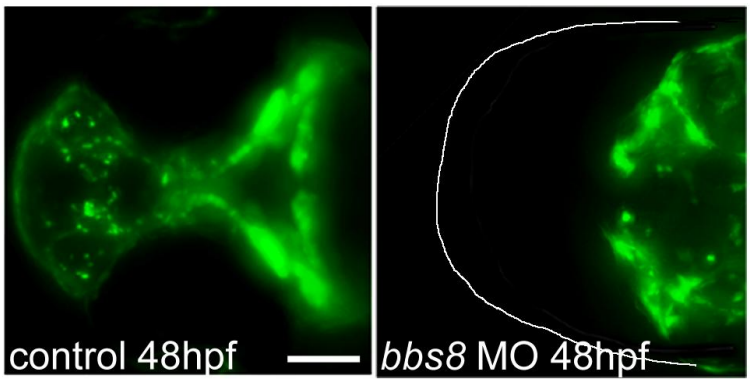

Figure 35. *sox10:eGFP* CNCCs at 48hpf.

Confocal imaging of the CNCCs at 48hpf showed the rudimentary formation of trabeculae in controls, which have begun to coalesce at their terminal ends to form the ethmoid plate. In morphants, the trabeculae have failed to extend by this stage, leaving

only the cells that will become the parabranchial cartilage. The white line indicates the extent of the front of the head in the morphant embryo. Scale bar = 100μm.

These cells begin to differentiate into chondrocytes, which form cartilage at around 72hpf and so are markers of where the cranial skeleton will eventually develop. Reduction in the extent of trabeculae at 48hpf, combined with the observed inhibition of CNCC migration at earlier stages, suggests that an NCC migration defect is responsible for the deficit in cranial cartilaginous structures at 5dpf.

Cell-transplantations show that the phenotype is cell-autonomous

In *bbs8* morphants, there is a typical convergent-extension phenotype universally penetrant amongst ciliary morphant and mutant embryos. This results in shortened and widened somites, presumably resulting in compression of the somatic mesoderm tissue through which NCCs migrate. As such, it is possible that the defect in NCC migration is a secondary effect of the compacted tissue environment through which the NCCs must migrate. This scenario is less likely due to equivalent CE defects in both *bbs4* and *bbs6* morphants not resulting in NCC migration defects as severe as for *bbs8*.

However, to test the possibility that non-cell autonomous factors contributed to the migration defect, I performed reciprocal cell transplantations. To begin with, I transplanted 20-30 cells from control *Sox10::eGFP* embryos at 4hpf injected only with rhodamine-labelled dextran into wild-type hosts (figure 36A). This tested that my transplantation technique in itself was not inhibiting migration of the NCCs and that transplanted cells were being targeted to the presumptive NC. I then imaged the position of CNCCs at 12, 16, and 20ss and measured the linear distance migrated by the cells during this period. This established a baseline for the distance migrated by control cells grafted into a normal cellular environment (Fig. 36A).

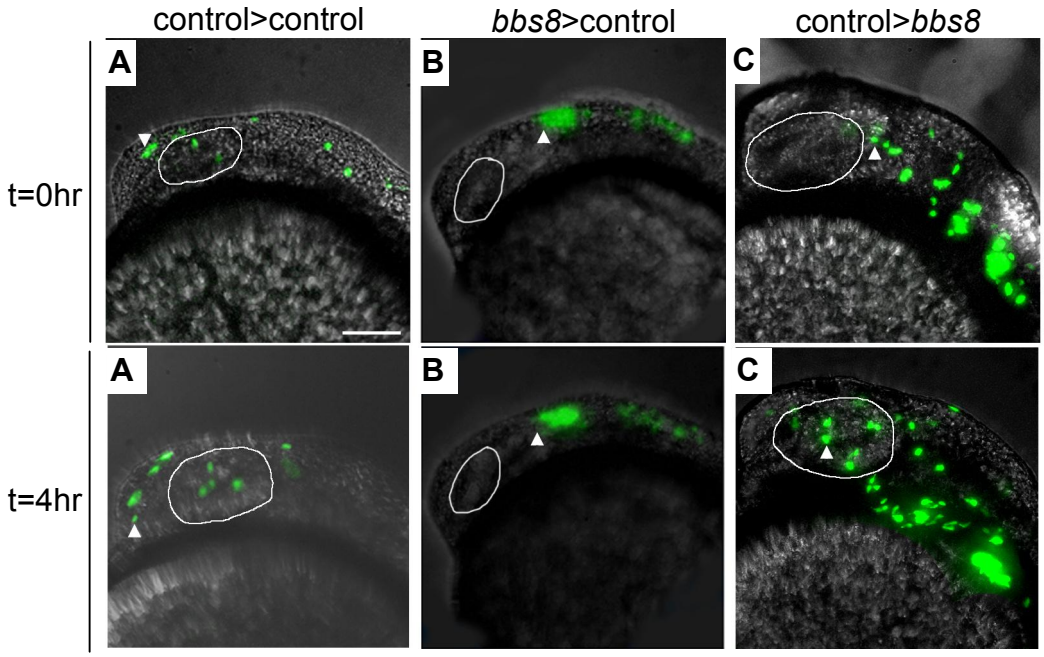

Figure 36. Cell transplantations between control and morphant embryos.

A and **A'**: between 12 and 20ss, labelled control cells transplanted into a control host migrated caudally, as evidenced by the advanced position of the leading cells (arrowheads). **B** and **B'**: morphant *sox10:eGFP* cells transplanted into a wild-type control host failed to migrate and remained in the same position throughout the 4-hour test period. **C** and **C'**: control donors transplanted into a *bbs8* morphant host migrated as normal, suggesting that the tissue environment is not responsible for inhibiting migration in morphants, rather it is a cell-autonomous defect. Scale bar = 100μm.

I next transplanted *bbs8* morphant *Sox10::eGFP* donors into control hosts. These cells failed to migrate despite being transplanted into a normal cellular environment, suggesting the inhibition of migration in *bbs8* morphants is cell autonomous (Fig. 36B). In other words, lack of Bbs8 protein in NCCs intrinsically alters the capacity of the cells to migrate. Finally, I tested whether control NCCs could migrate in *bbs8* host embryos to test whether the CE defect was inhibiting migration. Control NCCs transplanted into morphant hosts were able to migrate to the same extent as in a control host environment, implying that the CE defect in *bbs8* morphants is not inhibiting CNCC migration in its own right (Fig. 36C).

Examination of cellular protrusions in migrating cells

Migrating cells, particularly NCCs, extend fine protrusions, or filopodia, polarised in the direction of migration. These are dynamic structures, which extend and collapse upon contact of an adjacent cell and are thought to be important for the cell to sense its neighbours to ensure an accurate migratory pathway. The extensions of these protrusions are markers of polarity of the cell, and they can be inappropriately extended if the cell has lost its intrinsic polarity mechanisms.

To see if morphant migrating CNCCs or trunk NCCs were extending polarised protrusions, I imaged cells at the leading edge of the rostral-most group of CNCCs migrating into the head as these migrated in the most stereotypical direction and so correlations could be made between direction of migration and cell protrusions. I also attempted to image streams of crest cells exiting the neural tube and migrating ventrally into the trunk. The problem with this experiment is that the *bbs8* morphants almost entirely lack migrating streams, making likewise comparison difficult.

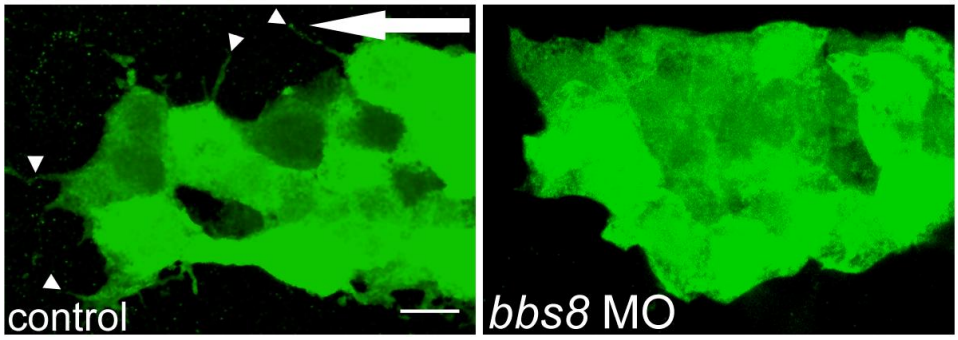

Figure 37. Cell protrusions in migrating CNCCs.

Control CNCCs extend fine projections (arrowheads) into the extracellular space as they migrate (the direction of migration is indicated by the arrow). The majority of these projections are polarised in the direction of migration. In *bbs8* morphants, the CNCCs fail to extend these projections and remain tightly clustered, with more rounded, and less polarised, cell morphology. Scale bar = 10μm.

High-power confocal imaging of these CNCCs at 16ss, a period of active cell migration, revealed that control CNCCs extended many protrusions (Figure 37). However, protrusions were almost completely absent from morphant CNCCs and the cells were tightly clustered together (Figure 37). This could be because the

cells have failed to migrate, but have proliferated, the cells are unable to detach from one another and migrate into open space. It is possible that the lack of protrusions is due to contact inhibition, but the cells at the leading edge still failed to extend projections in their presumptive direction of travel.

To investigate this further, I made time-lapse confocal movies lasting one hour to examine the behaviour of these protrusions in real time. As expected, the control protrusions dynamically form and collapse over a very short time frame (5 minutes) but the *bbs8* morphants fail to do so.

As the cell protrusions are formed by extensions of the actin cytoskeleton, and this is partly controlled by the planar cell polarity (PCP) (non-canonical Wnt) signalling pathway, it is possible that a defect in PCP signalling in morphants affects their ability to remodel the actin cytoskeleton in a polarised manner prerequisite for directed motility.

Possible role of non-canonical Wnt signalling in the migration defect

There are already published associations between Bbs proteins and the PCP pathway. *Bbs* morphants have defective gastrulation movements (CE) reminiscent of PCP mutants, in the mouse they interact genetically with the PCP pathway, and Bbs suppressant cells show induction of canonical Wnt activity, thought to be antagonistic to the PCP pathway.

Given the importance for PCP signalling for NCC migration in *Xenopus*, the genetic interaction of *bbs8* morphants with *trilobite*, a PCP mutant (our unpublished data), and the lack of polarised protrusions on migrating CNCCs, I performed some experiments to test whether Bbs8 was potentially mediating PCP signalling in NCCs to control migration.

Both induction and suppression of PCP signalling inhibits NCC migration. I injected two different mutant Dishevelled constructs: *Dvl-ΔN* has an N-terminal truncation which eradicates the N-terminal region of the protein but maintains the

PDZ and DIX domains important for morphogenetic movements associated with PCP signalling. Therefore, overexpression of *Dvl-ΔN* induces PCP signalling. The second Dvl construct contains sites for myristoylation and palmitoylation, which localises it constitutively to the membrane. Cytoplasmic Dishevelled is associated with canonical Wnt signalling but membrane targeting activates PCP.

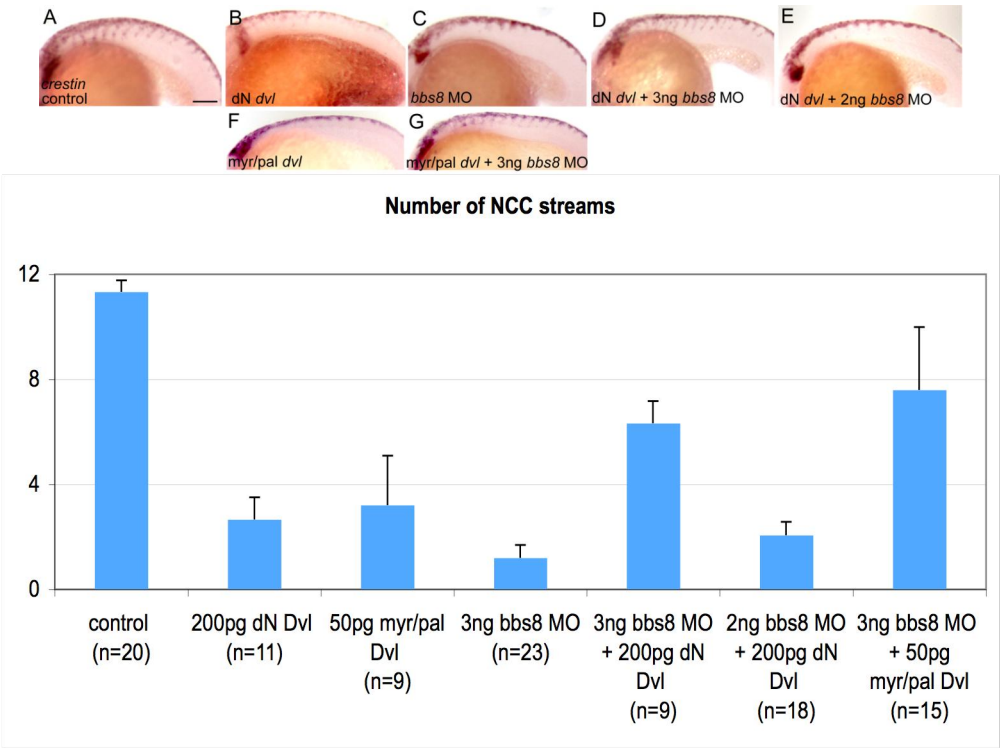

Figure 38. Mutant *dishevelled* constructs can partially rescue the *bbs8* morphant NCC migration defect.

A: control embryos at 20ss showing normal streams of NCC migration revealed by *crestin in situ* hybridisation. **B**,**F**: injection of a dominant-negative form of *dvl* lacking the N-terminal region, or a membrane-targeted form of *dvl*, both caused inhibition of migration. **C**: *bbs8* morphants with reduced streams of migrating NCCs. **D,G**: co-injection of 3ng *bbs8* MO with either the dominant-negative or membrane-targeted *dvl* constructs partially rescued the migration phenotype, as evidenced by a significant increase in the number of migrating streams of NCCs. **E**: injection of 2ng *bbs8* MO with the dominant-negative *dvl* construct did not rescue the phenotype, suggesting a dose-dependent effect. Scale bar = 100μm.

Injection of either of the two mutant Dvl constructs inhibited NCC migration as shown by counting the number of migrating NCC streams in *crestin* stained 20ss embryos (Fig. 38B,F, and H). Injection of 3ng of *bbs8* MO also blocked migration (Fig. 38C). However, combining either mutant Dvl construct with 3ng of *bbs8* MO caused partial restoration of the migration inhibition (Fig. 38D,G, and

H). Injection of 2ng of *bbs8* MO with *Dvl-ΔN* did not rescue the phenotype (Fig. 38E).

These results suggest, but do not prove, that knockdown of *bbs8* might be balancing the level of PCP signalling back to normal from the induced state of the mutant Dvl constructs. This might mean PCP signalling is inhibited in *bbs8* morphants, which is, at least in part, causing the migration defect.

As there are no validated direct quantitative read-outs for PCP signalling it is difficult to confirm these findings. However, one role PCP is thought to play is in the localisation of the centrosome between the nucleus and leading edge of the cell in migrating cells.

Attempt to visualise centrosome movements in migrating crest cells

Because *bbs8* is a centrosomal and basal body-expressed gene, and the position and function of the centrosome is important for the direction of cell migration, I next tried to investigate if the centrosome was mislocalised in CNCCs. To do this, I injected *sox10::eGFP* transgenic embryos with H2B-RFP, which marks the nucleus with RFP. I co-injected *centrin-RFP* which marks the centrosome with RFP.

However, the Centrin localisation was unreliable and because the centrosome is so small, it tended to get obscured by the intense fluorescence of the nuclear RFP. Furthermore, both GFP- and RFP-tagged centrin were unreliable markers of centrosome position *in vivo*, as it was difficult to distinguish the centrosome from background fluorescence as it is a tiny organelle. As such, no reliable data were obtained from this experiment but its optimisation would lead to potentially exciting mechanistic insights.

The aim is to make real-time movies showing migrating CNCCs revealing the position of the centrosome in relation to the nucleus and the leading edge of the cell. This is confounded further by the 3D quality of the embryo, which makes it

impossible to get a single fluorescent nucleus in focus at once, particularly as they migrate out of the field of view. This confounds the region of interest with surrounding fluorescent, non-NCC nuclei.

Neural crest cells are ciliated

It is unknown whether NCCs are ciliated, and nobody has ever examined this. There are several lines of evidence to suggest that NCCs might be ciliated:

1) There are several papers that show that cilia are crucial for PCP signalling, and in fact, conversely, that PCP signalling is involved in primary ciliogenesis. If PCP is important for NCC migration, these cells should bear cilia.
2) CNCCs are patterned at the mid-facial region by Shh-ligand secreted from the oral ectoderm. Numerous reports have demonstrated the reliance of Hedgehog signalling on cilia.
3) The observed role for Bbs8, a ciliary protein, in NCC migration.

To investigate this possibility I fixed *sox10::eGFP* transgenic embryos at 20ss and performed immunohistochemistry using an anti-acetylated tubulin antibody to reveal the primary cilia. Using confocal microscopy with a 63x water immersion lens, I was able to observe cilia on a large proportion of Sox10-positive cells (Fig. 39A). Confocal optical sectioning proved that these cilia emanated from the peri-nuclear region of neural crest cells (Fig. 39B and B').

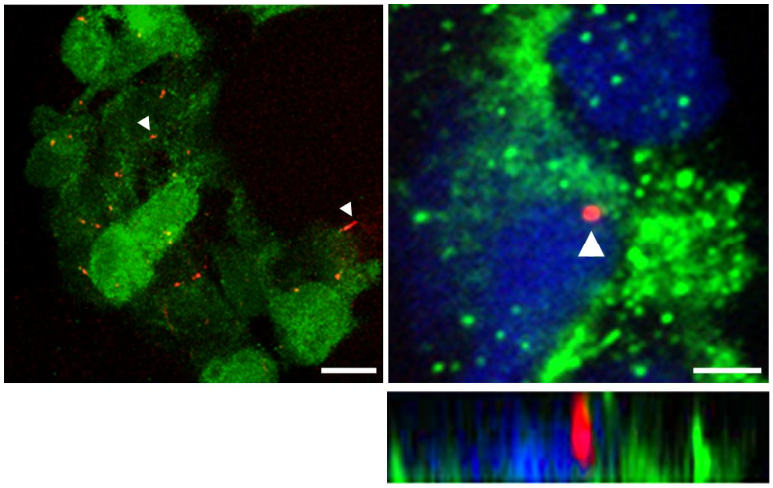

Figure 39. Primary cilia on NCCs.

A: Sox10:eGFP expression demarcates NCCs while cilia are revealed by an anti-acetylated tubulin antibody (in red). **B**: a cilium (in red) on an NCC. **B'**: confocal section through this cell showing the red cilium clearly extending apically from the perinuclear (nucleus stained in blue) from the green NCC. Scale bars: A = 20μm; B = 5μm.

Examination of cell polarity in migrating NCCs *in vivo*

The lack of polarised protrusions and migration defects in the morphants prompted me to examine the actin cytoskeleton in migrating NCCs, whose remodelling is essential for cell motility. To do this, I fixed transgenic embryos at 16ss and stained the embryos with Phalloidin to visualise the actin filaments. Unfortunately, it was very difficult to resolve the internal cytoskeleton in an individual NCC due to the confounding effect of all the surrounding cells stained with Phalloidin. It was possible to get a clear outline of the cell, but not of the individual actin microfilaments within the cell.

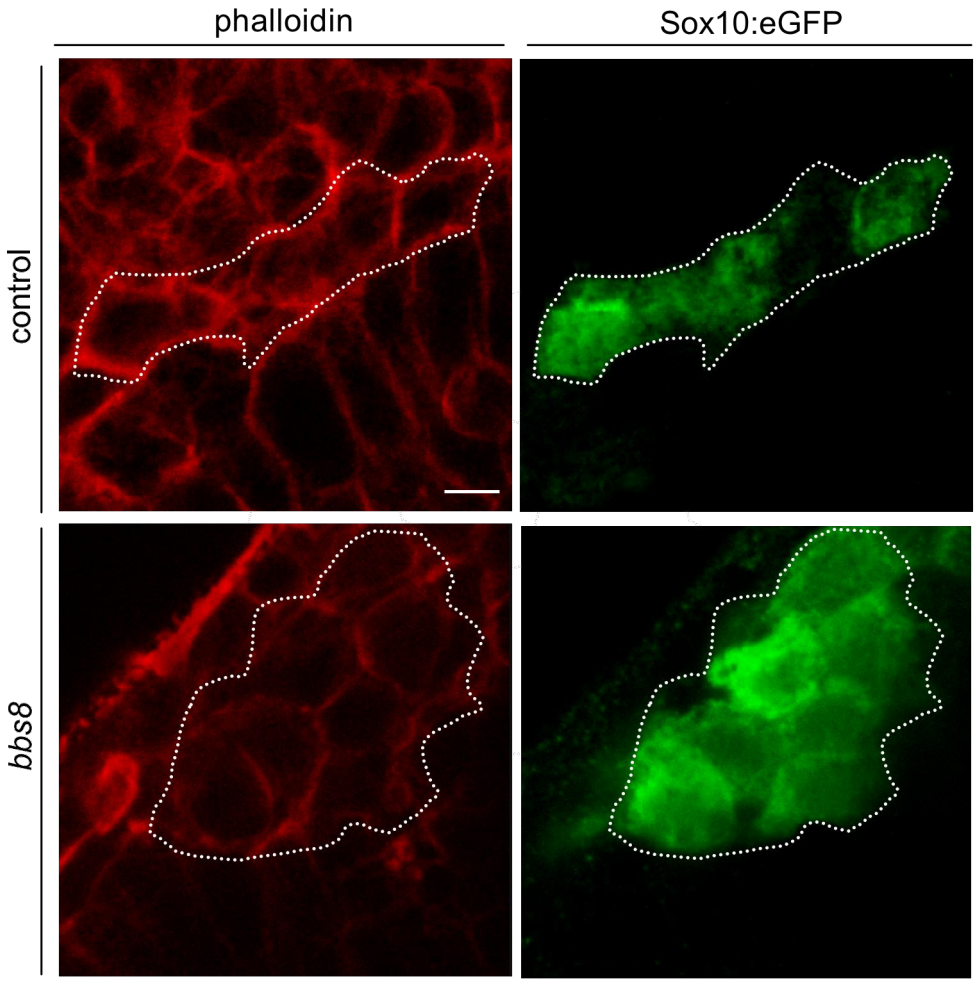

Figure 40. Actin cytoskeleton in migrating CNCCs.

Control CNCCs migrating (green cells, dotted outline) showing phalloidin expressed at a higher level and seemingly with more intracellular microfilaments than morphant cells. Scale bar = 10μm.

Some images suggested that there might possibly be an effect on the cytoskeleton in morphant migrating CNCCs but the images were not clear enough to say with any confidence (Figure 40). As such, it was essential to examine the migration of cells *in vitro* where the actin cytoskeleton can be resolved much more clearly.

Cell migration assays in immortalised and primary fibroblasts

I used an *in vitro* model of cell migration for two reasons: firstly, to try to resolve the actin cytoskeleton in *Bbs8* knockdown cells, even if they were not NCCs; and secondly to see if the migration defect applied to other migratory cell types. To do this, I performed *in vitro* scratch wound healing assays on cultured 3T3 mouse

embryonic fibroblasts. These had been stably transfected with either lentivirally-expressed shRNA against *Bbs8* or a scrambled sequence control.

The actin cytoskeleton was examined immediately after scratching, and at 6, 24, 48, and 72 hours afterwards. A low-power view was taken to measure the gap at 10 different positions between the two fronts of cells migrating into the gap. In control-transfected cells, this gap had closed completely by 48 hours. In *Bbs8* suppressants, the gap took longer to close and the cells migrated significantly slower (approx. 30μm/hour controls vs 10μm/hour *Bbs8* suppressants) (Figure 41).

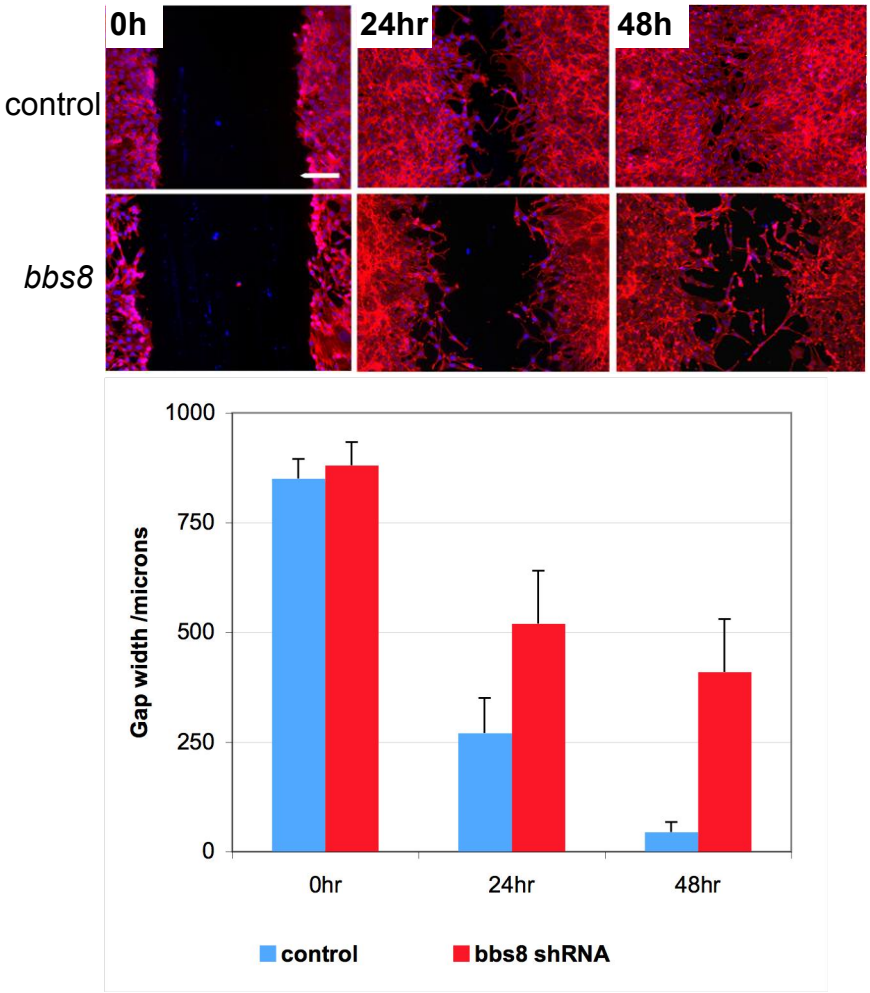

Figure 41. 3T3 scratch wound healing cell migration assay.

Immediately after the scratch (0hr), there is a large gap between the two fronts of cells. By 24 hours after the scratch, control cells have migrated into the gap and closed it by around 80%. *Bbs8* suppressant cells have only reduced the gap by around 40%, suggesting they are migrating at around half the speed of control cells. By 48 hours, the gap is almost completely closed in the control but still only about 55% closed in the knockdown cells. Scale bar = 200μm.

High power imaging of the cells showed that the actin cytoskeleton in control cells was polarised, with microfilament stress fibres arranged in parallel rows aligned along the long axis of the cell. Control cells had begun to polarise themselves orthogonal to the scratch line 6 hours after the wound simulation (Fig. 42A,B). However, in *Bbs8* knockdown cells, the cells were disordered and the microfilaments tended not to be aligned in parallel rows (Fig. 42C,D). Often, the actin bundles criss-crossed each other and formed a disorganised array in the cytoplasm, not elongated along the axis of the cell.

Examination of the cells migrating across the gap between the two frontiers of cells 24 hours after scratching showed that the control cells formed an organised array with the long axes of the cells pointing orthogonal to the line of the scratch, in the direction of cell migration, and their microfilaments aligned along this axis. In contrast, knockdown cells were scattered in an uncoordinated pattern across the gap, and their microfilaments did not appear to align in any particular direction (Fig. 42E,F). Examination of these cells crossing the gap at higher power revealed the extent of the mispolarisation of actin microfilaments (Fig. 42G,H).

The extent of microfilament mispolarisation was quantified using the high-power images such as Fig. 42G and H. The angle of each microfilament in eight to ten different cells from separate images was measured relative to the horizontal. For each cell, the average angle was calculated and the standard deviation of the angles was calculated. The average standard deviation, and the deviation of the standard deviations were calculated to give a crude measure of the degree of disorder of microtubules in control and suppressant cells. A value of 0 would mean that all the microfilaments in all cells were parallel, whilst a high value shows their orientation to be more randomised and less ordered. Indeed, Fig. 43A shows the high degree of disorganisation of suppressant microfilaments relative to controls.

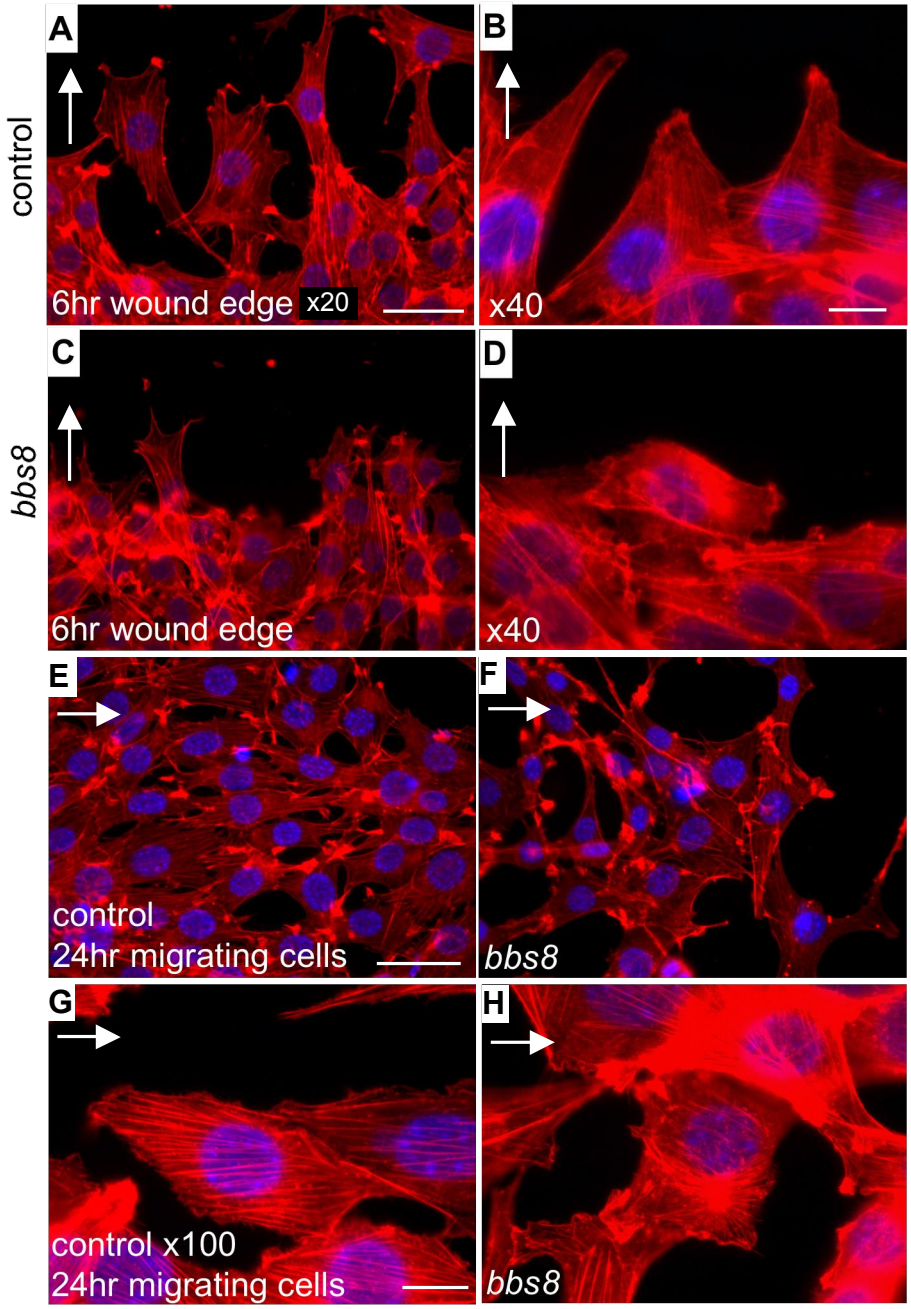

Figure 42. Actin cytoskeleton in migrating 3T3 cells.

A: control cells 6 hours after wounding are polarised orthogonal to the wound edge and are beginning to project into the gap. **B**: higher power imaging shows the polarisation of microfilaments in these cells. **C**: *bbs8* knockdown cells fail to project into the gap 6 hours after wounding. **D**: the microfilaments of these cells are less aligned than controls. **E**: control cells 24 hours after wounding crossing the middle of the gap intercalate and polarise in the direction of migration, orthogonal to the direction of the scratch. **F**: *Bbs8* knockdown cells do not align across the gap and appear disorganised and chaotic. **G**: high magnification image of control cells migrating into the gap shows polarisation of the actin stress fibres in the direction of migration. **H**: suppressant cells have a random, disordered array of actin filaments, with nucleations and clustering inside the cytoplasm. Scale bars: A,C = 20μm; B,D = 5μm; E,F = 20μm; G,H = 5μm. Arrow indicates direction orthogonal to wound gap (direction of migrating cells).

For eight different cells, the deviation in angle of each microfilament from the average orientation was plotted on a radar diagram. In controls, this shows how the microfilaments deviate very little from the average, meaning that most microfilaments are parallel within a given cell (Fig. 42B). In *Bbs8* knockdown cells, the microfilaments deviate widely in angle from the average (Fig. 42C). Each line represents a different cell and each point a different microfilament from that cell.

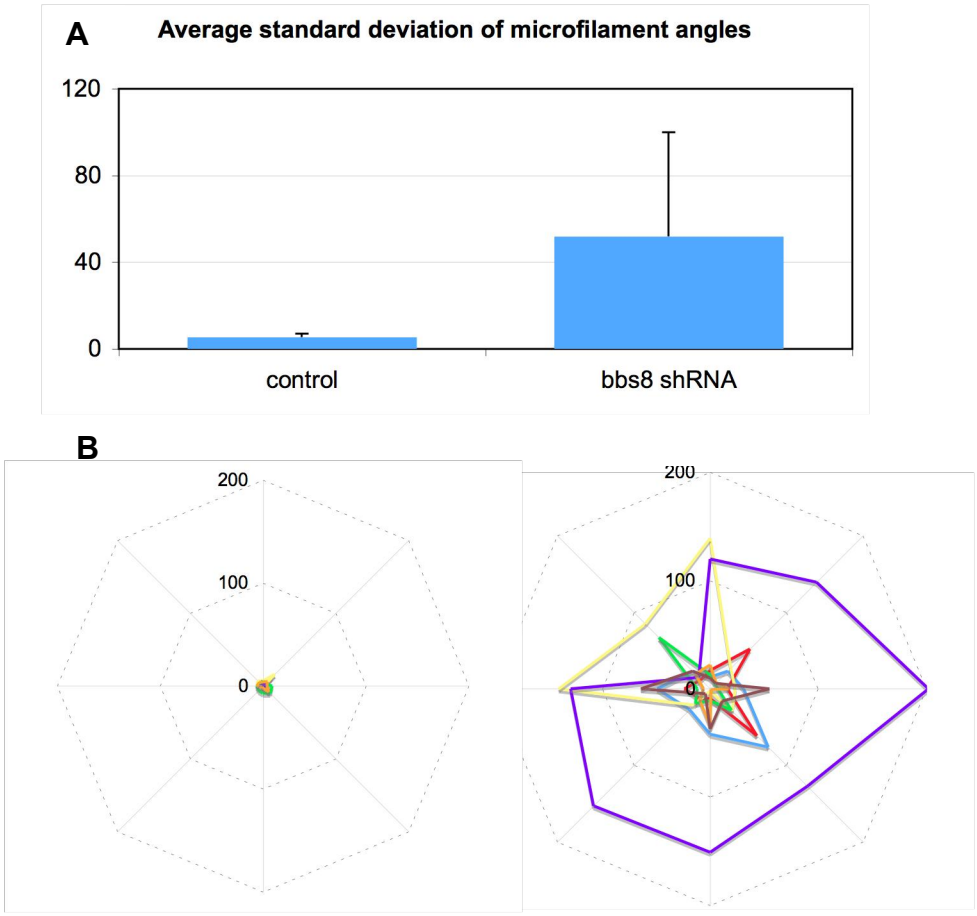

Figure 43. Quantification of microfilament organisation.

A: graph showing the average standard deviation of the angle of microfilaments in each of ten cells. This shows that the control cells; microfilaments are mostly parallel, or show a small deviation from parallel, whereas *Bbs8* suppressant microfilaments are much more randomly aligned. **B**: radar diagram showing deviation of 8 microfilaments in 8 different cells from the average angle of alignment. This shows the extent of mispolarisation in suppressant cells. See text for a description of how this statistic was calculated.

I repeated this set of experiments using primary fibroblasts taken from skin biopsies from an adult patient with *BBS8*$^{-/-}$ null mutations, or a healthy, unaffected adult control. Again, the mutant fibroblasts tended to migrate slower, not completely closing up the gap by 48 hours post-scratching, unlike the controls,

which had completely closed the gap by this stage (Figure 43). Also, the mutant primary cells had a disorganised actin cytoskeleton compared to the controls, where the microfilaments were ordered parallel to the long axis of the cell (Figure 43).

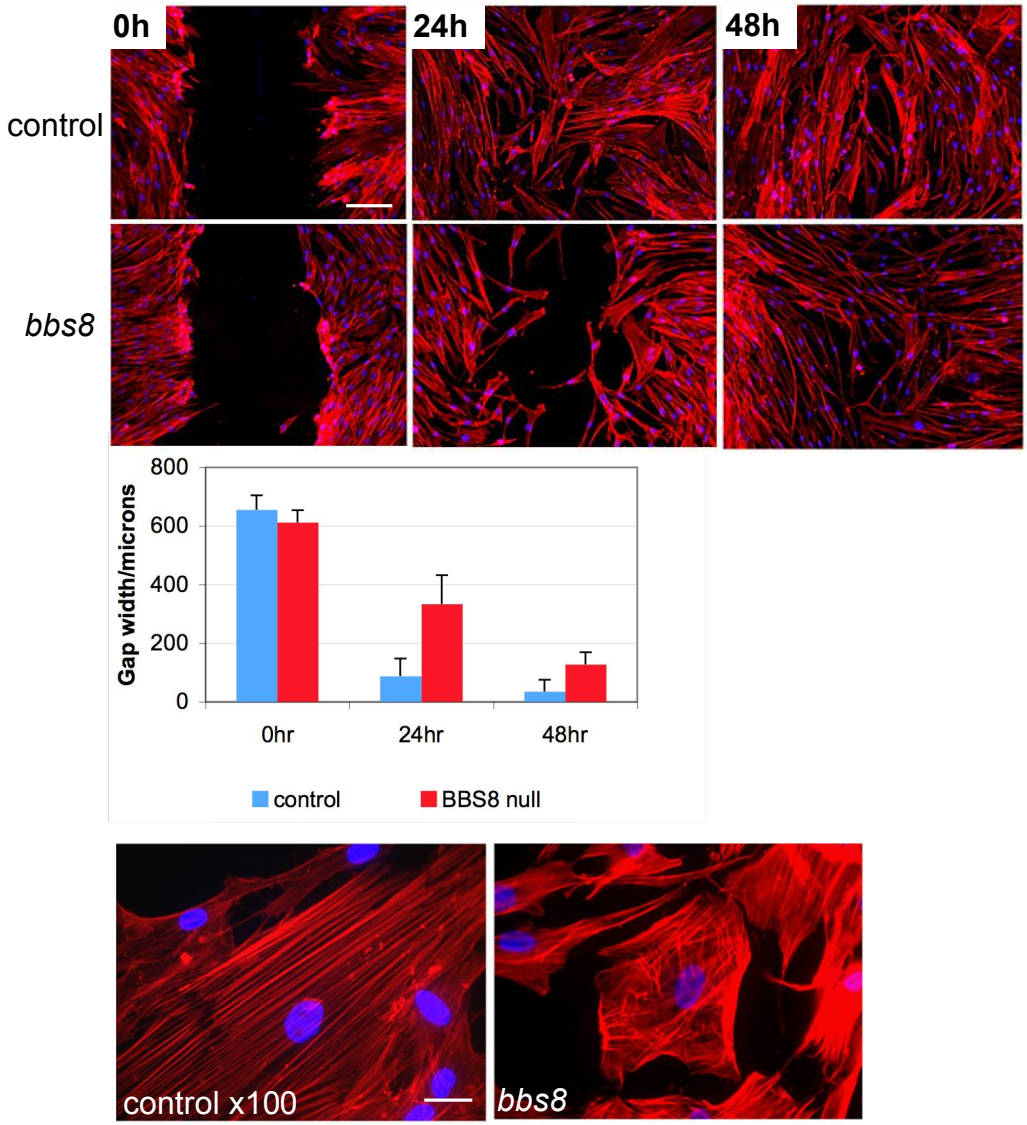

Figure 44. Migration of primary fibroblasts.

Immunofluorescence shows that the control cells completely fill the gap by 48 hours whereas fibroblasts from a patient with *BBS8* null mutations fail to migrate as fast. Again, mutant cells migrate at approximately half the speed of controls. Like the *Bbs8* knock-down immortalised fibroblasts, the actin cytoskeleton in mutant primary cells is disordered compared to the highly ordered "harp-string" like organisation of the primary cells' actin cytoskeleton. Scale bars: top = 200μm; bottom = 5μm.

The number of enteric neurons is reduced in *bbs8* morphants

Bbs8 protein seemed to be important in the migration of many different cell types, so I next tested whether it was important for the development of the enteric nervous system. This is also derived from NCCs migrating from the vagal and sacral regions of the neural tube to colonise the gut. This cell type is highly pertinent given the published association of BBS with Hirschsprung's Disease, caused by aganglionosis of the colon.

I performed immunohistochemistry using the pan-neuronal marker HuC/HuD/ElaV, with a modified protocol to prevent labelling neurons outside the gut and DRGs (Kuhlman and Eisen, 2007). Control embryos contained, on average, 120 neurons along the entire length of the hindgut, terminating at the anus (Figure 45). Embryos injected with 2ng of *bbs8* MO only contained an average of about 20 neurons and they typically only colonised half the length of the gut. Using 4ng of MO prevented any neurons from migrating along the gut, resulting in almost complete absence of gut innervation (Figure 45).

A detailed molecular analysis of enteric nervous system development in morphants

The next aim was to try to establish a time course of events giving rise to the miscolonisation of the gut. I first analysed the expression of the NCC marker *crestin* at 36hpf, a time point when NCCs migrate out of the vagal region of the hindbrain and converge at the midline in two parallel streams. Expression was comparable in both controls and morphants indicating that early exit from the hindbrain was not affected in morphants (Fig. 46A,B).

At 48hpf, expression of *phox2b* in lateral views of controls indicated that the NCCs had migrated through the branchial arch region and begun to migrate into the proximal region of the foregut (Fig. 46C,E arrowhead). In morphants, the dorsal-most strand of cells migrating into gut was absent, despite expression (albeit attenuated) in the branchial arch region (Fig. 46D,F arrowhead). This suggested the onset of the gut migration deficit stemmed from around this stage.

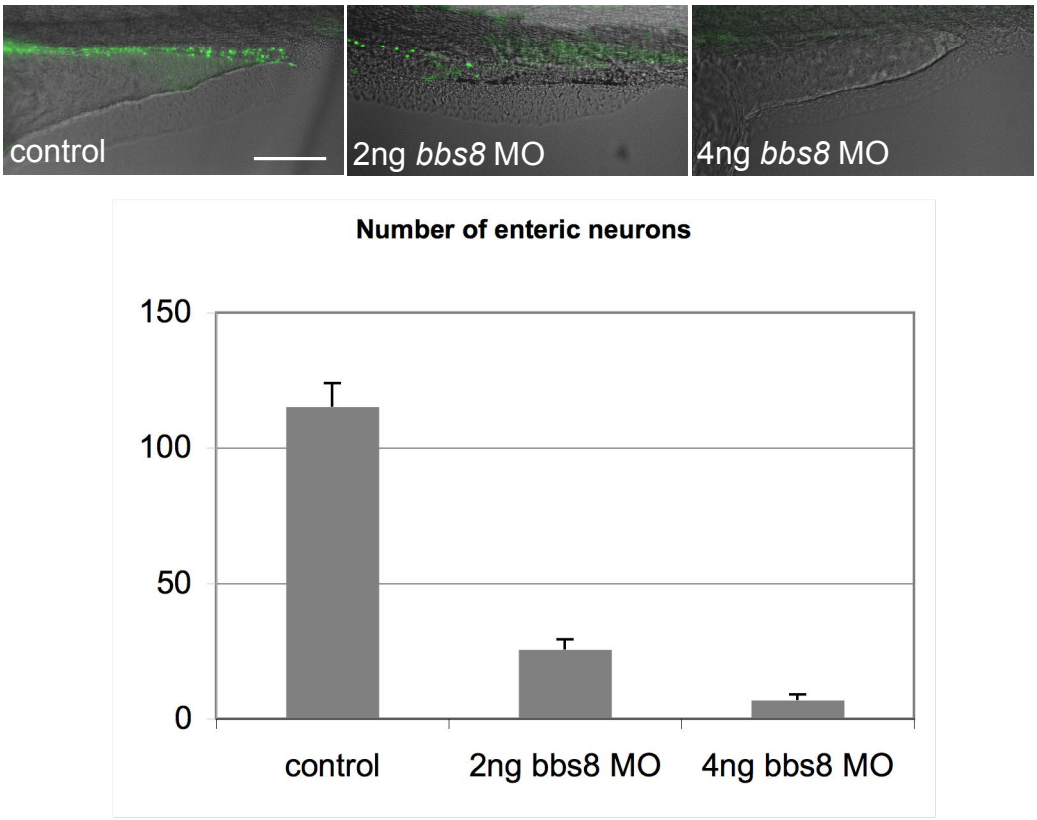

Figure 45. Enteric neurons in *bbs8* morphants.

HuC/D wholemount immunofluorescence reveals colonisation of the entire length of the gut by enteric neurons in controls (asterisk indicates position of anus). Injecting 2ng *bbs8* MO caused enteric neurons only colonise the most proximal region of the gut, while 4ng MO completely abolished migration into the gut. This was quantified by counting the number of neurons in the gut from midway along the yolk sac to the anus. The graph shows a massive reduction in enteric neurons in morphant embryos. Scale bar = 200μm.

At 72hpf, *phox2b* effectively labels the NCCs that have migrated along the gut and will differentiate into mature neurons. By this stage, the whole gut is colonised in controls, evidenced by a band of *phox2b* expression stretching along the entire length of the gut tube (Fig. 46G). In 2ng MO-injected embryos, *phox2b* expression only extends halfway along the gut to the anus, correlating with the expression of HuC/D in mature neurons 24hpf later (Fig. 46H). In 4ng MO-injected embryos, expression of *phox2b* in the gut is lacking altogether, confirming the results seen with the HuC/D immunostaining (Fig. 46I).

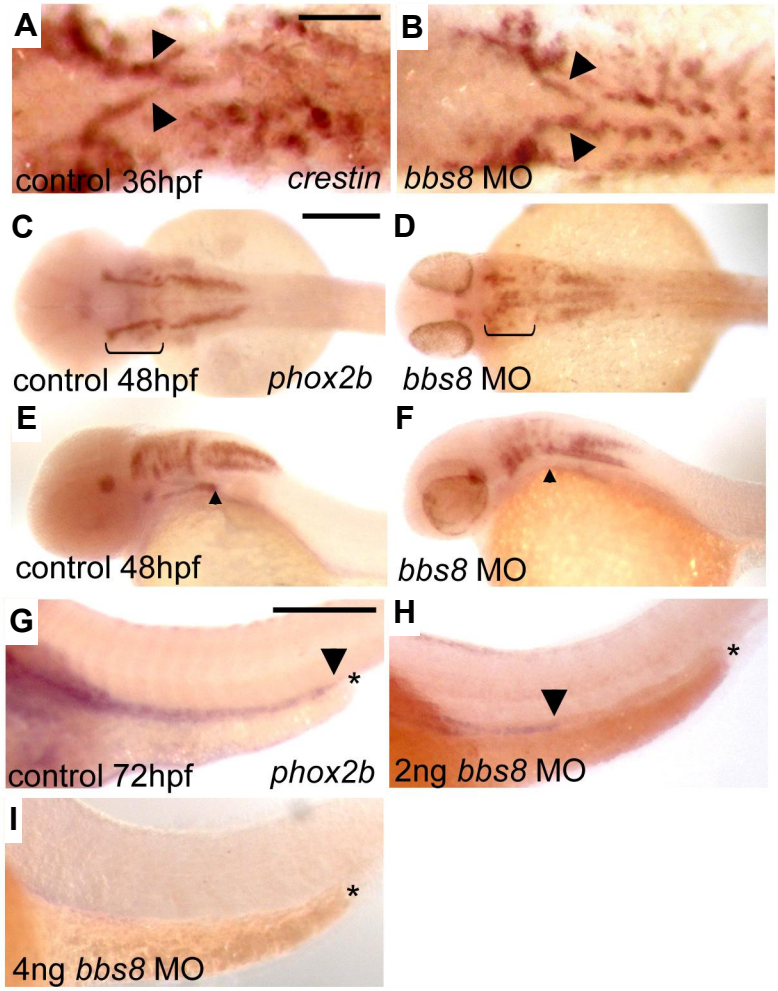

Figure 46. Molecular analysis of the time course of ENS migration.

A,**B**: *crestin* expression at 36hpf is comparable in controls and morphants showing exit from the vagal region is unaffected. **C,D**: *phox2b* expression at 48hpf shows reduced expression in the presumptive branchial arches (bracket) but equivalent expression in the hindbrain, just caudal to this. **E,F**: the stream of NCCs entering the gut tube in controls (arrowhead in E) is missing in the lateral view of the morphant (arrowhead in F). **G**: *phox2b* expression at 72hpf delineates the NCCs colonising the entire gut. The arrowhead indicates the position of the extent of migration and the asterisk identifies the anus. **H,I**: in *bbs8* morphants with low and high doses, there is limited to no colonisation of the gut by NCCs respectively. Scale bars: A,B = 100μm; C-F = 500μm; G-I = 200μm.

Time-lapse imaging of gut motility in zebrafish embryos

To see if this lack of neurons affected gut motility, I performed high-speed time-lapse imaging, capturing 5-minute movies of control and morphant 4.5dpf embryos' guts. In controls, there were regular, spontaneous waves of peristalsis occurring in the proximal region of the gut (Figure 47). In 2ng MO-injected

embryos, no peristalsis was ever observed in any portion of the gut, despite imaging several different embryos (Figure 47).

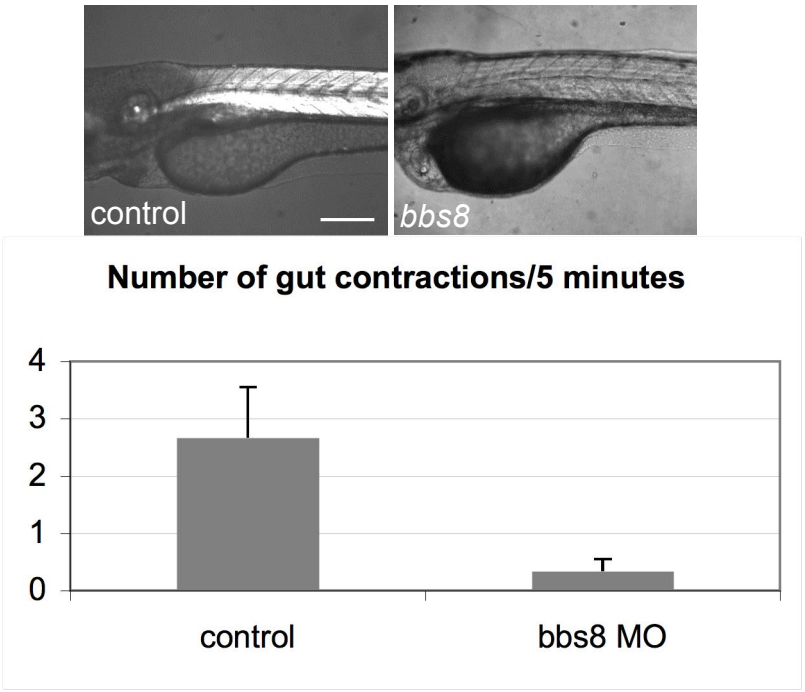

Figure 47. Gut motility in zebrafish embryos.

Stills taken from high-speed time-lapse microscopy of the gut region analysed. Counting the number of peristaltic waves in a 5-minute period in 5 separate 5dpf embryos showed a significant reduction in gut motility in morphant embryos, correlating with the lack of gut innervation. Scale bar = 200μm.

Attempting to analyse neural crest migration in morphant chicken and quail embryos

Despite being a relatively new model organism, the zebrafish is generally regarded as a valid system for investigating mechanisms of human development and disease. However, to try to corroborate the phenotypes observed in the zebrafish, and given the lack of a *Bbs8* mutant mouse, I chose to try to generate morpholino-based knockdown of Bbs8 in the chick neural crest.

The chick embryo is a classical system for studying neural crest migration, and the migratory pathways of neural crest cells emerging at all axial levels of the neural tube are stereotypical and well characterised. Much of what we know about the migratory pathways of different NCC populations comes from studies of

the chick, and it has been particularly illuminating through use of grafting experiments.

A translation (ATG) blocking morpholino specific to the chicken *Bbs8* (also called *Ttc8*) sequence was designed and ordered from Gene Tools (Oregon, USA). The MO was tagged at its 5' end with FITC to act as a fluorescent marker to monitor the efficiency of uptake after electroporation. The MO was diluted to 1mM in water and 0.5% phenol red was added to visualise the solution *in ovo*. It was found that Fast Green, often used to visualise plasmids for electroporation, inhibited the activity of the MO.

HH stage 10-12 chicken embryos were electroporated with the MO into the neural tube at the level of somites 3 to 7. This drives the construct into the vagal region of the neural tube from which emigrate the NCCs. Because electroporation only drives the construct into one side of the neural tube, there is a contralateral control.

Embryos were sectioned 24, 48, and 72 hours after electroporation and stained with HNK1, a marker of NCCs. Unelectroporated sides of the neural tubes, or embryos injected with a GFP-expressing plasmid as a negative control, had streams of neural crest cells beginning to migrate ventrally out of the dorsal aspect of the neural tube. By 48hpf, these cells had migrated further ventrally to populate the sympathetic chains of neurons in the trunk and the foregut. By 72hpf, HNK1-positive cells were observed in the hindgut as well (Figure 48A,B: right-hand side of embryos).

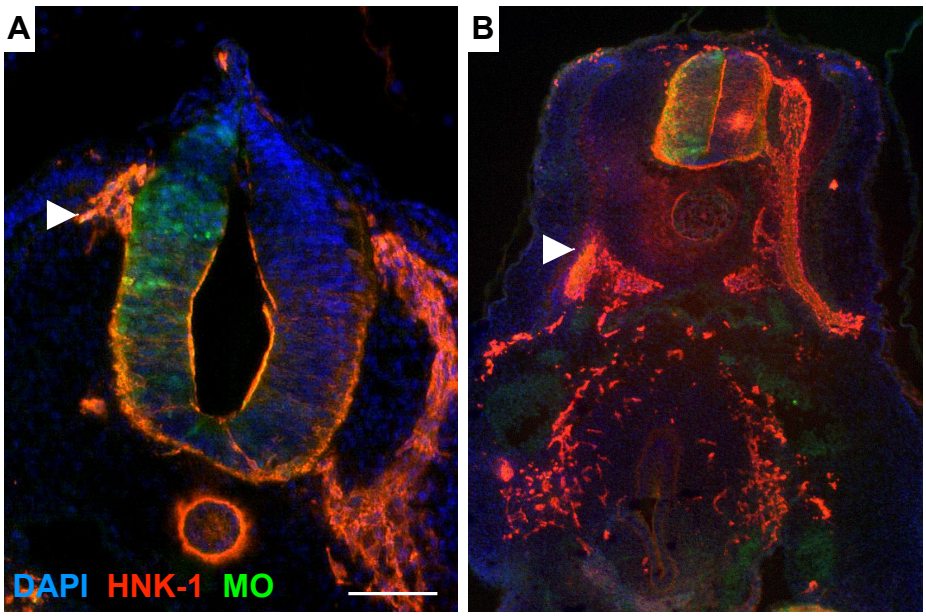

Figure 48. NCC migration in electroporated chick neural tubes.

A: 24 hours post electroporation (hpe) the electroporated side (left) can be determined by the presence of green fluorescence due to the FITC-tagged MO. Migrating NCCs are visualised in red with an anti-HNK-1 antibody. The arrowhead shows the curtailment of the stream of migrating NCCs in the electroporated side. **B**: 48hpe there appears to be a lack of a migrating stream on the electroporated side. However, this could well be a sectioning artefact due to the streams not migrating in the plane of the section and then re-emerging ventral to the neural tube. Scale bar = 100μm.

In the sides of the neural tube electroporated with 1mM of *Bbs8* MO, there appeared to be consistently shorter, or even absent, streams of NC migrating from the neural tube 24 hours after electroporation (Figure 48A arrowhead). By 48hpf, it was impossible to tell if there was a deficit of cells populating the gut because cells from the contralateral uninjected side compensate by contributing to the gut. Also, it is possible that this observation, in some cases, was due to sectioning artefact. This can be seen in Figure 48B, where there appears to be no stream emigrating from the electroporated side of the neural tube, but there are cells more ventrally (arrowhead). As such, the chick assay is inconclusive. The other problem is that the MO is electroporated at around, or after, the time the NCCs begin to delaminate and migrate, and so may only start working once the cells have already begun to move away from the neural tube.

A second assay was performed to try to measure the degree of inhibition of knockdown cells in avian embryos. The same *Bbs8* MO was electroporated into

quail embryos. The neural tubes of the quails were removed 24 hours later using pancreatin and cultured on glass coverslips coated with fibronectin and laminin. Images of the neural tubes were taken 24 hours later and the distance that the leading front of cells had migrated from the neural tube was calculated (Fig. 49A,A'). It appeared that the electroporated cells had not migrated to the NCC front (Fig. 49B). However, it was difficult to distinguish as the FITC-positive morphant cells were surrounded by unelectroporated cells. Also, the distance the cells had migrated varied greatly depending on the time they exited the neural tube. As such, this assay proved inconclusive.

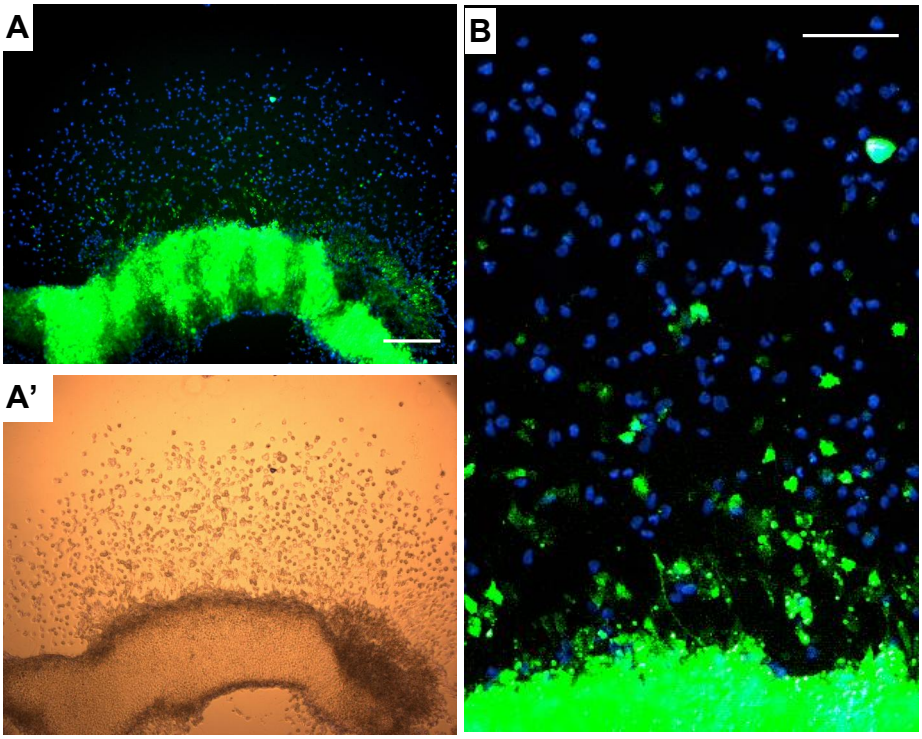

Figure 49. *Ex vivo* quail neural tube culture.

A: the electroporated cells are clearly visible in green (FITC) amongst the total cell population in blue (DAPI). **A'**: this shows the cultured whole quail neural tube with the NCCs migrating away from the neural tube 24hpe. **B**: high-power image of the neural tube (bottom of image) with the FITC-positive electroporated cells amongst the NCC population. The electroporated cells do not extend to the front of NCC migration, but this is inconclusive as the starting position and time of emigration from the neural tube are unknown. Scale bars: A,A' = 100μm; B = 100μm.

Aberrant craniofacial cartilage morphology in other ciliopathy morphants

Given the importance for BBS proteins in neural crest migration, and the observation of cilia on NCCs, I reasoned that other ciliopathy morphants might also show craniofacial dysmorphology. To investigate this, I examined Alcian blue-stained 5dpf *Ofd1*, *Mks1*, and *mks3* morphants.

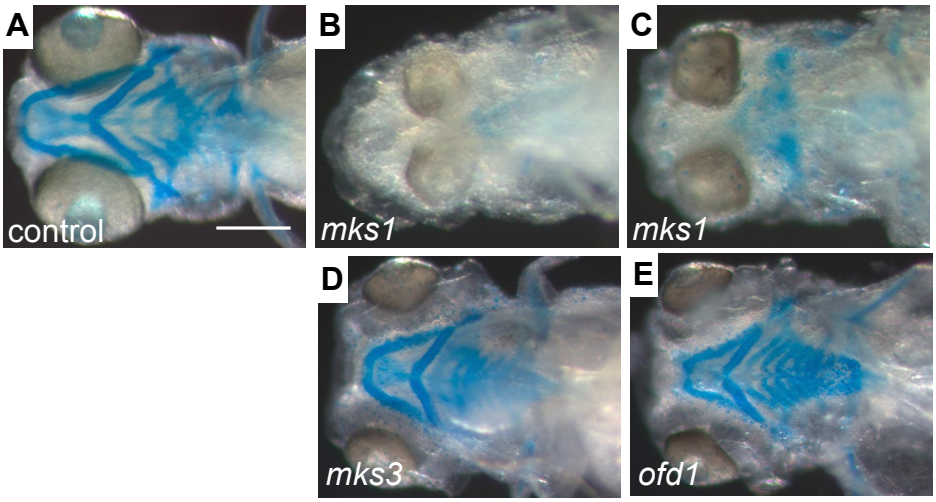

Figure 50. Ciliopathy morphant cranial cartilages

A: control embryos at 5dpf. **B**: *mks1* morphant embryo with cyclopia and lacking cranial cartilages. **C**: *mks1* morphant with a slightly less severe phenotype, but also having a drastically reduced cranial cartilage. **D**: *mks3* morphants have hypoplastic cranial cartilages. **E**: *ofd1* morphants also have smaller cranial cartilages, although all the branchial arches are present. Scale bar = 200μm.

mks1 morphants often lacked craniofacial cartilage altogether (Fig. 50B). Embryos that had developed cartilage had hypoplasia, absence of branchial arches, and reduced or absent mandibles (Fig. 50C). Trabeculae were often fused at the midline and synophthalmia (convergence of the eyes) was common. These morphants resembled a more severe form the *bbs8* morphants, in keeping with Meckel Syndrome being considered as a phenotypically extreme form of BBS.

Mks3 morphant cranial cartilages also resembled those of *bbs8*, but were much less severely disrupted than *mks1* Fig. 50D). The cartilages are much smaller than controls, despite the body being of a comparable size.

Ofd1 morphant embryos had very small craniofacial cartilage elements compared to controls (Fig. 50E). The jaws and branchial arches were narrower, not filling the full width of the head as they did in controls. Despite the severe hypoplasia of these cartilages and the strong phenotype elsewhere, such as renal oedema and kinked body-axis, the gross morphology and patterning of the craniofacial cartilages was normal. All the branchial arches were present, albeit narrower than in controls.

Discussion

Novel roles for Bbs proteins in neural crest cell migration

Here, Bbs proteins, in particular Bbs8, were shown to be important for migration of NCCs into the head, trunk, and gut. This has implications for our understanding of the pathomechanisms of disease and helps explain the aberrant craniofacial morphology and Hirschsprung's disease common amongst BBS patients.

Tan et al observed mechano- and thermosensory deficits in humans, mice, and *C. elegans* BBS mutants, and showed erroneous localisation of key receptor proteins in dorsal root ganglia (DRG) of *Bbs1*$^{-/-}$ and *Bbs4*$^{-/-}$ mice. The innervation of the paws by the peripheral neurons was also faulty. DRG and peripheral neurons are neural crest derived cells and so it is possible that lack of BBS proteins affects their development or migration to the correct targets. Tan et al also showed that DRGs are ciliated, a previously unrecognised phenomenon (Tan et al., 2007).

Pigmentation defects in *bbs8* morphants

The most striking neural crest phenotype of *bbs8* morphants is their overt lack of pigmentation. These cells are neural crest derived and are the last lineage of cells to emigrate from the neural tube. Pigmentation defects such as piebaldism (but not albinism) exist in some neurocristopathy syndromes, such as Waardenburg-Shah syndrome (*SOX10* mutation). However, this is likely due to hypoproliferation of NCCs and so insufficient numbers of melanocytes are produced. Sufficient numbers of NCCs are induced and they proliferate normally in *bbs8* morphants, but their migration is inhibited, albeit not completely.

No patients with BBS have been reported with piebaldism or other pigmentation defects. In fact, the first patients to be identified with *BBS8* mutations were Pakistani and so had highly pigmented skin. However, abundant naevi have been reported in a large proportion of BBS patients (Beales et al., 1999, 22% had

naevi). These are caused by the benign hyperproliferation of melanocytes in the skin, and can predispose to skin cancer if they become invasive.

Karaman (2008) described one such patient who he reported as having a dysmorphic face (micrognathia, thin philtrum, thin upper lip) and multiple pigmented nevi (Karaman, 2008). It is possible that the melanocytes in some BBS patients proliferate inappropriately because they migrate later, or slower, than they should in the embryo and so become exposed to different signals when they differentiate into melanocytes. One way to test this would be to take a melanocyte cell line, such as CRL-2811, derived from a primary melanoma, and knock down BBS genes. Then, one would analyse cell cycling, proliferation, and cell behaviour in response to differentiation stimuli.

Hirschsprung's disease

Hirschsprung's disease is commonly associated with BBS (estimates range from 5% to 45% of the total patient cohort, but are likely to be around 10% (findings from our own patient cohort)). HSCR is to neurocristopathy what kidney cysts are to ciliopathy – it is the common denominator. Not all neurocristopathies present with other NCC development phenotypes such as facial dysmorphism, piebaldism, and pharyngeal arch defects, however all have HSCR. The high incidence of this disease in BBS patients (around 1000 times more common than the general population), in addition to the ENS development and functional data from the zebrafish, gives a good idea that this may be due to NCC migration defects. This work suggests that there might be an overlap between certain ciliopathies and neurocristopathies, and provides a cell biological rationale for this.

Ciliation of neural crest cells

Previously, it was not known whether NCCs were ciliated, and I have shown clear primary cilia emanating from NCCs. It is impossible to tell whether these cells were actively migrating when they were observed, and not all NCCs appeared to bear cilia. To see if there is a difference in ciliation between migrating and static

NCCs, one would need to label cilia *in vivo* by expressing a tagged marker such as acetylated tubulin. However, because the NCCs are migrating in such a dense matrix of cells, the cilia of the NCCs are difficult to distinguish from neighbouring cells.

In vivo NCC assays will inform on the mechanics of PCP-dependent migration

In the future, it will be useful to perform *in vivo* assays on migrating NCCs. This will have to be performed in *Xenopus*, as it is far easier to explant and culture the NCCs. This would also enable a thorough molecular analysis in which the localisation of PCP intermediates, such as Dishevelled, could be monitored in real-time. Matthews et al (2008) showed that Dishevelled localises to the membrane of the leading edge of the migrating cell, and that this localisation was perturbed by knockdown of *Syndecan 4*, a PCP intermediate. They performed *in vivo* FRET analysis on Rho, Rac, and cdc42 - PCP-mediated modulators of the cytoskeleton, and showed them to regulate the direction of cell protrusions in migrating cells.

Park et al (2008) have demonstrated that Dishevelled is necessary for localisation of the basal body, and hence correct positioning of the cilium (Park et al., 2008). Given the importance of PCP for NCC migration, and the role of Bbs8 in PCP, it would be interesting to examine the position of the basal body in migrating NCCs. Dawe et al found that MKS3 is important for centrosome migration prior to ciliogenesis (Dawe et al., 2007). This might explain the craniofacial defects in *mks3* morphant zebrafish. If the cilium fails to form on migrating NCCs, or forms in the wrong place, they may fail to migrate properly in response to the extracellular cues, such as Shh. I tried to perform examine the position of the basal body in migrating NCCs *in vivo*, but found it extremely hard to differentiate the basal body from the red fluorescent nuclei. To improve this, one could have to develop a blue-fluorescent centrin construct to mark the basal body. Alternatively, one could perform the experiment *in vivo* on *Xenopus* NCCs and label the nucleus, Golgi apparatus, and basal body. One would then compare the

alignment of these three organelles with the directionality of migration and see if Bbs8 knockdown perturbed it.

Bbs proteins tend to be ubiquitously expressed at low levels during zebrafish development, with stronger expression in the eye and brain. The exact level of expression in the NCCs is almost impossible to determine, but Bbs8 expression in NCCs is important for their migration as cell transplantations demonstrated a cell autonomous role for this protein.

A potentially more general involvement of Bbs8 in cell migration

The finding of a role for Bbs8 in NCC migration was extended to include other cell types after it was observed that cultured fibroblasts and primary cells deficient in Bbs8 protein showed reduced migration in *in vitro* scratch wound healing assays. Furthermore, the actin cytoskeleton of these cells was mispolarised relative to the direction of migration. The finding that skin cells from BBS patients had migration and polarity defects might have implications for possible wound healing or scarring defects in patients. These have never before been reported, but it might be something for clinicians to be aware of in future.

Because PCP signalling is important for the positioning of the basal body and the correct polarity of the actin cytoskeleton in migrating cells, it would be interesting to analyse the position of the basal body relative to the axis of migration in these cells. A future experiment would be to perform time-lapse imaging of these migrating cells to determine whether the directionality or just the velocity of migration was affected.

Matthews et al noticed that knocking down *syndecan 4* appeared to completely inhibit NCC migration, but when they traced the paths of these NCCs, they found that the cells moved in tortuous paths and regularly doubled back on themselves, whereas control cells moved in straight, persistent paths. As such, the velocity of migration was only slightly reduced, rather the persistence and directionality of the cells was disrupted.

Craniofacial dysmorphology in other ciliopathies

Knockdown of *ofd1*, *mks1*, and *mks3* also produced craniofacial dysmorphology in the zebrafish, albeit differently to Bbs knockdown. Mks morphants show very severe craniofacial disruption, and given the severity of the patient phenotype and similarity to BBS, it is possible that MKS proteins are also involved in NCC migration. Because MKS3 is so similar in structure to the PCP receptor Frizzled (Dawe et al., 2007), one could envisage PCP-mediated NCC migration defects if this gene was knocked out.

Craniofacial dysmorphology in OFD1 patients is well documented and the facial hypoplasia is repeated in zebrafish morphants. However, cartilaginous elements are not missing, nor is pigmentation, as in BBS morphants. This suggests that the craniofacial defects in OFD1 are not due to aberrant NCC development, but rather to defects in cartilage and bone formation.

Aberrant bone development in the skeletal ciliopathies, such as EVC, JATD, and OFD1, confounds an analysis of facial dysmorphology attributable to NCC development. Extending the facial analysis to other non-skeletal ciliopathies such as NPHP might determine which genes are involved in craniofacial development, and possibly NCC migration. Performing *in vitro* assays on cell migration for all ciliopathy proteins might reveal differential and specific roles for different ciliopathy proteins in cell migration, such as microtubule transport outside the cilium, IFT, signalling, and cytoskeletal remodelling.

The results from these experiments were published in the *Proceedings of the National Academy of Sciences, USA* in July 2008 (Tobin et al., 2008).

Chapter 5: Involvement of ciliopathy proteins in Sonic Hedgehog signal transduction

Introduction

The features of different Shh pathway mutants

The mechanics of the Shh signalling pathway were outlined in the introduction. Due to the complexities of the pathway, there is not simply a "loss of function" or "gain of function" phenotype associated with Shh mutants. Because Shh functions in so many anatomically disparate systems in the developing embryo, mutations to the pathway cause complex and widespread phenotypes. Nevertheless, there are three systems in which Shh pathway dysfunction is well characterised and has a stereotypical role: control of digit identity, neural tube patterning, and craniofacial morphology.

Several different missense mutations exist in the *SHH* gene in humans, which affect different regions of the gene thereby affecting its protein's post-translational modification, kinetics, or receptor binding. These mutants show differing severity of HPE, hence a spectrum of the disorder exists which, at its mildest (e.g. the I111F mutation), may consist of a single central incisor, possibly combined with hypoplasia of the corpus callosum, a feature that can only be detected by MRI of the brain (OMIM). Extreme forms of HPE can be formed by nonsense alleles such as E284X (OMIM).

Null mutation in the *Shh* gene in mice causes complete loss of function of the signalling pathway, as the ligand is crucial for activation (Litingtung et al., 2002). When this happens, digits fail to form in the limb, and instead a single, stumpy digit with no joints is produced at the end of the limb. A single eye forms at the midline of the face with a proboscis instead of a nose – characteristic of complete holoprosencephaly, whereby midline structures are lost. The neural tube loses its

ventral cell-types and the forebrain fails to divide into two hemispheres (Rallu et al., 2002).

In contrast, addition of exogenous Sonic Hedgehog to chick limbs causes growth of ectopic limbs, while increased Shh in the face causes widening of the face and duplication of midline structures such as the nose and jaw (Hu and Helms, 1999). Transgenic over expression of Shh in the mouse also causes tumorigenesis, particularly in the skin and brain, and overactive Shh signalling is associated with tumour growth (Oro et al., 1997).

Null mutation of the downstream transcription factor Gli3 results in polydactyly. Double knock-out of Shh and Gli3 still results in polydactyly suggesting that Gli3 acts independently of Shh to mediate repression of target genes, cell survival, and digit growth in the limb (Litingtung et al., 2002). $Gli3^{+/-}$ $Shh^{-/-}$ embryos do not exhibit polydactyly but do grow some digits, unlike the Shh nulls which lack digits altogether.

Haploinsufficiency, often caused by microdeletion, of *GLI3* results in Greig cephalopolysyndactyly (GCPS) in humans. This consists of pre-axial polydactyly with fused digits, a wide face with hypertelorism, and agenesis of the corpus callosum. This human phenotype closely matches the mouse *Extra toes* (*Xt*) mutant, in which the 5' end of the *Gli3* gene is deleted (Schimmang et al., 1992).

In contrast to GCPS , a mutation truncating or frame-shifting the GLI3 protein causes Pallister-Hall syndrome (PHS) (Johnston et al., 2005). PHS causes more severe features including: post-axial polydactyly, hamartomas in the hypothalamus, macrocephaly, cleft palate and craniofacial dysmorphism such as retrognathia, and genital abnormalities such as hypospadias and micropenis. Johnston et al showed that mutation in the first third of *GLI3* cause GCPS while mutation in the second third causes PHS. The molecular mechanisms responsible for causing either pre- or post-axial polydactyly, depending on the type of mutation, are not understood.

Mutations to intermediate members of the Shh pathway have varying effects, depending on their position in the pathway. Mutating Smoothened, the membrane-bound receptor to which Patched binds, phenocopies the *Shh* null condition (Zhang et al., 2001). Conversely, null mutation in *Patched1* leads to constitutive de-repression of Smoothened resulting in inappropriate activation of Smoothened. This leads to ectopic induction of the Shh pathway and results in gain of function phenotypes such as neoplasia and hypertelorism (Goodrich et al., 1997). In humans, *PATCHED1* mutation causes Gorlin, or basal cell nevus syndrome. Mutation of *Suppressor of Fused* (*SuFu*) also causes ligand-independent activation of the Shh pathway resulting in tumours (Svärd et al., 2006).

The Shh pathway consists of a series of agonistic and antagonistic steps and so mutation to each of these causes different phenotypes. Interpretation of phenotypes is confounded by the graded response to differing concentrations of Shh ligand, which is translated into a gradient of Gli3 transcriptional activator to repressor ratio.

The features of BBS that are reminiscent of Shh mutants are as follows:

BBS feature attributable to Shh	**Similar Shh pathway mutant**
Post-axial polydactyly	*GLI3* (PHS) (Gain of function phenotype)
Craniofacial abnormalities: Mid-facial hypoplasia with retrognathia Single central incisor Agenesis of the corpus callosum	Mild loss of function mutations in *SHH*
Genital abnormalities: Hypospadias Micropenis	*GLI3* mutations (PHS) (Gain of function phenotype)

Table 10. Comparison of BBS features to Shh pathway mutants.

Table 10 demonstrates the apparent paradox that in BBS, Shh pathway activity is reduced in the head at the same time as being increased in the limb. This can be reconciled by considering the now accepted role for IFT in Shh signalling.

The ciliary basis of Shh signalling

Huangfu et al (2003) performed a large-scale ENU-based mutagenesis screen for embryonic patterning mutants and identified two IFT mutants, *IFT88* and *IFT172*, both with hallmarks of Shh pathway dysfunction. These mutants lacked ventral cell types in the neural tube and were polydactylous. The authors showed that the IFT proteins were acting downstream of Patched, but upstream of transcriptional targets of Shh, and so were playing a role in the intermediate stages of the pathway.

Liu et al (2005) then showed that IFT proteins in general were essential for regulating the balance of Gli3 repressor and activator isoforms. Corbit et al (2005) made the surprising discovery that Smoothened localises to the primary cilium in response to stimulation by Shh ligand, and that this localisation was essential for downstream activity of the pathway. Further weight was added to this assertion when Rohatgi et al (2007) showed ciliary localisation was also essential for Patched activity – only in this instance, Patched left the cilium upon activation by Shh, freeing up the repression of Smo in the cilium. It has also been shown that SuFu, Gli2 and Gli3 also localise to the cilium (Haycraft et al., 2005).

Processing and transport of Gli3 from the cilium to the nucleus is dependent on IFT. Tran et al (2008) identified a new mutant encoding a protein called THM1 (tetratricopeptide hedgehog modulator 1) in which retrograde IFT was impaired. This caused sequestration and accumulation of IFT proteins in the tips of cilia and resulted in over-activated Shh signalling. They proposed that anterograde IFT was necessary for Gli3 activation. The subsequent fate of this Gli3 is unclear from this model.

Ocbina and Anderson (2008) showed that primary cilia were required for primary fibroblast cells from mice to respond to stimulation by exogenous Shh (Ocbina and Anderson, 2008). As such, only fully confluent cells would respond to stimulation by upregulation of Gli1 because only confluent cells ciliate. They concluded that IFT-dependent trafficking of Shh pathway components through the cilium was essential for Shh pathway activation. It is also observable that

unciliated cell lines, such as Cos7, fail to respond to stimulation with Shh (personal observation and communication with J. Briscoe).

This growing body of evidence suggests that the cilium is indispensable for Shh signalling and that IFT proteins are important in regulating the processesing of Gli3 from its full-length activator isoform to its repressive form. Exactly how this happens, and the precise role for IFT proteins, is not clear. What is also not clear is at precisely which point in the pathway the IFT proteins intersect, just that they function somewhere around the level of Gli3 but do not function in the nucleus.

The Shh-like phenotypes of BBS outlined above are consistent with the phenotypes of other *bona fide* IFT mouse mutants. *Ift88* and *Ift172* null mutants show very severe phenotypes and die at E9.5, before digit patterning can be investigated. However, the downregulation of *Patched* and lack of ventral cell types in the neural tube is indicative of downregulated Shh signalling. However, embryos with a hypomorphic *Ift88* allele survive until E12.5 – long enough to examine digit patterning. These embryos are polydactylous and show expanded expression domains of downstream Shh genes such as Gli3 in the limb bud (Huangfu and Anderson, 2005). Furthermore, *Ift52* hypomorphic embryos showed midline fusion of the olfactory pits, another loss-of-function Shh feature.

Therefore, it is clear that BBS shows a similar pattern of phenotypes, albeit not quite so severe. This apparently concurrent loss and gain of Shh function phenotypes probably represents a defect in Gli3 processesing. The fact that facial and limb tissues are affected differently reflects the differential outcome of Gli3 activation or repression in different developmental systems.

Mouse models of BBS do not exhibit polydactyly

Despite faithfully reproducing all the cardinal features of BBS, none of the six mouse models (*Bbs1*, *Bbs1* M390R KI, *Bbs2*, *Bbs3*, *Bbs4*, *Bbs6*) produced to date exhibit polydactyly, a feature present in 70% of patients at birth. The reasons for this are perplexing because other mouse IFT mutants show polydactyly, as do

Gli3 mutants. The reason could be that the effect of lack of BBS proteins on the limb is subtle. Because the mouse limb bud is much smaller than the human limb bud, lack of BBS protein may not perturb the response to the gradient of Shh morphogen sufficiently to induce polydactyly. It may also simply be due to the particular genetic background of the mouse strains used.

Nobody has ever checked if mouse mutants have brain abnormalities associated with Shh signalling, such as agenesis of the corpus callosum, but they do have ventriculomegaly. Due to the striking lack of polydactyly in the mouse, and my aim to see if BBS proteins were involved in Shh signalling, the zebrafish became a more tractable model organism to use.

Using the zebrafish to explore the involvement of ciliopathy proteins in the Shh pathway

The zebrafish has never been used to model Shh signalling in ciliopathy mutants or morphants. Many ciliary genetic mutants in zebrafish exist from large-scale mutagenesis screens for renal phenotypes but Shh signalling has never been investigated in these. The Shh signalling pathway in the fish is identical to the mammal and the pathway components are conserved. It is involved with homologous developmental processes, including neural tube and brain patterning, and outgrowth of the paired fins.

Corbit et al (2005) used the zebrafish to show that a ciliary localisation defective mutant allele of *smoothened* was unable to rescue the phenotype of $Smo^{-/-}$ embryos while the wild type allele could. Tayeh et al (2008) found an expanded domain of *shh* expression in the fin bud of *bbs1* and *bbs7* morphant embryos and altered fin cartilaginous elements (Tayeh et al., 2008), although the data are difficult to interpret.

Given the physiological relevance of the zebrafish BBS models generated, including the craniofacial deformities, renal cysts, convergent-extension defect, and neural crest migration phenotype, I aimed to use the fish to examine Shh

signalling in the absence of Bbs proteins. The *bbs8* morphant craniofacial phenotype is strikingly similar to that of the *shh* and *smoothened* mutants, as well as embryos treated with cyclopamine, a potent inhibitor of Smoothened, between 4 and 8hpf (Wada et al., 2005). This specific midline trabecular fusion is not seen in any other craniofacial mutant zebrafish and so is indicative of Shh signalling defects.

Responses to Shh can be quantified with *in vitro* assays

While the zebrafish can be used to show phenocopy of Shh-like phenotypes and analyse gene expression levels of downstream pathway components, it cannot be used to quantify the level of signalling response. Because of the relative subtlety of the BBS phenotype compared to Shh-pathway mutants or *bona fide* IFT null mutants, I expected that any putative defects in Shh signalling would not be as striking as they are in these knockouts. In order to reveal subtle, possible secondary effects on Shh signalling, a quantitative output can be achieved using *in vitro* cell-based assays, analysing the response of cells to exogenous Shh stimulation.

Because IFT proteins and the cilium have been shown to function downstream of Patched, upstream of transcriptional activation, and are involved with Gli3 processing, I did not expect to see a complete loss or gain of pathway function. Instead, I wanted to see if the response to graded morphogen signalling was affected. This would more likely explain the subtle phenotypes seen in patients.

To do this, a luciferase reporter construct has been developed which expresses luciferase under the control of six Gli1 binding sites. When the pathway is activated, the Gli3 protein binds to these sites to activate Gli1 transcription. The amount of luciferase expressed is directly proportional to this downstream transcriptional response and can be measured luminometrically.

Additionally, cell lines can be used to assess the ratio of active to repressive Gli3 isoforms in the absence and presence of exogenous Shh stimulation. Wu et al

discovered a molecule, purmorphamine, which binds directly to smoothened and agonises it (Wu et al., 2004). It is therefore a potent activator of the Shh pathway and is more reliable than using recombinant Shh peptide which is unfeasibly expensive and whose dose-response can be variable. In addition, purmorphamine is capable of stimulating the pathway more powerfully even than ShhN itself, and so can be used to test fine and coarse responses to stimulation.

The aims of this study

The phenotypic clues from humans and zebrafish suggest that Shh signalling is defective in some form. In this section, I aimed to answer the following questions:

1) Do BBS proteins have a role in the Shh pathway?
2) How significant is this role, and are different BBS proteins differentially involved?
3) If there is involvement in the pathway, at what level in the pathway do BBS proteins act?
4) Are BBS proteins involved in Gli3 processesing?

Results

Cursory analysis of *Bbs6*$^{-/-}$ mouse embryo neural tubes shows no evidence of altered Shh signalling

Human BBS patients show several features consistent with defective Shh signalling, such as: post-axial polydactyly, frequent agenesis of the corpus callosum, and infrequent single central incisor. Surprisingly, none of these features has ever been detected in mouse models of the disease (including *bbs1*, *2, 4,* and *6*). However, nobody has ever examined molecular readouts of disrupted Shh signalling.

In the neural tube, Shh ligand is secreted from the notochord where it diffuses dorsally to the neural tube and induces expression of motor-neuron precursor markers such as Nkx2.2 and Mnr2 in the ventral neural tube. I aimed to see if expression of these genes was affected in BBS mouse mutants. *Bbs4* null mice have the strongest phenotype, but these mice were sub-fertile and so I was unable to obtain any null embryos of this genotype. The *Bbs6* mice reproduced normally and so were used despite having an extremely mild phenotype, which suggests that the model is a hypomorph and not a true, null allele.

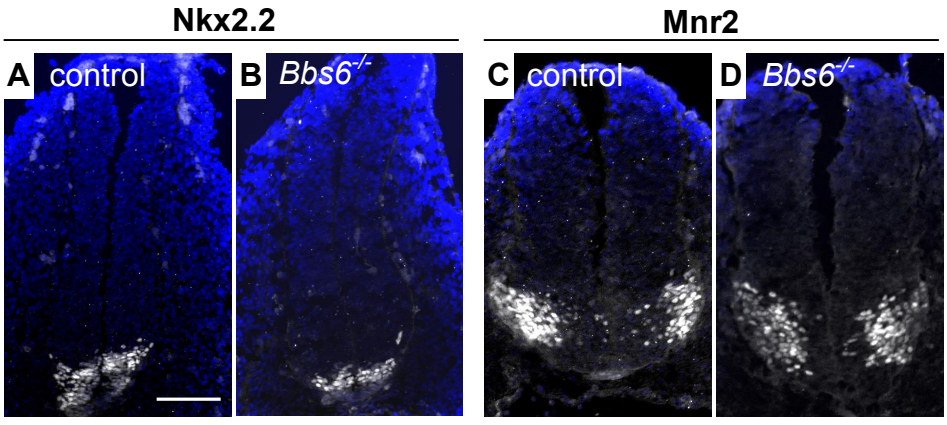

Figure 51. Expression of Shh markers in mouse neural tubes

A,B: Nkx2.2 is a marker of ventral cell-types in the neural tube and is activated in response to high-levels of Shh. Its expression is unaffected in *Bbs6* null embryos. **C,D**: Mnr2 is a marker of motor neurons in the ventral neural tube. Again, its expression is comparable between wild type and null embryos. Scale bar = 100μm.

Bbs6 null embryos and wild-type littermates were fixed at E10.5 and sectioned transversely. The serial sections were stained with either Nkx2.2 or Mnr2 antibodies, which stain motor neuron precursor cells. Inhibited Shh signalling might lead to a down regulation of these markers, while induction of the pathway would lead to upregulation. No difference in the expression of these markers was observed between null and control embryos (Fig. 51A-D). Furthermore, no difference in the expression of the dorsal neural tube marker, Pax7, was noted between mutants and controls (data not shown). This could be for a number of reasons: 1) there is no defect in Shh signalling in the neural tube; 2) because of differences in embryology between mouse and human which also results in the mouse lacking polydactyly; 3) the possibly hypomorphic nature of the *Bbs6* allele.

Attempts to model polydactyly in the developing chick limb

Mutations in *BBS8* in human patients only accounts for around 2% of total mutations but the clinical manifestations of their phenotype tend to be most severe. Because no mouse model for *Bbs8* exists, I tried to apply a *Bbs8* morpholino to the developing limb bud of chick embryos to see if I could induce limb defects.

To begin with, I tested to make sure *Bbs8* was expressed in the limb bud. I removed limb buds and divided them into anterior and posterior, and proximal and distal halves from stage 18 and stage 24 chick embryos. I extracted total RNA using Trizol, of which I used 500ng to synthesise cDNA and performed semi-quantitative RT-PCR to determine the presence and relative abundance of *Bbs8* (and *Bbs11* – as it was newly discovered at the time as an E3 ubiquitin ligase). *Bbs8* and *Bbs11* are both expressed in the limb bud. It seems that both genes are expressed at higher level in the posterior portion relative to anterior. (Figure 52). Expression of both genes is equivalent in proximal and distal halves (not shown). This could be interesting in light of the fact that Shh signals from the posterior margin of the limb bud.

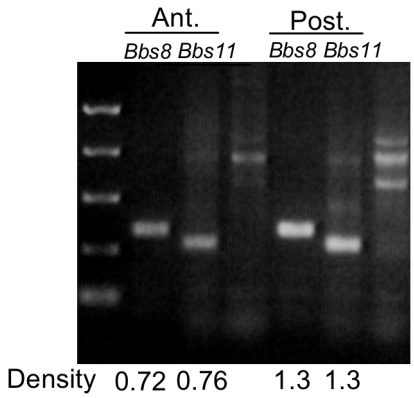

Figure 52. RT-PCR expression of BBS genes in the chick limb bud.

Bbs8 and *Bbs11* are both expressed in the developing chick limb bud. It is possible that both genes are expressed at higher level in the posterior half of the limb bud, in which Shh is secreted. (Ant. = anterior, Post. = posterior).

The limb bud of a chick consists of mesenchyme overlaid by epithelial tissue and as such does not contain a lumen convenient for introduction of genetic material for electroporation. I tried to electroporate the limb bud by injecting 1mM of *bbs8* MO at various sites in the limb bud followed by electroporation, but this failed and the MO only entered very small foci around the points of injection.

To deliver MO systemically to the whole limb bud I tried a different approach, dissolving the MO in 30% pluronic gel. This substance liquefies when cooled on ice but sets into a gel when the temperature is raised. To administer the gel, pipette tips were cooled on ice to keep the gel liquid. A tear was made in the vitelline membrane overlying the limb bud of 2dpf chick embryos to expose the embryonic tissue. The MO dissolved in pluronic gel was then expelled over the limb bud whereupon it set on contact with the warm tissue. The eggs were then covered over with tape, incubated, and examined 24 hours later for evidence of incorporation of the MO into the tissue, evidenced by green fluorescence of the FITC-tag on the MO.

Fluorescence was inconsistent and tended to be at very low level, often not focussed in the limb bud itself, implying that the gel had diffused away from the site of delivery. This was a problem before the MO had even permeated into the limb tissue, and precluded any worthwhile assessment of the subsequent limb

morphology, whose cartilaginous elements do not begin to appear until 2 days after MO administration.

Localisation of Smoothened in fibroblasts

A paper published in Nature at the start of this PhD described how the localisation of Smoothened to primary cilia was necessary for proper activation of the Shh signalling cascade (Corbit et al., 2005). Because BBS proteins are involved in ciliary transport, I reasoned that mutations abrogating the function of BBS proteins could potentially prevent the ciliary localisation of proteins by affecting transport into, or along, the cilium. Consistent with this hypothesis is the fact that all *bona fide* IFT mouse mutants show Shh signalling phenotypes, including polydactyly and misexpression of downstream proteins in the neural tube.

I used primary fibroblasts taken from the skin of a healthy adult to examine Smoothened localisation. These were stained with an antibody detecting Smoothened, which revealed its localisation in a highly punctate pattern in unstimulated cells (Fig. 53A). The movement of Smo into cilia in response to Shh stimulation reported by Corbit et al was recapitulated in adult primary fibroblasts. When recombinant Shh was added to these cells, Smo was redistributed from puncta around the cell to become concentrated in the cilium (Fig. 53B).

However, because the Smoothened was observed dispersed in puncta around the membrane, it was impossible to say with any confidence whether its ciliary localisation was affected in the case of primary cells taken from *BBS8* null adult humans. Also, these primary cells were taken from the skin of adults, which may not signal via Sonic hedgehog in the same manner as embryonic cells, particularly when cultured *in vitro*. To make this experiment more accurate, one would have to look at Smoothened localisation *in vivo*, or at least in response to stimulation by exogenous Shh ligand *in vitro*.

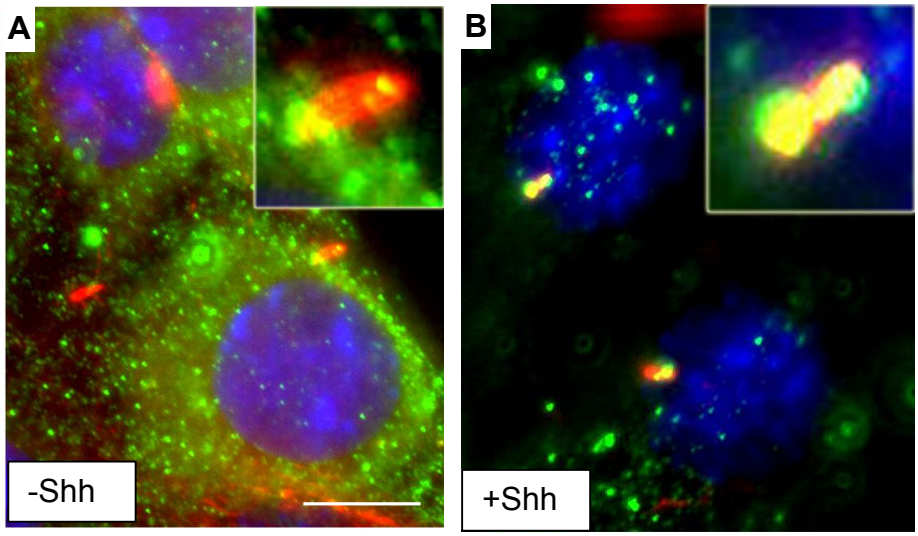

Figure 53. Localisation of Smoothened in primary fibroblasts.

A: In the absence of exogenous Shh, Smo localises in puncta throughout the cell and is excluded from the cilium (inset). **B**: in response to Shh stimulation, the Smo is redistributed from the dispersed puncta to the cilium, where it becomes concentrated (inset). Scale bar = 5μm.

Localisation of Gli3 in fibroblasts

Gli3 is the downstream transcription factor effecting the transcriptional response to upstream Shh signalling. In the absence of Shh signal, Gli3 is cleaved into a shorter 83kDa repressive fragment (Gli3R), and in the presence of Shh it exists as a full-length, 190kDa transcriptional activator (Gli3A). These proteins must be translocated from the cilium, where the Shh signal is perceived, to the nucleus. This process is reliant upon both IFT and on microtubule-based transport in the cytoplasm. Because BBS proteins are thought to be important for both of these processes, I examined the localisation of Gli3 in primary fibroblasts.

In wild-type fibroblasts, the Gli3 protein localised in puncta along the microtubule cytoskeleton (Fig. 54 A,B). Gli3 was absent from the nucleus in controls. In *BBS8* mutant cells, Gli3 was present on the microtubules but seemed to be present in large puncta inside most of the nuclei (Fig. 54C). This is a surprising finding and may be artefactual, or may represent an accumulation of either full-length or cleaved Gli3 in the nucleus. Also, the Gli3 antibody could be staining the microtubules non-specifically and so the only way to check this would be to test the antibody on some primary cells taken from a *Gli3*-null mouse

embryo. Even so, the inclusion of the Gli3 from the nuclei of mutant cells was consistent. To determine whether there was a gross difference in distribution of Gli3 activator or repressor isoforms, I stained cells with an antibody only recognising the repressor form. However, this antibody failed to work on either immunofluorescence or Western Blot.

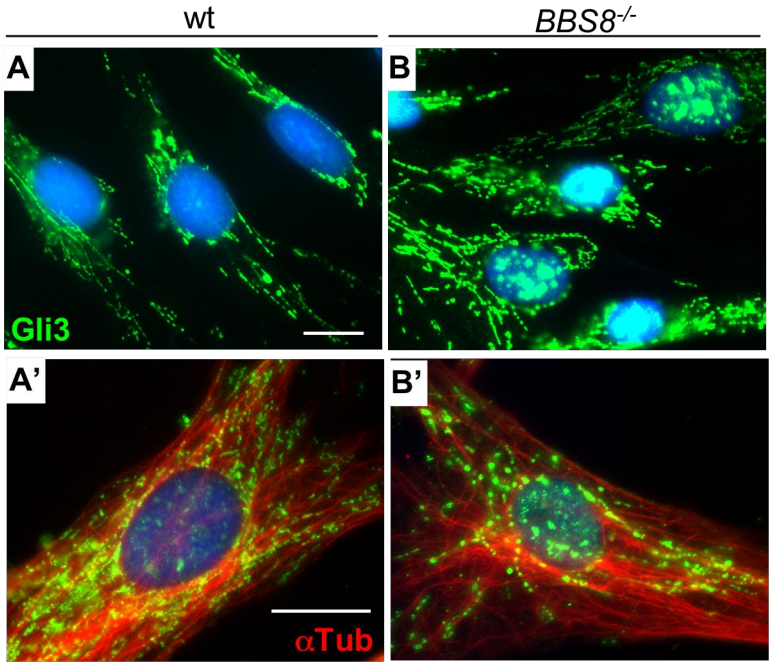

Figure 54. Gli3 localisation in primary human fibroblasts.

A: Gli3 is localised in puncta in the cytoplasm but is excluded from the nuclei (blue). **B**: co-staining with an anti α-tubulin confirmed that the Gli3 protein was localised on the microtubules. **C,D**: in *BBS8* mutant fibroblasts, Gli3 persisted on the microtubules but was also present in large puncta inside the nuclei. Scale bars = 5μm.

Cellular fractionation

The next experiment aimed to see if there was a difference in the amount of activator and repressor isoforms of Gli3 in the nuclear versus the cytoplasmic and membrane fractions of the cells. This aimed to determine whether the Gli3 puncta observed in the *BBS8* null nuclei consisted of Gli3R or Gli3A. To do this I fractionated wild type and mutant primary fibroblasts, extracted the total cellular protein, and performed a Western Blot with a Gli3 antibody recognising both active and repressive isoforms.

By blotting the nuclear fraction for Gli3 protein, it appeared that there was more Gli3R in the mutant (blue arrow) than wild-type cells. This might suggest that Gli3 was being cleaved more in BBS8 mutants than in wild types (Fig. 56A). To control for protein levels, I blotted for α-tubulin and showed there to be comparable levels in each sample (blue arrow, Fig. 56B). To be sure that the nuclear and cytoplasmic fractions were distinct, I blotted the proteins from each fraction with an antibody against C23, a nucleolar marker. This was convincingly present in the nuclear fraction and absent from the cytoplasmic fraction (blue arrow, Fig. 56C). Because Gli3A cleavage is repressed by Shh signalling, this suggests a possible lack of response to Shh pathway stimulation in the null fibroblasts.

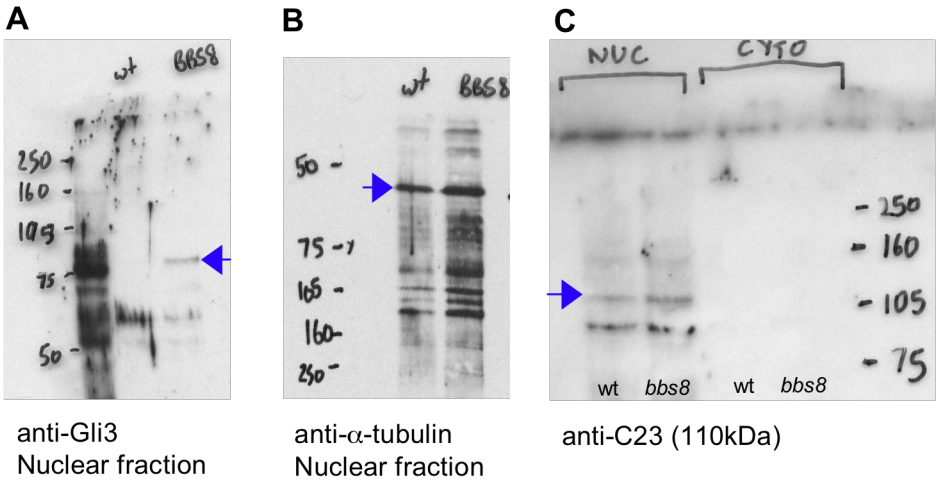

Figure 55. Gli3 protein levels in cellular fractions.

A. Nuclear fractions of control and *Bbs8* suppressed 3T3 cells blotted with an anti-Gli3 antibody showing greater levels of Gli3R in the nucleus of *Bbs8* suppressants. **B**. Anti-α-tubulin shows a comparable level of protein between control and suppressed nuclear fractions. **C**. anti-C23 blotting for a nucleolar protein proves the efficacy of the cellular fractionation as it is present in the nuclear fraction (blue arrow), but absent from the cytoplasm.

To determine if Bbs8 protein might be interacting with Gli3 in an IFT process, I performed co-immunoprecipitation experiments by transfecting cells with full-length GFP-tagged Bbs8. I then immunoprecipitated with an anti-Gli3 antibody, ran the protein out on a gel and blotted with an anti-GFP antibody to detect tagged Bbs8. When cells were transfected with a C-terminally tagged Bbs8 construct, a

faint band was observed, corresponding to a physical interaction between Bbs8 and Gli3 (Figure 55, lane 1). This band was observed in the lysate at the same size – around 90kDa, which corresponds to the size of Bbs8 (55kDa) plus GFP (38kDa). This band was not observed in the absence of anti-GFP antibody, nor using N-terminally tagged Bbs8, so it is possible that the interaction occurs at the N-terminus of Bbs8, as the N-terminal GFP could sterically abrogate an interaction (Figure 55). Endogenous Gli3 protein was used for this IP. Elevating Gli3 levels by transfection may yield a stronger interaction, confirming the result, but is more of an artificial system.

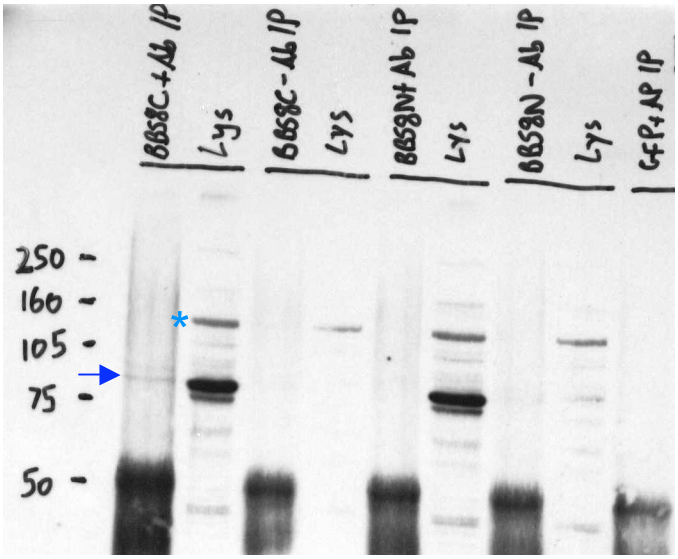

Figure 56. Co-immunoprecipitation of BBS8 and Gli3.

Gli3 was immunoprecipitated and then BBS8 tagged with GFP at the C-terminus was detected on the blot. A single feint band at around 90kDa corresponds to GFP-tagged BBS8 protein (blue arrow) (Lane 1). The lysate from the transfected cells shows a strong band at 90kDa corresponding to tagged BBS8 (Asterisk is a non-specific band in all lysate lanes) (lane 3). No Gli3 antibody added to the immunoprecipitation and then blotted to detect BBS8 revealed no band at 90kDa, suggesting that IP and interaction in Lane 1 is specific. Cells were transfected with an N-terminally tagged BBS8 construct. IP with anti-Gli3 followed by blotting to detect BBS8 failed to detect an interaction (lane 5). The N-tagged BBS8 construct was expressed at the same level as the C-tagged revealed by blotting the cell lysate with anti-eGFP (lane 6). Lack of Gli3 antibody also failed to pull-down any N-terminal tagged BBS8 protein (lane 7). GFP alone did not interact with Gli3 (lane 9).

Luciferase assays show Bbs8 and Ift80 mutant cells have a blunted response to Shh stimulation

It appeared that there were some defects in localisation and abundance of Gli3 in mutants, but the effect this was having on the cells was unknown. To investigate this, I performed luciferase assays using a reporter construct comprising six Gli1-binding sites driving expression of the luciferase reporter gene. To determine the optimum concentration of Purmorphamine, I treated Shh-Light[2] cells with a range of purmorphamine concentrations from 0 to 5μM, dissolved in 1% DMSO. Figure 58 shows a dose-response to purmorphamine with a maximum response reached by 2μM. These values are comparable to those reported in (Sinha and Chen, 2006). As 2μM is more stimulatory than physiological conditions, I chose to treat cells with 0.5μM, where the pathway is stimulated around 2.5 to 3-fold, a range more in keeping with high-level Shh signalling *in vivo* (Dessaud et al., 2007).

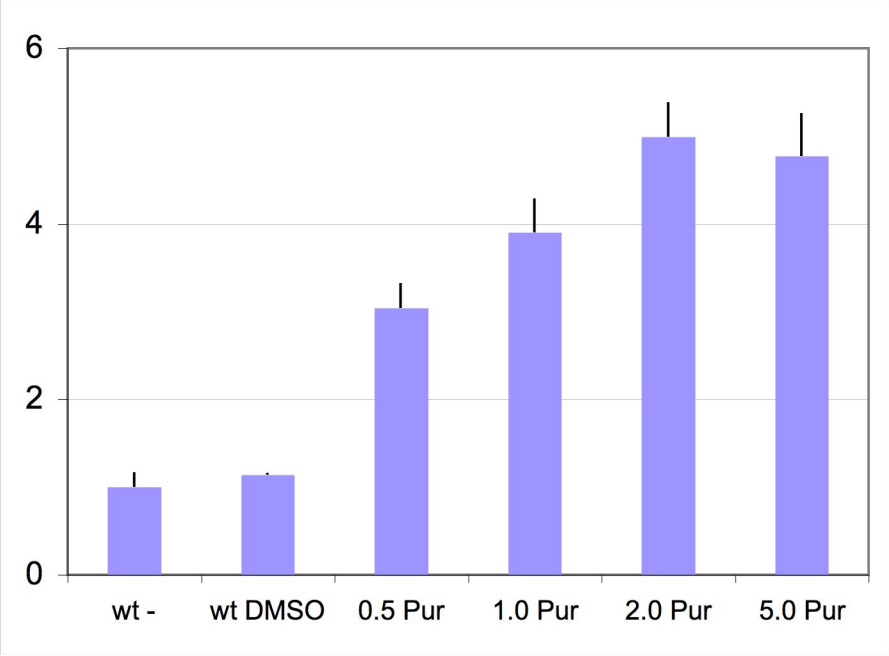

Figure 57. Purmorphamine gradient assay.

3T3 Shh-Light cells were treated with varying amounts of purmorphamine and their response measured by luciferase assay. Unstimulated cells were given a baseline value of 1. Addition of increasing amounts of purmorphamine stimulated the pathway progressively, with maximal activity being reached with 2 or 5μM purmorphamine. This

[2] Shh-Light cells are stably transfected with the Gli-luciferase reporter construct and a Renilla internal transfection control.

shows that the assay works and is reproducible and can sensitively distinguish between different levels of pathway activation.

I then co-transfected 3T3 cells with shRNA targeted against *Bbs8*, *Bbs7*, and *Bbs4*, as these are the proteins whose roles have been most closely associated with IFT. In each case, three samples of each cell type were treated with DMSO (vehicle) alone, and three were treated with 0.5μM purmorphamine, the Shh pathway agonist. The relative luciferase assay value was calculated by dividing the result for the firefly luciferase activity by the result for the Renilla luciferase activity. This normalises the luciferase values by controlling for the transfection level in each sample.

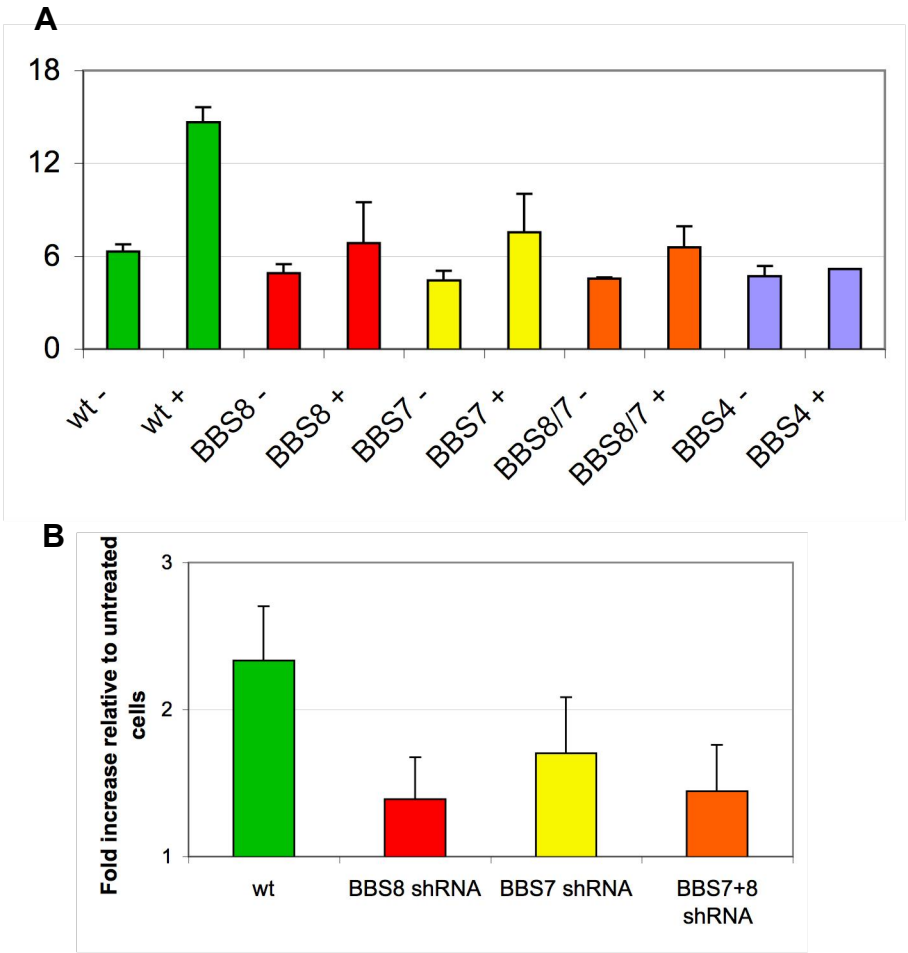

Figure 58. Luciferase assays of Shh response in BBS knockdown cells.

The top graph shows how addition of 0.5μM purmorphamine to control cells induces the Shh pathway. This response is dulled in all BBS shRNA-treated cells tested. The bottom graph shows the fold increase in pathway activity in response to Shh relative to untreated cells. This is significantly lowered (by around 75%) in *Bbs8* knockdown cells relative to controls. The response is around 50% lower in *Bbs7* knockdown cells. Knockdown of both *Bbs7* and *Bbs8* failed to show any synergistic effect on response to Shh.

In control cells, addition of purmorphamine resulted in approximately 2.3-fold induction of Shh signalling. The graphs show how this induction is attenuated in cells transfected with all the BBS shRNA constructs (Figure 58). Knocking down both *Bbs7* and *Bbs8* together does not reduce signalling level below either knockdown alone, suggesting that they do not act synergistically in modulating Shh transduction, and may be redundant. *Bbs4* knockdown produced the most dulled response to Shh stimulation suggesting it has an important role in transduction of the pathway.

In all cases, the baseline level of Shh signalling activity in the absence of purmorphamine was slightly reduced in suppressant cells. However, this reduction was not statistically significant. These results imply that BBS proteins are important for the cell's response to Shh stimulation, but do not significantly interfere with the function of the pathway in the absence of ligand stimulation.

To confirm these results further, I performed the same luciferase assay on cells that had been stably transfected with the *Bbs8* shRNA construct to ensure that all cells were knocked-down for the gene, and that the result was not skewed by cells not expressing the construct. I recapitulated the same results as previously and the *Bbs8* suppressant cells showed an attenuated response to stimulation with purmorphamine.

Bbs8 may be important for the graded response to the Shh morphogen

Purmorphamine is a powerful agonist of the Shh pathway and is not as physiologically relevant as recombinant Shh, the natural ligand. I next performed a luciferase assay on control and *Bbs8* knockdown in mouse embryonic 3T3 fibroblasts using a range of concentrations of Shh peptide derived from the conditioned medium of Shh-transfected COS7 cells. These results showed that controls were stimulated in a similar manner with Shh as they were with purmorphamine (Figure 59). Stimulation of *Bbs8* suppressant cells failed to

activate the pathway, especially at low levels of Shh signalling (Figure 59). These results suggest that Bbs8 is most important in the cell's response to lower concentrations of Shh ligand. As such, lack of BBS8 may impair a cell's ability to discriminate between the fine-grained concentration gradients of Shh morphogen in the developing embryo. This might result in polydactyly due to an inability to interpret the morphogen gradient at the posterior end of the limb bud.

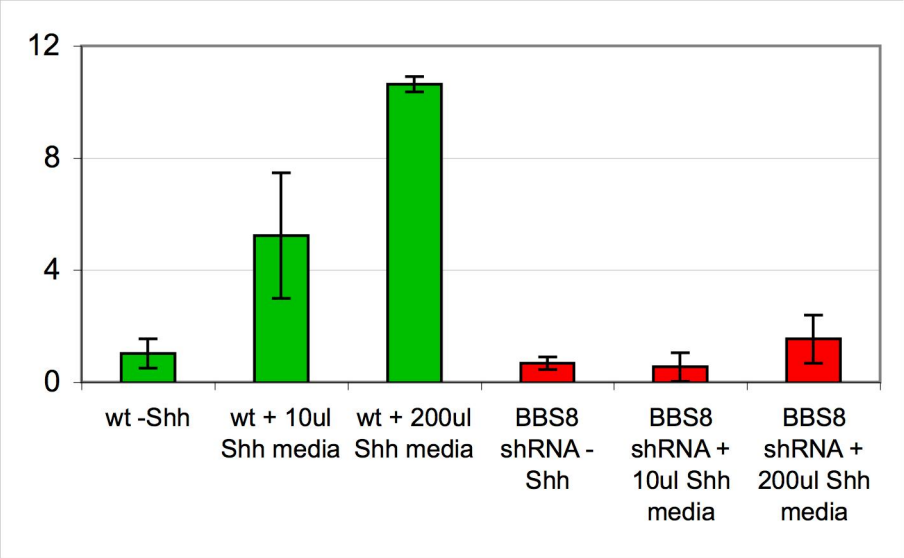

Figure 59. Stimulation of 3T3s with recombinant Shh protein.

Adding recombinant Shh to the media of control cells stimulates the Shh pathway, even with relatively small amounts of Shh-conditioned media (around 1 in 2,000). Adding recombinant Shh to *Bbs8* suppressant cells fails to stimulate the cells at low levels (10μl), and there is a dulled response at higher levels of Shh (200μl).

Quantitative RT-PCR analysis of downstream Shh components

For a finer analysis of the effect of BBS knockdown on the Shh pathway, I used qRT-PCR to analyse the expression level of several genes downstream of Gli3, upregulated by Shh signalling. *Ptc1* and *Gli1* are all direct transcriptional targets of Gli3A. In control transfected 3T3 cells, all these targets were upregulated by addition of purmorphamine. This was most pronounced in the case of Gli1 which was upregulated 6-fold by purmorphamine in controls (Figure 60). In the *Bbs8* knockdown cells both *Ptc1* showed absolutely no increase of expression upon stimulation, and *Gli1* was only upregulated 2-fold (Figure 60).

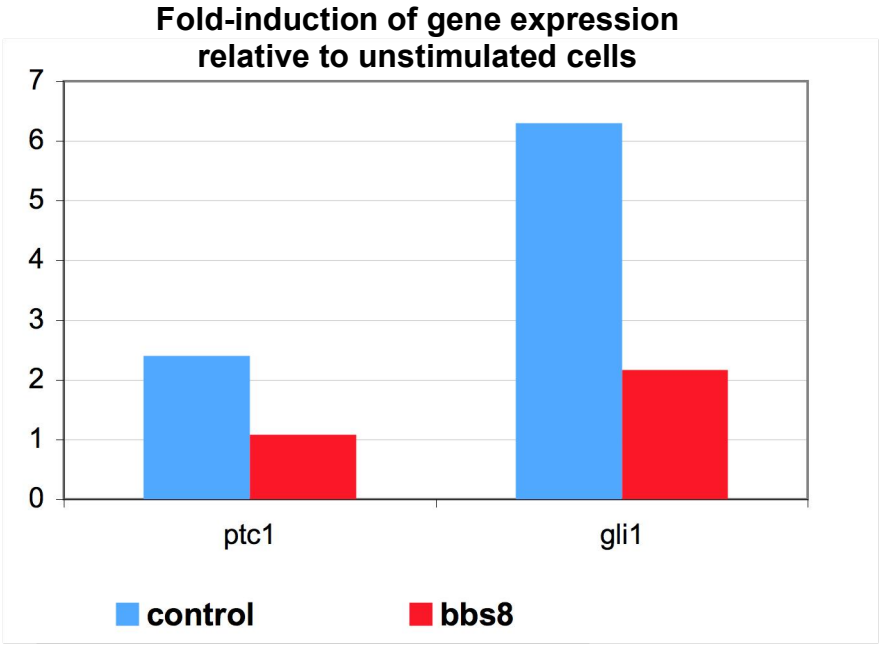

Figure 60. qPCR expression levels of downstream Shh targets.

Adding purmorphamine to controls caused the upregulation of *ptc1* mRNA by around 2.3-fold compared to almost nothing by *Bbs8* suppressants. *Gli1* expression was increased around 6-fold in controls but only by 2-fold in *bbs8* suppressants.

An involvement for Bbs8 in the processing of Gli3

Of all the BBS proteins identified, BBS8 has the most characterised function as a regulator of IFT particles, and is important for transport of IFT complexes along the cilium. I have shown that BBS8 is important for transduction of the Shh signal but it is unknown at what point in the pathway BBS8 is involved. Given that IFT is essential for processing and transport of Gli3 to the nucleus, I next designed an experiment to see if processing of Gli3 into its active and repressive isoforms was affected in BBS8 knockdown cells.

To do this, I added 0.5μM purmorphamine to control or *Bbs8* knockdown cells, extracted the protein, and blotted it with the anti-Gli3 antibody. I then used

densitometry to compare the ratio of Gli3A to Gli3R. When the control cells were stimulated with purmorphamine, the ratio of Gli3A to Gli3R increased approximately four-fold (Figure 61). This is due to inhibition of the proteolytic cleavage of Gli3A. When *Bbs8* knockdown cells were stimulated with purmorphamine, the ratio of Gli3A:Gli3R was only increased by about 1.4-fold, and this difference was not statistically significant.

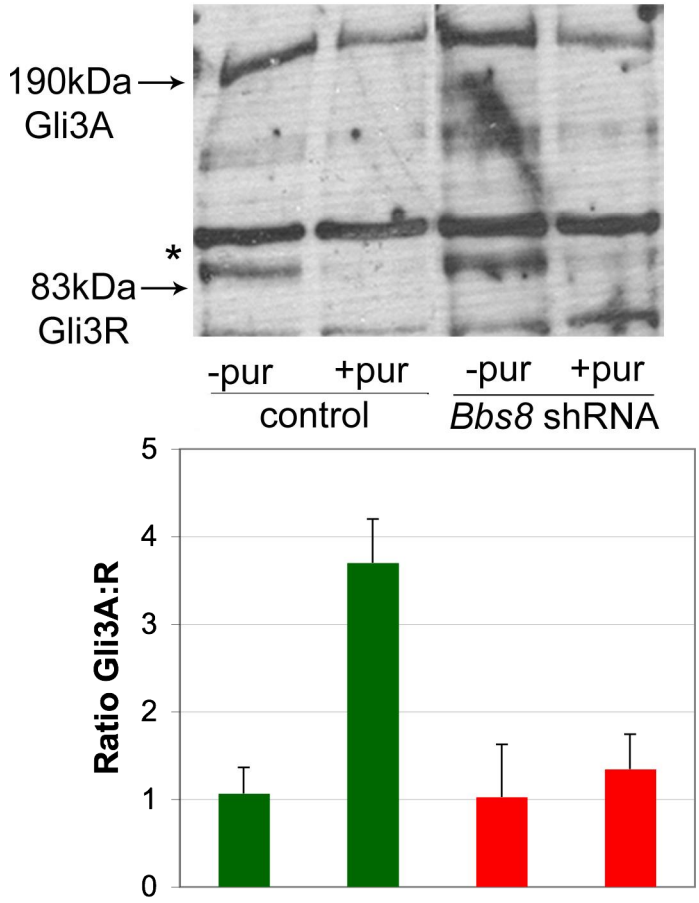

Figure 61. Gli3 processing in response to Shh stimulation.

The image of the blot shows that addition of 0.5μM purmorphamine to control cells results in the abolition of Gli3R, and therefore an increase in the ratio of Gli3A:Gli3R by approximately 4-fold. In *Bbs8* suppressant cells, addition of purmorphamine had less of an effect on reducing Gli3R levels, resulting in an attenuated level of Gli3A to Gli3R.

Markers of Sonic Hedgehog signalling are misregulated in *bbs* morphant zebrafish

The data from the cell culture experiments revealed that, at least *in vitro*, BBS8 protein is important for transduction of the Sonic Hedgehog signal, and that a lack

of this protein, and other BBS proteins, impairs the response of the cell to Shh stimulation. To see if this effect persisted *in vivo*, I turned to the zebrafish embryo to study markers of Shh signalling activity and to try to dissect the point at which *Bbs8* intersects the pathway.

bbs8 morphants show phenotypic signs of Shh pathway misregulation. These include: cyclopia, U-shaped somites, and midline fusion of the trabeculae of the ANC. I next wanted to investigate molecular readouts of Shh signalling. Previous work done by a colleague in our laboratory has shown that expression of *shh* transcript itself is unaffected in *bbs8* morphants (H. May-Simera, thesis). If the Shh transduction mechanism is defective, as indicated by the cell culture data, it is possible that direct transcriptional targets of the pathway could be misregulated in *bbs8* morphants.

To investigate this possibility, I performed *in situ* hybridisation to examine the expression of two genes positively regulated by Shh signalling: *ptc1*, and *nkx2.2*. Despite *ptc1* being a negative regulator of the pathway by inhibiting Smoothened, it is autoregulated by the pathway in a negative feedback loop that prevents over-activation of the pathway. It is for this reason that loss of *ptc1*, when mutated, causes hyperactivity of the pathway and results in malignancy. *nkx2.2* is responsive to high concentrations of Shh signalling in the ventral neural tube.

ptc1 was downregulated in *bbs*4, *6*, and *8* morphants relative to controls, but most markedly so in *bbs8* morphants (Fig. 62A-D). *pax6*, a gene negatively regulated by Shh, was upregulated in the neural tubes of *bbs8* morphants relative to controls (Fig. 62E and H). The reduction in expression of Shh target genes *ptc1*, *gli1*, and *shh* was shown by qRT-PCR of whole embryos (Fig. 62I). Focussing on the head, *nkx2.2*, a direct target of high-level Shh signalling, was downregulated in *bbs8* morphants, as was *ptc1* (Fig. 62J-M). The neural tube, revealed by *nkx2.2 in situ* hybridisation, was kinked in *bbs8* morphants. This was reminiscent of mutants with defects in the PCP pathway (Fig. 62N and O).

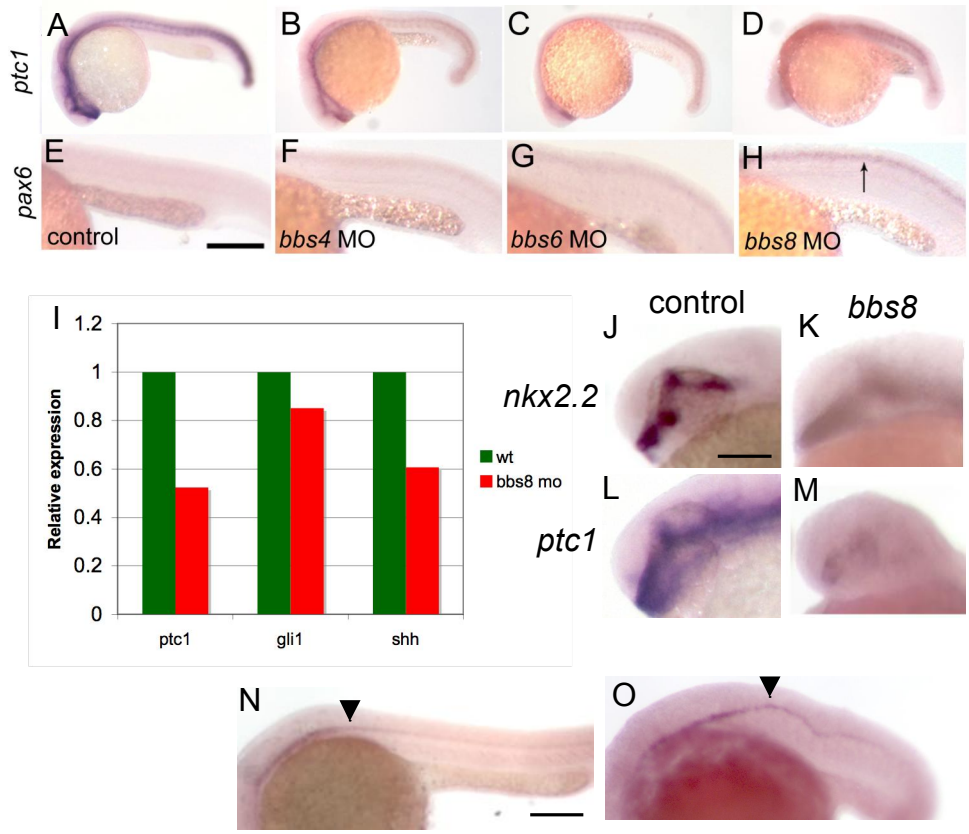

Figure 62. Expression of Shh target genes in morphant zebrafish.

A-D: expression of *ptc1*, a direct target of the Shh pathway, was downregulated in *bbs4*, *bbs6*, and *bbs8* morphants. **E-F**: expression of *pax6* in these morphants; it was distinctly upregulated in the *bbs8* morphant neural tube (arrow). **I**: qRT-PCR analysis showing downregulation of three downstream Shh pathway targets in *bbs8* morphants. **J-M**: downregulation of expression of both *nkx2.2* and *ptc1* in the heads of *bbs8* morphants. **N,O**: kinking of the neural tube (arrowhead in O) in *bbs8* morphants relative to controls (arrowhead in N). Scale bars: A-H = 500μm; J-M = 100μm; N,O = 200μm.

I next examined the expression of *nkx6.1*, a gene expressed in the middle of the neural tube, in between the ventral domain responsive to high-level Shh signalling, and the dorsal domain, whose patterning genes are inhibited by Shh. As such, *nkx6.1*, like *pax7*, represents a gene that is responsive to low levels of Shh signalling. Expression of *nkx6.1* in morphants was not obviously different between control and morphant embryos (Figure 63). This suggests that genes not reliant on high-levels of Shh transduction are unaffected by loss of Bbs8.

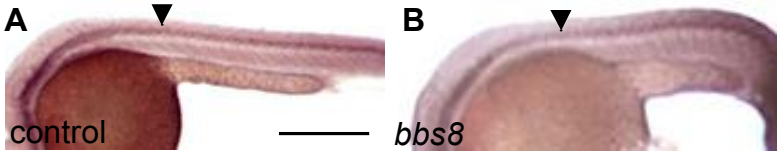

Figure 63. Expression of *nkx6.1* in morphants.

Expression of *nkx6.1* was comparable in control (A) and morphant (B) neural tubes (arrowheads). Scale bar = 500μm.

Epistasis analysis to determine the point at which Bbs8 intersects the pathway

To try to examine the point at which Bbs8 was interacting with the Shh pathway, I performed some epistasis experiments. As mentioned earlier, Ptc1 negatively regulates Shh signalling, and so knockdown of *ptc1* causes induction of the pathway. I injected *ptc1* MO either alone or in combination with *bbs8* MO. When 1ng *ptc1* MO was injected, it caused induction of *ptc1* expression due to upregulation of the Shh pathway and consequential activation of *ptc1* transcription (Fig. 64A). Co-injection with the *bbs8* MO restored the expression level of *ptc1* to the control level, but not to the low level seen in *bbs8* morphants alone (Fig. 64B). This suggested that Bbs8 was functioning downstream of Ptc1 in the pathway but was not absolutely required for signalling to take place, due to the intermediate expression level of *ptc1* after induction of the pathway.

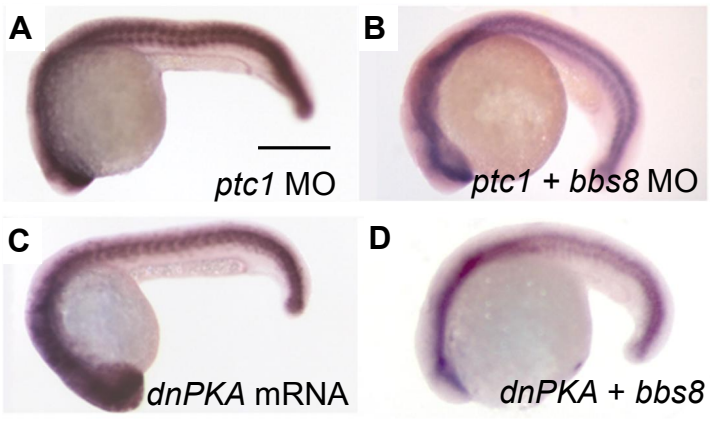

Figure 64. Epistasis experiments to determine the level of Bbs8 activity.

A: injection of *ptc1* MO induces the Shh pathway seen by increased amount of *ptc1* mRNA. **B**: co-injection with *bbs8* MO partially rescues this pathway induction. **C**: injection of *dnPKA* mRNA also induces the Shh pathway by preventing cleavage of

Gli3A into Gli3R. **D**: co-injection with *bbs8* MO is also able to rescue the dnPKA-mediated pathway induction. Scale bar = 500μm.

I next modulated the downstream end of the pathway at the point at which Gli3 is processed. Protein Kinase A (PKA) negatively regulates the Shh pathway by phosphorylating components of the pathway that targets Gli3 for proteosomal degradation into its repressive form. I injected the mRNA of a dominant negative form of PKA (dnPKA). Injection of 100ng of this RNA caused ectopic induction of the Shh pathway, manifested by ubiquitous, high-level expression of *ptc1* (Fig. 64C). Co-injection of *bbs8* MO was, again, able to partially rescue this induction (Fig. 64D). This suggests that *bbs8* is functioning at or downstream of the level of Gli3 proteolytic processing. While the precise mechanism is unclear, there is good evidence that IFT is essential for proper processing of Gli3. It is likely that Bbs8 is intersecting the Shh pathway at the level of Gli3 transport. This is also consistent with the co-IP data.

ift80 knock-downs also show signs of Sonic Hedgehog signalling defects

Because Bbs8 is an IFT-associated protein that perturbs the Shh signalling pathway, I decided to perform some of the same assays on Ift80 null models. This was because patients with Jeune Syndrome show some of the same Shh-related phenotypes as BBS, and given IFT80's central role in IFT, known to be key in regulating Shh transduction.

Firstly, I performed the Gli3 processing assay on 3T3 cells stably transfected with an shRNA construct suppressing *Ift80* expression. The cells showed the same indifference to stimulation by purmorphamine as did the *Bbs8* suppressants. This implied that the defect in Gli3 processing reported for other *bona fide* IFT proteins, such as IFT88, IFT172, and IFT57, also applied to IFT80, and most likely to IFT proteins in general.

I next performed wholemount *in situ* hybridisation for *ptc1* expression in *ift80* morphant zebrafish embryos. As with *bbs8* morphants, *ptc1* was expressed at

lower level throughout the body, particularly in the head (Fig. 65A,B). To confirm this, I extracted RNA from control and morphant embryos and performed quantitative RT-PCR to measure the amount of *ptc1* mRNA. In morphant embryos, it was expressed at 43% of the control level. The same epistasis experiment involving co-injection with a *ptc1* MO also showed that *ift80* lies downstream of Ptc1 in the pathway, as it was able to rescue the induction of the pathway (Fig. 65C,D).

The Gli3 processing assay showed a similar defect to Bbs8 suppression in response to Shh stimulation. The ratio of Gli3A to Gli3R did not increase in *ift80* knockdown cells as it did in controls (around 4-fold) (Fig. 65E,F).

I then prepared flatmounts of the neurocranial cartilage from controls and *ift80* morphants at 5dpf. These demonstrated midline fusion of the trabeculae, again reminiscent of the Sonic Hedgehog pathway mutants, or early cyclopamine treated embryos (Fig. 66). The branchial arches and mandibles were present in *ift80* morphants and the degree of hypoplasia of the chondrocranial cartilages was much less than the *bbs8* morphants.

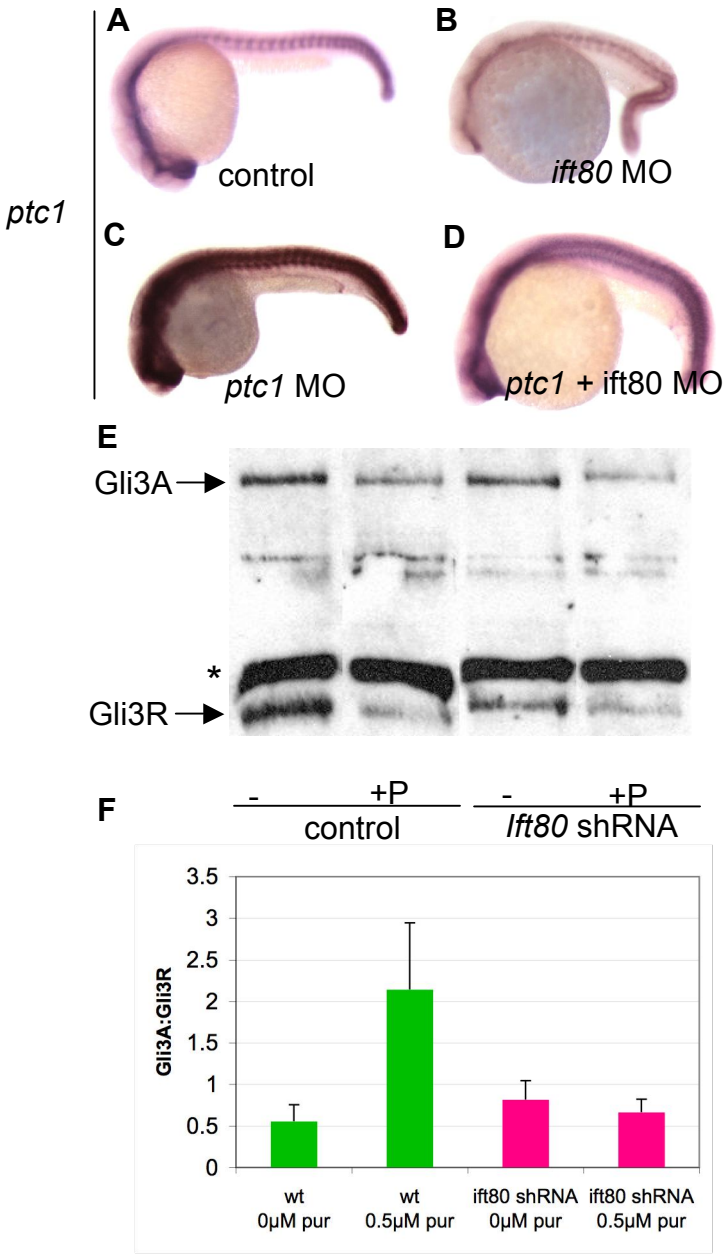

Figure 65. Shh pathway activity in response to *ift80* depletion.

A,**B**: *ptc1* expression is reduced in *ift80* morphants. **C,D**: co-injection of *ift80* MO with *ptc1* MO rescues the induction of the pathway brought about by suppression of *ptc1*, suggesting *ift80* lies downstream of *ptc1* in the Shh pathway. **E,F**: addition of purmorphamine to *Ift80* suppressant cells fails to induce the pathway by preventing Gli3 cleavage as it does in controls. Asterisk represents non-specific band detected by the anti-Gli3 antibody. Scale bar = 500μm.

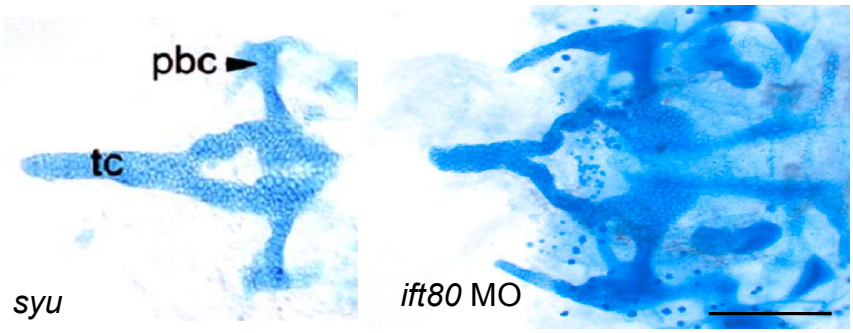

Figure 66. The chondrocranium of *ift80* morphants.

Midline fusion of the trabeculae in *ift80* morphants (right) is reminiscent of *syu* mutant embryos (left). Scale bar = 500μm.

Although I did not check with specific NCC markers, the *ift80* morphants showed no signs of aberrant NCC migration, such as depigmentation. Despite a severe convergent-extension phenotype and the hypoplasia of the cranial cartilages, the pigmentation was entirely normal. This implies that the midline fusion of the trabeculae is due to a faulty response to Shh signalling, whilst the mandibular and branchial hypoplasia is largely a result of inhibited NCC migration.

Investigating a possible role for *ift80* in Indian Hedgehog signalling

Indian Hedgehog (Ihh) is a homologue of Shh which functions as a ligand that binds to patched in a similar manner to Shh, albeit with different kinetics, due to different post-translational cholesterol modification. Ihh is important for bone development by encouraging the proliferation of chondrocytes in the growth plate of developing bones. JATD patients' most prominent and fatal feature is the failure of bones to grow properly, resulting in a small rib cage that causes asphyxiation.

Considering the importance of IFT in Shh signalling, the role of the ciliopathy protein Bbs8 in Shh signalling, the necessity for Ihh signalling in bone growth and the similarity between Ihh and Shh transduction, I tried to discover if Ihh signalling was affected in *ift80* morphants.

Firstly, I performed wholemount *in situ* hybridisation for *ihha*, one of two *ihh* paralogues in zebrafish, on 5dpf embryos. It should be expressed in the developing cartilaginous elements of the face and fin buds. The probe failed to yield a distinct signal, possibly because *ihh* expression was obscured by overlying tissue in the head.

Because there is almost no literature on Ihh signalling in the zebrafish, save for one paper describing its expression pattern in chondrocytes of the jaw, I designed a MO to investigate the effects of its knockdown on embryonic development. At 24hpf, morphants were indistinguishable from controls, showing that the MO caused no toxicity. Also, *ptc1* expression was indistinguishable from controls, in keeping with the fact that Ihh is involved specifically with cartilage development, a later-onset process (Fig. 67A). By 5dpf, morphants almost completely lacked any cartilage in the head, despite the rest of the body looking morphologically normal (Fig. 67B,C). This suggests a conserved and very specific role for Ihh in the zebrafish, and suggests that the critical role of Ihh during bone development in fish and mammals is conserved. This model should enable study of the mechanisms of Ihh signalling further.

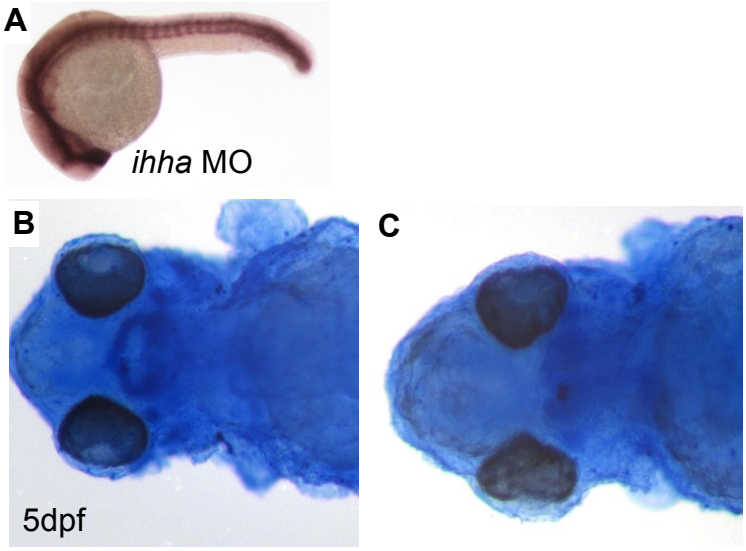

Figure 67. *Indian hedgehog* knockdown phenotype.

A: knockdown of *ihha* has no phenotype at 24hpf and *ptc1* is normally expressed. **B** and **C**: alcian blue stained 5dpf embryos injected with 4ng *ihha* MO showed a massive reduction in cranial and fin cartilage. Only a rudimentary ANC was retained.

Discussion

The first demonstration that Shh signalling is defective in Bbs and JATD patients

Numerous IFT proteins (IFT52, IFT57, IFT88, IFT172) have been implicated in Shh signal transduction. Several ciliopathies show gross features that one typically sees when components of the Shh pathway are mutated, such as polydactyly, agenesis of the corpus callosum, single central incisor (rare), midface defects, and genital anomalies. Zebrafish *bbs8* morphants show clear Shh-like phenotypes: synophthalmia, midline fusion of the trabeculae, and U-shaped somites. This is the first time it has been demonstrated that Shh signalling is perturbed in ciliopathy models.

The results showed that Bbs8 and Ift80 both had significant effects on the pathway and likely acted downstream of Patched at the level of Gli3 processing and transport. It is possible that Bbs8 is important for shuttling Gli3A and Gli3R to the nucleus where they activate their transcriptional targets. Cells deficient in Bbs8 are less responsive when stimulated with exogenous Shh protein or Smo agonist than control cells. The likely meaning of this is a failure to process the Gli3 transcription factor. In epistasis experiments in the zebrafish, *bbs8* MO was able to rescue induction of the pathway induced by *ptc1* knockdown and partially rescue the phenotype caused by PKA inactivation. Because the pathway is so complex, it is difficult to produce an exact pinpoint of where Bbs8 functions in the pathway. To do this, one would have to perform proteomic assays on cells unstimulated and stimulated with different concentrations of purmorphamine to see with which proteins Bbs8 interacts.

Another useful experiment would be to perform real time imaging of Shh transduction at the cilium. To do this, cilia of control and *Bbs8* suppressant cells with long cilia (such as MDCK) would be labelled with fluorescently tagged acetylated tubulin (or other ciliary marker such as Polaris). I performed some feasibility studies on MDCK to show that they respond well to Shh signalling, and also created a line stably expressing shRNA against *Bbs8*. GFP-tagged Smo or

Gli3 would be transfected into the cells. A time-lapse movie would be recorded after photobleaching a portion of the cilium to visualise the movements of Shh pathway components in response to stimulation with Purmorphamine. This would enable real-time monitoring of the behaviour of Shh pathway components in the absence of Bbs8. This could be extended for other ciliary and IFT proteins to dissect the roles of each ciliary protein in Shh signalling.

A proposed model for the role of Bbs and IFT proteins in Shh signalling

From these experiments, it is clear that Bbs8 and Ift80 are not essential for Shh signalling, although Ift80 may be more important, particularly for Ihh transduction. Immunoprecipitations showed some evidence for a possible weak interaction between the C-terminus of Bbs8 (which bears the TPR motifs) and Gli3. Further experiments will have to be performed to validate this result convincingly. These could include: GST-pulldown experiments with GST-tagged Gli3 or BBS8 proteins, yeast 2-hybrid interactions, and FRET between BBS8 and GLI3 reporter proteins. This suggests that Bbs8 might have an accessory role in transporting Gli3 between the cilium and the cytoplasm. It is conceivable that Bbs8 aids in the transport of Gli3 along the cilium towards the nucleus. This is highly speculative and, at present, the molecular-scale function of IFT proteins in Shh transduction is completely unknown. Proteomic analysis will be useful in understanding this. A simple method of doing this might be to perform pairwise yeast-two hybrid interaction assays for proteins such as Bbs8 with each key protein in the Shh pathway, and then test these interactions in cell culture and then by FRET (fluorescent resonance energy transfer).

The functions of Shh and Ihh overlap and the downstream signalling components are shared. If a protein important for Shh transduction is expressed in the Ihh signalling domain, it is likely to perturb Ihh signalling and cause bone growth defects, as Ift80 does. Defining the precise spatial expression pattern of *Ift80* will be important in determining its potential role in Ihh signalling, and whether Ihh and Shh have different reliance on the cilium. Also, Bbs8, which is highly

expressed in the testis, might mediate Desert hedgehog (Dhh) signalling, which is expressed exclusively in the testis, where it is essential for male germline development (Bitgood et al., 1996). This raises the possibility that Bbs proteins might be important in testis development, as hypogonadism (small and undescended testes) is highly penetrant in the BBS cohort.

Possible cross-talk between the Shh and Wnt signalling pathways at the cilium

Several high-profile papers have linked Shh and Wnt signalling. Alvarez-Medina et al showed that Gli3 expression is controlled by Wnt activity, likely by Tcf binding sites surrounding human GLI3 (Alvarez-Medina et al., 2008). They also showed that Gli3R transcriptional repression in the dorsal neural tube restricted graded Shh signalling to the ventral neural tube. Lei et al showed that *Nkx2.2*, a ventrally expressed gene responsive to high-level Shh signalling, is repressed by Tcf (Lei et al., 2006). They showed that canonical Wnt signalling opposes positively regulated Shh gene targets to spatially restrict downstream genes to discrete domains. Ulloa et al found that Gli3R inhibited canonical Wnt activity and showed a physical interaction between the C-terminus of Gli3R and β-catenin (Ulloa et al., 2007). Furthermore, Glis2 (Gli-like 2) interacts with p120 catenin, a transcriptional regulator of canonical Wnt signalling (Hosking et al., 2007). *GLIS2* mutations have been found to cause NPHP in humans, linking Shh and Wnt signalling to the primary cilium in ciliopathies.

The importance of the cilium as a nexus for signalling was also highlighted by Park et al, who showed that it mediated both non-canonical Wnt and Shh pathways concurrently. Clearly, more work is needed in elaborating the precise roles for individual ciliary proteins in the control of these pathways.

A model for craniofacial dysmorphology in BBS morphants

Shh is not necessary for NCC migration *per se*. However, Shh derived from the oral ectoderm in the head patterns the migrating CNCCs and keeps the two

streams migrating to form the two trabeculae and also separates the eyes. This is why Shh signalling defects cause midline fusion of the trabeculae and cyclopia. Evidence for this came from the fact that inhibiting Shh signalling in embryos by administration of cyclopamine to *sox10::eGFP* embryos between 4 and 24hpf did not affect NCC migration but clearly resulted in cyclopia and midline craniofacial patterning defects. Meanwhile, it is known that PCP is essential for early migration of the CNCCs into the head. We also know that both pathways are perturbed when *bbs8* is suppressed.

I propose a model to account for the craniofacial dysmorphology in BBS whereby disrupted PCP signalling slows migration of CNCCs, which populate the face, leading to hypoplasia (Figure 68). Because these cells have a dulled response to Shh ligand, when they arrive in the head they are mispatterned about the midline. In the *bbs8* morphants, the CNCC streams fail to separate at the midline. This happens in a minority of BBS patients, who lack a corpus callosum and have a single central incisor. The ENS is also patterned by Shh, and *Shh* mutant mice lack an ENS. It is possible that the same phenomenon is contributing to aganglionosis in BBS.

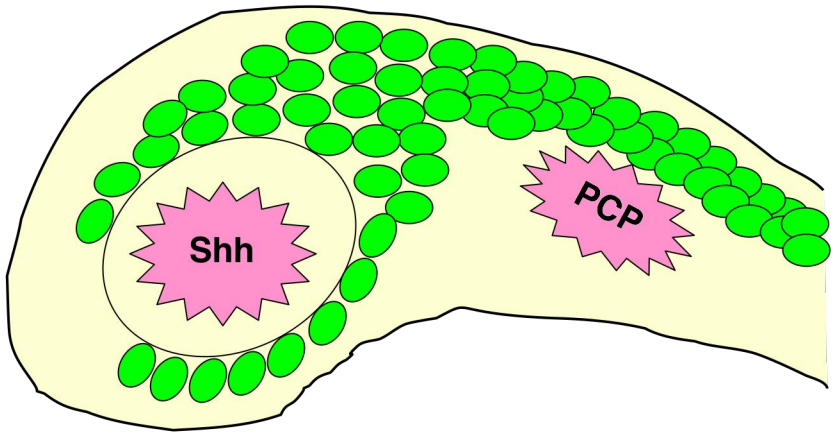

Figure 68. Model describing craniofacial perturbation in BBS.

With *Bbs8* knockdown, early CNCC migration into the head is inhibited or retarded by reduced PCP signalling. When cells finally reach the head they fail to respond properly to Shh ligand secreted from the oral ectoderm and rostral neural tube. This leads to midline patterning defects in the fish reminiscent of Shh mutants, and features concordant with subtle HPE in humans.

Chapter 6: Restoration of renal function in zebrafish models of ciliopathies

Introduction

Renal disease is a common denominator in ciliopathies

All of the nine diseases currently considered "ciliopathies": BBS, MKS, JBTS, ALMS, OFD1, SL, NPHP, and JATD, share renal disease in common. While other phenotypes are hallmarks of ciliopathies, such as polydactyly, brain abnormalities, and *situs inversus*, these are not represented amongst every single ciliopathy. In addition, it is the renal component that is the commonest cause of death from ciliopathies such as BBS and NPHP. Therefore, it is important to develop models to understand the progression of this disease and develop therapeutics.

In general, ciliopathy patients' renal disease involves cystic kidneys, but it is more complex than this in reality, and the different ciliopathies present differential renal pathology. In BBS, O'Dea et al found that, in a Newfoundland cohort of 38 patients, 96% had fetal lobulation, clubbing, or calyceal cysts (which form in the inner region of the kidney in the region just before the urine enters the renal pelvis) (O'Dea et al., 1996). These authors also reported that 70% (n=20) of BBS patients were unable to produce concentrated urine, even after vasopressin treatment. Alton and Macdonald reported that 30% of BBS patients die from uraemia, the condition caused by kidney failure when urea and other toxic waste enters the blood stream and leads to coma and death (Alton and McDonald, 1973). This fate can only be offset by chronic renal dialysis or transplantation. Due to a greater susceptibility to infection, many BBS transplantees become septic or reject their transplant.

In NPHP the renal involvement can be more severe and results in death between 4 and 15 years of age (Fanconi et al., 1951). Many patients develop medullary cysts, and interstitial lymphohistiocytic cell infiltration is common. Later on,

these features develop into sclerosing tubulointerstitial nephropathy, which is what causes kidney failure. Senior-Loken syndrome, described as NPHP with the addition of retinitis pigmentosa, manifests similar cystic and dysplastic kidneys.

Meckel syndrome results in massively enlarged cystic kidneys, which cause distension of the abdomen in the fetuses that bear them. Polycystic kidneys are also observed in OFD1 patients. Biopsy of ALMS patients showed mesangial cell (basement membrane cells surrounding the glomerular blood vessels) proliferation (Ozgül et al., 2007). In summary, cystic kidneys are the most common cause of renal disease, but also present are renal dysplasia, sclerosis, fibrosis, lobulation, and divertiula.

Current theories explaining cyst formation

Most of what we know about cyst formation comes from studies of polycystic kidney disease (PKD), of which there are two types. Autosomal dominant (ADPKD), which is adult onset, occurs at a frequency of 1 in 1,000, and causes fluid-filled cysts. Autosomal recessive (ARPKD), which is juvenile onset, is less common at 1 in 20,000, and is more serious, frequently leading to infant mortality.

The formation of cysts in both types of PKD is thought to arise by the same mechanism, involving increased proliferation and apoptosis in renal epithelial cells, loss of epithelial cell polarity, dysregulation of cell/ECM interactions, and transformation from an absorptive epithelial cell phenotype to a secretory phenotype. Cysts then separate from their tubule of origin once they have grown over 200μm in diameter and begin to fill with fluid, as chloride channels pump chloride into the cystic lumen, lowering the osmotic potential and causing water to enter via aquaporins.

The proteins that cause PKD, Polycystins 1 and 2 (PC1 and 2) in the case of ADPKD, and fibrocystin for ARPKD, localise to the primary cilium, leading some to call PKD a “ciliopathy”. Cilia on the tubular epithelium project into the

lumen where they act as mechanical flow sensors, bending in response to urine flow through the tubule (Yoder et al., 1998). This triggers an influx of Ca^{2+} into the ciliary membrane, mediated by PC1 and 2. This calcium flux is intrinsically linked to cell cycle regulation via the cilium and the ciliopathy proteins. It is thought that the transcription factor STAT6 dissociates from its binding to PC1 when the cilium is sheered by fluid flow, whereupon STAT6 translocates to the nucleus and activates downstream targets associated with cell proliferation (Low et al., 2006). This is summarised in Figure 69.

Another role for the cilium in regulating kidney development comes from the discovery that the cilium acts as a switch between the canonical and non-canonical/PCP Wnt signalling pathways. The β-catenin-dependent canonical Wnt pathway is associated with cell proliferation and is important for the branching morphogenesis associated with embryonic kidney development. Transgenic overexpression of β-catenin in mouse kidneys caused cystogenesis (Saadi-Kheddouci et al., 2001). Inversin, a ciliary protein, targets cytoplasmic Disheveled for degradation, thereby inhibiting the canonical Wnt pathway. Therefore, knockdown of Inversin, for example in NPHP2 patients, causes unopposed activity of the Wnt pathway leading to overproliferation in the kidney. This is also the case in both mouse and zebrafish *Inversin* knockdown models (Simons et al., 2005).

The PCP signaling pathway, known to be disrupted in BBS mutants, is essential for asymmetrical distribution of the cytoskeleton, thereby modulating cell polarity. If the molecular "switch" model is correct, an excess of the canonical Wnt pathway results in a downregulation of the PCP pathway at its expense (Simons et al., 2005). This is true in BBS where the canonical Wnt pathway is known to be hyperactivated, and the PCP pathway downregulated.

PCP signaling is known to control the orientation of the mitotic spindle (Gong et al., 2004). During tubular development, cell proliferation lengthens the tubules without widening their bore. As such, the spindle axis of dividing tubular cells aligns with the tubular axis (Fischer et al., 2006). In the rodent model of PKD,

pcy (*Pkhd1* mutant), the mitotic spindles are misorientated, even before the onset of cyst formation. This suggests that any subsequent cell divisions will not be parallel to the tubule, resulting in an increased girth of the tubule. Mispolarised cell division will lead to disordered growth in the tubule and cystic enlargement.

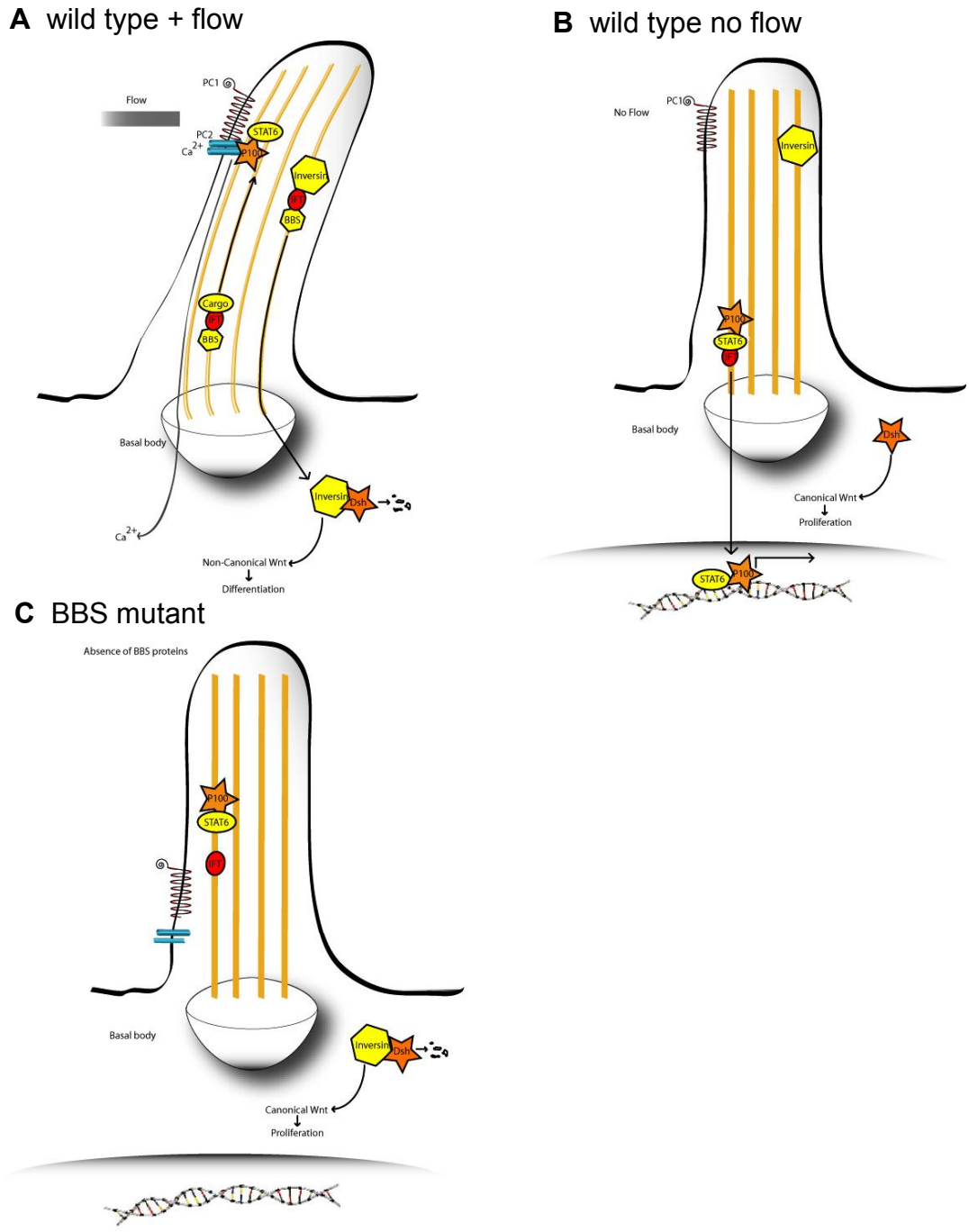

Figure 69. Signalling at the cilium in the kidney.

A: Urine flow through the kidney tubule causes an influx of Ca^{2+} ions through polycystin 2 (*PC2*), while polycystin 1 (*PC1*) anchors the transcriptional complex of P100 and STAT6 in the cilium. Concurrently, inversin is translocated to the nucleus, where it

targets cytoplasmic Disheveled for destruction, activating the non-canonical pathway and causing cells to differentiate. The ciliary localisation of PC1/2 and inversin may be dependent on BBS proteins. **B**: Absence of urine flow reduces Ca^{2+} influx and causes release of P100 and STAT6, allowing them to enter the nucleus to activate transcription. It also prevents translocation of inversin to the cytoplasm, maintaining the cytoplasmic pool of Disheveled, which activates the canonical Wnt pathway and causes proliferation. **C**: A lack of BBS protein function may inhibit proper transport of PC1/2 to the distal tip of the cilium and also prevent translocation of inversin to the cytoplasm. This would cause inappropriate activation of STAT6 target and maintenance of cytoplasmic Disheveled, leading to unregulated cell proliferation. Additionally, lack of BBS protein function could disturb planar cell polarity (PCP). The combination of disorganised cell polarity and cell division could cause the various abnormalities seen in BBS. Taken from (Tobin and Beales, 2007)

At present, the precise mechanism by which PCP regulates the orientation of the spindle is not known. However, PCP signaling relies on ciliary function and the basal body at the proximal end of the cilium, together with the second centriole, produces the microtubule spindle during mitosis after resorption of the cilium. The orientation of the cell is controlled by the alignment of the actin cytoskeleton, which is modeled by Rho, Rac, and cdc42, which are, in turn, regulated by PCP signaling. As such, it can be hypothesized that absence of ciliopathy proteins is affecting downstream PCP signaling, which, in turn, affects the polarity of the cell and subsequently the centrioles do not align along the axis of the cell.

Current therapies for cystic kidney disease

ADPKD is one of the most common genetic diseases, with an incidence of around 1 in 1,000. The onset of the disease is much later than ARPKD, with a median of around 15 years (Zerres et al., 1993). Cysts grow progressively larger and kidney mass has been reported to reach up to 20kg (Germino and Somlo, 1993). As such, therapies to slow the development of the cysts prolong symptom-free status, as the health only becomes compromised when the cysts impair the filtering capacity of the kidney. This results in end stage renal failure (ESRF) in approximately 50% of patients with ADPKD.

Currently there is no treatment for PKD, there are only drugs that slow cyst development, with some promising molecules in preclinical development in the mouse, but no compounds have entered the market to treat humans yet. Present

treatment involves a low protein diet to offset renal failure. Current advances in understanding the mechanism of cystogenesis will inform drug discovery strategies. Several important mouse models are being used as PKD models: the *orpk* mouse (Oak Ridge PKD) is a *polaris* mutant which encodes IFT88; the *inv* mouse in which *Nphp2* is mutated; and conditional knock-out of *Kif3a* in the kidney causes cysts.

Current pathways targeted for therapy include the Ras pathway, a mitogenic signalling pathway upregulated in PKD. Ras signals via Raf to translocate the MAP kinase ERK to the nucleus, whereupon it phosphorylates transcription factors associated with cell division. Another pathway involved in cyst progression is the G-protein coupled receptor (GPCR) pathway where cAMP activates Raf kinase activity to drive cell proliferation. Therefore, cAMP inhibitors are another option for therapy.

This table summarises the drugs which have been shown to work in rodent models of PKD adapted from (Torres, 2004):

Treatment	**Mode of action**	**Model used**
Acetazolomide	Carbonic anhydrase inhibitor; diuretic	Han:SPRD rat (PKD model). Did not work in PCK rat
Amiloride	Diuretic	Han:SPRD rat. Did not work on PCK rat
Batimastat	Matrix metalloprotease inhibitor, anti-cancer drug	Han:SPRD rat
c-myc antisense	Prevents excess cell division	*Cpk mouse*
c-Src inhibitor	Prevents excess cell division	*Bpk* mouse (ARPKD model)
EGFR inhibitor	Inhibits receptor for epidermal growth factor	Han:SPRD rat
Lovastatin	HMG-CoA reductase, lowers cholesterol level	HAN:SPRD rat
Methylprednisolone	Corticosteroid, blocks inflammation	Han:SPRD rat and *pcy* mouse
Paclitaxel	Stabilises microtubules to prevent cell division. Used in cancer chemotherapy	*Cpk* mouse (ARPKD model). Did not work on *pcy* (*Nphp3*) mouse, *orpk* mouse, or Han:SPRD rat.
Rapamycin	Inhibits mTOR, antiproliferative compound	*Bpk* and *orpk* mice
Roscovitine	CDK-inhibitor; prevents cell division	*Jck* (*Nek8*) and *cpk* mouse
V2R antagonist	Vasopressin receptor antagonist	PCK rat, *cpk*, *pcy*, *Pkd2* mice

Table 11. Drugs previously used on rodent models of polycystic kidney disease.

Of these drugs, only Rapamycin (also called Sirolimus) has entered clinical trials in humans (Serra et al., 2007). In mouse models, Rapamycin caused apoptosis and shedding of cystic cells, reducing the size of the kidneys from 16% of total body weight to 4%, compared to 0.7% in wild types (Shillingford et al., 2006). This had the effect of completely restoring renal function, as measured by the concentration of blood urea nitrogen. These authors suggested that inappropriate activation of mTOR is common to all forms of cystic kidney disease, because addition of Rapamycin ameliorates cysts in several different mouse models. Furthermore, because Rapamycin alone rescued the kidney phenotype, they asserted that the mTOR pathway was the predominant cause of cystogenesis in all PKD models.

mTOR is a kinase that controls cell proliferation. It is regulated upstream by two centrosomal proteins, TSC1 and TSC2, whose genes, when mutated, cause renal cysts. mTOR also interacts with the cytoplasmic tail of PC1 and so functions, at least in part, at the cilium. Because Rapamycin specifically interferes with signalling at the cilium to restore diseased kidneys, and given its proven function in a range of polycystic kidney models involving ciliary gene mutations, it is a valid candidate to test on ciliopathy models.

Bukanov et al (2006) reasoned that because cilia function in cell cycle regulation, and this is disrupted in PKD, this would be the most proximal target for preventing cyst growth (Bukanov et al., 2006). Roscovitine is a cell cycle inhibitor that acts by binding to cyclin dependent kinases (CDK), and is currently in clinical trials to treat cancer. They showed that administration of Roscovitine to *jck* mice reduced the kidney to bodyweight ratio from 9% to 4%, while blood urea nitrogen was also lowered. Bukanov et al also showed that administration of 150mg per kilogram bodyweight for 3 weeks, followed by 2 weeks off treatment was sufficient to reduce cyst size. This shows that Roscovitine has long lasting effects, and daily administration is not required.

Bukanov et al also showed Roscovitine to be effective on the more aggressive ARPKD mouse model, *cpk*. Roscovitine reduced the kidney to bodyweight ratio from 25% to about 18% and reduced cystic volume by around 25%. Therefore, Roscovitine is not as effective at treating very severe disease, and Rapamycin may be more effective.

Bukanov et al showed an increase in proliferating cells lining the tubule of human and *jck* mouse kidneys, which was reduced by Roscovitine treatment. They attributed this excessive activation to upregulation of the Ras/Raf/ERK pathway, which was demonstrated by upregulated components of the pathway, such as Erk2, by Western blot. They also showed that Cdk7 and 9 were upregulated, which were the likely targets of Roscovitine. These Cdks activate RNA polymerase II to drive transcription and cell division. Roscovitine simultaneously reduces the amount of apoptosis in the *jck* kidney. The relevance of this model is that *jck* contains a mutation in *Nek8*, a gene mutated in the ciliopathy NPHP, and whose protein functions at the cilium and interacts with PC1 and 2 (Sohara et al., 2008).

Because Roscovitine and Rapamycin have been shown to work on specific ciliary models of PKD, and have well characterised modes of action with appropriate targets, they are likely to be useful candidate drugs for testing on ciliopathy models for potential use in humans. Because ciliopathies are so rare, it is not economically viable for pharmaceutical companies to develop orphan drugs, nor perform clinical trials for them. However, because the mode of cystogenesis is likely to be similar to that of the more common PKD models tested, these drugs can be trialled as candidates for ciliopathy treatments such as BBS, NPHP, and OFD1.

Because of the time taken to breed mice, section them, and analyse the kidneys, plus the requirement for genetic models, I have been exploring the utility of the zebrafish in screening drug candidates for ciliopathic renal disease.

Kidney development in the zebrafish

Despite its small size, rapid development, and relative anatomical simplicity, the zebrafish kidney functions in almost exactly the same way to the mammalian one. The main difference is that while the adult human kidney comprises some one million nephrons, the embryonic zebrafish pronephros contains just two.

Two glomeruli are fused at the midline just ventral to the aorta from which the blood is filtered. These glomeruli are anatomically similar to mammals, containing fenestrated epithelial cells and podocytes for ultrafiltration, and polarised epithelial cells. Two pronephric tubules connect the glomeruli to the pronephric ducts, which run caudally and fuse before connecting to the cloaca, which secretes waste to the outside world (Figure 70). Despite the anatomical similarity with mammals, the zebrafish pronephros is primarily for osmoregulation, rather than excretion, as the animal contains salty blood but lives in a fresh water environment. Disruption to kidney function causes oedema, as animals fail to expel water, so become oedematous, and die.

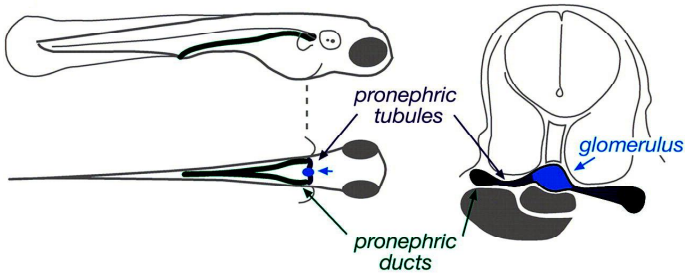

Figure 70. Kidney development in the zebrafish.

Two pronephric tubules link the midline glomerulus, which overlies the dorsal aorta, with the lateral paired pronephric ducts. The zebrafish glomerulus functions in a manner similar to the mammalian kidney and so is a good model for kidney development and function. From (Drummond, 2005).

Pronephric development begins at around 24hpf, when mesodermal fibroblasts form a polarised epithelial tube to produce the pronephric duct, homologous to the collecting duct of the mammalian kidney. The glomerular primordia and ducts then fuse and blood vessels invade the podocytes to form a functional glomerulus. This process is complete and functional by about 40hpf (for review, see Drummond, 2005). Kidney function can be assessed by injection of fluorescent

tracer dyes into the systemic circulation of the animal. The presence of fluorescent endosomes in the cytoplasm of pronephric duct cells shows that the dye has passed through the glomerulus into the duct.

Modelling cystogenesis in the zebrafish

The zebrafish is a good model for studying cystic kidneys, because the presence of a large bubble-like cyst can easily be seen from outside the animal from 3dpf. Drummond et al (1998) took advantage of this to perform a large-scale mutagenesis screen in which they identified 15 separate mutants with pronephric cysts. 12 of these mutants also had a curved body axis and presented the most rapid and severe cyst development. Sun et al (2004) performed a separate screen using retroviral mutagenesis and identified 10 more cystic mutants (Sun et al., 2004). They then cloned these genes and found 4 of the 10 to encode IFT proteins.

Zebrafish ciliopathy models that show cystic kidneys have been produced in the past. Liu et al (2002) knocked down *nek8* with MO and found kidney cysts (Liu et al., 2002). *Nek8* is mutated in the mouse model *jck* and was later found to be a causative gene of NPHP. Knockdown of *polycystin 2* in zebrafish also causes cysts. This table summarises all the mutants and morphants, published to date, with renal cysts. Ciliary genes are marked in bold.

Gene	Phenotype	Reference
Mutants		
Double bubble, *bazuka joe*, *dizzy*, *junior*, *mr bubble*, *blow-up*, *fusion*, *bubbleicious*, *big league chew*, *hubba bubba*, *inflated*	Pronephric cyst, down-curved body axis	(Drummond et al., 1998)
Fleer, *elipsa*	As above with eye degeneration	
Pao pao tang, *cyster*	Cyst	
Vhnf1	Pronephric cyst, gut and hindbrain abnormalities	(Sun and Hopkins, 2001)
Locke	Cyst, axis asymmetry, axis curvature	(Sullivan-Brown et al., 2008)
Scorpion, pontin, qilin, seahorse, pkd2	Cyst	
Ift57, ***ift81***, ***ift172***	Cyst	(Sun et al., 2004)
Plce1	Cyst	(Hinkes et al., 2006)
Morphants		
Nek8	Pronephric cyst, down curved body axis	(Liu et al., 2002)
Inversin	Cyst, body curvature and asymmetry	(Simons et al., 2005)
Nphp6	Cyst	(Sayer et al., 2006)
Arhgef11	Cyst, mispolarised epithelium	(Panizzi et al., 2007)
Wt1a and *wt1b*	Cyst	(Perner et al., 2007)
Lrrc50	Cyst	(van Rooijen et al., 2008)
Ift80	Cyst, down curved body	(Beales et al., 2007)

Table 12. Zebrafish mutants and morphants published to date with renal cysts. Many of these gene products are involved with the primary cilium.

At present, zebrafish models for three ciliopathy genes have been generated (*inversin* - NPHP2, *nek8* - NPHP8, *ift80* - JATD) and all show cystic kidneys. While the mechanism of cystogenesis in the mammal is generally accepted as being hyperproliferation, dysplasia, and mispolarity, it is much less clear in the zebrafish and several mechanisms have been proposed.

Kramer-Zucker et al showed that, unlike mammalian renal tubular cilia, zebrafish pronephric cilia are motile, beat with a frequency of about 20Hz, and drive a fluid current through the duct (Kramer-Zucker et al., 2005). They suggested that mutations in ciliary proteins result in reduced ciliary motility causing a back-up of fluid and increase in pressure which causes the cysts to form. They showed that a cyst could form in 30 minutes if the cloaca is obscured with forceps.

Sullivan-Brown et al (2007) examined the mechanism of cyst formation in a number of mutants. They found tubule dilation to onset as early as 48hpf, and excess cell proliferation in the tubule was a secondary effect of this. They also showed that, despite the three mutants tested having differing degrees of ciliary motility, the mechanism and extent of cyst progression was the same. This suggests that a motility defect is not the cause of cystogenesis.

Further confounding this body of work is a paper by Kishimoto et al (2008), who characterised the cystic mutant *seahorse*. They showed that *seahorse* is dispensable for ciliogenesis and motility, yet mutants still develop cysts. In *seahorse* mutants, Wnt signalling is ectopically induced at the expense of PCP signalling. Seahorse physically interacts with the DEP domain of Dishevelled, a region of the protein essential for membrane localisation and PCP signalling. Abrogation or mutation of critical residues of the DEP domain abolishes PCP signalling (Axelrod et al., 1998).

These data therefore suggests that increased canonical Wnt signalling could be responsible for cyst formation in this mutant. Because canonical Wnt signalling is known to be increased in ciliopathy knockdowns (*bbs1*, *bbs4*, *bbs6*, and *kif3a*) (Gerdes et al., 2007), this could be the route of cystogenesis in ciliopathy patients. The three studies outlined here present somewhat contradictory evidence of the mechanism of cyst formation in the zebrafish. As such, no clear conclusions can be drawn about the precise aetiology of the cysts, only that they are recapitulated in all ciliary knockdowns tested so far, and their morphology is consistent.

Use of the zebrafish in pharmacological screening

Given the penetrance of the cystic phenotype in ciliopathic zebrafish and the rapidity with which one can screen for the presence of the cyst, I examined the possibility of using the zebrafish to test compounds to restore renal structure and function. As well as being a useful vertebrate model for large-scale mutagenesis,

the zebrafish is emerging as a tool for screening drug compound libraries for efficacy.

In contrast to traditional drug discovery, where the target is known and bioassays are performed to identify a molecule that binds to it, zebrafish drug screening usually involves unknown targets. Rather, the desired phenotype is scored for. The advantage of this approach is that the full signalling mechanism does not need to be understood *a priori* to drug screening. As such, this is a perfect system in which to test drugs on zebrafish ciliopathy models, as there is much confusion and misunderstanding about the precise molecular mechanism of cystogenesis, but there is a clear and scoreable phenotype.

The utility of the zebrafish as a small molecule screening system was first identified by Peterson et al who used it to identify small molecule modulators of embryonic development (Peterson et al., 2000). They placed 3 wild-type embryos into each well of a 96 well plate with 200µl of water. 1,100 small molecules from a commercially available library were diluted in DMSO and fish water and robotically added to the embryo water at the 8-16 cell stage. Embryos were examined at 1, 2, and 3dpf. They identified molecules that specifically affected the development of the CNS, heart, pigmentation, ear, and otolith. This study provided proof of principle that it was feasible to perform high throughput studies on zebrafish embryos. Moon et al subsequently used the fish to successfully screen a library for microtubule polymerisation inhibitors (Moon et al., 2002).

Behra et al used the fish for a toxicological screen of several acetyl cholinesterase inhibitors (Behra et al., 2004). They used it to specifically identify one compound out of four that was active. Chan et al used zebrafish in a cancer model to test anti-angiogenic molecules and showed that a human VEGF-inhibitor also worked in zebrafish (Chan et al., 2002).

The use of transgenic zebrafish models coupled to robotic drug administration, high-throughput imaging systems and computer algorithms has enabled real *in vivo* high-throughput screening to take place in zebrafish. Peterson et al (2004)

screened 5,000 compounds and found two which suppressed the aortic blockage phenotype of the *hey2* mutant (*gridlock*) (Peterson et al., 2004). This mutant is a model for aortic coarctation, a common congenital defect in humans and so the identification of drugs in zebrafish is potentially of major clinical benefit.

Burns et al (2005) developed a transgenic zebrafish expressing GFP in the myocardium (Burns et al., 2005). They developed computer software to automatically identify individual fish hearts arrayed in a 96 well plate and count the heart rate. They then added compounds that slowed the heart rate and showed how the technique could rapidly generate dose-response curves for the effect of different concentrations of the drug on heart rate. This is the first time an automated technique has been used for phenotypic analysis of vertebrate organs.

Tran et al (2007) arrayed *fli1:gfp* transgenic zebrafish which express GFP in blood vessels in 384 well plates (Tran et al., 2007). They generated an algorithm to quantify the number of angiogenic blood vessels in the fish and used this to screen a 1,280-molecule library. From this they identified two molecules with known anti-angiogenic properties as well as a third novel compound. They then tested this new compound in an *in vitro* assay on human umbilical endothelial cells (HUVECs) and showed it be effective at inhibiting angiogenesis.

While screens in zebrafish are lower throughput than for cell lines, specific, physiologically relevant disease models can be tested, in which cell-cell and cell-matrix interactions are present. The scalability of the system for studying disease models may improve in the future. For instance, a fully robotic system for injecting morpholinos into embryos which can exceed the capacity of a human investigator has been reported (Wang et al., 2007).

In summary, while the use of zebrafish is not as high-throughput as isolated protein targets or cell lines, it is now possible to screen several thousand compounds, given an assay amenable to automation. It has benefits in that it is physiologically relevant and phenotypes can be readily scored. Disadvantages include different mechanisms of absorption, distribution, metabolism, and

excretion, making bioavailability and pharmacokinetic comparisons to humans difficult. However, the main advantage is that it is a cheaper, quicker, and more physiologically relevant technique for "pre-pre-clinical" drug discovery. Lead compounds can then be tested on a mouse model with more confidence of efficacy, while gaining knowledge of dosage and toxicity.

The aims of this study

Given the phenotypes of the plethora of non-ciliopathic and ciliopathic zebrafish models of renal cysts and the potential to perform drug compound screening on the zebrafish, I made the following aims:

1) To create zebrafish models of all the major ciliopathy syndromes: BBS, NPHP, SNLS, JBTS, MKS, OFD1, and JATD.
2) To examine the kidney morphology of these morphants
3) To try to determine some of the molecular mechanism behind the pathology and see if cellular proliferation was increased in the morphant kidneys.
4) To test known anti-cystic compounds on these morphants and develop a quantitative assay for morphological rescue.
5) To develop a functional assay to see if these compounds ameliorated renal function.

The ultimate aim of this project was to try to develop a physiologically relevant way of testing compounds known to work on common rodent models of ciliopathy (such as *orpk* and *jck*) on zebrafish ciliopathy morphants. Because only a few mouse models of ciliopathies exist (currently only for a few BBS genes), I wanted to create zebrafish models of genes for which no mouse models had been made. I then wanted to identify compounds that could subsequently be tested on our available mouse models of BBS (*Bbs4* and *Bbs6*), which develop renal cysts.

Results

Validation of the morpholino oligonucleotides

In order to perform a study representing the whole spectrum of ciliopathy genes and phenotypes, I designed and ordered MOs directed against both start ATG and splice sites of the following genes (see Appendix 2 for sequences):

Bardet-Biedl syndrome: *bbs4*, *bbs6*, *bbs8*
Meckel syndrome: *mks1*, *mks3*
Nephronophthisis: *nphp2*, *nphp5*
Joubert syndrome: *nphp6*
Oro-facial-digital Type I: *ofd1*
Jeune syndrome: *ift80*

These ten different genes represent the ciliopathies from their most mild clinical phenotype (NPHP), to the most extreme (Meckel syndrome), with BBS, OFD, and Jeune syndrome as intermediates.

Initially, I performed a series of injections at different doses: 1, 2, 3, 4, 6, and 8ng of MO. For most MOs, the phenotypes were consistent between both ATG and splice blocking sequences, but often the effective dosage was different. As such, this had to be determined empirically and was taken as the concentration of MO inducing a consistent phenotype in over 90% of embryos, without signs of toxicity, non-specific cell death, or lethality. For each dose of each MO, I injected 50-60 embryos and then scored each embryo at 3dpf for no, mild, and strong phenotypes, and also lethality. In general, most MOs were used in the range of 2-4ng per embryo.

As controls, some of the MOs were tested against 5-base mispairing MOs in which five of the 25 residues are altered to abrogate binding to the target. This checks that the MO itself is not causing toxicity. None of the mispairing MOs

caused any gross phenotypes or developmental delay, even when injected at a relatively high dose (8ng).

Injection of the *ift80* MO gave highly reproducible phenotypes consistent with ciliopathy. At 24hpf, embryos had a down-curved body axis relative to control MO injected embryos (Fig. 71A,B). At 3dpf, morphants had a highly down curved body axis, cardiac oedema, and a palpable pronephric cyst (Fig. 71C,D). By 5dpf, the curvature of the body axis persisted but the cyst had swelled in size due to abdominal oedema (Fig. 71E,F).

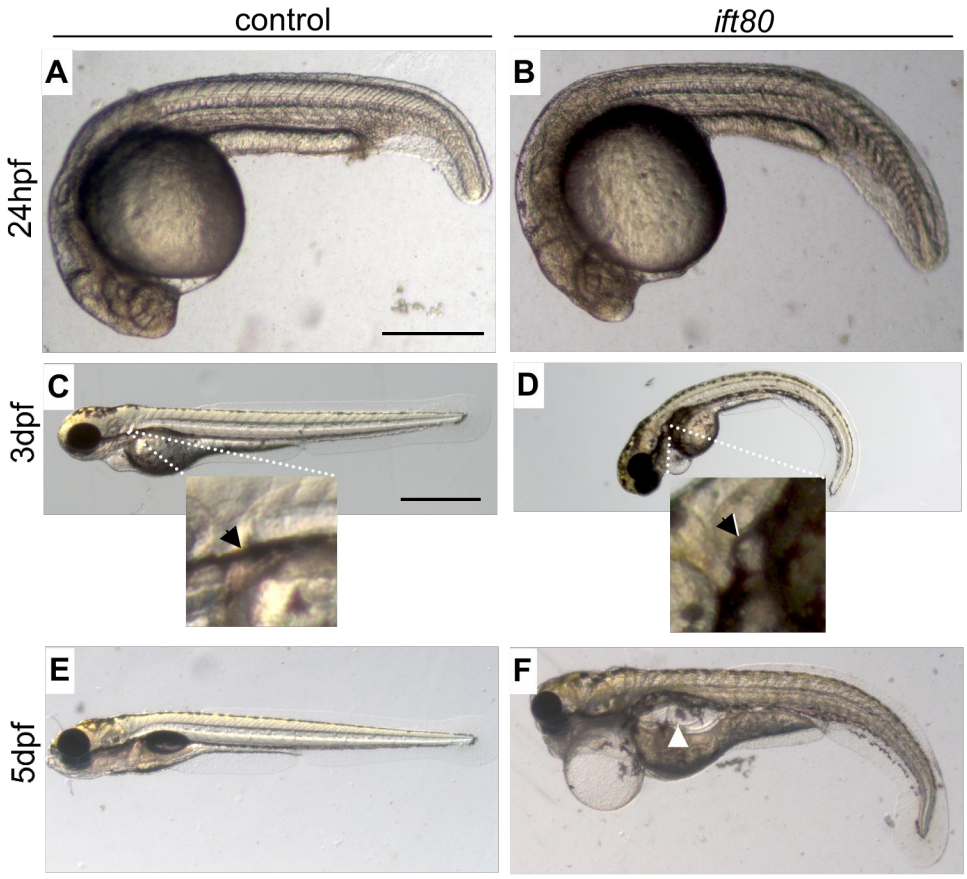

Figure 71. *ift80* morphant phenotypes.

A,**B**: *ift80* morphants have a down turned tail at 24hpf relative to controls. **C,D**: At 3dpf, a kidney cyst is clearly visible and the curvature of the body-axis has become more pronounced. **E,F**: by 5dpf the kidney has swollen due to oedema (arrowhead in F). Scale bars: A,B = 500μm; C-F = 1mm.

For two of the MOs (*bbs8*, *ift80*), I checked the specificity of the phenotype by co-injecting the MO with a human (*bbs8*, 71% sequence identity with zebrafish) or mouse (*ift80*, 61% sequence identity with zebrafish) full-length mRNA. In both cases, the mRNA was able to almost completely rescue the phenotype (Fig. 72A and C). A minority of the rescued embryos retained a very moderate phenotype such as mild cardiac oedema, very mild tail kinking, and a small kidney cyst. This may be because the precise dose of mRNA injected did not perfectly match the degree of knockdown and the endogenous expression level. The other problem with injecting mRNA is that it is expressed constitutively in all cells, not in the spatially and temporally regulated manner in normal conditions. In addition, Bbs8 and Ift80, similar to other ciliary and IFT proteins, have gain-of-function phenotypes as well, consisting of CE defect. Gain-of-function phenotypes here are likely due to the disruption of stoichiometric ratios important for proper assembly of complexes in which they participate.

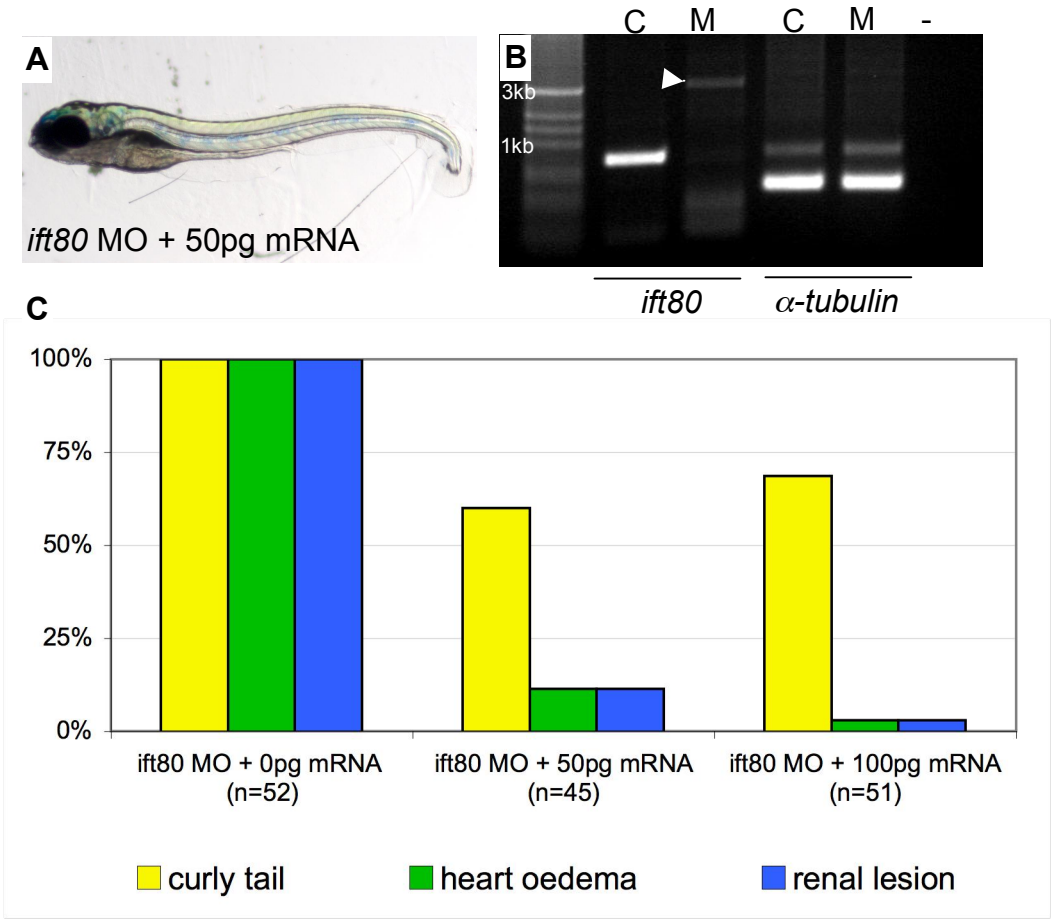

Figure 72. Rescue of *ift80* morphant phenotypes.

A: co-injection of 50pg mouse *ift80* mRNA rescues the morphant phenotype. **B**: RT-PCR showing a strong band in controls in the two exons flanking the exon-intron boundary against which the MO is designed. This band is missing in morphants and is replaced by a 3.5kb band due to the inclusion of an intron in the mRNA. *α-tubulin* mRNA products are the same in control and morphant embryos showing that non-specific mRNAs are not affected. Lack of reverse transcriptase (-RT) has no band when used with control cDNA and *ift80* primers, showing the band is a specific product.

For splice-blocking MOs, the efficiency of splice blocking, and by inference the proportion of mis-translated protein, could be determined by designing PCR primers in the exons flanking the splice site targeted by the MO. In the case of the *ift80* splice-blocking MO, this blocked the removal of a 3kb intron resulting in a much higher mass band on the PCR gel. This processed 100% of the *ift80* mRNA at 24hpf (Fig. 72B). Over time during development, the amount of MO inherited into each daughter cell decreases as the MO becomes diluted, and also can diffuse out of the tissue or become degraded.

Specific ciliary-related phenotypes in the fish

All the ciliopathy MOs trialled in this experiment showed phenotypes consistent with their human counterparts, in addition to convergent-extension, which is ubiquitously associated with zebrafish ciliary mutants and morphants.

The most dramatic phenotype associated with ciliary dysfunction is *situs inversus*. In zebrafish this can be easily scored by examining the direction of heart looping, or at earlier stages, by determining the sidedness of *south paw* (*spaw*) expression. This marker is a downstream component of the Nodal signalling pathway and in normal conditions, its expression domain is restricted to the paraxial mesoderm of the left-hand side of the embryo. *Situs inversus* is manifest by right-sided expression of *spaw*, while bilateral expression indicates randomisation of laterality (Fig. 73A-C).

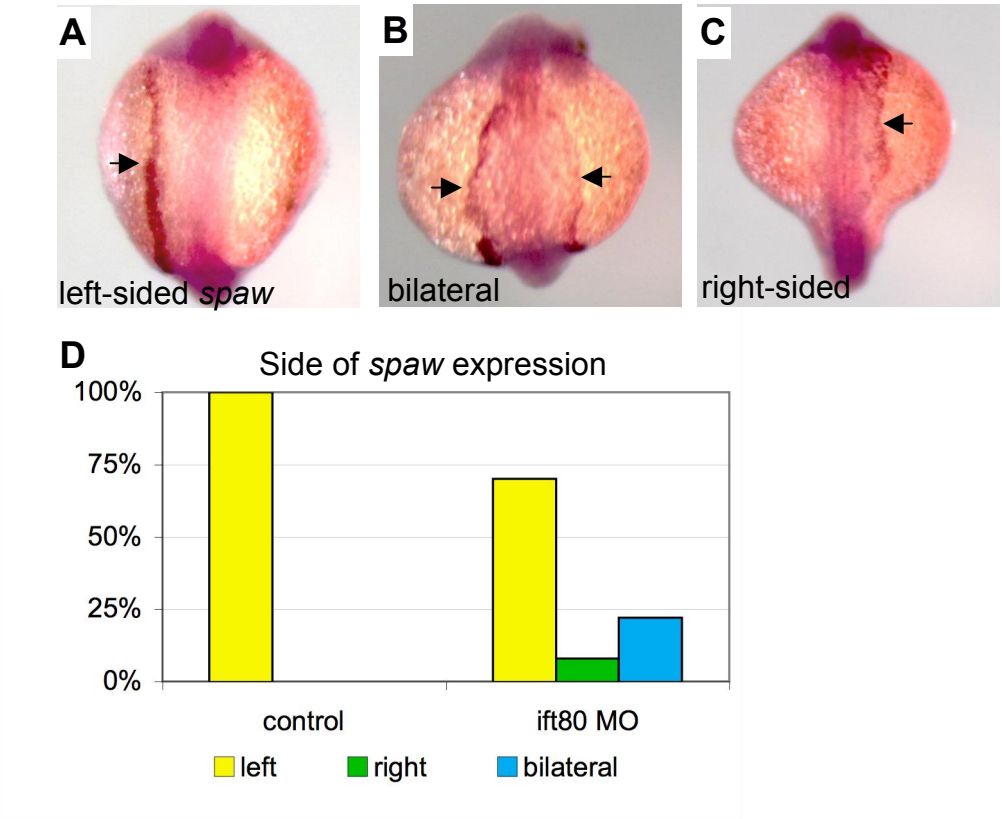

Figure 73. Sidedness of *spaw* expression in *ift80* morphants.

A,D: left-sided expression of *spaw* is normal and present in 100% of control embryos. **B**: 22% of *ift80* and 46% of *bbs8* morphants show bilateral expression of *spaw* but controls do not. **C**: 8% and 7% of *ift80* and *bbs8* morphants, respectively, show right-sided, or inverted, *spaw* expression.

In control embryos at 15ss, the expression of *spaw* is restricted to the left side of the body axis in 100% of embryos (n=31). In 30% (n=52) of *ift80* morphants, the sidedness of *spaw* expression is anomalous: 22% of embryos showed bilateral expression and 8% right-handed (or inverted) expression. In *bbs8* morphants, *spaw* expression was anomalous in 53% (n=43) of embryos: 46% showed bilateral expression and 7% right-handed expression (Fig. 73D). This phenotype is specific and, whilst not conclusive in its own right, suggests that there is a problem with cilia function in Kupffer's Vesicle (KV), a ciliated organ functionally analogous to the mammalian node.

The beating of cilia in this organ drives leftward fluid flow resulting in asymmetric distribution of signalling molecules and activation of the Nodal signalling pathway only in the left-hand side of the embryo. This breaks the symmetry of the embryo and gives each side either left or right sided character. Unpublished data from another member of our laboratory has shown that the length of KV cilia is reduced in *bbs8* morphants and this results in misdirected movement of vesicles suspended within the lumen of the vesicle. These phenotypes suggest defective ciliary structure and function in these ciliopathy morphants and support the efficacy and specificity of the gene knockdown.

Otolith defects are another ciliary phenotype

Zebrafish ears are remarkably similar in function to the mammalian ear, albeit much simpler. They function for both auditory perception and balance, important for coordinated swimming. Each ear contains two otoliths, small crystallisations of calcium carbonate that are analogous to the otoconia in the vestibular apparatus of the mammalian ear. They function in balance and maintenance of an upright swimming posture. Underneath the otoliths lie bundles of sensory hair cells that are deflected when the otoliths move about in response to the body position of the fish. These deflections inform the brain as to the position of the body axis so the animal knows which way is "up". Mutations in genes important for otolith formation, such as *starmaker*, cause malcoordinated swimming and imbalance.

Gross examination of several of the ciliopathy morphants revealed anomalous numbers, sizes, and shapes of the otoliths present in the ears of the embryos. In control embryos, 100% (n=42) have two otoliths at 72hpf, one large and one smaller, in each ear (Fig. 74A,D). In *bbs8* morphants, only 7% of otic vesicles (n=56) contained normal otoliths. In 43% of cases the otoliths were fused, producing one large otolith with two distinct lobes (Fig. 74B). In 35% of cases, there was only a single otolith present, and in 15% there were three or more otoliths present (Fig. 74C). Some otic vesicles contained up to six small otoliths. In *ift80* morphants many embryos had fused or only one otolith, but never more than two, as is the case in some *bbs8* morphants. Otolith defects were widespread in *bbs4*, *bbs6*, *ofd1*, *mks1*, *mks3*, and *nphp2* morphants as well. These results suggest randomisation of otolith number likely arising earlier in development.

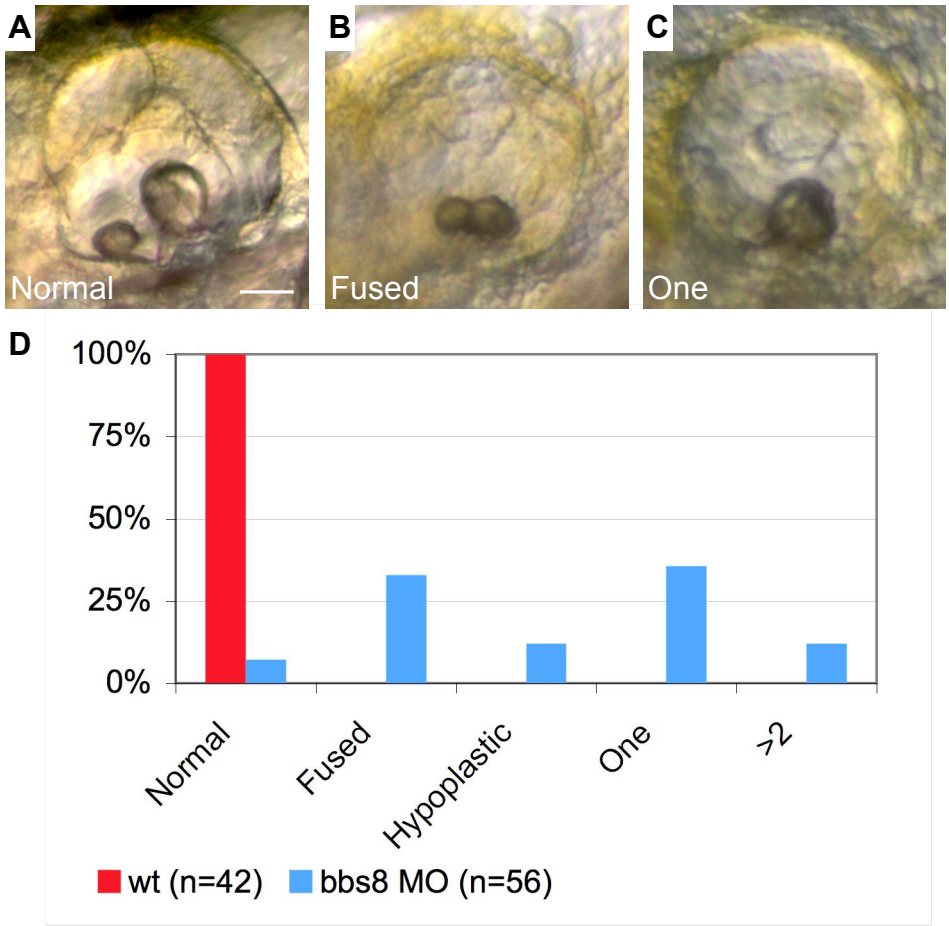

Figure 74. Otolith numbers in *bbs8* morphants.

A,D: normal arrangement of otoliths in an otic vesicle; one large and one small otolith as present in 100% of controls. **B**: 43% of *bbs8* otic vesicles contained fused otoliths. **C**: 35% of *bbs8* otic vesicles contained only a single otolith. Scale bar = 50μm.

Formation of the otoliths begins at around 18hpf when kinocilia, which are specialised primary cilia of hair cells in the otic vesicle, entrap seeding particles, which cause the accretion of the otolith. Motile cilia beating in the otic vesicle agitate the fluid in the otic vesicle and prevent premature formation of ectopic otoliths (Riley et al., 1997). After 24hpf, these motile cilia recede, leaving the two bundles of kinocilia tethering the accreting otoliths and by 30hpf, the motile cilia are completely absent.

I examined the cilia in the otic vesicle by immunostaining wholemount embryos with an anti-acetylated tubulin antibody. In control embryos at 24hpf, there exist two discreet bundles of long kinocilia projecting into the lumen of the otic vesicle (Fig. 75A). These will later become the nucleation sties of the two distinct otoliths. In *bbs8* morphants at this stage there do not appear to be any discreet bundles of kinocilia, rather all the cilia are of uniform length and are likely to be motile cilia (Fig. 75B). In 27hpf controls, the motile cilia had receded and appeared as dots surrounding the otic vesicle. In morphants, however, there was no recession of these cilia and the motile cilia appeared to persist long after they had disappeared in controls (Fig. 75C). The persistence of the motile cilia in *bbs8* morphants, and the absence of the primary kinocilia, might suggest the abnormal numbers of otoliths observed in these morphant embryos.

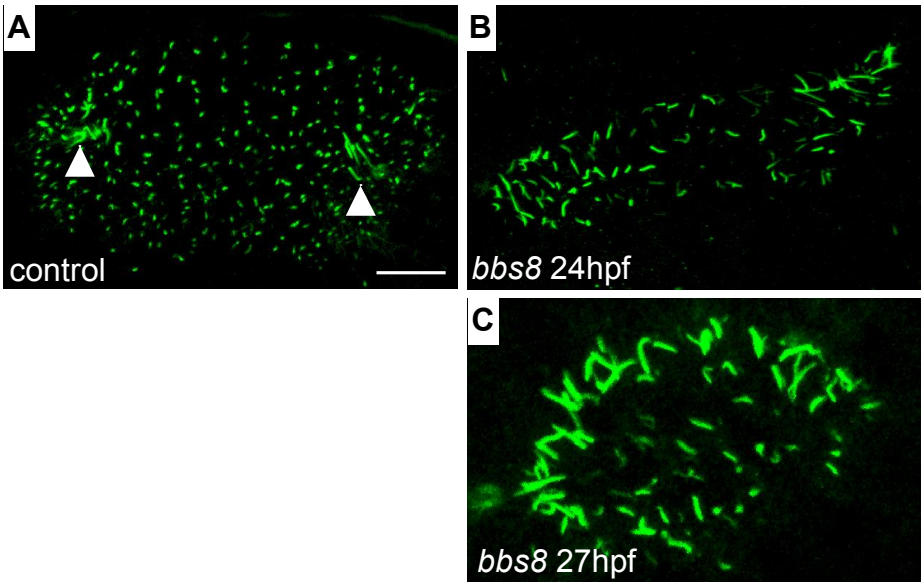

Figure 75. Otic vesicle cilia.

A: in controls the otic vesicle contains many short motile cilia, which have regressed, and two long patches of kinocilia (arrowheads), which tether the nascent otoliths. **B**: in morphant otic vesicles, the motile cilia remain long and there are no clear patches of motile cilia. **C**: at 27hpf these long motile cilia persist and have failed to regress. Scale bar = 50μm.

Renal cysts are common to all morphants

Renal disease, consisting of either dysplastic, hypoplastic, or cystic, kidneys is a common denominator of nearly all ciliopathies described, and is one of the hallmarks used to identify potential new ciliopathy candidates. I aimed to see if I could recapitulate some of these renal phenotypes in zebrafish. Zebrafish have been developed as a valid model for mutagenesis screens identifying novel genes causing cystogenesis in the kidney. Amongst many genes discovered, several have been shown to encode *bona fide* ciliary proteins.

MO-mediated knockdown of every one of the ten ciliopathy genes tried in this study caused renal cysts to develop by 3dpf. This phenotype was most penetrant in *ift80* morphants, where 100% of embryos developed a round cyst in the kidney, identical to those seen in zebrafish mutants such as *double bubble* and *bazuka joe*. By 5dpf, this cyst had swollen into an oedematous bulge. The most severe renal phenotypes were always seen with *ift80* morphants, despite their relatively mild phenotype at 24hpf. All the other MOs also induced this renal oedema by 5dpf, although to differing degrees.

Rapamycin ameliorates cyst formation

Rapamycin is an antiproliferative drug that has been shown to slow cyst progression in rodent models of polycystic kidney disease and has entered clinical trials for some indications in humans. Drugs can easily be dissolved in DMSO and applied directly to the zebrafish's embryo water, where they pass through the skin to act on their target tissues.

I first tested Rapamycin on *ift80* morphants as these had the most penetrant and extreme renal phenotype. Because Rapamycin has never been used on the zebrafish to target the kidney before, I had to determine appropriate concentrations empirically. I used a range of dilutions: 0, 1, 10, 100, and 1,000nM dissolved in 1% DMSO. In addition, I tested adding the drug at different stages of development: 4hpf (just before gastrulation) and 24hpf. Addition of the compound to control embryos produced no adverse effects at or below 100nM, and adding it early or later in development made no difference.

Addition of between 2 and 100nM of the drug to *ift80* morphants completely ameliorated the renal oedema by 5dpf. The lowest dose at which at least 95% of embryos were rescued was 10nM, so I chose to use this dose for subsequent experiments. Addition at either 4hpf or 24hpf made no difference to the outcome and so I chose to add the drug at 24hpf to minimise off target effects before the onset of kidney development. The Rapamycin had no effect on the other affected tissues in the *ift80* morphants: the body axis was still curled down, the heart oedema persisted (albeit slightly less so, presumably due to better kidney function), and the cranial cartilage defect persisted (Fig. 76G,G').

Because the Rapamycin was so effective on *ift80* morphants, I added it to all the other ciliopathy morphants developed during this study. The same effect was recapitulated in every morphant tried upon treatment with 10nM Rapamycin (Fig. 76A-G').

95% (n=64) of *mks1* morphants had died by 5dpf without addition of Rapamycin, and the fry were necrotic. At 4dpf, the embryos all had renal oedema, as did the few surviving embryos at 5dpf (Fig. 76F). When Rapamycin was added at 24hpf only 25% of the embryos were dead at 5dpf. None of the 75% surviving embryos had renal oedema – it had been ameliorated by the Rapamycin (Fig. 76F').

This increase in survival correlating with a morphological rescue of the kidney oedema suggests that the cystic kidney in the *mks1* morphants is pathological and ultimately lethal, and that addition of Rapamycin might be rescuing renal function to ameliorate this pathology. It is possible that the Rapamycin was rescuing lethality via another, unknown mechanism. However, as with the other morphants, the other phenotypes, such as curved body-axis, persisted in the surviving morphants treated with Rapamycin, again suggesting that its effects are confined to the kidney.

Quantifying the surface area of renal oedema in morphants showed a consistent increase in size without Rapamycin and this was rescued back to control levels by the addition of Rapamycin (Fig. 77A).

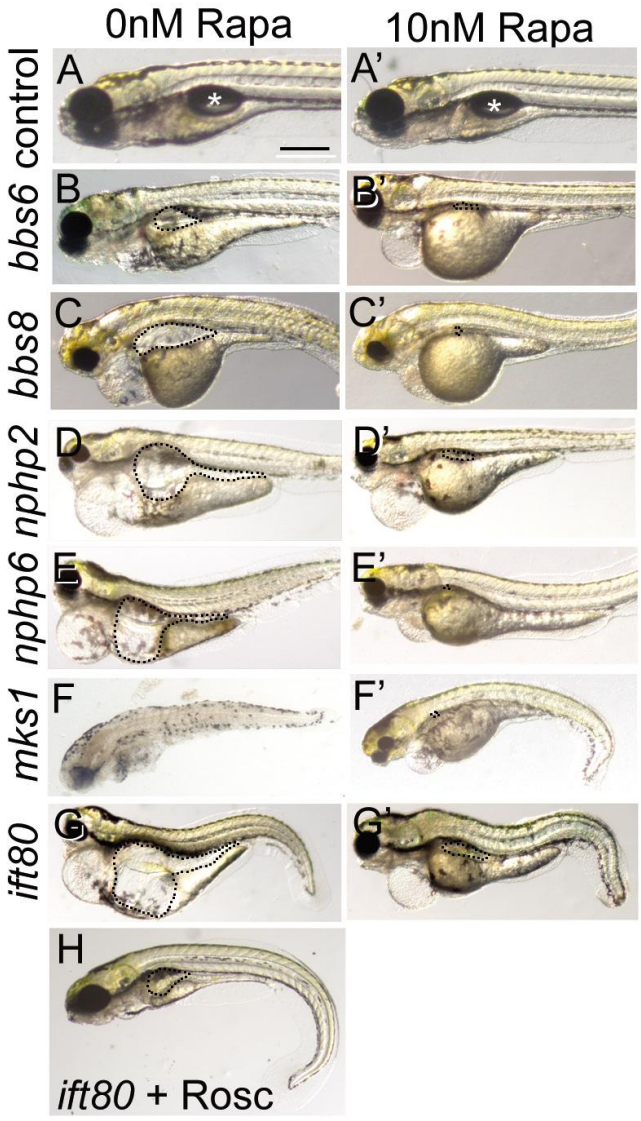

Figure 76. Addition of Rapamycin to ciliopathy morphants.

A,A': Addition of 10nM Rapamycin has no effect on controls (* represent the swim bladder absent in morphants). **B-G'**: renal cyst (dotted outline) is rescued by addition of Rapamycin in all morphants tested: *bbs6, bbs8, nphp2, nphp6, mks1, ift80*. Scale bar = 500μm.

The effect of Roscovitine on the renal phenotype

Based on the effectiveness of the Rapamycin, I extended the study to include other compounds with published success at restoring polycystic kidneys in rodent models. Roscovitine is a CDK-inhibitor previously shown to alleviate cyst development in two rodent models: *jck* (juvenile cystic kidney, *nek8* mutation) and *cpk* (congenital polycystic kidney, *cystin* mutation). Continuous

administration of Roscovitine is not required to yield these effects; a single dose is sufficient to provide long lasting arrest of cyst progression.

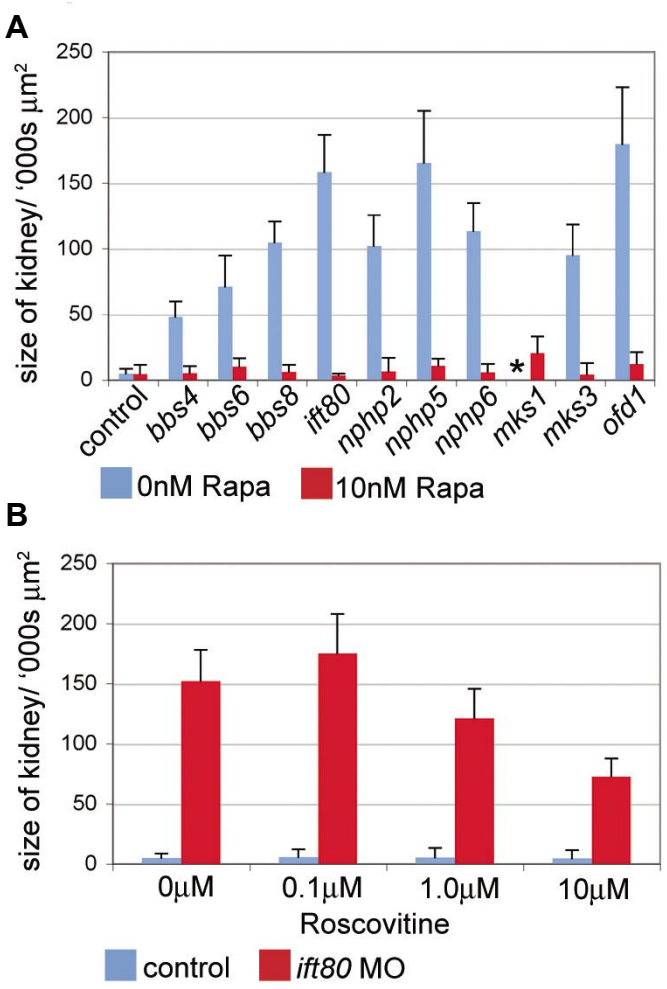

Figure 77. Quantifying the size of untreated and treated morphant kidneys.

A: in every case, addition of 10nM Rapamycin restores the size of the kidney to control levels. The asterisk in *mks1* morphants represents the lethality precluding measurement of the kidney. **B**: a dose-response curve shows that addition of Roscovitine has no effect on controls, but reduces the size of the *ift80* morphant kidney by about 50%.

I tested the effect of adding Roscovitine to *ift80* morphants. There were no published uses of Roscovitine on zebrafish before, only its use on cultured cells as a cell cycle inhibitor where it was used in the micromolar range. As such, I tested a range of Roscovitine concentrations: 0, 1, 10, and 100µM. 1µM had no effect on the embryos and 100µM caused the same effect as 10µM, so I used 10µM to be conservative (Fig. 77B). Addition of the drug either before, (4hpf) or during

(6hpf), gastrulation caused massive cell death and killed the embryos before somitogenesis had begun. This is not surprising as Roscovitine functions as a cell cycle inhibitor.

Adding the Roscovitine to *ift80* morphants at 24hpf did not cause any lethality. It partially rescued the size of the oedematous bulge to about half the size without treatment. It was not as effective at reducing the size of the oedema as Rapamycin and had to be used at 1,000-times the concentration. While Rapamycin had no effect on the extra-renal phenotypes associated with the morphants, Roscovitine was able to partially rescue the size of the pericardial oedema in *ift80* morphants (Fig. 76H). Also, the degree of body axis curvature was reduced in Roscovitine treated embryos. There is no clear explanation of why this should be so.

Functional assays to test the therapeutic potential of these compounds

The morphological rescue of the renal oedema suggested that Rapamycin was preventing the development of cysts in the morphants. *Mks1* knockdown caused lethality by 5dpf, which was rescued by Rapamycin, suggesting, not conclusively, that it was restoring the function of the kidney, thereby preventing death. I next wanted to see if Rapamycin could restore the functional capability of the kidney by improving its filtering capacity.

I employed a modified protocol of Hentschel et al, where it was used to quantify the rate of renal filtration in a model of acute renal failure induced by administration of the nephrotoxic antibiotic, Gentamicin. I injected the pericardial cavity of embryos at 3dpf with approximately 50pg of rhodamine-labelled 10kDa dextran. This perfused rapidly into the systemic circulation and within 5 minutes the whole embryo glowed red when viewed on a fluorescent dissecting microscope. This dextran is then filtered by the glomerulus and excreted from the body in the urine. The rate of filtration can be determined by measuring the

intensity of fluorescence in a defined region of the heart immediately after injection, and 24 hours post-injection (hpi).

An absence, or decrease in the amount, of fluorescence in both the heart and peripheral vasculature indicates that the kidney has effectively removed the dextran. By comparing the difference in the decrease in fluorescence over this time period between controls and morphants, one can evaluate how effectively the kidney is filtering the blood in morphants.

In control embryos, most of the fluorescence is removed from the body within 24 hours of injection of the dye (Fig. 78A,A'). In *ift80* morphants, fluorescence persists in the body, suggesting impaired renal function (Fig. 78B,B'). The degree of kidney function can be measured by calculating the percentage of fluorescent intensity remaining in the heart 24hpi. In controls, it almost vanishes (Fig. 78C,C'). In *ift80* morphants, residual fluorescence can be seen in the heart and pronephric duct (Fig. 78D,D' arrowhead). Addition of Rapamycin reduces the amount of this residual fluorescence (Fig. 78E,E'). Roscovitine also reduces the residual fluorescence but to a lesser extent than Rapamycin (Fig. 78F,F').

In control embryos, 9% of fluorescence persists in the heart 24 hpi; meaning 91% of the dextran has been removed by the kidney (some of this 9% residual fluorescence could in fact be background or autofluorescence). In both i*ft80* and *bbs4* morphants only about 55% of the dextran is excreted leaving residual fluorescence in the embryo (Fig. 78G).

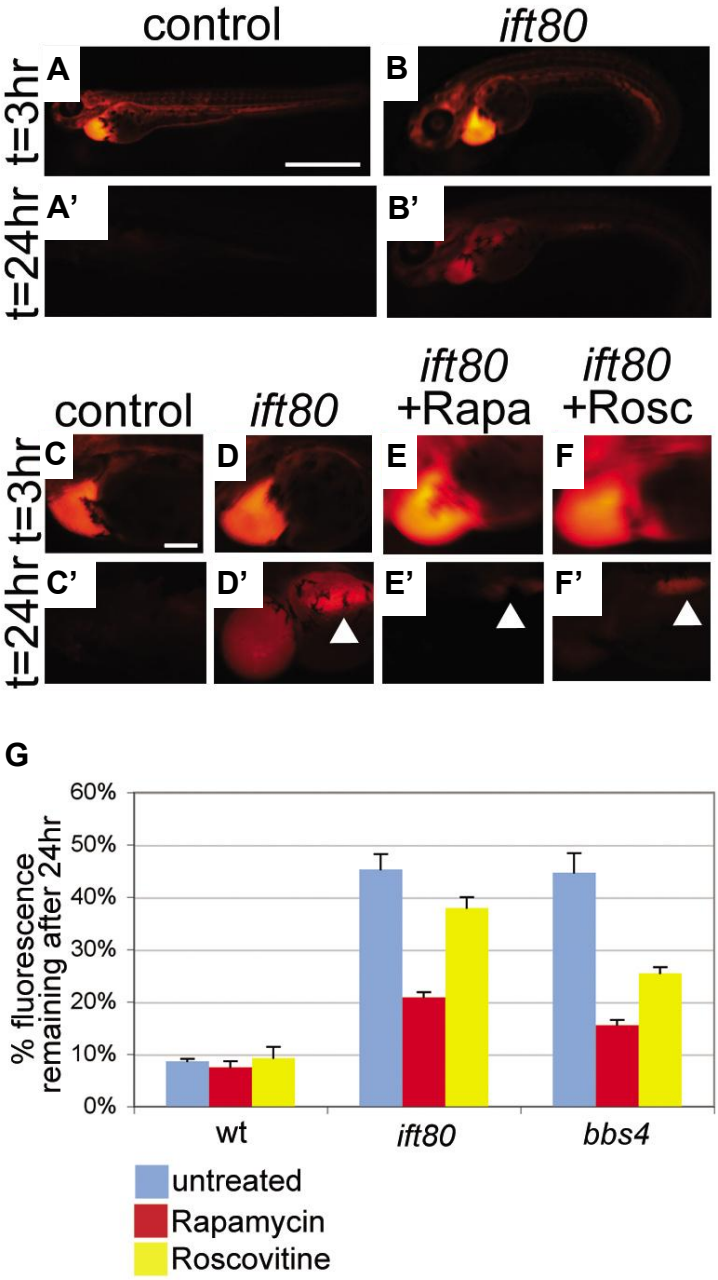

Figure 78. Renal function assay.

A,A': cardiac and systemic fluorescence 3hpi in controls. 24 hours later, the fluorescence has been eliminated as the dextran has been filtered out of the bloodstream. **B, B'**: At 3hpi, the amount of systemic fluorescence is comparable to controls, but it persists at 24hpi. **C,C'**: fluorescence in the heart is eliminated within 24 hours in controls. **D,D'**: residual fluorescence persists in the morphant, particularly in the kidney where it is getting backed up (arrowhead). **E,E'**: administration of Rapamycin reduces the level of residual fluorescence in *ift80* morphants. **F,F'**: roscovitine partially ameliorates the kidney dysfunction but is not as effective as Rapamycin as some fluorescence persists in the kidney (arrowhead). **G**: the percentage of fluorescent signal remaining in the heart 24hpi was used to quantify the degree of functional impairment and restoration in *ift80* morphants. Scale bars: A-B' = 1mm; C-F' = 200μm.

As well as causing changes to renal morphology, the ciliopathy morpholinos also impair renal function, and so the renal cysts are likely to be responsible for the impaired filtration. Considering that Rapamycin is able to rescue the morphology, I next tested if it rescued the function. To do this, I performed the same assay as above, but adding Rapamycin, and in separate experiments, Roscovitine, to the controls and morphants. Adding Rapamycin to controls has no effect on filtering capacity. When it is added to either *ift80* or *bbs4* morphants filtering capacity of the kidney is improved by roughly 2.3-fold and 3-fold respectively relative to vehicle treated morphants. In other words, only about a half to one third of the fluorescent dextran persisted in the treated embryos 24hpi. This effect was greater when the Rapamycin was added at 24hpf than when it was added at 4hpf.

Roscovitine was also tested and shown to have consistent, but milder, amelioration of renal function. In *ift80* morphants, filtering was improved by 1.2-fold, and in *bbs4* morphants by 1.8-fold. In the cases of both drugs, *bbs4* morphants were restored more fully than *ift80*. This might be because the *ift80* renal phenotype is more severe. Also, the Rapamycin always restored renal filtering capacity to a greater extent than Roscovitine, just as it also improved renal morphology better, suggesting that the renal cysts are directly responsible for impaired filtering capacity, in keeping with renal disease being the most common cause of premature death in ciliopathy patients.

Hyperproliferation may be responsible for cyst formation

I then turned to try to understand the cellular basis of the cyst development in morphant zebrafish. In mice and humans, it is widely regarded that over-proliferation of tubular cells, often at the expense of differentiation, is responsible for cyst formation. In zebrafish, there are a few theories for why cysts form. One theory is simple overproliferation, as in mammals. Some authors have suggested that it is due to a lack of polarity of renal tubule cells, resulting in disrupted flow causing blockage. Others have suggested that abnormal beating of cilia lining the tubule disrupts fluid flow and causes fluid to back up. Yet another theory suggests that the lumen of the pronephric duct gets blocked.

It is unlikely that a single one of these causatory factors occurs in isolation; it is more likely that they occur in combination. Unfortunately, the sequence of events is complex and difficult to elucidate. Sullivan-Brown et al showed that over-proliferation of cells was a secondary consequence of tubular dilation in cilia motility mutants. However, they also show that knockdown of *pkd2* does not affect cilia motility but still causes cysts by a different, uncharacterised, mechanism.

Any of the above factors might be responsible for the cyst formation in the morphants studied here. However, the fact that antiproliferative drugs, particularly the CDK-inhibitor Roscovitine, are able to rescue the cysts, suggests that they might have their origin, at least in part, in hyperproliferation. It is difficult to determine conclusively whether this is the first stage of cystogenesis or secondary to fluid blockage, or something else. To investigate this, I immunostained embryos with the mitotic marker phosphohistone 3 (PH3) at 60hpf, before the cysts become visually palpable in wholemount.

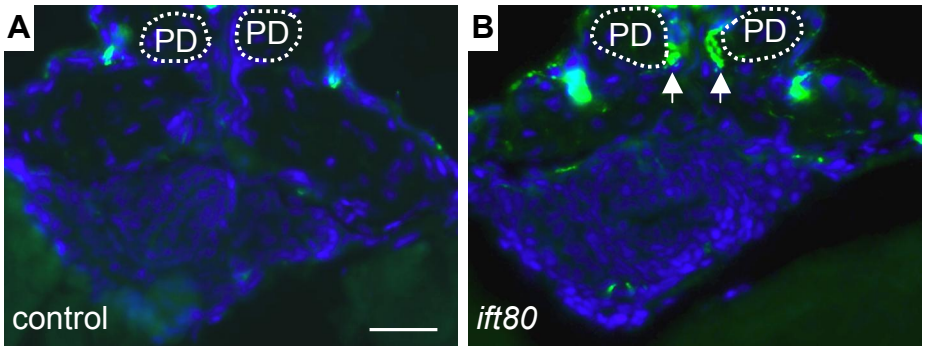

Figure 79. Phosphohistone 3 immunofluorescence in morphant kidneys.

A: PH3 staining in an uninjected kidney in transverse section shows no fluorescence in the pronephric duct (PD, surrounded by dotted line). The two bright PH3-positive spots lateral to the ducts are probably the lateral line organs. **B**: PH3 positive cells are seen lining the medial sides of the pronephric ducts in *ift80* morphants. Scale bar = 100μm.

In *ift80* morphants, there were distinct clusters of PH3-positive cells around what is anatomically concordant with the pronephric duct (Fig. 79A and B). Without a pronephric duct specific marker to reliably identify these cells, it is hard to be

absolutely sure they are the ducts. These cells seem to cluster around the medial edge of the duct and there do not appear to be any proliferating cells at the lateral boundaries of the ducts. In contrast, control embryos lacked PH3-positive cells entirely in this region.

The expression of PH3 in other regions of the embryo at this axial level were the same in controls and morphants, showing the effect is confined to, what appears to be, the pronephric duct. PH3 expression is particularly strong in the neural tube where the developing nervous system is undergoing rapid expansion. To prevent this region overpowering the much weaker fluorescence from the pronephric region I excluded it from the frame during imaging. These data suggest, but do not prove, that there is excess cell proliferation in the pronephric duct of *ift80* morphants. To prove this more conclusively, one would have to co-stain for PH3 with a marker that specifically labelled pronephric duct cells, or use a transgenic expressing GFP in this tissue. A possible marker could be the Na^+/K^+/ATPase.

Attempts to examine activity of the mTOR pathway in zebrafish

Rapamycin is an anti-proliferative compound that acts by inhibiting the protein mTOR, a central component of the mTOR pathway. Because Rapamycin ameliorated cyst formation, I tried to analyse whether mTOR signalling was affected by knockdown of *ift80*. It has been shown that TSC1 and TSC2 (Tuberous Sclerosis 1 and 2), which are key intermediates in the mTOR pathway, physically interact with Polycystin, a ciliary protein whose gene is mutated in polycystic kidney disease.

To examine the function of the pathway, I performed Western Blots to determine the protein level of three key pathway components: mTOR, phospho-mTOR, and S6-kinase. Of the three antibodies, only mTOR gave a signal. This is probably because the antibodies used were raised against mouse antigens. There did not appear to be a difference in the gross level of mTOR protein in *ift80* zebrafish lysates. However, activation of the pathway results in phosphorylation of mTOR and so one expects to see an increase in phospho-mTOR. Unfortunately, the

antibodies for phospho-mTOR and S6-kinase failed to work. Also, the Western Blots only examined whole-embryo lysates and were not specific to the kidney, which represents only a small fraction of total embryonic protein. To resolve this, I tried to perform immunofluorescence to detect the levels of the proteins within the renal cells themselves. The antibodies failed to detect any of the proteins. Another method to resolve the problem is to perform Western blots on proteins isolated from the renal cells by flow sorting *pax2a::eGFP* transgenic zebrafish, which express GFP only in the kidney and optic nerve.

Because post-translational modification is critical in mTOR signalling, *in situ* hybridisation is useless in discriminating expression levels. As such, to resolve this problem one would have to either obtain anti-zebrafish specific antibodies, or perform the experiments on mouse tissues or cultured cells.

Attempting to examine markers of renal patterning

While some evidence suggests that pronephric duct cells of the morphants may be hyperproliferative, there is also a possibility that the renal tissue is mispatterned, which could affect filtration and therefore cause cysts to develop. To investigate this I performed *in situ* hybridisation for two kidney markers: *wt1a*, which marks the glomerulus, and *pax2a*, which marks the pronephric ducts. It is difficult to get a clear view of the expression pattern in wholemount, as the tissue lies deep within the mesoderm, underneath the yolk. However, there were no obvious differences in the overall patterning of these renal tissues.

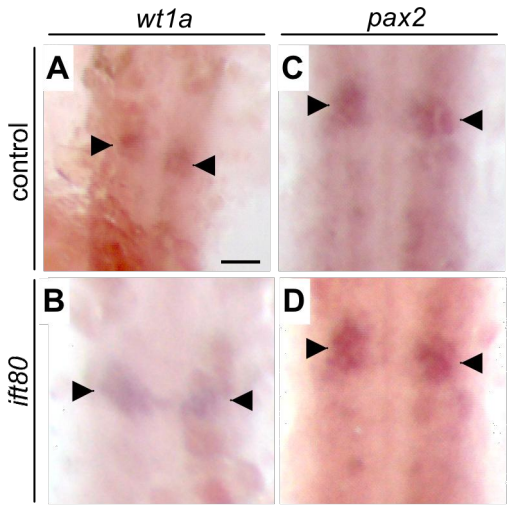

Figure 80. Renal patterning markers in *ift80* morphants.

A: expression of *wt1a* demarcates the glomerulus (arrowheads) in controls at 56hpf. **B**: expression of *wt1a* in morphants is comparable. **C**: *pax2* expression demarcates the pronephric tubules. **D**: expression of *pax2* in morphants is similar to controls. Scale bar = 100μm.

Discussion

A recapitulation of human ciliopathy phenotypes in zebrafish

The phenotypes observed in the ciliopathy morphants are a testament to how reliable and useful the zebrafish can be in modelling human genetic syndromes. *Ift80* morphants show several features specific to ciliary knockdown and human ciliopathy. These include: heterotaxia, down-curved body-axis, renal cysts, eye development abnormalities, and *bbs8* morphants have stunted cilia in the KV (unpublished data from our lab).

As mentioned earlier, the phenotypes are exaggerated in the zebrafish which has advantages and disadvantages: it makes screening for phenotypes easier, but on the other hand, it can make it harder to distinguish between toxic and artefactual effects, and real phenotypes. The presence of all of the above phenotypes in a single embryo, clear structural abnormalities in the fish, combined with effective rescue of the phenotypes (*bbs8* and *ift80* morphants) shows that these phenotypes are specific and not due to toxicity or developmental delay. This provides a reliable platform on which to examine the function of ciliopathy proteins.

A potentially novel role for ciliopathy proteins in the development of the vestibular apparatus

Several of the ciliopathy morphants had aberrant numbers of otoliths in the otic vesicle. This was most evident in *bbs8* morphants, where instead of two distinct otoliths, between one and six otoliths were present. This seemingly random production of otoliths suggests a defect in their embryonic formation. The number of otoliths is established by the presence of two long bunches of kinocilia (primary cilia) in the otic vesicle, surrounded by motile stereocilia. Otoliths accrete at the end of these kinocilia, which tether them in position while they develop. In *bbs8* morphants, these kinocilia fail to form but the stereocilia persist. It is possible that the otoliths form at random, as they do not have any defined

nucleation or tethering point. This likely arises due to a specific ciliary defect induced by loss of Bbs8.

BBS patients are known to have problems with coordination and balance. Beales et al (1999) wrote that many patients "complain of clumsiness, incoordination, and poor balance, and cite the latter as their main mobility problem, far outweighing the inconveniences of blindness". MRI scans of the cerebella of 10 patients failed to find any structural abnormalities. As such, it is possible that balance defects are due to anomalies of the vestibular apparatus.

In zebrafish, the two otoliths react to gravity to maintain an upright position in the water – equilibrioception. In humans, otoliths are present in the utricle and sacule of the inner ear. These rest on a viscous gel layer and respond to acceleration by moving relative to the gel. This induces a neural output by an unknown mechanism that translates into information regarding linear acceleration and direction of gravitational pull. This combines with visual information to produce the ocular-vestibular reflex, which results in muscular responses to changes in body position.

BBS patients have poor sight combined with possibly poor vestibular function resulting in malcoordination, imbalance, and poor posture. This may be associated with ciliary-dependent developmental defects in the vestibular apparatus.

Functional restoration of renal phenotypes

Zebrafish morphants representing all the main ciliopathy genes were created and all developed kidney cysts, in keeping with their human and mouse counterparts. These cysts manifested as a small bubble in the kidney at 72hpf. By 5dpf, this had massively expanded, as the body cavity became oedematous due to osmotic imbalance caused by impairment of renal function. Administration of two drugs, shown to reduce cyst growth in mice, Rapamycin and Roscovitine, were able to restore the kidney back to its normal size. Rapamycin was particularly effective.

Its failure to rescue other elements of the phenotype suggested a kidney-specific effect.

These drugs were also able to restore filtering function in the kidney, evidenced by restored ability to excrete fluorescent dextran from the circulation. Because the functional assay is quantitative, the relative efficacy of each compound can be evaluated. Also, the zebrafish is amenable to toxicology studies and so poisonous side effects can be rapidly detected. In the case of Rapamycin and Roscovitine, addition of the drugs to control embryos had no effect, suggesting no toxicity. This is the first study to use the zebrafish to identify drugs that can restore renal function. It is also the first study to trial any drug compounds on ciliopathy models.

The potential to extend this study to mammals

The encouraging data from the zebrafish has prompted researchers in our laboratory to extend the study to mouse models of BBS. Other useful mouse models to test would include: the *jck* mouse, which affects *Nek8*/*Nphp8*; the *pcy* mouse affecting *Nphp3*; and the Wistar polycystic kidney (*Wpk*) mouse mutant for *Mks3*. Because the mouse models take up to several months (in the case of *Bbs4* nulls) to develop cysts, it is useful to have preliminary *in vivo* data on the efficacy of the drug on that genetic model in question.

Because of the rapidity with which the zebrafish model can be screened, obtaining functional data in one week, compounds can enter pre-clinical testing in the mouse with a lower attrition rate. This increases the likelihood of success in the mouse, with the possibility of identifying compounds and dosages to trial in human patients. This is important to do, as currently kidney disease is the major cause of early mortality in ciliopathy patients and is untreatable without dialysis or transplantation.

Expanding the study to screen small-molecule libraries

This study provides proof of principle that: 1) the zebrafish can reliably model human genetic disease phenotypes; 2) these phenotypes can be ameliorated by compounds known to work on mouse models of similar conditions; 3) functional restoration can be quantified with simple assays. Using this approach, a medium-throughput screen of several hundred candidate compounds could be employed. In order to scale up the operation to a high-throughput screen, more automation is needed. To do this, one could use the transgenic zebrafish line, which expresses GFP in the kidney (*Na^+/K^+ATPase:eGFP*).

If fluorescence was expanded in a cystic model due to renal expansion, one could automatically quantify the reduction in cyst size using a fluorescent plate reader. Using robotic drug dispensing, embryos grown in 96 well plates could be rapidly screened and several thousand compounds could be tested. To do this one would need to use genetic ciliopathy mutants such as obtained from TILLING (targeting induced local lesions in genomes) projects.

Investigating mTOR pathway signalling in ciliopathies

At present, the aetiology of kidney cysts in humans and mice is thought to result from hyperproliferation, apoptosis, and dysplasia. This is thought to rely, in part, on increased canonical Wnt signalling at the expense of PCP, resulting in a disordered, hyperproliferative, cystic kidney. The cause of cysts in zebrafish is controversial and several models have been proposed, involving blockage of the duct, hyperproliferation, and altered cell polarity.

Because Roscovitine, a CDK inhibitor, is able to rescue the zebrafish cysts, it suggests that the cyst is formed by hyperproliferation of cells. What causes this proliferation is less clear. Rapamycin is an antiproliferative that specifically inhibits mTOR to prevent overproliferation. Overactive mTOR signalling has been implicated in kidney cyst formation and it interacts with the ciliary protein PC1.

Because Rapamycin is able to prevent cyst formation in the ciliopathy morphants, this suggests that overactive mTOR signalling is responsible. The complete rescue of the cyst suggests that this is the primary cause of cystogenesis. Canonical Wnt signalling upregulates the mTOR pathway by inhibiting TSC2, a protein that normally inhibits mTOR (Inoki et al., 2006). Inoki et al therefore suggested that Rapamycin could be used to treat cancers arising as a result of hyperactive Wnt signalling. As such, the induction of the canonical Wnt pathway observed in BBS and *Kif3a* mutants might be responsible for activation of mTOR in the kidney and hyperproliferation of cells (Gerdes et al., 2007). Future work will dissect the activity of the mTOR pathway in the fish and mouse kidney in BBS mutants to determine if this hypothesis is correct.

The renal phenotype of BBS and NPHP patients is more complex and variable than that of AD or ARPKD patients. In addition to cysts, the kidney is dysplastic and often fibrosed with connective tissue. The calyces are often clubbed and lobed and the appearance of the kidney is disorganised. Concurrently with activated Wnt signalling, knockdown of BBS proteins causes deficits in PCP. This is known to cause mispolarisation of tubular epithelial cells resulting in a disorganised, dysplastic kidney with inefficient filtering capacity. It is possible that these two effects combined are the cause of the kidney phenotype in BBS patients.
The results of these experiments were published in *Pediatric Nephrology* in July 2008 (Tobin and Beales, 2008).

Chapter 7: Characterising the functions of the obesity and diabetes-related gene *FTO*

Introduction

The genetic component of obesity

Obesity is one of the most serious public health problems facing the developed world, with 30% of the British adult population being affected, as defined by a BMI (body-mass index; weight divided by height squared) of over 30. Obesity is associated with some serious clinical sequelae:

- Cardiovascular disease: atherosclerosis, embolism
- Endocrine dysfunction: polycystic ovary syndrome, infertility
- Gastrointestinal disease: colon cancer, fatty liver syndrome
- Kidney and liver failure
- Back pain and immobility
- Asthma, sleep apnoea, depression

Monogenic obesity accounts for around 7% of cases, is caused by mutations in around 75 genes, and includes the diseases: BBS, ALMS, leptin receptor and melanocortin deficiencies. In addition, 5% of obese children carry mutation in the melanocortin-4 receptor (*MC4R*), a membrane-bound receptor for the appetite-controlling hormone melanocortin (Loos et al., 2008). In these cases, age of onset of weight gain is very young, often before two years.

The majority of obesity cases are not monogenic and weight gain begins later in life. This has been attributed to life style factors such as overeating and being sedentary. The thrifty gene hypothesis suggests that our genome has evolved to make the most of scarce resources in the past, when food has not been abundant. In our current times of plenty, these genes that once provided a survival advantage may predispose to obesity in a sedentary, gluttonous society.

Obesity is more complex than simply excess calorie intake, as the question arises as to why some people overeat in the first place, and why some people who eat moderate amounts tend to put on more weight than others. Neurobiological explanations for obesity reside in the control of appetite and satiety, rooted in the hypothalamus. Here, the arcuate nucleus outputs to the lateral hypothalamus (LH), which controls feeding, and the ventromedial hypothalamus (VMH), which controls satiety. The hormone leptin is produced by adipocytes and signals an increase in appetite when fat reserves are low, and vice-versa. Leptin stimulates the pro-opiomelanocortin (POMC) expressing neurons, which normally stimulate the VMH, increasing satiety and decreasing the desire to feed. It is thought that obese people may be resistant to leptin signalling, meaning it takes more to satisfy their appetites.

Studies on monozygotic twins reveal a 77% heritability of non-monogenic obesity, suggesting a strong genetic component to the disease. As such, obesity is a complex and heterogeneous condition in which several factors, both genetic and environmental, contribute to the phenotype. Over the past twenty years, epidemiological studies using quantitative trait loci (QTL) and genome-wide linkage have identified around 15 QTLs linked to obesity, but these are not powerful at resolving the effects of individual genes, and the sample sizes are too small to draw conclusions about risk factors for the population at large.

Recently, genome-wide association studies have been used as an unbiased means to identify candidate genes predisposing to obesity in the adult population. It is a useful means of generating hypotheses, which can then be tested functionally, with the ultimate aim of finding ways to treat, or control, obesity. The Wellcome Trust Case Control Consortium (WTCCC) was set up in 2005 to undertake genome-wide association for major common complex diseases including: Type 1 and Type 2 diabetes, Crohn's disease, breast cancer, coronary heart disease, hypertension, bipolar disorder, rheumatoid arthritis, multiple sclerosis, malaria, and tuberculosis (http://www.wtccc.org.uk).

In each study, 500k Affymetrix chips were used to provide SNP data on 2,000 affecteds and 3,000 healthy controls. These chips capture about 80% of the

genetic variation in the human HapMap, which details all the common genetic variation in the human population. Statistical analysis is then used to calculate the significance of the association of particular regions of the genome with the disease in the affected group versus the controls. This then identifies candidate loci and can be used to calculate risk factors of particular SNP genotypes for the disease in question.

The discovery of FTO as an obesity-associated gene

The first association study carried out by the WTCCC was for type 2 diabetes (non-insulin dependent) and identified a group of SNPs in the first intron of a novel gene, *FTO*, associated with this disease. After adjusting for variation in BMI, the association between *FTO* and type 2 diabetes was abolished, implying that *FTO* was actually mediating body weight, which in turn predisposes to type 2 diabetes (Frayling et al., 2007).

Since then, association of obesity with *FTO* has been recapitulated in Chinese, Korean, Japanese, Oceanic, and African populations in at least 10 additional studies (For review, see Loos and Bouchard, 2008). Homozygotes for the risk allele had a 67% greater chance of being obese and weighed an average of 3kg more than individuals with no risk allele (Frayling et al., 2007). 16% of Europeans are homozygous for the risk allele. These data conclude that having the "AA" genotype in two *FTO* alleles is a major factor contributing to the development of obesity. The question arising is: is the *FTO* gene responsible for the obese phenotype? If so, what is the function of FTO and how does it contribute to obesity?

Functions of the FTO protein

Considering the number and strength of genetic association studies linking *FTO* with obesity, very little is known about the structure or function of the FTO protein. *FTO* is a novel gene with no homology to other known genes and no obvious motifs giving clues about putative function. In wild type mice, *Fto* mRNA is most abundant in the pancreas and brain, and in particular, the region of

the hypothalamus regulating energy-expenditure. Tschritter et al (2007) suggested that FTO may affect insulin sensitivity, as homozygous individuals exhibited a reduced insulin sensitivity in the brain (Tschritter et al., 2007). Fredriksson et al (2008) found that *Fto* was upregulated by 41% in the hypothalami of wild type rats deprived of food for 48 hours (Fredriksson et al., 2008). Wahlen et al (2007) showed that the level of *FTO* mRNA increases with BMI, suggesting a peripheral role for FTO protein (Wåhlén et al., 2008).

Only two studies have revealed any clues about the molecular-level function of FTO. Sanchez-Pulido et al (2007) used bioinformatics to place *FTO* as a novel member of the non-haem oxygenase superfamily, requiring 2-oxoglutarate and iron to function (Sanchez-Pulido and Andrade-Navarro, 2007). Other members of this family, such as hypoxia-inducible factors (HIFs), function as metabolic sensors and nuclear effectors in response to low oxygen.

Gerken et al (2007) used bioinformatics to reach the same conclusion as Sanchez-Pulido's study. They also performed a biochemical assay to show that recombinant FTO protein could demethylate single-stranded DNA in a Fe^{2+} and 2-oxoglutarate dependent manner (Gerken et al., 2007). They demonstrated a nuclear localisation of recombinant FTO and that its mRNA in mice was expressed in the arcuate nucleus of the hypothalamus and was regulated in response to feeding and fasting. They suggested that FTO alters DNA methylation status, which somehow regulates energy balance and fat storage.

The *Fused toes* mutant mouse

Before its discovery as an obesity-associated gene, *Fto* was known as one of six genes deleted in the *Fused toes* (*Ft*) spontaneous mouse mutant. *Ft* was first identified in 1994 as a dominant mutation causing fusion of the toes, thymic hyperplasia, and random body *situs* (van der Hoeven et al., 1994). It was generated serendipitously during the integration of a retroviral transgene into the mouse genome. Homozygous *Ft* embryos die at midgestation with craniofacial

defects, polydactyly, ventral neural tube defects, and random left-right asymmetry.

In 1999, Peters et al cloned the *Fatso* gene (*Fto*) from the *Ft* mutant and showed that Fto had a predicted mass of 58kDa but had no motifs indicating putative function (Peters et al., 1999). They ascribed the function of Fto to control of left-right asymmetry and craniofacial development. In 2002, Peters et al showed that *Fto* was part of a 1.6Mb region comprising six genes deleted in *Ft*: *Fto*, *Ftm*, *Fts*, *Irx3*, *Irx5*, and *Irx6* (Peters et al., 2002). Gotz et al (2005) ascribed the lack of ventral cell types in the *Ft* neural tube to a loss of Shh signalling (Götz et al., 2005).

In 2007, Anselme et al described how anteroposterior and dorsoventral patterning of the *Ft* brain was affected, and that these were the likely cause of the craniofacial deformities including small eyes, hypoplastic facial features, and anterior neural tube closure defects (Anselme et al., 2007). They also showed that cranial neural crest cell migration was delayed in *Ft* embryos and the branchial arches were smaller.

The problem with studying protein function in the *Fused toes* mouse is that six genes are deleted, so attributing function to any one gene is problematic and exacerbated by the possibility of genetic interactions and epistasis amongst the six genes. This is likely given the fact that the *Ft* heterozygotes also display a phenotype, whereas mice heterozygous for individual genes from the *Ft* interval are not phenotypic.

Reasons for considering *Fto* as a candidate ciliary-associated protein

Vierkotten et al (2007) generated an *Ftm* knockout mouse. They showed that homozygotes had polydactyly, neural tube patterning defects, left-right asymmetry defects, and the ratio of activator to repressor Gli3 was affected. $Ftm^{+/-}$ embryos were unaffected. They localised Ftm to the basal body of cilia

and suggested it was a novel ciliary protein involved in Shh signalling. Mutations in *RPGRIP1L*, the human homologue of *Ftm*, were found in patients with Joubert and Meckel syndromes, and the RPGRIP1L protein interacted with NPHP4 and NPHP6 (Arts et al., 2007). This firmly established *Ftm* as a ciliopathy protein.

Ftm and *Fto* are adjacent on chromosome 8 in mice and chromosome 16 in humans, and are transcribed in opposite directions. Stratigopoulos et al (2008) examined the expression of *Fto* and *Ftm* in several obese mouse mutants such as *Tubby* and *Obese*. They showed *Fto* and *Ftm* expression was indistinguishable in response to under or over feeding, and hypothermia (Stratigopoulos et al., 2008). They suggested that the two genes were therefore coregulated. The overlapping putative regulatory region between the two genes contained binding sites for Cutl1, a gene product with a SNP associated with human obesity. Knockdown of *CUTL1* in human fibroblasts dramatically downregulated both *FTO* and *FTM* (*Ibid.*).

Because the *Ft* heterozygotes have phenotypes reminiscent of *Ftm* homozygous nulls, it is possible that *Fto* and *Ftm* interact, as haploinsufficiency of both genes is sufficient to give the phenotype. The similarity between phenotypes, regulatory mechanism, and chromosomal position of *FTO* and *FTM*, hint at the fact that FTO, like FTM, might play a role in the cilium.

Aims of this project

Alleles of *FTO* predispose to obesity in the population at large, while null mutations in the mouse might give phenotypes reminiscent of ciliopathy including craniofacial dysmorphology, polydactyly, *situs inversus*, and Shh signalling defects. Obesity is a major feature in several ciliopathy nulls (BBS and ALMS). I aimed to test whether Fto might have a role in ciliary biology by performing the following experiments:

1) Generate a zebrafish model of *fto* knockdown. Because there are common phenotypes associated with ciliary protein knock-down in zebrafish,

including: convergent-extension defect, down-turned body axis, otolith defects, kidney cysts, and laterality defects, it is possible to get a clue about whether a gene product is involved with cilium function.

2) Investigate the localisation of Fto in ciliated cells *in vitro* and *in vivo*.
3) Test pancreatic function and development in *fto* morphants
4) Examine signalling pathway activity in *fto* morphants
5) Test to see if there is a genetic interaction between *fto* and *ftm in vivo*.

Results

Fto morphant zebrafish show some characteristics of ciliopathy

To determine the possible cellular functions for the FTO protein, I generated a zebrafish morphant model and designed MOs against translation and splice sites (see Appendix 2 for MO sequences). The splice-blocking MO gave a phenotype at 24hpf showed the common convergent-extension defect ubiquitously associated with ciliopathy knockdowns (Fig. 81A,B). The embryos had a down-curved body axis with squashed somites. Examination at 48hpf showed that this down-curved axis persisted and the embryos did not show any signs of MO-induced toxicity (Fig. 81C,D).

Because the SNP in FTO associated with obesity is of unknown function, I next tested the effect of over-expression of the protein to explore the possibility that this might result in phenotypes. Consistent with many of the ciliopathy proteins, over-expression of Fto with 200pg of zebrafish mRNA amplified from a cDNA library, phenocopied the knockdown phenotype (Fig. 81E,F). This included the CE defect and flattened somites. The body axis was distorted in a manner very similar to the knockdown situation. Injection of 50pg or 100pg of mRNA caused no phenotype suggesting that a high degree of over-expression is necessary to induce the morphological phenotype. To test if the effect of the mRNA and MO were specific, I co-injected 4ng of the splice-blocking MO with 100pg of zebrafish *fto* mRNA and saw complete rescue of the phenotype (Fig. 81G). This confirmed specificity of both mRNA and MO, and that the observed phenotypes were real effects.

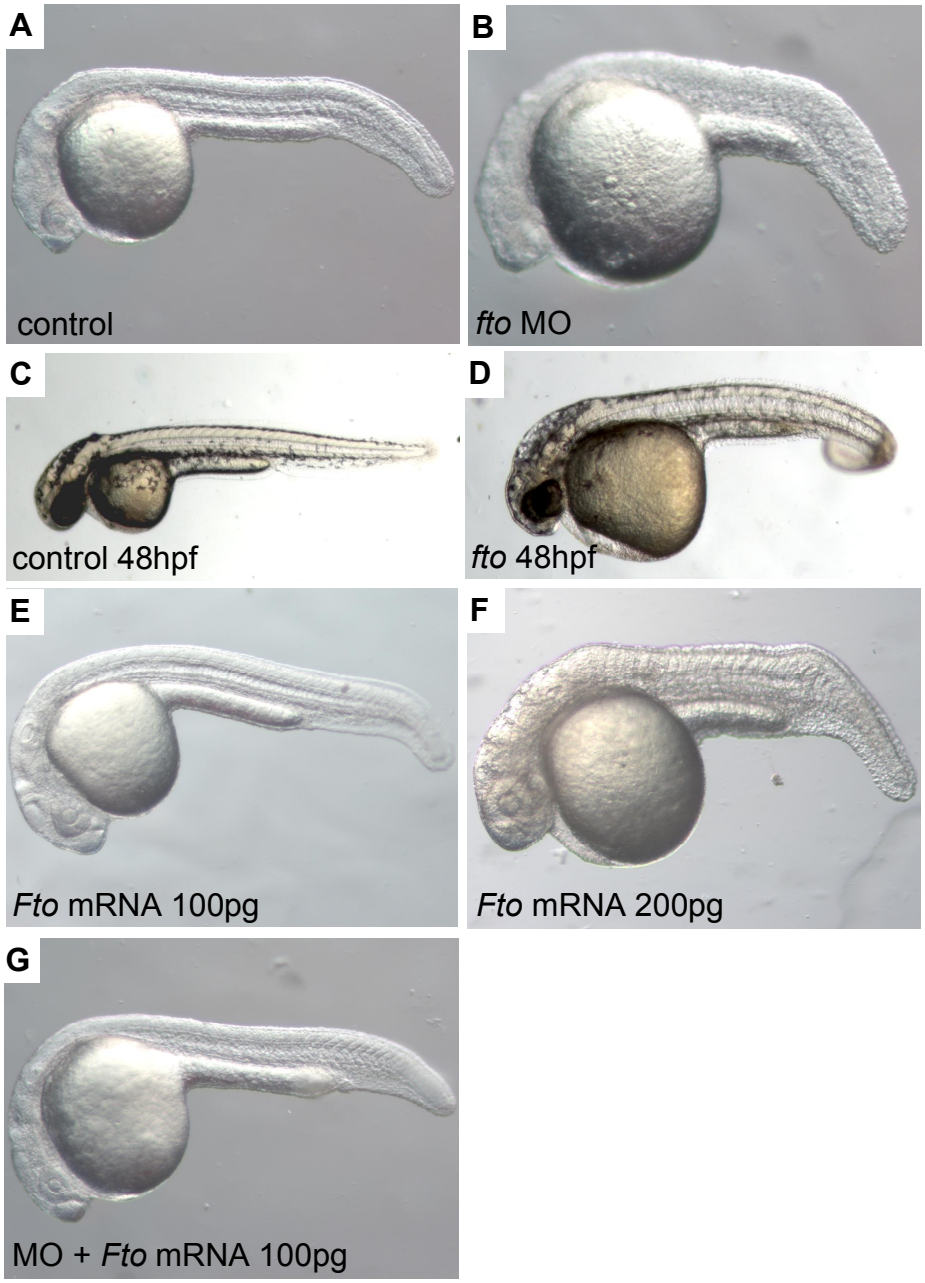

Figure 81. *fto* morphant phenotypes.

A: control embryos at 24hpf. **B**: *fto* morphant embryos have a convergent extension defect, squashed somites, and a down-curved tail. **C,D**: at 48hpf morphants have a curved body-axis. **E**: injection of 100pg of *Fto* mRNA has no effect on morphology. **F**: 200pg *Fto* mRNA yields a similar phenotype to the morphant. **G**: co-injection of the MO with 100pg mRNA rescued the morphant phenotype.

At 5dpf, both ATG and splice-blocking morphant embryos showed more signs of ciliary features: the kidney was oedematous and swollen like other ciliopathy models (Fig. 82A-E). More tellingly, otic vesicles frequently contained a single otolith, a defect often prescribed to aberrant cilia form or function (Fig. 84F,G).

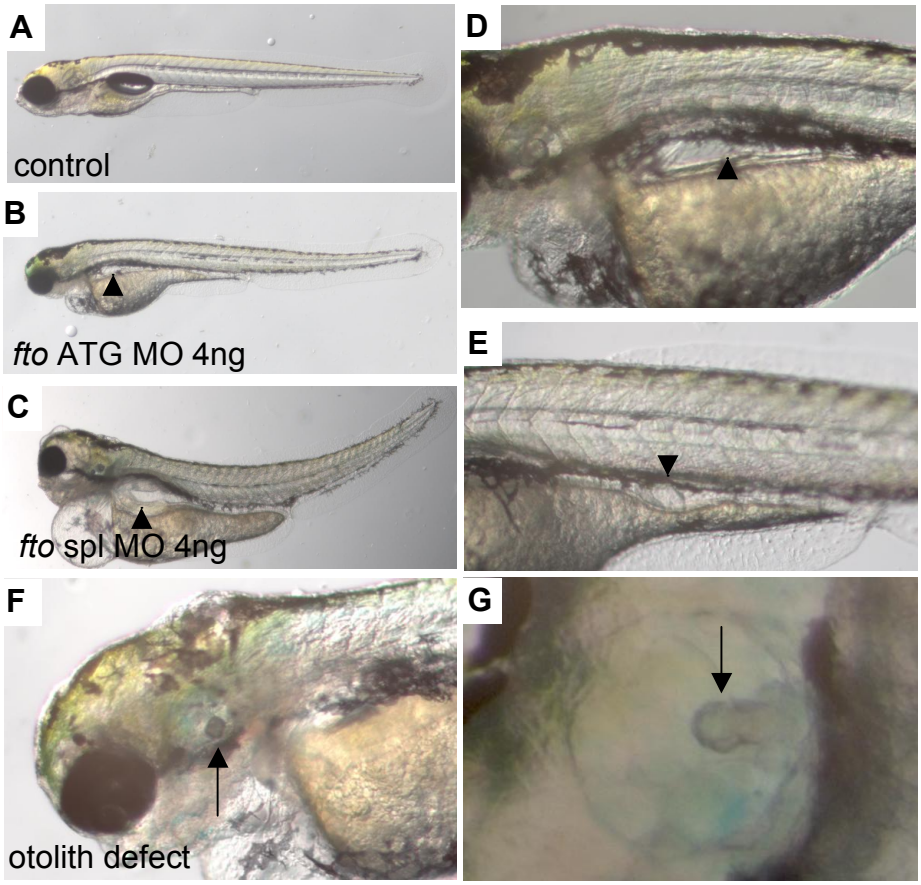

Figure 82. Phenotypes of *fto* morphants at 5dpf

A: control embryos at 5dpf. **B,C**: both ATG and splice-blocking MOs produced renal oedema. **D**: close-up of the kidney of *fto* ATG MO. **E**: swelling of the pronephric duct of *fto* splice-block morphants. **F**: presence of a single otolith in the otic vesicle of morphants. **G**: close-up of morphant otic vesicle showing fused otoliths.

Despite these phenotypes, the structure of the cilia lining the pronephric duct appeared grossly normal in *fto* morphants (Figure 83).

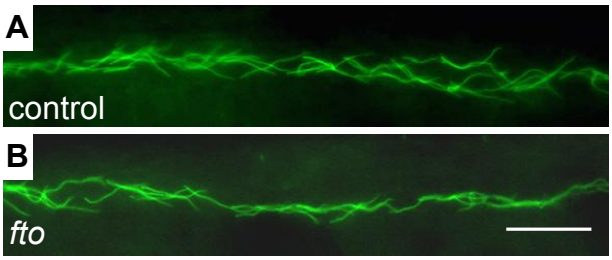

Figure 83. Pronephric cilia in *fto* morphants.

Cilia in *fto* morphant pronephric ducts at 27hpf appear grossly similar to controls. Scale bar = 50μm.

I next performed *in situ* hybridisation for *southpaw* to see if laterality was affected in morphants. At 15ss, *spaw* expression was left-sided in 100% of controls (n=35) (Figure 84). Using the ATG-blocking MO, *spaw* expression was left-sided in 80% (n=35) of embryos while 1% of embryos showed right-sided expression and 19% were bilateral. In splice-blocking morphants, 64% (n=50) of embryos had left-sided expression of *spaw*, 4% were right-sided and 32% were bilateral (Figure 84). These figures are comparable to the degree of laterality abnormality associated with *bbs* and *ift80* morphants.

Bilateral expression of *spaw* suggests complete randomisation of body *situs*, whilst right-sided expression suggests, but does not prove, reversal of ciliary beating and therefore interpretation of the signal is reversed. Because bilateral expression is much more common than inverted expression, it is possible that there is disorganised or reduced ciliary beating in the Kupffer's Vesicle (KV) in these morphants. There was no change to the gross structure of the KV cilia in morphants compared to wild types (not shown), but it is possible that their function is affected. While these phenotypes are suggestive of ciliary involvement, phenocopy of ciliary-like phenotypes is not conclusive proof that the protein is involved in ciliary function.

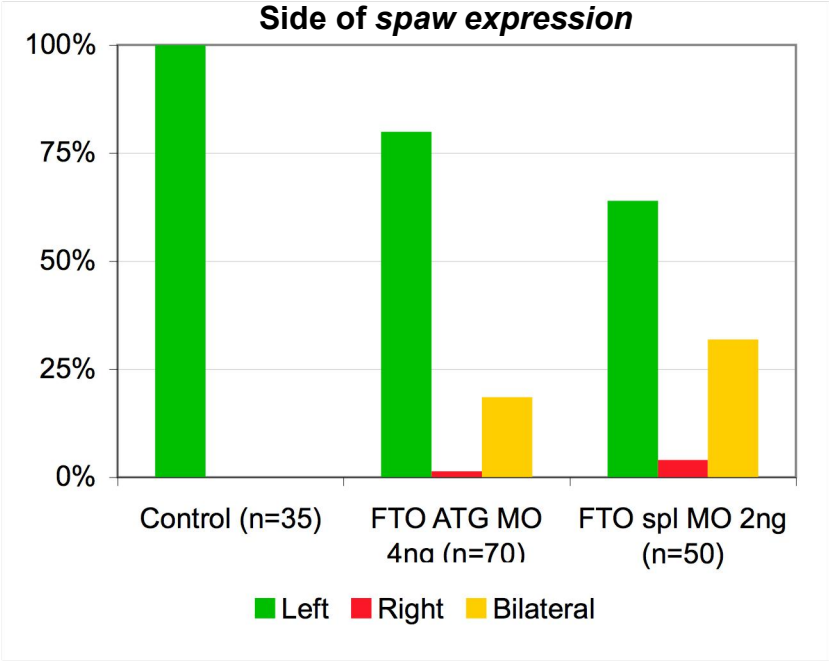

Figure 84. *spaw* localisation in *fto* morphant embryos.

In controls, all embryos had left-sided expression of *spaw*. In both ATG and splice-blocking MOs, there was significant mislocalisation of *spaw* expression, suggesting incomplete randomisation of laterality and heterotaxia.

Fto protein localises to the nucleus in cultured cells and in zebrafish embryos, but to the basal body in cultured cells

The zebrafish phenotypic analysis suggests a possible role in ciliary function. To see if Fto protein localised to the cilium, I injected Myc-tagged *fto* mRNA into one-cell stage zebrafish embryos and examined the localisation of the tagged protein at gastrulation stage (5hpf), because the sheet of cells on the top of the animal pole is easy to visualise. In all cells, the Fto protein localised clearly to the nucleus and there was no cytoplasmic, basal body, or ciliary localisation observed. Nuclear localisation was expected, given the later report (Sanchez-Pulido et al., 2007) that the protein contains a bipartite nuclear localisation signal (Figure 85).

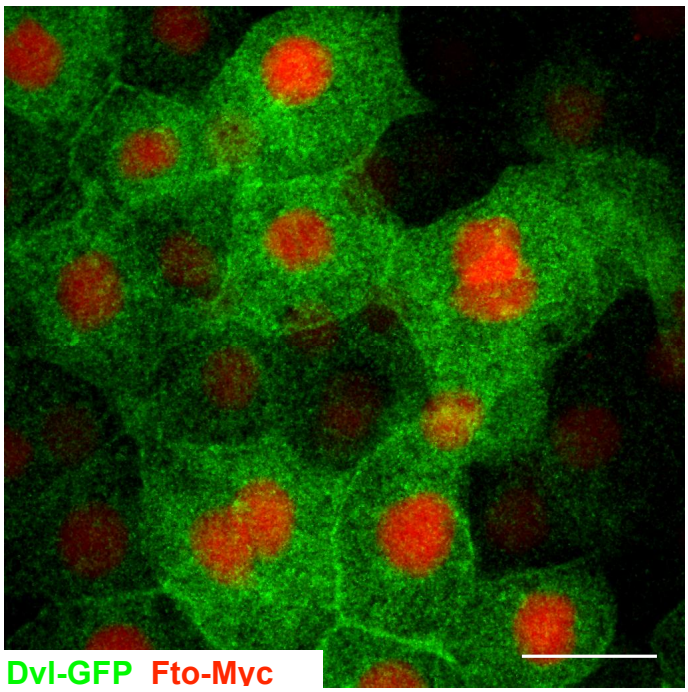

Figure 85. Fto protein localisation in zebrafish embryos.

GFP-tagged Dvl protein is visualised in green and Myc-tagged Fto (in red) shows nuclear localisation in gastrula stage (5hpf) zebrafish embryos. Scale bar = 10μm.

To extend these studies, another person in the lab transfected ciliated 3T3 and IMCD3 cultured cells with a Myc-tagged mouse FTO construct. Here, the FTO protein colocalised with gamma-tubulin, indicating a basal body and centrosomal localisation. It is unclear why the localisation data differed between the zebrafish and cultured cells. One explanation could be the rare, but misleading, mislocalisation of tagged proteins to the basal body, where they are sequestered by gamma- or acetylated-tubulin.

Shh signalling is not affected in Fto morphants

The data suggested that FTO might be a nuclear and possibly a ciliary protein. Because the *bbs* and *ift80* morphants tested previously had Shh signalling defects, and given the fact that *fused toes* mouse mutants have polydactyly and mid-facial anomalies, I tested this in FTO morphants by *in situ* hybridisation of *ptc1* mRNA. This revealed no change in expression compared to controls and gave a rough indication that Shh signalling was not affected in *fto* morphants (Figure 86).

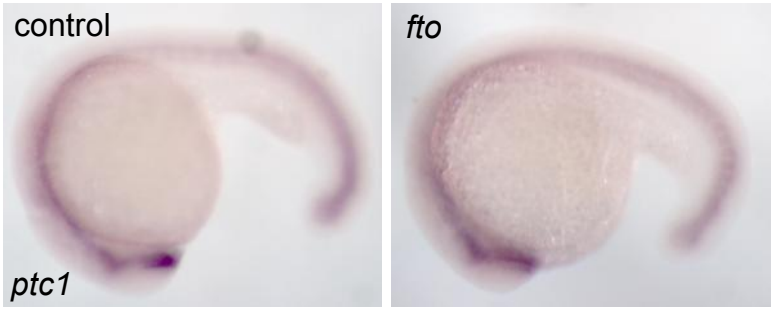

Figure 86. *ptc1* expression in *fto* morphants.
ptc1 expression is comparable in control and *fto* morphants.

Glucose homeostasis may be disrupted in Fto morphants

In addition to obesity, genome-wide association studies have connected *FTO* with Type II diabetes. *FTO* is expressed in many tissues, but is at the highest levels in the brain and pancreatic islets cells, including insulin-secreting β-cells. To test the expression of endogenous protein in pancreatic cells, I raised a proprietary polyclonal antibody (Sigma, UK) to detect FTO protein in cultured mammalian cells raised against two peptides; N-terminal and C-terminal, common to both human and mouse sequences. This antibody failed to yield any signal when tested on human or mouse cells for either Western Blot or immunocytochemistry.

Given the possible role for FTO in ciliary function, its expression in pancreatic cells, association with diabetes, and the known importance for cilia in pancreas development and function, I next tested the glucose homeostasis of *fto* morphants. To do this, I adapted the protocol of Elo et al (2007) where they used zebrafish larvae to test anti-diabetic compounds on models of glucose metabolism. By 4dpf, larval zebrafish begin to run out of nutrition supplied by the yolk and so model the effects of starvation and therefore hypoglycaemia.

Addition of 40mM of glucose at 4dpf to embryonic water results in the upregulation of the pre-pro-insulin gene, *insa*, to induce glycogenesis. Concomitantly, embryos downregulate the gene encoding Phosphoenolpyruvate carboxykinase (PEPCK), an enzyme essential for gluconeogenesis, which

converts oxaloacetate into phosphoenolpyruvate and carbon dioxide. The expression level of these genes was determined 24 hours later in 5dpf larval zebrafish by quantitative real-time PCR performed in triplicate using cDNA generated from mRNA extracted from 10 embryos per batch.

I performed three repeat experiments using triplicate batches of embryos, testing glucose concentrations of 40mM and 100mM. The results were slightly variable because, in the first run, the control embryos showed no response to glucose stimulation. However, I repeated the experiment dissolving the glucose in 1% DMSO in case it had failed to enter into the zebrafish tissue. In this case, addition of 40mM glucose caused a 2.5-fold increase in *insa* expression. Addition of 100mM glucose caused a 1.5-fold increase in *insa* expression but had deleterious effects on the morphology of the embryo, particularly the morphants. Addition of 40mM glucose had no effect on *insa* expression in *fto* morphants, while the relative expression of *insa*, normalised to β-actin expression levels, was similar to controls (Fig. 87A). *gapdh* was not used to normalise expression levels as it is a metabolically regulated gene.

Adding glucose to controls reduced *pepck* expression to 20% of the unstimulated level (1% DMSO alone), presumably as a result of less gluconeogenesis. In morphants, relative *pepck* expression was reduced to around 70% of control levels in unstimulated embryos, possibly indicating lower metabolic activity. Stimulation with glucose did not cause downregulation of *pepck* expression; rather, it was slightly upregulated, although this change is unlikely to be biologically significant (Fig. 87B). This supports the *insa* expression data suggesting that glucose homeostasis is aberrant in *fto* morphant zebrafish.

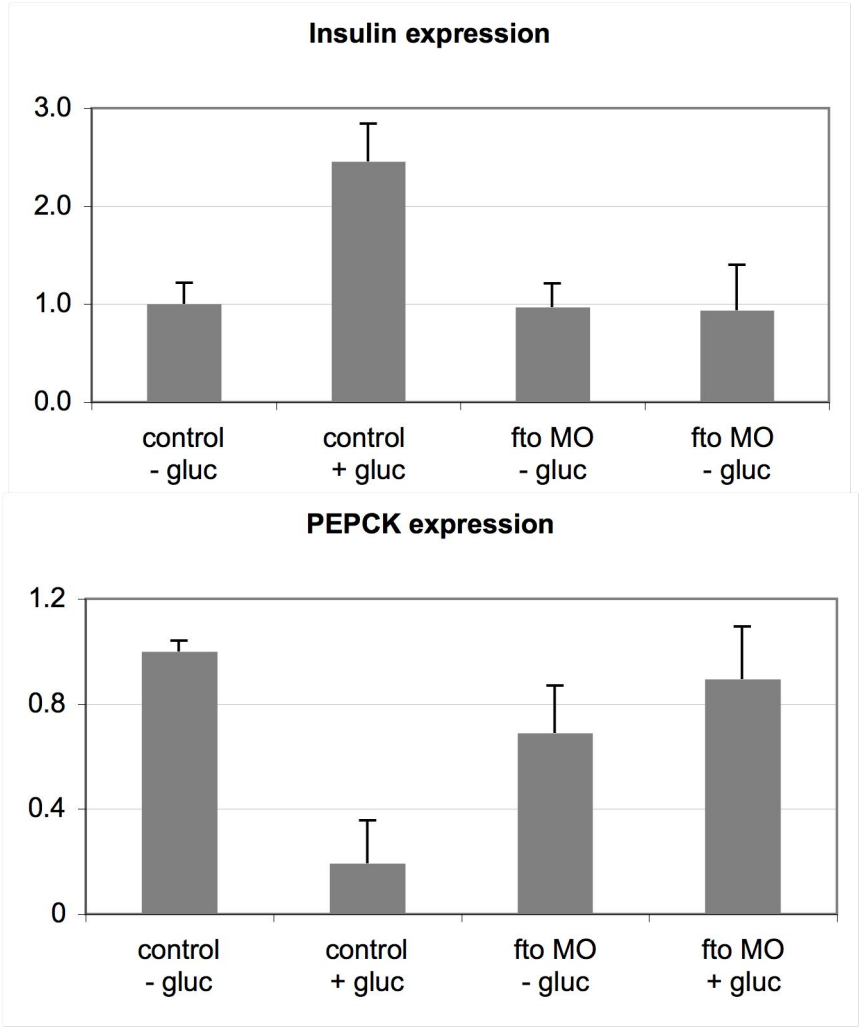

Figure 87. Glucose responsiveness assay in *fto* morphants.

A: addition of glucose to control embryos stimulated the expression of *insa* by 2.5-fold. This upregulation failed to take place in *fto* morphants. **B**: *pepck* was downregulated in controls upon addition of glucose. This downregulation did not occur in *fto* morphants.

These results must be interpreted cautiously, as morphant embryos show a very strong phenotype by 4dpf, including renal oedema, probably resulting in impaired function. The general ill health of the embryos might be a contributory factor in their lack of cellular response to glucose stimulation. However, the results of these experiments have led to studies on insulin secretion and response performed on RNAi models in cultured mouse pancreatic β-cells. As yet, a mouse model for FTO knockout has not been published and so the cultured cells are a substitute system.

To investigate the zebrafish phenotype further, I attempted to visualise the size and shape of the pancreas by *in situ* hybridisation using the markers *insa* for the

mature pancreas and *pdx1* as a marker of early, presumptive pancreas. Unfortunately, no reliable data was obtained from these studies as the probes failed to hybridise specifically to the pancreas in several, repeated attempts, despite published examples of their efficacy.

Investigating potential involvement of Fto with the non-canonical Wnt pathway

Fto morphants show the CE-defect reminiscent of several ciliopathy morphants showed to be important in non-canonical Wnt signalling. Non-canonical Wnt signalling is important for the development of vertebrate islet cells in the pancreas. Disruption of *TCF7L2*, a downstream transcription factor in the Wnt pathway, is highly associated with Type II diabetes and obesity in human genome-wide studies. Considering these facts, I decided to try to determine if Fto was involved in non-canonical Wnt signalling. Despite the published finding that type 2 diabetes in humans appears to be secondary to obesity, strong and specific expression of *FTO* in the pancreas suggests it is having a role here.

To do this, I took advantage of the fact that over-expression of Frizzled-7 (Fz7), a seven-pass transmembrane receptor of Wnt ligands, induces a change in localisation of Dishevelled from the cytoplasm to the plasma membrane. I performed analyses on gastrula-stage embryos, because non-canonical Wnt signalling is important during gastrulation and the cells are easy to visualise at this stage.

Injection of 100pg *fz7* mRNA induced the membrane localisation of GFP-tagged Dishevelled. To see if this response was affected by expression of *fto* I co-injected 50pg Myc-tagged *fto* mRNA, 100pg *fz7* mRNA, and 100pg *Dvl-GFP* mRNA. I then visualised the localisation of Dishevelled by confocal microscopy. When Dvl-GFP and Fz7 mRNA were co-injected, Dvl localised at the plasma membranes of 5hpf zebrafish cells due to induction of the non-canonical Wnt pathway by Fz7 (Fig. 88A). When these constructs were injected alongside a Myc-tagged *fto* mRNA, the Dvl became more diffusely cytoplasmic, and less

strongly expressed at the plasma membranes (Fig. 88B). Fto protein could be detected in the nuclei. This suggested that over-expression of Fto induced the canonical Wnt pathway at the expense of PCP, consistent with the CE defect seen in *Fto* over-expressing embryos. However, this assay is crude and may not be sensitive enough to reveal subtle effects on the signalling pathway. However, knock down of *fto* failed to affect the subcellular localisation of Dvl-GFP in the absence of Fz7.

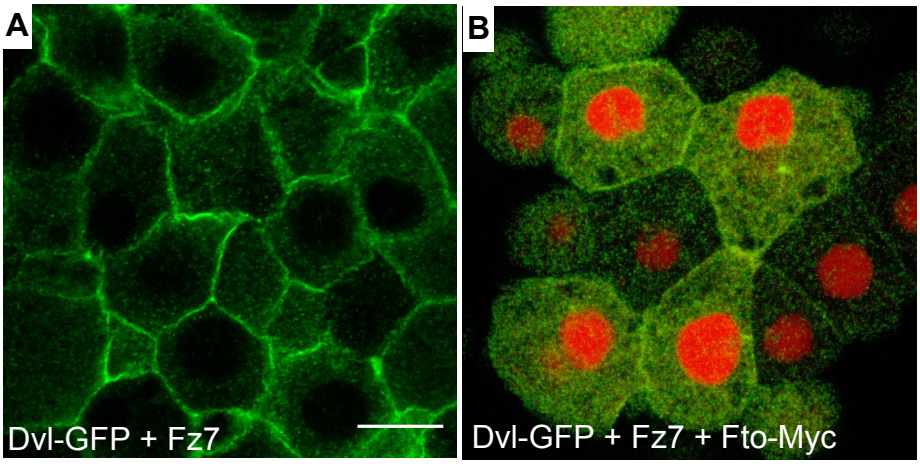

Figure 88. Dishevelled localisation upon Fto over-expression.

A: co-injection of *fz7* and *dvl-GFP* mRNA caused membranous localisation of Dvl-GFP. **B**: co-injecting these constructs with myc-tagged *Fto* mRNA showed nuclear localisation of Fto and more cytoplasmic localisation of Dvl-GFP. Scale bar = 10μm.

An epistatic relationship between Fto and Ftm

Ftm is a gene directly adjacent to *Fto* in the 1.6Mb interval containing the six genes deleted in the *fused toes* mouse mutant. Ftm (Rpgrip1L) is a *bona fide* ciliary protein, localising to the basal body. Mouse mutants have laterality, limb, and neural tube defects. Ftm plays a role in Shh signalling by regulating the processing of Gli3, just like other ciliary and IFT proteins. *Fused toes* homozygous mutants die during gestation but the heterozygote embryos survive and show similar phenotypes to the *Ftm* null, suggesting that *Ftm* might be the major contributor to the phenotype. However, Peters et al (1999) found that expression of *Fto* was absent in *fused toes* homozygous mutants and concluded that this gene was the major contributor.

Ftm is transcribed in the opposite direction to *Fto* and it has been suggested that the intronic SNPs in *Fto* associated with increased fat mass might regulate the expression of *Ftm*. These intronic SNPs are of unknown function, but it is feasible that they may alter splicing and it is known from work in our lab that there exist both long and short isoform in humans, which are differentially expressed in the brain and pancreas (our unpublished data). Given the clues that Fto might be involved with ciliary function, Ftm's ciliary localisation, *FTM* mutation causing Joubert syndrome, and the chromosomal proximity of *Fto* and *Ftm*, I aimed to test if there was any interaction between the two genes, to see if they functioned in the same pathway.

To do this, I performed double injections of *fto* and *ftm* MOs. A range of MO concentrations were tested, each time quantifying the percentage of embryos with a morphological phenotype consisting of a shortened body axis at 24hpf. Injection of 1.5ng of each MO individually caused no phenotype in any of the embryos (Fig. 89A,B). Injecting 4ng of either *fto* or *ftm* MO caused severe shortening and downward curvature of the body axis in both cases (Fig. 89C,D). *Ftm* morphants were more severely affected, with misshapen, flattened somites, and a malformed head.

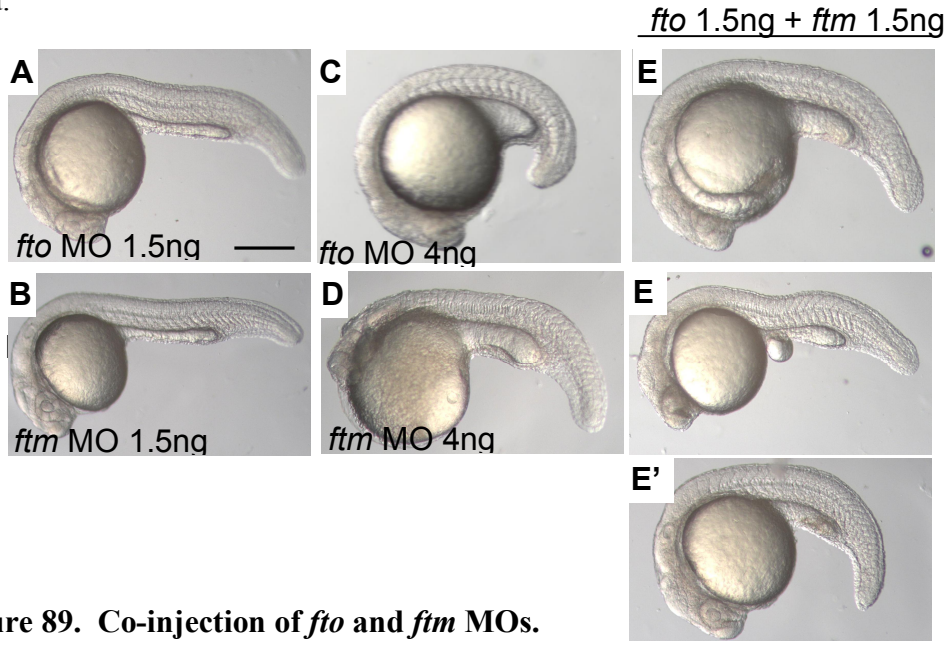

Figure 89. Co-injection of *fto* and *ftm* MOs.

A,B: injection of 1.5ng of *fto* and *ftm* had no observable phenotype. **C,D**: 4ng of either MO caused a severe phenotype. **E,E',E''**: co-injection of 1.5ng of *fto* and *ftm* MOs caused a severe phenotype reminiscent of the 4ng single MO injections. Scale bar = 500μm.

When 1.5ng of each MO were co-injected, embryos exhibited the downward curved body axis and widened somites of the individual morphants (Fig. 89E,E',E''). The phenotype more closely resembled the *fto* single morphants, as the head patterning was not affected and the somites and yolk stalk were not as misshapen. These data suggest that *fto* and *ftm* function in the same pathway and that Ftm might lie upstream of Fto as the double knockdown revealed the *fto* phenotype.

Discussion

Functional characterisation of Fto

FTO is the first gene to be identified as a potential cause of complex obesity in the general population. While the genetic association between an intronic SNP in *FTO* and increased fat mass and type 2 diabetes is unquestionable, the function of the FTO protein is less well characterised. Evidence suggests that it functions in DNA methylation, but how this influences fat deposition is unknown. Its expression in the satiety centre of the brain and pancreas suggests that it could serve to regulate appetite or energy metabolism, but it could function in the pancreas to regulate insulin secretion. It is possible, but unlikely, that it can cause obesity by all three mechanisms.

The effect of the intronic SNP on protein function is also not known. It could affect splicing of the protein as is the case for *TCF7L2* (Douglas et al., 2001). It is likely that any alteration to the peptide will cause a loss of function to the protein, evidenced by homozygotes being more severely affected than heterozygotes for the SNP.

No *in vivo* data exist on the function of FTO, but clues can be derived from the *Ft* mutant mouse and other data, which suggest possible co-regulation with the adjacent *Ftm* gene, a *bona fide* ciliary gene involved in Shh signalling. Because genetic changes in an intronic SNP are difficult to model *in vivo*, I took a simple approach and used the zebrafish to produce both gain- and loss-of-function *fto* models. Both loss- and gain-of-function models produced a phenotype, but the morphant phenotype was more severe, suggesting that *fto* is important in development. Human *Fto* mRNA was able to fully rescue the morphant phenotype.

The localisation studies on zebrafish showed a ciliary localisation of Fto in gastrula stage embryos. However, the tagged protein localised to the basal body in the ciliated cell lines 3T3 and IMCD3. It is known that some tagged proteins artefactually localise to the basal body and so this data may be spurious. We

produced a proprietary Fto antibody to recognise mouse and human epitopes and it will be important to characterise sub-cellular localisation in mammalian cells and tissues.

FTO is associated with type 2 diabetes, in which the body is insulin-resistant. It is possible that this is secondary to obesity, wherein the body over-produces insulin in a response to overeating after which the receptive cells become progressively less responsive to it. The best way to manage this type of diabetes is through dietary control, as administration of exogenous insulin is ineffectual.

To test if *fto* morphants had defects in glucose homeostasis, I treated 4dpf embryos with glucose adapting the protocol of (Elo et al., 2007). In controls, this resulted in the upregulation of the *preproinsulin* gene and the downregulation of *pepck*. *fto* morphants failed to respond to glucose treatment, suggesting a defect in glucose homeostasis, or at least transcriptional response to glucose stimuli. Baseline levels of *preproinsulin* were unaffected, suggesting there was not a problem with pancreatic production of insulin. To test if this was due to a defective pancreas, I tried to examine expression of pancreatic markers but failed to get reliable data.

Upregulation of the *preproinsulin* gene in response to glucose is a long-term effect. What normally happens in physiological conditions is that insulin self-cleaves and is secreted from cells in response to the hypothalamic detection of increased blood glucose concentration. Measuring serum insulin levels in zebrafish embryos is almost impossible, and so to do this a mouse model, or at least a cell line, would be used. In the absence of a mouse model, a member of our lab has used siRNA to knockdown *Fto* in a pancreatic β-cell line. Glucose is then added to the cells and insulin secretion measured by ELISA. At the time of writing, no data were available from these experiments, but it will be interesting to see if *Fto* knockdown affects pancreas function.

The Wnt pathway is known to play an important role in pancreatic development. Canonical Wnt signalling induces proliferation of islet cells (Rulifson et al.,

2007). Conditional expression of *Axin3*, a potent inhibitor of canonical Wnt signalling in β-cells, resulted in a reduction of insulin production. Kim et al (2005) showed that knockdown of *wnt5a*, a non-canonical Wnt ligand, and *fz-2* – a noncanonical pathway receptor, both yielded hypoplastic pancreas because of impaired cell migration (Kim et al., 2005). *Wnt5a*$^{-/-}$ also had reduced pancreatic mass.

In light of this, I tried to see if Fto perturbed canonical Wnt signalling in a Frizzled-dependent manner. Overexpression of myc-tagged Fto protein abrogated the membrane localisation of Dvl in response to Fz7. This suggests that overexpression of Fto is capable of inhibiting the non-canonical Wnt pathway. To test to see if there is an interaction between FTO and the non-canonical Wnt pathway in development, *fto* MO could be injected at sub-phenotypic doses into PCP mutant zebrafish embryos, such as *trilobite* and *strabismus*, to see if this enhanced the mutant phenotype. A similar approach was carried out by Ross et al (2005) to show a genetic interaction between *bbs4* and the PCP pathway. This has also been used to demonstrate genetic interactions between ciliopathy genes such as *bbs1*, *bbs4*, *bbs6*, and *bbs8* (H. May-Simera, thesis) with the PCP pathway (Gerdes et al., 2007).

Chapter 8: Determining the functional importance of the interaction between ACAT1 and BBS1

Introduction

The association of a metabolic enzyme and BBS1 in *C. elegans* fat storage

Obesity is the most persistent feature of BBS, yet its molecular aetiology is unknown. Understanding the mechanism of lipid accumulation in monogenic diseases will be informative about non-syndromic obesity prevalent in the population in general, whose basis is complex and under the control of many loci.

Mak et al (2006) performed a screen for mutants which enhanced the fat accumulation phenotype of the nematode orthologue of *Tubby*, a mouse mutant with BBS and ciliopathy-like features: obesity, retinal degeneration, and hearing loss (Mak et al., 2006). They proved that this increase in lipid accumulation was not due to reduced movement, reproduction, or increased food consumption or retention.

They isolated a single gene that consistently enhanced lipid accumulation and found it to encode a 3-ketoacyl-coA thiolase (encoded by *kat-1*), a conserved member of the mitochondrial fatty acid β-oxidation pathway. *Tub-1* or *kat-1* single mutants both showed 50-100% increase in fat accumulation relative to wild types. However, double knockout enhanced fat accumulation to 9-times wild type levels, indicating a genetic interaction, or synergism. They then showed that *kat-1* activity, in the gut in particular, contributed to lipid accumulation and suggested that *tub-1* function in ciliated neurons was controlling the release of a neuroendocrine signal regulating fat storage in the gut.

They then performed another screen for mutants that enhanced the *kat-1* single mutant phenotype, and isolated *bbs-1*. They narrowed down the site of control of lipid accumulation to a subset of 15 out of the total 60 ciliated neurons in *C.*

elegans, possibly linked to these neurons' requirement in sensation of external and internal nutrient level and their control of the β-oxidation pathway.

β-oxidation is the biochemical process by which fats are broken down into acetyl-coenzyme A molecules, the entry molecule for the Krebs cycle. β-oxidation takes place in the peroxisome or mitochondria and occurs via four recurring steps: 1) the fatty acid is oxidised by a dehydrogenase; 2) the newly formed double bond is hydrated, forming a hydroxyl group; 3) this new hydroxyl group is oxidised by NAD^+ to form a ketone group; 4) a thiol group (containing sulphur) is inserted between two acetyl groups to yield two molecules of acetyl coA. The last step is catalysed by the β-ketothiolase encoded by *kat-1*.

The human orthologue of *kat-1* is *ACAT1* (acetyl coA thiolase, also called *T2*) and has 41% identity with the *C. elegans* sequence at the protein level. Mutations in *ACAT1* cause 3-ketothiolase deficiency, a rare autosomal disease affecting only 50-60 patients worldwide. It manifests clinically with dehydration, tiredness, seizures, ketoacedosis, damage to the CNS, and possibly coma. Mutations in humans do not cause obesity but lead to accumulation of ketones (ketoacedosis) in the bloodstream when fats are broken down. As such, it is intriguing that mutations in this gene should modulate the severity of the fat accumulation in ciliopathy-derived obesity.

Testing the association in BBS patients

Mak et al showed that *kat-1* genetically interacted with several obesity-related ciliary genes, particularly *bbs-1*. In light of this, scientists from our group tested if there were changes in *ACAT1* in patients with *BBS1* mutations, common in the Caucasian cohort and accounting for approximately 20% of all BBS patients. They found a highly significant over-representation of a non-synonymous SNP resulting in an alanine to proline substitution at amino acid position 5 (A5P). This is present at a frequency of around 20% in *BBS1* mutant patients, compared with 5% in the general population.

Collaborators at Johns Hopkins University repeated this screen for the other BBS genes and found similar over-representations of the *ACAT1* SNP (unpublished data). This increase in allele frequency amongst BBS patients is too great to be due to chance and so is likely to have some functional relevance modifying obesity presentation, as it did in *C. elegans*.

The aims of this study

Given the functional epistatic relationship between *bbs-1* and *kat-1* in *C. elegans*, and the genetic association in humans, I wanted to test if the A5P substitution had an effect on protein function by modelling the mutation in the zebrafish. Japanese collaborators tested the enzymatic activity of the mutant protein and showed it not to be affected in *in vitro* assays. This may be because the substitution occurs well outside of the catalytic domain. A member of our lab also showed that tagged mutant protein still localised to the mitochondria like the wild type protein, but the data was not fully conclusive due to indistinct staining and high levels of background immunofluorescence.

I aimed to perform the following experiments:
1) Test whether *acat1* and *bbs1* interact in the zebrafish
2) Test whether the mutant allele of *ACAT1* could rescue the morphant phenotype

Results

ACAT1 and BBS1 genetically interact in the zebrafish

Mak et al (2006) showed that *kat-1* and *bbs-1* functionally interacted in *C. elegans*. The human orthologue of *kat-1* is *ACAT1*, acetyl co-enzyme A transferase 1 (also called acetyl coA thiolase T2). Sequence analysis performed in our laboratory identified a non-synonymous SNP in the human *ACAT1* gene highly over-represented in patients with *BBS1* null mutations (20% vs 5% in controls).

To see if this association between *BBS1* and *ACAT1* had functional consequences, I performed double knock-down experiments in the zebrafish and assessed the severity of the phenotypes by counting the number of embryos morphologically normal, with a CE defect (phenotype), or dead.

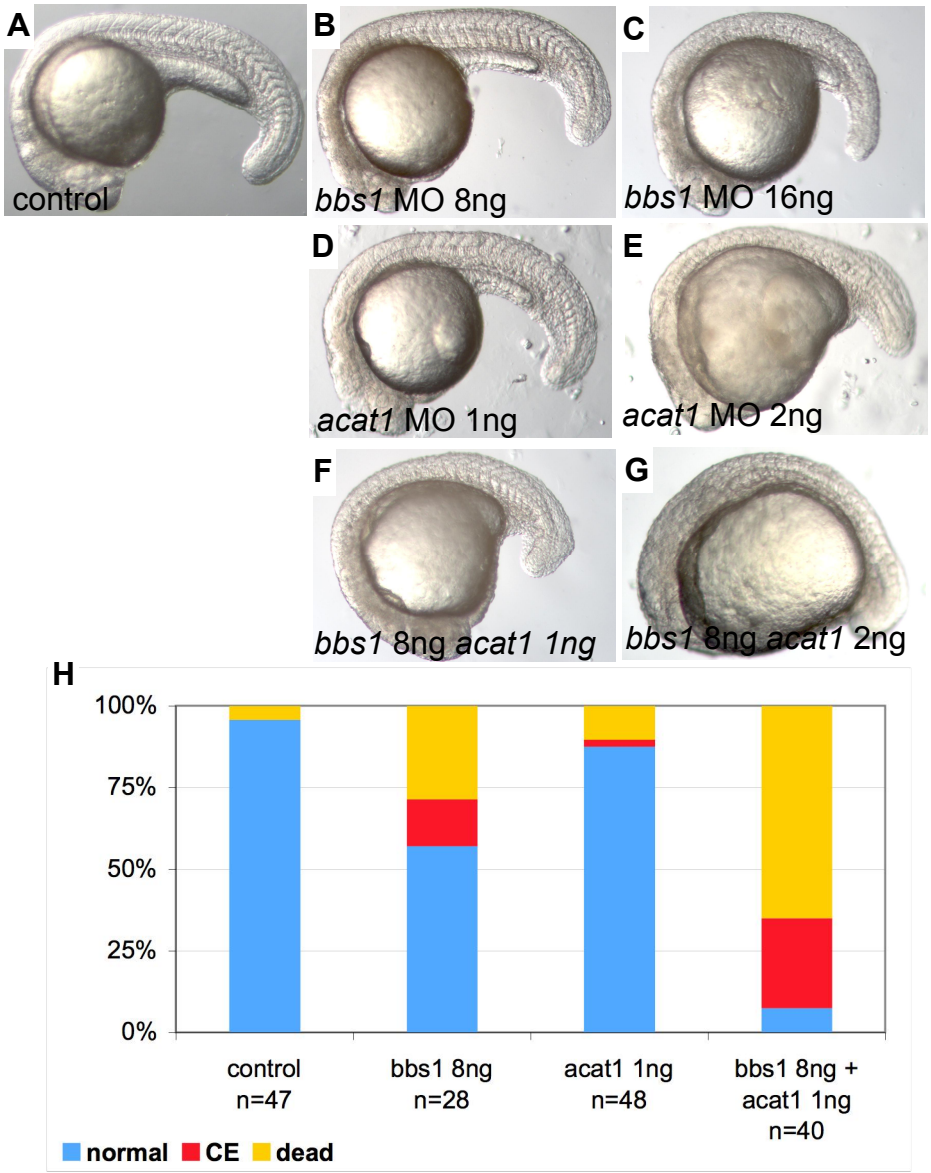

Figure 90. *acat1/bbs1* MO double injections.

A: control embryo at 24hpf. **B**: 8ng *bbs1* MO yields a mild phenotype with 43% of embryos affected. **C**: 16ng *bbs1* MO gives a more severe CE defect and a higher percentage (89%) are affected. **D**: 1ng *acat1* MO gives a moderate phenotype, 13% of embryos are affected. **E**: 2ng *acat1* MO gives a severe phenotype with 45% affected. **F**: co-injection of the lower doses of *bbs1* and *acat1* MOs gives a synergistic phenotype with 93% of embryos affected and the phenotype is much more severe than either MO alone. **G**: injecting 8ng *bbs1* MO with 2ng *acat1* MO gives an extremely strong phenotype where the tail fails to extend at all. **H**: graph quantifying the effects of the MOs showing that the double injection demonstrates an interaction between the two genes.

In controls, 96% of embryos were normal at 24hpf and 4% were dead (n=47) (Fig. 90A,H). Injection of 8ng or 16ng of *bbs1* MO led to 43% (n=28) and 89% (n=36) respectively of embryos showing a phenotype or being dead (Fig. 90B,C,H). Injection of 1ng *acat1* MO caused 13% (n=48) of embryos to be affected (dead or phenotype) (Fig. 90D,H). Co-injection of 8ng *bbs1* MO with 1ng *acat1* MO led to 93% of embryos being affected (Fig. 90F,H). If these effects were additive one would expect approximately 57% of embryos to be affected by the co-injection. The fact that 93% were affected suggests that the two genes function synergistically to give a multiplicative effect. These data suggests that Bbs1 and Acat1 functionally interact in an unknown cellular process.

The obesity-related SNP in *ACAT1* fails to rescue *acat1* knockdown

I next wanted to test if the SNP found in the human gene affected the function of the protein. To do this I generated a wild type and mutant human constructs and used these to create wild type and mutant mRNA. I then injected these into zebrafish *acat1* morphants and tested the potential of each transcript to rescue the *acat1* morphant phenotype.

Knocking down *acat1* with 2ng of MO resulted in 96% of embryos being either phenotypic or dead (Fig. 91A). 100pg of wild type mRNA was insufficient to rescue this, but co-injection with 200pg reduced the number of affected embryos to 63% and the severity of the embryos with the phenotype was much less (Fig. 91B). It is difficult to quantify this objectively, but the images show a representative group of rescued embryos, some of which are still classified as having a phenotype, but are clearly much less severely affected than when MO was used alone.

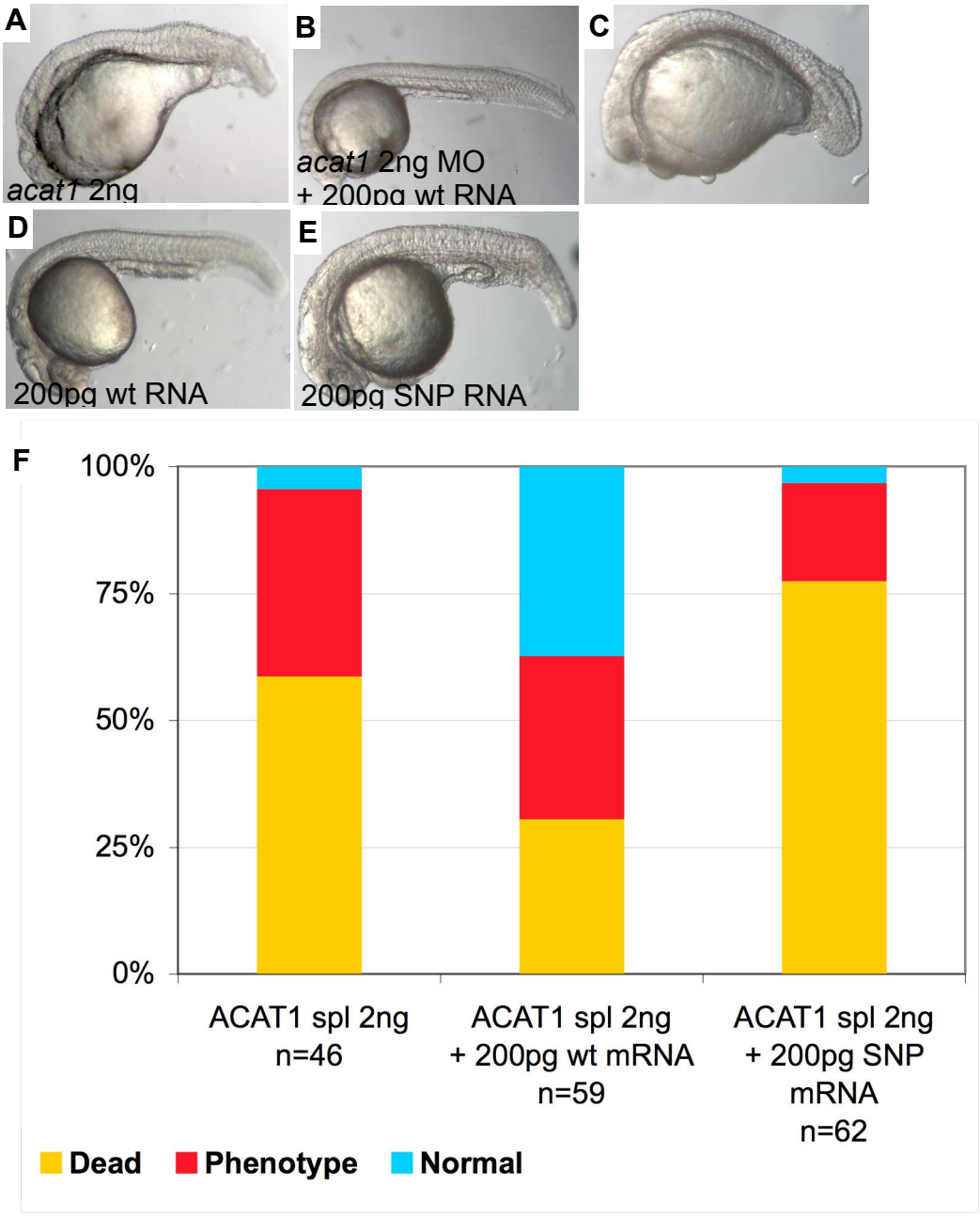

Figure 91. Rescue of the *acat1* morphant phenotype with mutant mRNA.

A: 2ng *acat1* MO causes a severe morphological phenotype at 24hpf. **B**: co-injection of 2ng MO with 200pg wt human mRNA rescues the phenotype in a large proportion of the embryos. **C**: co-injection of the MO with the A5P mutant mRNA fails to rescue the phenotype and arguably makes it worse. **D**: 200pg of human mRNA alone causes no phenotype. **E**: 200pg mutant (A5P SNP) mRNA gives a phenotype with a misshapen body-axis and poorly extended yolk stalk. **F**: quantification of the phenotype shows partial rescue with the wt human mRNA but not with the mutant mRNA.

When the mutant mRNA was co-injected with 2ng of MO, the phenotype was not even partially rescued, rather it was slightly exacerbated with the number of dead

embryos increased from 59% (MO alone) to 77% (Fig. 91C). The morphology of the mutant rescue embryos shows severe shortening of the body axis and significant amounts of cell death. The fact that the mutant mRNA made the phenotype worse suggests that it is having a dominant negative effect. Indeed, injection of 200pg of mutant mRNA alone caused a phenotype in its own right, while the same amount of wild type mRNA had no effect (Fig. 91D,E).

Discussion

The original paper by Mak et al showed the nematode *kat-1* gene to genetically interact with *bbs-1* to enhance lipid accumulation. Work performed in our laboratory showed that a non-synonymous SNP (A5P) in the human orthologue of *kat-1*, *ACAT1*, is highly associated with patients with homozygous mutations in *BBS1*. The frequency of this SNP in *BBS1* patients is around 20% compared with <1% in the general population. Elaboration of this study by collaborators in Baltimore showed this SNP to be associated with all BBS patients, regardless of underlying mutation.

This is a surprising result, since it is difficult to imagine why this allele should be so enriched in patients with mutations in ciliopathy genes. Furthermore, the most promising current hypothesis to explain obesity in BBS patients is a defect in the satiety regulating neurons of the hypothalamus. ACAT1 is a metabolic enzyme involved in fat metabolism. It is thought that metabolic rate and energy metabolism is normal in BBS patients. It is possible to speculate that output from the hypothalamus regulates the activity of ACAT1's fat metabolism by signalling to adipocytes in which ACAT1 potentially functions. Why genetic changes in *ACAT1* should be associated with BBS mutations is unknown.

It is known that the *ACAT1* SNP is reproducibly associated with BBS. The SNP is not thought to abolish enzyme activity, but it might alter mitochondrial localisation of the protein. I found that knockdown of *acat1* in the zebrafish produced a very dramatic phenotype, even with moderate amounts of MO. I titrated the dose down to a level where almost no phenotype was seen and co-injected this with an equally low amount of *bbs1* MO. The re-emergence of a phenotype suggested that *bbs1* and *acat1* functionally interact in some way, suggesting that they act in the same biological pathway. What the epistasis experiments in the zebrafish show is that the nematode-based relationship between *BBS-1* and *ACAT-1* is conserved in vertebrates. What the biological mechanism underpinning this relationship might be remains a mystery.

The *acat1* morphant phenotype could be rescued by co-injecting wild-type *ACAT1* human mRNA. However, co-injecting the A5P mutant mRNA failed to rescue the morphant phenotype. This shows that the A5P substitution negatively affected the function of the protein. Whether this is due to affects on enzyme activity, subcellular localisation, or something else is unknown. It will be important to understand the exact effect of the A5P allele on subcellular localisation and biochemical activity. It is also important to determine if the A5P mutant protein is stable or degraded in the cytoplasm. This could explain the loss-of-function phenotype associated with it. This could be done by Western blotting the wild type and mutant proteins. Enzymatic assays for the activity of the mutant enzyme should also be performed.

To extend these studies, it would be worth screening all other known obesity- and non-obesity related ciliopathies to see if the genetic association persists. If the association is present only in obesity-related ciliopathies, it might be that the *ACAT1* allele is contributing to the obesity phenotype. If it is present in all ciliopathies, it might mean that *ACAT1* is in someway associated with the cilium, or reliant on microtubule transport. It is important to combine genetic, hypothesis-generating experiments with functional studies on proteins in order to understand the biological significance of the genetic phenomena observed. Potential mitochondrial roles for BBS proteins are the subject of current further, ongoing investigation in the laboratory.

Chapter 9: Conclusion

Summary of findings

This work aimed to understand more about the basis of ciliopathies. This resulted in the following findings being made:

1) Craniofacial dysmorphology in man, mouse, and zebrafish BBS knockouts was modelled and attributed to midfacial bone hypoplasia.
2) A new role for Bbs8 in NCC migration was established, possibly via a role in PCP signalling and regulating actin cytoskeletal dynamics. This is the first time ciliary proteins have been directly linked to cell migration.
3) Bbs8 and Ift80 are involved in Shh signalling, at the level of Gli3 function.
4) Rapamycin and Roscovitine are able to restore renal function in zebrafish models of ciliopathies, providing proof of principle for pre-clinical studies in mouse models.
5) The possibility of Fto as a new cilia-related protein was explored using the zebrafish as a model.
6) The genetic association of an *ACAT1* SNP with BBS mutations was modelled in zebrafish and shown to have functional relevance to development.

Together, these findings add to our, at present, scant knowledge of ciliopathies. The craniofacial investigation is the first time characterisation of human dysmorphology has been used to elucidate novel biological roles for a protein. This approach is a model for the study of other malformation syndromes. Modelling the ciliopathies in zebrafish provided, for the first time, potential therapeutic avenues to treat the kidney disease associated ubiquitously with all ciliopathies. This is the first time a therapeutic investigation has been carried out for ciliopathies. It is also the first time the zebrafish has been used as a model to test drugs to treat renal disease.

Characterisation of craniofacial dysmorphology

The facial gestalt of BBS patients has been reported before in the literature, (Beales et al., 1999, Lorda-Sanchez et al., 2001) but it has been difficult for clinical dysmorphologists to characterise it, due to its variability. Peter Hammond has performed dense-surface modelling to show statistically significant midfacial flattening and hypoplasia of the nasal bridge, maxilla, and retrognathia. Skull preparations from BBS mutant mice showed homologous bones in the snout were hypoplastic, resulting in a shortened snout and a higher cranial vault.

Zebrafish morphants of three BBS genes: *bbs4*, *bbs6*, and *bbs8* showed shortening of the trabeculae, which are structures homologous to the upper jaw of mammals. Mandibles and branchial arches were hypoplastic, and sometimes absent from *bbs8* morphants. These embryos also had cyclopia and midline fusion of the trabeculae with absence of the anterior ethmoid plate. These defects were strikingly similar to Shh pathway mutants, or embryos treated with chemical inhibitors of Smo. Midline defects in the zebrafish skull were extreme examples of two mild HPE phenotypes infrequently observed in BBS patients: fusion of the maxillary incisors, and hypoplasia or agenesis of the corpus callosum.

The application of dense surface modelling to a syndrome with subtle and variable features, such as BBS, is novel, as previously it has only been used to characterise obvious facial deformities. This application provides proof of principle for its use in other syndromes with previously undocumented facial features. The use of 3D laser scanning on mouse skulls has not been reported before this work, and its application provides a way of validating the biological significance, and exploring underlying cellular and molecular aetiologies, of a condition. Further extension of the analysis to the zebrafish allows a finer scale resolution of the underlying pathways potentially involved.

Discovery of a new role for BBS proteins in neural crest migration

The bony regions of the face affected by BBS knockdown all derive from the cranial neural crest, a migratory population of cells deriving from the anterior

neural tube. I showed that the degree of CNCC migration inhibition was correlated with the severity of the craniofacial phenotype, and was consistently most pronounced in *bbs8* morphants. Neural crest induction, maintenance, or proliferation was unaffected in *bbs8* morphants and the number of crest cells was similar to controls. However, the cells failed to emigrate from the neural tube, and the distance migrated was around one quarter of controls. At later stages, cells did populate the head, but failed to extend into the most anterior portions to extend the trabeculae and form the ethmoid plate. A similar mechanism would also account for the craniofacial defects also seen in humans and mice.

Evidence that Bbs8 might play a role in pan-NCC migration came from the clear observation that *bbs8* morphants lacked pigmentation and melanocyte precursors, a trunk NCC-derived lineage. Furthermore, these embryos had incomplete colonisation of the gut by enteric neurons, which correlated with a loss of gut peristalsis. This finding offers a likely explanation as to why Hirschsprung's disease is so common amongst BBS patients.

The function of Bbs8 in NCC migration was shown to be cell autonomous. Higher-power images of CNCCs at the leading edge of the dorsal stream of cells migrating caudally around the eye, showed morphant cells to lack filopodial or lamellipodial protrusions. In contrast, these protrusions were generally aligned in the direction of migration in controls. This hinted at a loss of cell polarity, and Bbs4 and Bbs8 have previously been implicated in the PCP pathway (Ross et al, 200, H. May-Simera, thesis). Epistasis experiments with two different mutant Dishevelled constructs suggested that downregulation of PCP by *bbs8* knockdown might be responsible, at least in part, for the inhibition of migration. These findings are in keeping with results from Roberto Mayor's laboratory, where they have shown PCP to be important for NCC migration in both *Xenopus* and zebrafish (De Calisto et al., 2005, Matthews et al., 2008).

Because PCP signalling controls cell polarity by organising the actin cytoskeleton, I attempted to visualise actin microfilaments in migration CNCCs. No clear data was obtained due to the confounding effects of surrounding cells. To get a clearer

view, I cultured mouse cell lines and human primary cells both deficient in *Bbs8*. To induce directional cell migration I performed a scratch assay. Surprisingly, both types of cultured fibroblast migrated significantly slower than their respective controls. Furthermore, the actin cytoskeleton was disordered and mispolarised in both cases. This finding is interesting in light of work by Park et al (2006), who showed that disrupting the actin cytoskeleton by perturbing PCP signalling resulted in mispositioned basal bodies and intracellular cilia, in which the axonemes projected into the cytoplasm. As such, this opens up a completely unexplored area of research whereby BBS proteins could also regulate the actin microfilaments, possibly via PCP signalling, and this could determine basal body, and hence ciliary, position.

These experiments highlight two findings to follow up: firstly, the possibility that BBS8 is important for cell migration in general, not just in the neural crest, and possibly for wound healing; and secondly, that the actin cytoskeleton is mispolarised in these knockout cells. Future work in this area will be to further elucidate the role of BBS proteins in cytoskeletal arrangement *in vivo*, as well as the potential role for BBS proteins in wound healing.

To better understand how Bbs8 is involved in NCC migration, preliminary work has been performed to elucidate differential gene expression profiles in NCCs at stages of active migration in control and morphant zebrafish embryos using gene expression microarrays. Protocols have been optimised for cell purification by FACS and RNA recovery. So far, no expression data has been obtained but this will be the next piece of work to carry out.

Involvement of ciliopathy proteins in Shh signalling

The high penetrance (70%) of post-axial polydactyly in BBS and other ciliopathies (MKS, JATD, OFD1), as well as evidence from published IFT mutant mice and the known role for cilia in Shh signalling, suggest that this pathway is disrupted in BBS. Further clues come from the craniofacial abnormalities, particularly the midline defects in *bbs8* morphants. Downstream Shh target

genes, *nkx2.2*, and *ptc1* were downregulated in all morphants, but particularly *bbs8*, especially in the head. The result was confirmed by the upregulation of the negatively regulated gene, *pax6* in morphants. Epistasis experiments showed that *bbs8* functions downstream of Ptc1 and is likely to be involved at the level of Gli3 processing and transport.

Cellular assays showed that *Bbs8* knockdown cells were insensitive to high levels of exogenous Shh ligand, but zebrafish data suggested that the cells could respond to medium levels, as seen by normal expression of *nkx6.1*. These data suggest that Bbs8 is not essential for Shh pathway activity, but is needed for maximal signalling activity. Gli3 processing in response to Shh stimulation was shown to be defective in Bbs8 knockdowns. Immunofluorescent and cell fractionation data hinted that Gli3 may be mislocalised in Bbs8 mutant cells, and co-immunoprecipitations suggested a potential physical interaction between Bbs8 and Gli3. However, uncertainties about the reliability of the Gli3 antibody for immunofluorescence confound the reliability of these results. Proteomics could reveal potential interactions between other ciliopathy proteins and Shh signalling pathway molecules.

Future work will involve examining pathway activity at the cilium in real time. To do this, the ciliary axoneme will be fluorescently labelled and the localisation of tagged Shh proteins, such as Smo and Gli3, will be visualised. Fluorescent recovery after photobleaching (FRAP) will be used to bleach a small region of the cilium, and the rate of movement of the signalling molecules will be measured in response to exogenous stimulation with purmorphamine. This is a highly ambitious project with many technical hurdles to overcome, but will be more revealing than the indirect luciferase and Gli3 processing assays currently performed.

Development of the zebrafish as a tool to test drugs for kidney disease

I then turned to expanding the repertoire of zebrafish ciliopathy models and created morphants of ten ciliopathy genes, chosen to be representative of the whole spectrum of diseases. All of these morphants developed kidney cysts, followed by renal oedema. In addition, I observed several other cilia-specific phenotypes: laterality defects and unusual numbers of otoliths in the ear. This has implications for understanding the malcoordination and balance problems BBS patients have.

The renal oedema could be specifically rescued by two drugs previously shown to be efficacious on mouse models of PKD: Rapamycin and Roscovitine. In addition to reducing the size of the kidney swelling back to control levels, Rapamycin was able to restore the filtering function of the kidney from around 10% of control levels to around 50%, therefore improving kidney function by about 5-fold. Roscovitine was also able to reduce swelling size and restore some function to the kidney, but was never as effective as Rapamycin.

The functional assay was able to differentiate quantitatively between the efficacies of the two treatments. This validates it as a tool to evaluate compounds to progress to trials on mouse models of ciliopathies. If data are promising from these experiments, it paves the way to perform trials in humans. This might have the potential to alleviate the need for ciliopathy patients to spend the rest of their lives on renal dialysis or be reliant on transplantation. However, more work needs to be done to reveal the precise molecular and cellular aetiology of the complex renal phenotype in diseases like BBS and NPHP.

Future work will involve scaling up the proof of concept experimental system developed here. This will involve developing medium to high-throughput small molecule screens to test kidney disease drugs. In future, this might be a valid method to identify candidate molecules *in vivo*, as it is more physiologically relevant than using isolated recombinant protein targets or cell-based bioassays. In addition, the zebrafish assay has the advantage of in-built toxicological

screening. Any candidates identified in the zebrafish can then be tested on mouse models and, ultimately, humans.

Determining the function of the FTO protein

While numerous genes have been identified as candidates for monogenic syndromic obesity, the genetic aetiology of complex, polygenic obesity is not so well understood. *FTO* was the first gene to be associated with obesity in the general population. An intronic SNP increases the risk of obesity by around 70%. FTO protein function is not clear, although some data suggests a role in DNA methylation, although how this contributes to weight gain is unknown.

To try to gain some insight into potential function, I created knockdown and over-expression models of *Fto* in the zebrafish. Both treatments caused phenotypes, but the SNP in humans is likely to produce a hypomorphic allele, if it does affect protein function, but is hard to model as it lies in an intron. These morphants show some phenotypes usually associated with ciliary dysfunction: aberrant otolith numbers, convergent-extension defect, kidney cysts, and laterality randomisation.

Subcellular localisation studies on over-expressed, tagged Fto protein in zebrafish showed nuclear localisation. However, Myc-tagged Fto in ciliated cell lines revealed a basal body localisation. An FTO-specific antibody failed to resolve the discrepancy in localisation, as it produced no immunofluorescent signal. The only way to resolve this to observe endogenous, untagged protein would be to raise another antibody to a different FTO epitope.

A ciliary function would account for features seen in the *Fused toes* mouse mutant, which shows laterality, polydactyly, and craniofacial anomalies. These features manifest in the heterozygote, which is haploinsufficient for six genes. However, *Ftm* null mice phenocopy the *Ft* heterozygotes. Given evidence that *Ftm* and *Fto* might be coregulated, it is possible that the two genes interact in the same pathway, and so haploinsufficiency for both genes gives the *Fused toes*

phenotype. As Ftm is known to be a ciliary protein (Vierkotten et al, 2007), it is possible that Fto is as well, or it could be a downstream nuclear effector of Ftm.

To test this, I performed double MO injections with *fto* and *ftm* MOs and found there to be a genetic interaction between the two genes. This supports the proposition that the two genes function in a common biological process. Ftm is a ciliary protein that functions in Shh transduction. It is possible that Fto acts downstream of Ftm at the cilium and in the nucleus. More experiments will be needed to understand how Fto function relates to Ftm.

FTO is associated with type 2 diabetes in humans. I tested the transcriptional response to glucose stimulation in zebrafish, an indirect measure of glucose homeostasis, by quantifying the level of two genes regulated by increased blood glucose concentration. *Preproinsulin* was upregulated in response to glucose in controls, but not in *fto* morphants. Concurrently, *pepck* was downregulated in controls but not changed in morphants. These data suggest that *fto* morphants have defective glucose homeostasis. However, these data cannot be readily transferred to mammals because the morphant zebrafish show other phenotypes that might indirectly compromise their pancreatic function and general health. Cultured cell assays are being performed to follow up on this result in the absence of an *Fto* knockout mouse.

Testing the association between *BBS1* and *ACAT1*

ACAT-1 is the human homologue of the *C. elegans kat-1* gene, a metabolic enzyme involved in β-oxidation of fatty acids. *kat-1* was identified in a screen for mutants that enhanced the lipid accumulation phenotype of the *tub* mutant, also a ciliary protein. When a screen for genes enhancing the *kat-1* phenotype was performed, *bbs-1* was identified as the top enhancer. Work in our laboratory found a nonsynonomous SNP, A5P, to be more than 5-times over-represented in patients with *BBS1* mutations, than in controls. Extending this analysis revealed a similar enrichment for the SNP in all BBS patients, regardless of genetic background. The reason for this enrichment is unclear.

To test whether the A5P allele was affecting the function of the *ACAT1* gene, I performed knockdown of *acat1* in zebrafish and showed it to genetically interact with *bbs1*, confirming the *C. elegans* results. I then co-injected *acat1* MO with both wild type and mutant *ACAT1* human mRNA. This showed that the human mRNA was able to rescue the phenotype, but the SNP was not. In fact, the A5P mutant mRNA made the phenotype worse, suggesting it might have a dominant negative effect. This domain of the protein is outside of the catalytic domain but may be involved in protein targeting to the mitochondrion, or may be important in overall stability of the tertiary structure. This suggests that the *ACAT1* SNP might modify the phenotype in BBS patients. It would be interesting to see if the SNP is association with obesity in the general population.

These experiments fail to illuminate how the *ACAT1* SNP might enhance the obesity phenotype of human patients. To do this, more experiments would need to be performed on the subcellular localisation, enzyme activity, and potential interaction with ciliary processes.

Beyond the cilium

Since the aetiology of BBS was pinpointed to the cilium in 2003, the field has focussed its attention purely on ciliary roles for ciliopathy proteins such as BBS. However, it is likely that these proteins have roles outside of the cilium, due to the deployment of microtubule-based transport in the cytoplasm. Processes such as fast-axonal transport are similar in mechanism to IFT. BBS proteins such as BBS4 have been associated with cytoplasmic microtubules and organisation in cochlear hair cells (unpublished data from our laboratory). BBS proteins have been implicated in diverse functions, from proteosomal degradation, vesicle trafficking, sensory neuron function, cell cycle regulation, and intracellular signalling. It is therefore likely that these proteins function outside of the cilium as well, and identifying these roles will be a task for the future.

Appendices

Appendix 1: primer sequences

Primer name	Sequence (5' to 3')	Use of primers
Ptc-1 F	CTCCAAGTGTCGTCCGGTTT	Amplifying mouse P*tc1* for qRT-PCR
Ptc-1 R	CTGTACTCCGAGTCGGAGGAA	
Gli-1 F	TGGATATGATGGTTGGCAAGTG	Amplifying mouse *Gli1* for qRT-PCR
Gli-1 R	ACAGACTCAGGCTCAGGCTTCT	
Shh F	TCCAAAGCTCACATCCACTGTT	Amplifying mouse *Shh* for qRT-PCR
Shh R	CAGAGAACTCCGTGGCGGCCAAAT	
Bbs8 F	GCGCTGACAGAGATGGTGTA	Amplifying mouse *Bbs8* for qRT-PCR
Bbs8 R	ATCGGGACTTGTAAGCATGG	
hsGli1 F	GAACCCTTGGAAGGTGATATGTC	Amplifying human *GLI1* for qRT-PCR
hsGli1 R	GGCAGTCAGTTTCATACACAGAT	
hsPtc1 F	GACCGGGACTATCTGCACC	Amplifying human *PTC1* for qRT-PCR
hsPtc1 R	GAGGCCCACAACCAAGAACTT	
hsGAPDH F	ATGGGGAAGGTGAAGGTCG	Amplifying human *GAPDH* as control for qRT-PCR
hsGAPDH R	GGGGTCATTGATGGCAACAATA	
hsShh F	CTCGCTGCTGGTATGCTCG	Amplifying human *SHH* for qRT-PCR
hsShh R	ATCGCTCGGAGTTTCTGGAGA	
hsBBS8 rt F	TGGGAACGGCTTTGTTTGAGT	Amplifying human *BBS8* for qRT-PCR
hsBBS8 rt R	CACAGGTTGATCCAATGAGACA	
zfPtc1 rt F	CCAACTTTTACCCCCATCCT	Amplifying fish *ptc1* for qRT-PCR
zfPtc1 rt R	GGGGTAGCCATTGGGATAGT	
zfGli1 rt F	CCTGTCCTGGGCAGTGTAAT	Amplifying fish *gli1* for qRT-PCR
zfGli1 rt R	ACTCTTTGCTGCAGCTCTCC	
zfShh rt F	AAAGCCCACATTCATTGCTC	Amplifying fish *shh* for qRT-PCR
zfShh rt R	GATGAAGTCGCTGAACACCA	
zfEF1a rt F	TGGGTGTTGGACAAACTGAA	Amplifying fish *ef1a* as control for qRT-PCR
zfEF1a rt R	CAACACCACCAGCAACAATC	
zfBBS8splF 1	GCGGATATCTGCTCCACACT	Validating splice *bbs8* splice blocking MO
zfBBS8splR 1	GACGCCTCAGTGATGTTCCT	
zfBBS8splF 2	ATTGATGAGGTGGAGGTGGA	Validating *bbs8* splice blocking MO
zfBBS8splR 2	GTCGACCTGACTGGGTCATC	
IFT80spliceF 1	GTGAGCGGAAAGAAACAAGC	Validating *ift80* splice blocking MO
IFT80spliceR 1	AGGCATCCCTTGTTGAGCTA	
IFT80spliceF 2	GAAGAGTGTGGAGGCCCATA	Validating *ift80* splice blocking MO
IFT80spliceR 2	AGGCATCCCTTGTTGAGCTA	
zBactinF 1	CTCTTCCAGCCTTCCTTCCT	Amplifying fish beta-actin as qRT-PCR control
zBactinR 1	CTTCTGCATACGGTCAGCAA	
zBactinF 2	CTCTTCCAGCCTTCCTTCCT	Amplifying fish beta-actin as qRT-PCR control
zBactinR 2	CACCGATCCAGACGGAGTAT	
hBBS8 F ClaI	ATTGCAATCGATATGAGCTCGGAGAT GGAGCCG	Cloning human *BBS8* for rescue of the fish morphant phenotype
hBBS8 R XhoI	ACATGACTCGAGTCAGAGCATAGCA AAATGCTGC	
mouse IFT80F ClaI	ATTGCAATCGATATGAGACTGAAGAT ATCTCTC	Cloning mouse *Ift80* for morphant rescue

mouse IFT80R XhoI	ACATGACTCGAGTTAGTGCTTTAAGC CCACAC	
zPEPCK F	GAGAATTCTCACACACAC ACACGTGAGCAGTA	Amplifying fish *pepck* for qRT-PCR
zPEPCK R	GTAAAAGCTTTCCGCCATAACATCTC CAGCAGAA	
zINSa F	AGTGTAAGCACTAACCCAGGCACA	Amplifying fish *insa* for qRT-PCR
zINSa R	TGCAAAGT CAGCCACCTCAGTTTC	
mFTO xhoI F	ATCTGACTCGAGATGAAGCGCGTCCA GACCGC	Amplifying mouse *Fto* for zebrafish injection
mFTO salI R	ATCTGAGTCGACATCTAGGATCTTGC TTCCAGCAGCTG	
mFTO EcoRI F	ATCTGAGAATTCATGAAGCGCGTCCA GACCGC	Amplifying mouse *Fto* for GST-tagged protein production
mFTO XhoI R	ATCTGACTCGAGCTAGGATCTTGCTT CCAGCAGCTG	
zFTOprobe F1	CATGCACGTGTCATACACCA	Production of zebrafish *fto in situ* probe
zFTOprobe R1	CCTTCATTCTTTGGCTCTGC	
zFTO probe F2	TTTCAGGACCTGTGGGACTC	
zFTO probe R2	CCATGTCTGTCTGTGCTGCT	

Appendix 2: morpholino oligonucleotide sequences

Gene	Dose	MO sequence	mRNA for rescue
Acat1 ATG	2ng	TGAAATACTGTACTCAATAAAGCGC	
Acat1 SPL	1-4ng	AGAGGAAGACCTGCATGAGGAAAAC	100pg
Bbs1 ATG	8ng	GGCTGGCAAATAAGCTGTCCACAG	
Bbs4 ATG	4ng	GAAAAAGATCACTACTGTAAAGCAT	50pg
Bbs4 ATG mis	n/a	GAAtAAGAgCcCTtCTGaAAAGCAT	
Bbs6 ATG	4ng	GCTTCTTCTTACTAATGCGAGACAT	50pg
Bbs8 ATG	2-4ng	TCTCACCGGAGAAACACCACACACA	100pg
Bbs8 SPL*	n/a	AGCTGTATACTCACGAGCCACCTGA	
Ftm ATG	1-4ng	TTCAGGATGGCCACCAAGTTGATCC	
Fto ATG**	n/a	GTTTACGCTGCCTCGGTTTCATAGC	100pg
Fto SPL	2ng	CACTTTTGACCTCTCACCTTCATTC	
Gli2 ATG	2ng	GGATGATGTAAAGTTCGTCAGTTGC	
Gli3 ATG	8ng	GGATGATGTAAAGTTCGTCAGTTGC	
Ift80 ATG*	n/a	TGAAGGATGCGATTGAAAACATCGT	
Ift80 SPL1	4ng	AGGTGTATGTGGAACCTGTGATAAG	100pg
Ift80 SPL2	4ng	TAGGTGGAAAGGTTACCATCAGAGC	
Ift80 SPL2 mis	4ng	TAcGTGcAAAGcTTAgCATCAcAGC	
Ihh ATG	4ng	GGAGACGCATTCCACCGCAAGCGGC	
Kcnj10 ATG	0.5ng	AGGGATAGGAGAGAGATGTTCATTT	50pg
Kcnj10 SPL	1-2ng	AATTGTGAGAGCTATACCTTGGCGA	
Mks1 SPL	2ng	CTCTTACACTAATCACCTACCTGAC	
Mks3 SPL	2ng	GTAAAAATGACAAGCGCCTACCCAG	
Nphp2 ATG**	n/a	CATTGCCTGATGCACACACACACAC	
Nphp2 SPL	4ng	GAGCAGCTTCCTAAAATGTATAAAC	50pg
Nphp5 ATG	2ng	ATTTCGTCTCCTGAAGGACCCATTG	
Nphp5 SPL	3ng	CAAGACGGCACTGCAAAAACAAGGG	
Nphp6 ATG**	n/a	TCTCAGAATCATCTGCTTTTAGGTC	
Nphp6 SPL	3ng	GCCTGCTGCTGCCTATAAAACCATC	
Ofd1 ATG*	n/a	GCAGCAAACACATTTACATTCAGTC	
Ofd1 SPL	3ng	CGGGATATGACCTAAAGTCAAAACC	
P53	***	GCGCCATTGCTTTGCAAGAATTG	
Ptc1 ATG	1ng	CATAGTCCAAACGGGAGGCAGAAGA	

* These MOs did not yield any phenotype.

** These MOs were toxic and killed embryos

*** *p53* MO used in some experiments to control for possible non-specific cell death. Used at the same concentration of the MO under test.

Table 13. Morpholino oligonucleotide sequences

MOs designated “mis” are 5-base pair mismatch MOs used as controls against the gene of interest. None of mis-pair MOs yielded any phenotype when injected at the same concentration as its gene-specific MO.

Appendix 3: development of a zebrafish model for a new human syndrome causing epilepsy and renal tubulopathy

Mutations in *KCNJ10* underlie a new human syndrome

In the latter months of my PhD project, I was approached by paediatric nephrologists (Drs. Detlef Bockenhauer and Robert Kleta) at Great Ormond Street Hospital, who had identified a new autosomal recessive human syndrome in a single consanguineous family. They wanted some functional assays performed in zebrafish embryos. This syndrome was characterised by renal tubulopathy and epileptic seizures. Using homozygosity mapping on 10k SNP chips, they identified a region containing a single gene encoding a potassium channel, *KCNJ10*. Sequencing revealed non-sense mutations in the patients occurring in the membrane-spanning domain of the channel.

KCNJ10 (also called *KIR4.1*) encodes a slow inward rectifier potassium ion channel (K_{ir}) exclusively expressed in human and mouse brain, ear, and kidney tissue. K_{ir} channels pass potassium ions (positive current) from the outside to the inside of the cell. When the membrane potential is below the resting potential, K_{ir} channels pass potassium ions back into the cytoplasm to restore the resting potential. Therefore, they regulate the resting potential in neurons. Because the maintenance of resting potential is affected by *KCNJ10* mutation, spontaneous action potentials result in involuntary epileptic seizures.

Maintenance of resting membrane potential is important for other cell types besides neurons. In the kidney tubule, K_{ir} channels are involved in filtration in the nephron. Here, they reabsorb K^+ ions from the filtrate back into the body, or they excrete excess K^+ into the urine, thus regulating plasma potassium concentration. This is why mutation to *KCNJ10* in the kidney causes tubulopathy.

There is a mouse knockout of *Kcnj10*, but it dies perinatally and never lives beyond around two weeks post-partum (unpublished data). The pups are runtish and the cause of death tends to be starvation, as before they die, they suffer

seizures and malcoordinated movement and so are unable to suckle properly. Because of the lack of a conditional mouse model to knock out *Kcnj10* in the kidney, it is difficult to assess the function of the gene from the mouse model. In order to validate the function of the gene, I produced a zebrafish *kcnj10* morphant.

Kidney and motion defects in morphant zebrafish

I designed ATG and splice blocking MOs against zebrafish *kcnj10*, which shares 71% identity with the human orthologue at the protein level. *Kcnj10* had not yet been annotated on the zebrafish genome. Injection of between 2 and 8ng of *kcnj10* ATG MO, or 4 to 8ng of SPL MO, caused severe morphological defects. Injection of 1ng *kcnj10* ATG MO, or 2ng of the splice blocking MO (*kcnj10* SPL), did not yield any morphological phenotype at 24hpf.

By 72hpf, around 50% of embryos injected with 1ng ATG or 2ng splice MO had oedema in the body cavity and a swollen pronephric duct. This probably represents tubulopathy in the kidney. Because the zebrafish body tissue is salty, but the fish lives in fresh water, failure to regulate potassium secretion and uptake in the urine will result in osmotic imbalance and fluid uptake, resulting in oedema. Figure 92 shows an embryo injected with 1ng ATG blocking MO.

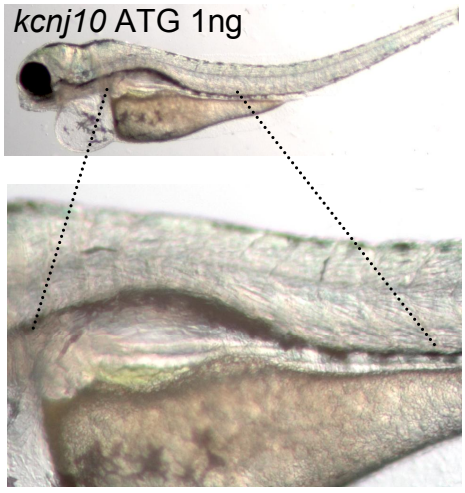

Figure 92. *kcnj10* morphant phenotype.

1ng *kcnj10* ATG MO was sufficient to cause oedema of the kidney and swelling of the pronephric duct, a sign of tubulopathy.

To prevent such gross oedema of the body, I reduced the amount of ATG MO injected to 0.5ng. At this dosage, the embryos did not develop oedema. However, although morphologically grossly normal, these embryos showed a striking movement disorder. Control embryos at 5dpf swam in smooth circles around their dish (Fig. 93, left panel). *Kcnj10* morphants exhibited two unusual swimming behaviours that to my knowledge, have never been documented in other morphants. Firstly, they had seizures resulting in tremors of the whole body, due to rapid, involuntary muscle contraction. These seizures were impossible to record due to the lack of a videomicroscope of high-speed. Secondly, instead of the embryos swimming in smooth lines, morphant embryos swam in tight loops (Fig. 93 right panel). Some embryos even circled around their own body axis. This looping behaviour was observed in over 15 separate embryos from different injections and was never seen in controls.

In order to document this phenotype and analyse it, I collaborated with Dr Anukampa Barth at UCL. We used a digital infrared camera that tracks the motion path of an embryo in a dish against a white background. The computer then draws a line representing the movement of the fish. We made 3-minute recordings for each embryo and compared the traces from control and morphant embryos. From the motion-captured images, it is clear that morphant embryos tend to swim in tight loops, often turning back on themselves. This is in contrast to controls, which swam in large circles, never looping back on their own tracks.

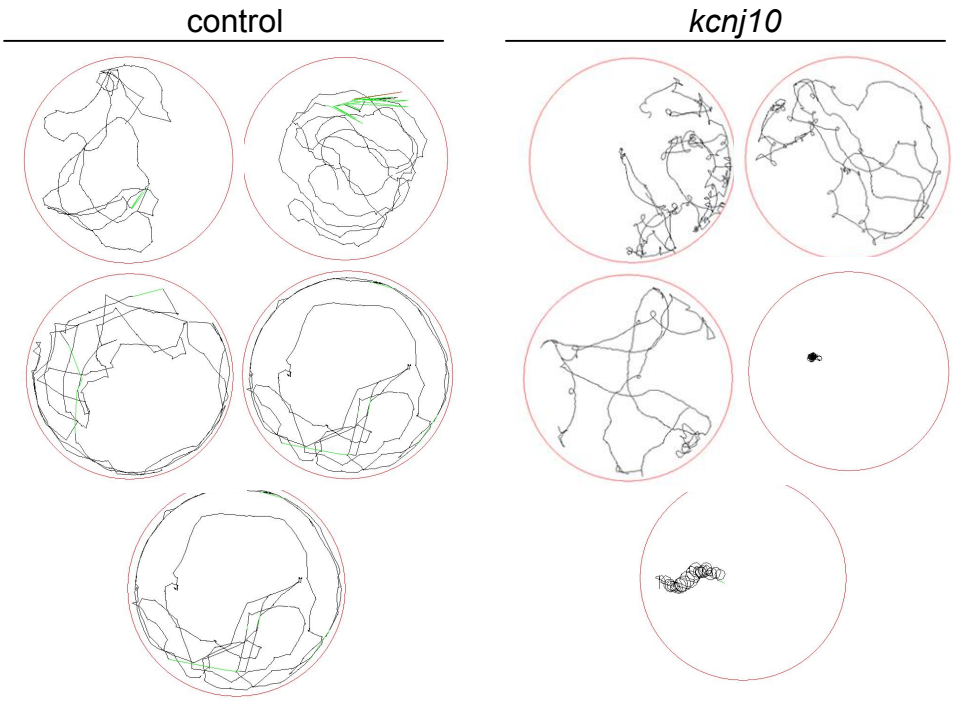

Figure 93. Movement analysis of *kcnj10* morphants.

Left side: 5.5dpf control embryos swim in large loops around the dish, often sticking to the margins. There are no small loops or sudden erratic changes of direction. **Right side**: morphant embryos swim in very tight loops, turning on their own axes. In some cases, the embryos pivoted around their own axis in tight spirals or on the spot.

To test the renal function of morphant embryos I injected 0.5ng of ATG MO, which did not result in oedema and performed the same functional assay used for the drug testing on ciliopathy morphants (Fig. 94A-B''). Fluorescence was reduced by 91% in controls (n=10) but by only 26% in morphants (n=15) (Fig. 94C). This shows that renal filtering function is impaired in these morphants.

Mutant human mRNA is unable to rescue the movement phenotype

Collaborators at the Royal Free Hospital in London working on this project tested the function of the mutant *KCNJ10* allele by injecting wild type and mutant mRNA (R65P substitution) into *Xenopus* oocytes. They then performed whole cell electrophysiological recordings with an electrode. They found that channel function in the mutant was reduced to 30% of the wild type level. They proved specificity by treating the oocytes with barium, which specifically blocks K_{ir}

channels. In this case, membrane potentials were the same in mutant and wild type oocytes.

To see if this reduction in channel function affected whole-organism physiology, I injected these wild type and mutant forms of mRNA into *kcnj10* morphants. To objectively and quantitatively assay function, I counted the number of body flexes dechorionated 30hpf embryos made in a random 30-second period. The embryos were placed in individual wells of a 12 well plate and left to equilibrate for 3 minutes before counting. Between 15 and 20 embryos were counted for each treatment.

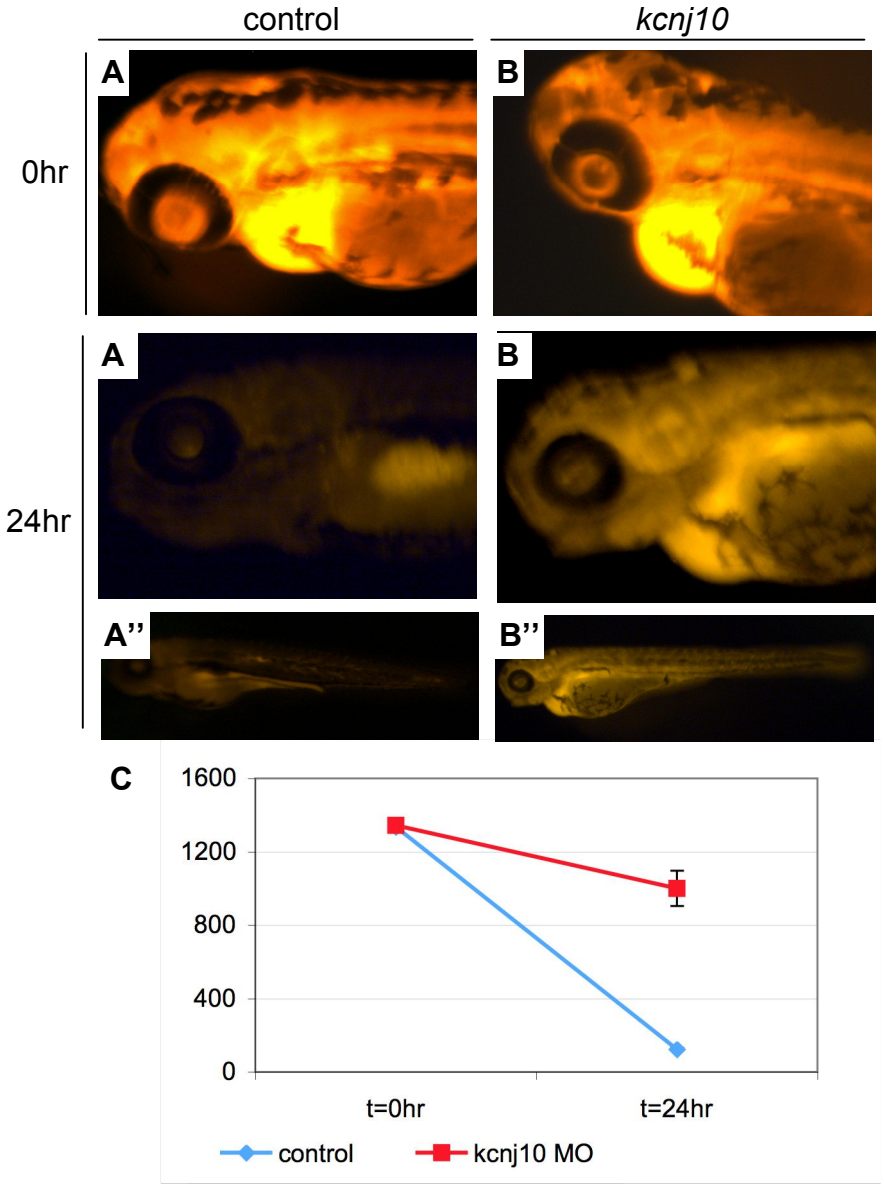

Figure 94. Kidney function assay on *kcnj10* morphants.

A-A': immediately after fluorescent dextran injection, the control embryo is brightly fluorescent. 24 hours later, this fluorescence has largely dispersed. **A''**: An image of the whole embryo shows it has been excreted from the systemic circulation. **B,B'**: *kcnj10* morphants retain much of the original fluorescence 24hpi. **B''**: the fluorescence persists in the circulation and in the pronephros. **C**: quantification of the amount of fluorescence in the heart at 0hpi shows the same amount of fluorescence in controls and morphants. 24hpi, control fluorescence has reduced by 91% of the original amount but only by 26% in morphants.

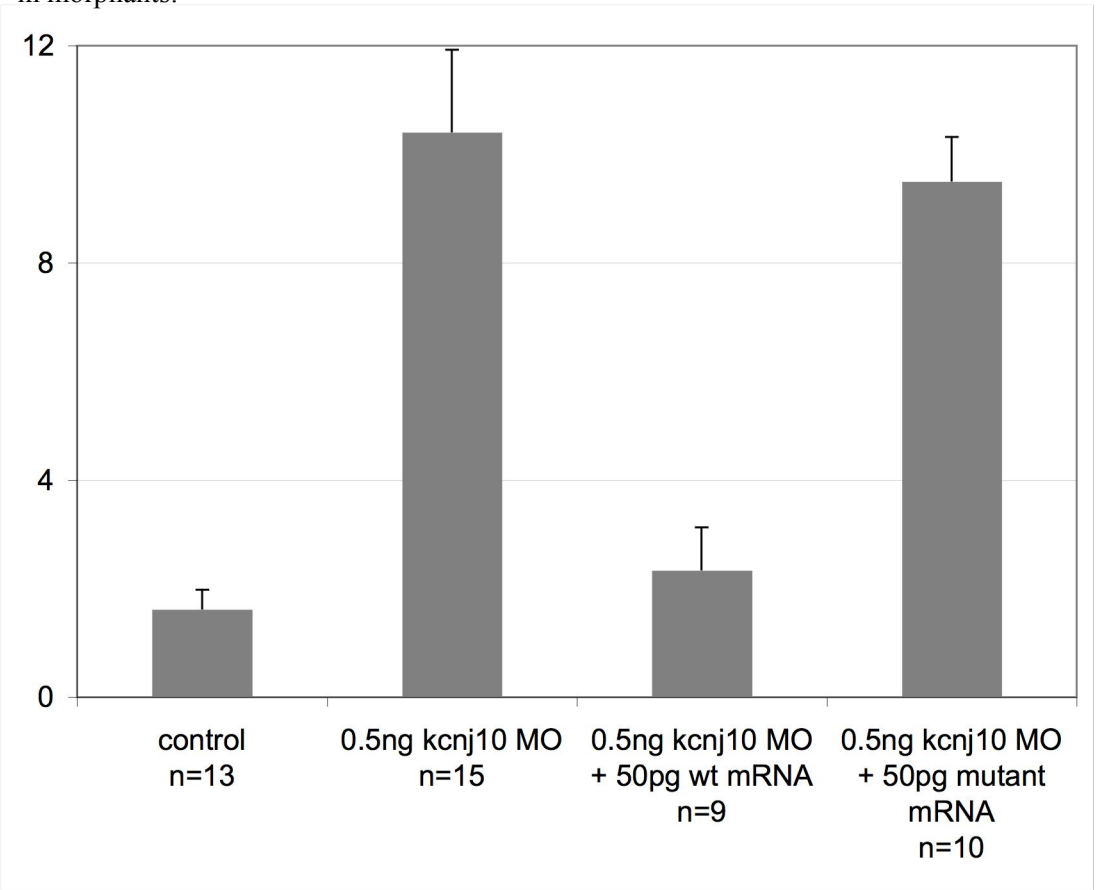

Figure 95. Effect of human *kcnj10* mutation on zebrafish body movements.

The number of body twitches was counted in a random 30-second period for each embryo placed in its own well. Morphants twitched around 6-times more frequently than controls. This excessive body movement was rescued by injection of 50pg wt human mRNA, but not by the mutant mRNA.

These data show that control embryos flexed an average of 1.6 times in each period (Figure 95). In contrast, morphants flexed 10.4 times, a 6.5-fold increase. Injection of 50pg or 100pg of wild type mRNA restored this movement defect to just 1.4 and 1.1-fold over control levels respectively. In contrast, injection of 50pg or 100pg of mutant mRNA resulted in no rescue of the excessive body twitching, with 5.9 and 6.1-fold more twitches compared to controls (Figure 95).

Together, the oocyte and zebrafish data suggest that the mutant mRNA is diminishing channel activity resulting in hyperactivity of the neurons in the brain and uncontrollable body seizures.

Appendix 4: bibliography of papers published during PhD

Tobin JL, Beales PL. *Restoration of renal function in zebrafish models of ciliopathies*. **Pediatric Nephrology**. 2008 (July).

Tobin JL, Di Franco M, Eichers E, May-Simera H, Garcia M, Yan J, Quinlan R, Justice MJ, Hennekam RC, Briscoe J, Tada M, Mayor R, Burns AJ, Lupski JR, Hammond P, Beales PL. *Inhibition of neural crest migration underlies craniofacial dysmorphology and Hirschsprung's disease in Bardet-Biedl syndrome*. **Proceedings of the National Academy of Sciences USA**. 2008 105(18):6714-9.

Beales PL, Bland E (co-first authors), **Tobin JL**, Bacchelli C, Tuysuz B, Hill J, Rix S, Pearson CG, Kai M, Hartley J, Johnson C, Irving M, Elcioglu N, Winey M, Tada M, Scambler PJ. *IFT80, which encodes a conserved intraflagellar transport protein, is mutated in Jeune asphyxiating thoracic dystrophy*. **Nature Genetics**. 2007 39(6):727-9.

Tobin JL, Beales PL. *Bardet-Biedl syndrome: beyond the cilium*. **Pediatric Nephrology**. 2007 22(7):926-36.

References

Abd-El-Barr, M. M., Sykoudis, K., Andrabi, S., Eichers, E. R., Pennesi, M. E., Tan, P. L., Wilson, J. H., Katsanis, N., Lupski, J. R. and Wu, S. M. (2007). Impaired photoreceptor protein transport and synaptic transmission in a mouse model of Bardet-Biedl syndrome. *Vision Res* **47**, 3394-407.

Ait-Lounis, A., Baas, D., Barras, E., Benadiba, C., Charollais, A., Nlend Nlend, R., Liègeois, D., Meda, P., Durand, B. and Reith, W. (2007). Novel function of the ciliogenic transcription factor RFX3 in development of the endocrine pancreas. *Diabetes* **56**, 950-9.

Alberts, B., et al. (2008). Molecular Biology of the Cell (5th Edition) (Garland Science).

Alter, P., Walthers, E. M., Schaefer, J. R. and Maisch, B. (2001). Angiography, CT and MR imaging of a high vena cava inferior interruption in a patient with Hirschsprung disease. *VASA* **30**, 299-302.

Alton, D. J. and McDonald, P. (1973). Urographic findings in the Bardet-Biedl syndrome, formerly the Laurence-Moon-Biedl syndrome. *Radiology* **109**, 659-63.

Alvarez-Medina, R., Cayuso, J., Okubo, T., Takada, S. and Martí, E. (2008). Wnt canonical pathway restricts graded Shh/Gli patterning activity through the regulation of Gli3 expression. *Development* **135**, 237-47.

Amiel, J., Laudier, B., Attié-Bitach, T., Trang, H., de Pontual, L., Gener, B., Trochet, D., Etchevers, H., Ray, P., Simonneau, M. et al. (2003). Polyalanine expansion and frameshift mutations of the paired-like homeobox gene PHOX2B in congenital central hypoventilation syndrome. *Nat Genet* **33**, 459-61.

Anselme, I., Laclef, C., Lanaud, M., Rüther, U. and Schneider-Maunoury, S. (2007). Defects in brain patterning and head morphogenesis in the mouse mutant Fused toes. *Dev Biol* **304**, 208-20.

Ansley, S. J., Badano, J. L., Blacque, O. E., Hill, J., Hoskins, B. E., Leitch, C. C., Kim, J. C., Ross, A. J., Eichers, E. R., Teslovich, T. M. et al. (2003). Basal body dysfunction is a likely cause of pleiotropic Bardet-Biedl syndrome. *Nature* **425**, 628-33.

Arsov, T., Silva, D. G., O'Bryan, M. K., Sainsbury, A., Lee, N. J., Kennedy, C., Manji, S. S., Nelms, K., Liu, C., Vinuesa, C. G. et al. (2006). Fat aussie--a new Alström syndrome mouse showing a critical role for ALMS1 in obesity, diabetes, and spermatogenesis. *Mol Endocrinol* **20**, 1610-22.

Arts, H. H., Doherty, D., van Beersum, S. E., Parisi, M. A., Letteboer, S. J., Gorden, N. T., Peters, T. A., Märker, T., Voesenek, K., Kartono, A. et al. (2007). Mutations in the gene encoding the basal body protein RPGRIP1L, a nephrocystin-4 interactor, cause Joubert syndrome. *Nat Genet* **39**, 882-8.

Attanasio, M., Uhlenhaut, N. H., Sousa, V. H., O'Toole, J. F., Otto, E., Anlag, K., Klugmann, C., Treier, A. C., Helou, J., Sayer, J. A. et al. (2007). Loss of GLIS2 causes nephronophthisis in humans and mice by increased apoptosis and fibrosis. *Nat Genet* **39**, 1018-24.

Baala, L., Audollent, S., Martinovic, J., Ozilou, C., Babron, M. C., Sivanandamoorthy, S., Saunier, S., Salomon, R., Gonzales, M., Rattenberry, E. et al. (2007). Pleiotropic effects of CEP290 (NPHP6) mutations extend to Meckel syndrome. *Am J Hum Genet* **81**, 170-9.

Badano, J. L., Ansley, S. J., Leitch, C. C., Lewis, R. A., Lupski, J. R. and Katsanis, N. (2003). Identification of a novel Bardet-Biedl syndrome protein, BBS7, that shares structural features with BBS1 and BBS2. *Am J Hum Genet* **72**, 650-8.

Badano, J. L., Mitsuma, N., Beales, P. L. and Katsanis, N. (2006). The ciliopathies: an emerging class of human genetic disorders. *Annual review of genomics and human genetics* **7**, 125-48.

Bainbridge, J. W., Smith, A. J., Barker, S. S., Robbie, S., Henderson, R., Balaggan, K., Viswanathan, A., Holder, G. E., Stockman, A., Tyler, N. et al. (2008). Effect of gene therapy on visual function in Leber's congenital amaurosis. *N Engl J Med* **358**, 2231-9.

Batlle, E., Sancho, E., Francí, C., Domínguez, D., Monfar, M., Baulida, J. and García De Herreros, A. (2000). The transcription factor snail is a repressor of E-cadherin gene expression in epithelial tumour cells. *Nat Cell Biol* **2**, 84-9.

Beales, P. L., Badano, J. L., Ross, A. J., Ansley, S. J., Hoskins, B. E., Kirsten, B., Mein, C. A., Froguel, P., Scambler, P. J., Lewis, R. A. et al. (2003). Genetic interaction of BBS1 mutations with alleles at other BBS loci can result in non-Mendelian Bardet-Biedl syndrome. *Am J Hum Genet* **72**, 1187-99.

Beales, P. L., Bland, E., Tobin, J. L., Bacchelli, C., Tuysuz, B., Hill, J., Rix, S., Pearson, C. G., Kai, M., Hartley, J. et al. (2007). IFT80, which encodes a conserved intraflagellar transport protein, is mutated in Jeune asphyxiating thoracic dystrophy. *Nat Genet* **39**, 727-9.

Beales, P. L., Elcioglu, N., Woolf, A. S., Parker, D. and Flinter, F. A. (1999). New criteria for improved diagnosis of Bardet-Biedl syndrome: results of a population survey. *J Med Genet* **36**, 437-46.

Behra, M., Etard, C., Cousin, X. and Strähle, U. (2004). The use of zebrafish mutants to identify secondary target effects of acetylcholine esterase inhibitors. *Toxicol Sci* **77**, 325-33.

Berbari, N. F., Johnson, A. D., Lewis, J. S., Askwith, C. C. and Mykytyn, K. (2008a). Identification of Ciliary Localization Sequences within the Third Intracellular Loop of G Protein-coupled Receptors. *Mol Biol Cell* **19**, 1540-7.

Berbari, N. F., Lewis, J. S., Bishop, G. A., Askwith, C. C. and Mykytyn, K. (2008b). Bardet-Biedl syndrome proteins are required for the localization of G protein-coupled receptors to primary cilia. *Proc Natl Acad Sci USA* **105**, 4242-6.

Bhuiyan, Z. A., Klein, M., Hammond, P., van Haeringen, A., Mannens, M. M., Van Berckelaer-Onnes, I. and Hennekam, R. C. (2006). Genotype-phenotype correlations of 39 patients with Cornelia De Lange syndrome: the Dutch experience. *J Med Genet* **43**, 568-75.

Bitgood, M. J., Shen, L., McMahon, A. P. (1996). Sertoli cell signaling by Desert hedgehog regulates the male germline. *Curr. Biol.* **6**, 298-304.

Blacque, O. E., Reardon, M. J., Li, C., McCarthy, J., Mahjoub, M. R., Ansley, S. J., Badano, J. L., Mah, A. K., Beales, P. L., Davidson, W. S. et al. (2004). Loss of C. elegans BBS-7 and BBS-8 protein function results in cilia defects and compromised intraflagellar transport. *Genes Dev* **18**, 1630-42.

Briscoe, J. and Ericson, J. (2001). Specification of neuronal fates in the ventral neural tube. *Curr Opin Neurobiol* **11**, 43-9.

Briscoe, J., Sussel, L., Serup, P., Hartigan-O'Connor, D., Jessell, T. M., Rubenstein, J. L. and Ericson, J. (1999). Homeobox gene Nkx2.2 and specification of neuronal identity by graded Sonic hedgehog signalling. *Nature* **398**, 622-7.

Bukanov, N. O., Smith, L. A., Klinger, K. W., Ledbetter, S. R. and Ibraghimov-Beskrovnaya, O. (2006). Long-lasting arrest of murine polycystic kidney disease with CDK inhibitor roscovitine. *Nature* **444**, 949-52.

Burns, C. G., Milan, D. J., Grande, E. J., Rottbauer, W., MacRae, C. A. and Fishman, M. C. (2005). High-throughput assay for small molecules that modulate zebrafish embryonic heart rate. *Nat Chem Biol* **1**, 263-4.

Cano, D. A., Murcia, N. S., Pazour, G. J. and Hebrok, M. (2004). Orpk mouse model of polycystic kidney disease reveals essential role of primary cilia in pancreatic tissue organization. *Development* **131**, 3457-67.

Chan, J., Bayliss, P. E., Wood, J. M. and Roberts, T. M. (2002). Dissection of angiogenic signaling in zebrafish using a chemical genetic approach. *Cancer Cell* **1**, 257-67.

Cherian, M. P., Al-Sanna'a, N. A. and Al-Mulhim, S. I. (2008). Hirschsprung's disease in Arab siblings with Bardet-Biedl syndrome. *J Pediatr Surg* **43**, 1213-7.

Chiang, A. P., Beck, J. S., Yen, H. J., Tayeh, M. K., Scheetz, T. E., Swiderski, R. E., Nishimura, D. Y., Braun, T. A., Kim, K. Y., Huang, J. et al. (2006). Homozygosity mapping with SNP arrays identifies TRIM32, an E3 ubiquitin ligase, as a Bardet-Biedl syndrome gene (BBS11). *Proc Natl Acad Sci USA* **103**, 6287-92.

Corbit, K. C., Aanstad, P., Singla, V., Norman, A. R., Stainier, D. Y. and Reiter, J. F. (2005). Vertebrate Smoothened functions at the primary cilium. *Nature* **437**, 1018-21.

Corbit, K. C., Shyer, A. E., Dowdle, W. E., Gaulden, J., Singla, V., Chen, M. H., Chuang, P. T. and Reiter, J. F. (2008). Kif3a constrains beta-catenin-dependent Wnt signalling through dual ciliary and non-ciliary mechanisms. *Nat Cell Biol* **10**, 70-6.

Cox-Brinkman, J., Vedder, A., Hollak, C., Richfield, L., Mehta, A., Orteu, K., Wijburg, F. and Hammond, P. (2007). Three-dimensional face shape in Fabry disease. *Eur J Hum Genet* **15**, 535-42.

Davenport, J. R., Watts, A. J., Roper, V. C., Croyle, M. J., van Groen, T., Wyss, J. M., Nagy, T. R., Kesterson, R. A. and Yoder, B. K. (2007). Disruption of intraflagellar transport in adult mice leads to obesity and slow-onset cystic kidney disease. *Curr Biol* **17**, 1586-94.

David, N. B., Saint-Etienne, L., Tsang, M., Schilling, T. F. and Rosa, F. M. (2002). Requirement for endoderm and FGF3 in ventral head skeleton formation. *Development* **129**, 4457-68.

Davis, E. E., Brueckner, M. and Katsanis, N. (2006). The emerging complexity of the vertebrate cilium: new functional roles for an ancient organelle. *Dev Cell* **11**, 9-19.

Dawe, H. R., Smith, U. M., Cullinane, A. R., Gerrelli, D., Cox, P., Badano, J. L., Blair-Reid, S., Sriram, N., Katsanis, N., Attie-Bitach, T., Afford, S. C., Copp, A. J., Kelly, D. A., Gull, K., Johnson, C. A. (2007). The Meckel-Gruber Syndrome proteins MKS1 and meckelin interact and are required for primary cilium formation. *Hum. Mol. Genet.* **16**, 173-86.

de Beer, G. (1937). Development of the vertebrate skull.

De Calisto, J., Araya, C., Marchant, L., Riaz, C. F. and Mayor, R. (2005). Essential role of non-canonical Wnt signalling in neural crest migration. *Development* **132**, 2587-97.

de Pontual, L., Pelet, A., Clement-Ziza, M., Trochet, D., Antonarakis, S. E., Attie-Bitach, T., Beales, P. L., Blouin, J. L., Dastot-Le Moal, F., Dollfus, H. et al. (2007). Epistatic interactions with a common hypomorphic RET allele in syndromic Hirschsprung disease. *Hum Mutat* **28**, 790-6.

Delous, M., Baala, L., Salomon, R., Laclef, C., Vierkotten, J., Tory, K., Golzio, C., Lacoste, T., Besse, L., Ozilou, C. et al. (2007). The ciliary gene RPGRIP1L is mutated in cerebello-oculo-renal syndrome (Joubert syndrome type B) and Meckel syndrome. *Nat Genet* **39**, 875-81.

Depew, M. J., Lufkin, T. and Rubenstein, J. L. (2002). Specification of jaw subdivisions by Dlx genes. *Science* **298**, 381-5.

Dessaud, E., Yang, L. L., Hill, K., Cox, B., Ulloa, F., Ribeiro, A., Mynett, A., Novitch, B. G. and Briscoe, J. (2007). Interpretation of the sonic hedgehog morphogen gradient by a temporal adaptation mechanism. *Nature* **450**, 717-20.

Ding, Q., Fukami, S., Meng, X., Nishizaki, Y., Zhang, X., Sasaki, H., Dlugosz, A., Nakafuku, M. and Hui, C. (1999). Mouse suppressor of fused is a negative regulator of sonic hedgehog signaling and alters the subcellular distribution of Gli1. *Curr Biol* **9**, 1119-22.

Dixon-Salazar, T., Silhavy, J. L., Marsh, S. E., Louie, C. M., Scott, L. C., Gururaj, A., Al-Gazali, L., Al-Tawari, A. A., Kayserili, H., Sztriha, L. et al. (2004). Mutations in the AHI1 gene, encoding jouberin, cause Joubert syndrome with cortical polymicrogyria. *Am J Hum Genet* **75**, 979-87.

Douglas, K. R., Brinkmeier, M. L., Kennell, J. A., Eswara, P., Harrison, T. A., Patrianakos, A. I., Sprecher, B. S., Potok, M. A., Lyons, R. H., MacDougald, O. A. et al. (2001). Identification of members of the Wnt signaling pathway in the embryonic pituitary gland. *Mamm Genome* **12**, 843-51.

Drummond, I. A. (2005). Kidney development and disease in the zebrafish. *J Am Soc Nephrol* **16**, 299-304.

Drummond, I. A., Majumdar, A., Hentschel, H., Elger, M., Solnica-Krezel, L., Schier, A. F., Neuhauss, S. C., Stemple, D. L., Zwartkruis, F., Rangini, Z. et al. (1998). Early development of the zebrafish pronephros and analysis of mutations affecting pronephric function. *Development* **125**, 4655-67.

Eberhart, J. K., Swartz, M. E., Crump, J. G. and Kimmel, C. B. (2006). Early Hedgehog signaling from neural to oral epithelium organizes anterior craniofacial development. *Development* **133**, 1069-77.

Efimenko, E., Bubb, K., Mak, H. Y., Holzman, T., Leroux, M. R., Ruvkun, G., Thomas, J. H. and Swoboda, P. (2005). Analysis of xbx genes in C. elegans. *Development* **132**, 1923-34.

Egeblad, M. and Werb, Z. (2002). New functions for the matrix metalloproteinases in cancer progression. *Nat Rev Cancer* **2**, 161-74.

Eggenschwiler, J. T., Bulgakov, O. V., Qin, J., Li, T. and Anderson, K. V. (2006). Mouse Rab23 regulates hedgehog signaling from smoothened to Gli proteins. *Dev Biol* **290**, 1-12.

Eichers, E. R., Abd-El-Barr, M. M., Paylor, R., Lewis, R. A., Bi, W., Lin, X., Meehan, T. P., Stockton, D. W., Wu, S. M., Lindsay, E. et al. (2006). Phenotypic characterization of Bbs4 null mice reveals age-dependent penetrance and variable expressivity. *Hum Genet* **120**, 211-26.

Elo, B., Villano, C. M., Govorko, D. and White, L. A. (2007). Larval zebrafish as a model for glucose metabolism: expression of phosphoenolpyruvate carboxykinase as a marker for exposure to anti-diabetic compounds. *J Mol Endocrinol* **38**, 433-40.

Endo, Y., Osumi, N. and Wakamatsu, Y. (2002). Bimodal functions of Notch-mediated signaling are involved in neural crest formation during avian ectoderm development. *Development* **129**, 863-73.

Fan, Y., Esmail, M. A., Ansley, S. J., Blacque, O. E., Boroevich, K., Ross, A. J., Moore, S. J., Badano, J. L., May-Simera, H., Compton, D. S. et al. (2004). Mutations in a member of the Ras superfamily of small GTP-binding proteins causes Bardet-Biedl syndrome. *Nat Genet* **36**, 989-93.

Fanconi, G., Hanhart, E., von Albertini, A., Uhlinger, E., Dolivo, G. and Prader, A. (1951). [Familial, juvenile nephronophthisis (idiopathic parenchymal contracted kidney).]. *Helvetica paediatrica acta* **6**, 1-49.

Ferrante, M. I., Giorgio, G., Feather, S. A., Bulfone, A., Wright, V., Ghiani, M., Selicorni, A., Gammaro, L., Scolari, F., Woolf, A. S. et al. (2001). Identification of the gene for oral-facial-digital type I syndrome. *Am J Hum Genet* **68**, 569-76.

Fischer, E., Legue, E., Doyen, A., Nato, F., Nicolas, J. F., Torres, V., Yaniv, M. and Pontoglio, M. (2006). Defective planar cell polarity in polycystic kidney disease. *Nat Genet* **38**, 21-3.

Fliegauf, M., Benzing, T. and Omran, H. (2007). When cilia go bad: cilia defects and ciliopathies. *Nat Rev Mol Cell Biol* **8**, 880-93.

Follit, J. A., Tuft, R. A., Fogarty, K. E. and Pazour, G. J. (2006). The intraflagellar transport protein IFT20 is associated with the Golgi complex and is required for cilia assembly. *Mol Biol Cell* **17**, 3781-92.

Forti, E., Aksanov, O. and Birk, R. Z. (2007). Temporal expression pattern of Bardet-Biedl syndrome genes in adipogenesis. *Int J Biochem Cell Biol* **39**, 1055-62.

Fredriksson, R., Hägglund, M., Olszewski, P. K., Stephansson, O., Jacobsson, J. A., Olszewska, A. M., Levine, A. S., Lindblom, J. and Schiöth, H. B. (2008). The obesity gene, FTO, is of ancient origin, up-regulated during food deprivation and expressed in neurons of feeding-related nuclei of the brain. *Endocrinology* **149**, 2062-71.

Frixione, E. (2000). Recurring views on the structure and function of the cytoskeleton: a 300-year epic. *Cell Motil Cytoskeleton* **46**, 73-94.

Fukumoto, T., Watanabe-Fukunaga, R., Fujisawa, K., Nagata, S. and Fukunaga, R. (2001). The fused protein kinase regulates Hedgehog-stimulated transcriptional activation in Drosophila Schneider 2 cells. *J Biol Chem* **276**, 38441-8.

Fürthauer, M., Van Celst, J., Thisse, C. and Thisse, B. (2004). Fgf signalling controls the dorsoventral patterning of the zebrafish embryo. *Development* **131**, 2853-64.

Galdzicka, M., Patnala, S., Hirshman, M. G., Cai, J. F., Nitowsky, H., Egeland, J. A. and Ginns, E. I. (2002). A new gene, EVC2, is mutated in Ellis-van Creveld syndrome. *Mol Genet Metab* **77**, 291-5.

Gammill, L. S. and Bronner-Fraser, M. (2003). Neural crest specification: migrating into genomics. *Nat Rev Neurosci* **4**, 795-805.

Gerdes, J. M., Liu, Y., Zaghloul, N. A., Leitch, C. C., Lawson, S. S., Kato, M., Beachy, P. A., Beales, P. L., DeMartino, G. N., Fisher, S. et al. (2007). Disruption of the basal body compromises proteasomal function and perturbs intracellular Wnt response. *Nat Genet* **39**, 1350-60.

Gerken, T., Girard, C. A., Tung, Y. C., Webby, C. J., Saudek, V., Hewitson, K. S., Yeo, G. S., McDonough, M. A., Cunliffe, S., McNeill, L. A. et al. (2007). The obesity-associated FTO gene encodes a 2-oxoglutarate-dependent nucleic acid demethylase. *Science* **318**, 1469-72.

Germino, G. G. and Somlo, S. (1993). Inherited diseases of the kidney. *Curr Opin Nephrol Hypertens* **2**, 430-40.

Gershon, M. D. (2007). Transplanting the enteric nervous system: a step closer to treatment for aganglionosis. *Gut* **56**, 459-61.

Gherman, A., Davis, E. E. and Katsanis, N. (2006). The ciliary proteome database: an integrated community resource for the genetic and functional dissection of cilia. *Nat Genet* **38**, 961-2.

Gong, Y., Mo, C. and Fraser, S. E. (2004). Planar cell polarity signalling controls cell division orientation during zebrafish gastrulation. *Nature* **430**, 689-93.

Goodrich, L. V., Milenković, L., Higgins, K. M. and Scott, M. P. (1997). Altered neural cell fates and medulloblastoma in mouse patched mutants. *Science* **277**, 1109-13.

Götz, K., Briscoe, J. and Rüther, U. (2005). Homozygous Ft embryos are affected in floor plate maintenance and ventral neural tube patterning. *Dev Dyn* **233**, 623-30.

Grace, C., Beales, P. L., Summerbell, C., Jebb, S. A., Wright, A., Parker, D. and Kopelman, P. (2003). Energy metabolism in Bardet-Biedl syndrome. *Int J Obes Relat Metab Disord* **27**, 1319-24.

Graham, A. (2003). Development of the pharyngeal arches. *Am J Med Genet A* **119A**, 251-6.

Green, J. S., Parfrey, P. S., Harnett, J. D., Farid, N. R., Cramer, B. C., Johnson, G., Heath, O., McManamon, P. J., O'Leary, E. and Pryse-Phillips, W. (1989). The cardinal manifestations of Bardet-Biedl syndrome, a form of Laurence-Moon-Biedl syndrome. *N Engl J Med* **321**, 1002-9.

Gupta, P. and Jain, S. (2008). MRI in a fetus with Meckel-Gruber syndrome. *Pediatric radiology* **38**, 122.

Habas, R., Dawid, I. B. and He, X. (2003). Coactivation of Rac and Rho by Wnt/Frizzled signaling is required for vertebrate gastrulation. *Genes Dev* **17**, 295-309.

Hall, B. K. (1988). Patterning of connective tissues in the head: discussion report. *Development* **103 Suppl**, 171-4.

Halloran, M. C. and Berndt, J. D. (2003). Current progress in neural crest cell motility and migration and future prospects for the zebrafish model system. *Dev Dyn* **228**, 497-513.

Hammond, P. (2007). The use of 3D face shape modelling in dysmorphology. *Arch Dis Child* **92**, 1120-6.

Hammond, P., Forster-Gibson, C., Chudley, A. E., Allanson, J. E., Hutton, T. J., Farrell, S. A., McKenzie, J., Holden, J. J. and Lewis, M. E. (2008). Face-brain asymmetry in autism spectrum disorders. *Mol Psychiatry* **13**, 614-23.

Hammond, P., Hutton, T. J., Allanson, J. E., Buxton, B., Campbell, L. E., Clayton-Smith, J., Donnai, D., Karmiloff-Smith, A., Metcalfe, K., Murphy, K. C. et al. (2005). Discriminating power of localized three-dimensional facial morphology. *Am J Hum Genet* **77**, 999-1010.

Hammond, P., Hutton, T. J., Allanson, J. E., Campbell, L. E., Hennekam, R. C., Holden, S., Patton, M. A., Shaw, A., Temple, I. K., Trotter, M. et al. (2004). 3D analysis of facial morphology. *Am J Med Genet A* **126A**, 339-48.

Haraguchi, R., Mo, R., Hui, C., Motoyama, J., Makino, S., Shiroishi, T., Gaffield, W. and Yamada, G. (2001). Unique functions of Sonic hedgehog signaling during external genitalia development. *Development* **128**, 4241-50.

Haworth, K. E., Healy, C., Morgan, P. and Sharpe, P. T. (2004). Regionalisation of early head ectoderm is regulated by endoderm and prepatterns the orofacial epithelium. *Development* **131**, 4797-806.

Haycraft, C. J., Banizs, B., Aydin-Son, Y., Zhang, Q., Michaud, E. J. and Yoder, B. K. (2005). Gli2 and Gli3 localize to cilia and require the intraflagellar transport protein polaris for processing and function. *PLoS Genet* **1**, e53.

Haycraft, C. J., Zhang, Q., Song, B., Jackson, W. S., Detloff, P. J., Serra, R. and Yoder, B. K. (2007). Intraflagellar transport is essential for endochondral bone formation. *Development* **134**, 307-16.

Heanue, T. A. and Pachnis, V. (2007). Enteric nervous system development and Hirschsprung's disease: advances in genetic and stem cell studies. *Nat Rev Neurosci* **8**, 466-79.

Hearn, T., Renforth, G. L., Spalluto, C., Hanley, N. A., Piper, K., Brickwood, S., White, C., Connolly, V., Taylor, J. F., Russell-Eggitt, I. et al. (2002). Mutation of ALMS1, a large gene with a tandem repeat encoding 47 amino acids, causes Alström syndrome. *Nat Genet* **31**, 79-83.

Hearn, T., Spalluto, C., Phillips, V. J., Renforth, G. L., Copin, N., Hanley, N. A. and Wilson, D. I. (2005). Subcellular localization of ALMS1 supports involvement of centrosome and basal body dysfunction in the pathogenesis of obesity, insulin resistance, and type 2 diabetes. *Diabetes* **54**, 1581-7.

Hellemans, J., Coucke, P. J., Giedion, A., De Paepe, A., Kramer, P., Beemer, F. and Mortier, G. R. (2003). Homozygous mutations in IHH cause acrocapitofemoral dysplasia, an autosomal recessive disorder with cone-shaped epiphyses in hands and hips. *Am J Hum Genet* **72**, 1040-6.

Helms, J. A. and Schneider, R. A. (2003). Cranial skeletal biology. *Nature* **423**, 326-31.

Helou, J., Otto, E. A., Attanasio, M., Allen, S. J., Parisi, M. A., Glass, I., Utsch, B., Hashmi, S., Fazzi, E., Omran, H. et al. (2007). Mutation analysis of NPHP6/CEP290 in patients with Joubert syndrome and Senior-Løken syndrome. *J Med Genet* **44**, 657-63.

Hichri, H., Stoetzel, C., Laurier, V., Caron, S., Sigaudy, S., Sarda, P., Hamel, C., Martin-Coignard, D., Gilles, M., Leheup, B. et al. (2005). Testing for triallelism: analysis of six BBS genes in a Bardet-Biedl syndrome family cohort. *Eur J Hum Genet* **13**, 607-16.

Hildebrandt, F., Otto, E., Rensing, C., Nothwang, H. G., Vollmer, M., Adolphs, J., Hanusch, H. and Brandis, M. (1997). A novel gene encoding an SH3 domain protein is mutated in nephronophthisis type 1. *Nat Genet* **17**, 149-53.

Hildebrandt, F. and Zhou, W. (2007). Nephronophthisis-associated ciliopathies. *J Am Soc Nephrol* **18**, 1855-71.

Hinkes, B., Wiggins, R. C., Gbadegesin, R., Vlangos, C. N., Seelow, D., Nürnberg, G., Garg, P., Verma, R., Chaib, H., Hoskins, B. E. et al. (2006). Positional cloning uncovers mutations in PLCE1 responsible for a nephrotic syndrome variant that may be reversible. *Nat Genet* **38**, 1397-405.

Hoefele, J., Wolf, M. T., O'Toole, J. F., Otto, E. A., Schultheiss, U., Dêschenes, G., Attanasio, M., Utsch, B., Antignac, C. and Hildebrandt, F. (2007). Evidence of oligogenic inheritance in nephronophthisis. *J Am Soc Nephrol* **18**, 2789-95.

Hosking, C. R., Ulloa, F., Hogan, C., Ferber, E. C., Figueroa, A., Gevaert, K., Birchmeier, W., Briscoe, J. and Fujita, Y. (2007). The transcriptional repressor Glis2 is a novel binding partner for p120 catenin. *Mol Biol Cell* **18**, 1918-27.

Hu, D. and Helms, J. A. (1999). The role of sonic hedgehog in normal and abnormal craniofacial morphogenesis. *Development* **126**, 4873-84.

Huangfu, D. and Anderson, K. V. (2005). Cilia and Hedgehog responsiveness in the mouse. *Proc Natl Acad Sci USA* **102**, 11325-30.

Huangfu, D., Liu, A., Rakeman, A. S., Murcia, N. S., Niswander, L. and Anderson, K. V. (2003). Hedgehog signalling in the mouse requires intraflagellar transport proteins. *Nature* **426**, 83-7.

Hyde, R. (2008). Europe battles with obesity. *Lancet* **371**, 2160-1.

Inoki, K., Ouyang, H., Zhu, T., Lindvall, C., Wang, Y., Zhang, X., Yang, Q., Bennett, C., Harada, Y., Stankunas, K. et al. (2006). TSC2 integrates Wnt and energy signals via a coordinated phosphorylation by AMPK and GSK3 to regulate cell growth. *Cell* **126**, 955-68.

Işlek, I., Küçüködük, S., Erkan, D., Bernay, F., Kalayci, A. G., Görk, S., Kandemir, B. and Gürses, N. (1996). Bardet-Biedl syndrome: delayed diagnosis in a child with Hirschsprung disease. *Clin Dysmorphol* **5**, 271-3.

Javitt, N. B. (2008). Oxysterols: novel biologic roles for the 21st century. *Steroids* **73**, 149-57.

Jessen, J. R., Topczewski, J., Bingham, S., Sepich, D. S., Marlow, F., Chandrasekhar, A. and Solnica-Krezel, L. (2002). Zebrafish trilobite identifies new roles for Strabismus in gastrulation and neuronal movements. *Nat Cell Biol* **4**, 610-5.

Johnston, J. J., Olivos-Glander, I., Killoran, C., Elson, E., Turner, J. T., Peters, K. F., Abbott, M. H., Aughton, D. J., Aylsworth, A. S., Bamshad, M. J. et al. (2005). Molecular and clinical analyses of Greig cephalopolysyndactyly and Pallister-Hall syndromes: robust phenotype prediction from the type and position of GLI3 mutations. *Am J Hum Genet* **76**, 609-22.

Jopling, C., van Geemen, D. and den Hertog, J. (2007). Shp2 knockdown and Noonan/LEOPARD mutant Shp2-induced gastrulation defects. *PLoS Genet* **3**, e225.

Joy, T., Cao, H., Black, G., Malik, R., Charlton-Menys, V., Hegele, R. A. and Durrington, P. N. (2007). Alstrom syndrome (OMIM 203800): a case report and literature review. *Orphanet journal of rare diseases* **2**, 49.

Karaman, A. (2008). Bardet-Biedl syndrome: a case report. *Dermatol Online J* **14**, 9.

Katsanis, N., Ansley, S. J., Badano, J. L., Eichers, E. R., Lewis, R. A., Hoskins, B. E., Scambler, P. J., Davidson, W. S., Beales, P. L. and Lupski, J. R. (2001). Triallelic inheritance in Bardet-Biedl syndrome, a Mendelian recessive disorder. *Science* **293**, 2256-9.

Katsanis, N., Beales, P. L., Woods, M. O., Lewis, R. A., Green, J. S., Parfrey, P. S., Ansley, S. J., Davidson, W. S. and Lupski, J. R. (2000). Mutations in

MKKS cause obesity, retinal dystrophy and renal malformations associated with Bardet-Biedl syndrome. *Nat Genet* **26**, 67-70.

Kau, C. H., Hunter, L. M. and Hingston, E. J. (2007). A different look: 3-dimensional facial imaging of a child with Binder syndrome. *American journal of orthodontics and dentofacial orthopedics : official publication of the American Association of Orthodontists, its constituent societies, and the American Board of Orthodontics* **132**, 704-9.

Kibar, Z., Torban, E., McDearmid, J. R., Reynolds, A., Berghout, J., Mathieu, M., Kirillova, I., De Marco, P., Merello, E., Hayes, J. M. et al. (2007). Mutations in VANGL1 associated with neural-tube defects. *N Engl J Med* **356**, 1432-7.

Kim, H. J., Schleiffarth, J. R., Jessurun, J., Sumanas, S., Petryk, A., Lin, S. and Ekker, S. C. (2005). Wnt5 signaling in vertebrate pancreas development. *BMC Biol* **3**, 23.

Kim, J. C., Badano, J. L., Sibold, S., Esmail, M. A., Hill, J., Hoskins, B. E., Leitch, C. C., Venner, K., Ansley, S. J., Ross, A. J. et al. (2004). The Bardet-Biedl protein BBS4 targets cargo to the pericentriolar region and is required for microtubule anchoring and cell cycle progression. *Nat Genet* **36**, 462-70.

Kimmel, C. B., Miller, C. T. and Moens, C. B. (2001). Specification and morphogenesis of the zebrafish larval head skeleton. *Dev Biol* **233**, 239-57.

König, G. and Hausen, P. (1993). Planar polarity in the ciliated epidermis of Xenopus embryos. *Dev Biol* **160**, 355-68.

Koyama, E., Young, B., Nagayama, M., Shibukawa, Y., Enomoto-Iwamoto, M., Iwamoto, M., Maeda, Y., Lanske, B., Song, B., Serra, R. et al. (2007). Conditional Kif3a ablation causes abnormal hedgehog signaling topography, growth plate dysfunction, and excessive bone and cartilage formation during mouse skeletogenesis. *Development* **134**, 2159-69.

Kramer-Zucker, A. G., Olale, F., Haycraft, C. J., Yoder, B. K., Schier, A. F. and Drummond, I. A. (2005). Cilia-driven fluid flow in the zebrafish pronephros, brain and Kupffer's vesicle is required for normal organogenesis. *Development* **132**, 1907-21.

Kuhlman, J. and Eisen, J. S. (2007). Genetic screen for mutations affecting development and function of the enteric nervous system. *Dev Dyn* **236**, 118-27.

Kulaga, H. M., Leitch, C. C., Eichers, E. R., Badano, J. L., Lesemann, A., Hoskins, B. E., Lupski, J. R., Beales, P. L., Reed, R. R. and Katsanis, N. (2004). Loss of BBS proteins causes anosmia in humans and defects in olfactory cilia structure and function in the mouse. *Nat Genet* **36**, 994-8.

Kyttälä, M., Tallila, J., Salonen, R., Kopra, O., Kohlschmidt, N., Paavola-Sakki, P., Peltonen, L. and Kestilä, M. (2006). MKS1, encoding a component of

the flagellar apparatus basal body proteome, is mutated in Meckel syndrome. *Nat Genet* **38**, 155-7.

LaBonne, C. (2002). Vertebrate development: wnt signals at the crest. *Curr Biol* **12**, R743-4.

LaBonne, C. and Bronner-Fraser, M. (1999). Molecular mechanisms of neural crest formation. *Annu Rev Cell Dev Biol* **15**, 81-112.

Laurier, V., Stoetzel, C., Muller, J., Thibault, C., Corbani, S., Jalkh, N., Salem, N., Chouery, E., Poch, O., Licaire, S. et al. (2006). Pitfalls of homozygosity mapping: an extended consanguineous Bardet-Biedl syndrome family with two mutant genes (BBS2, BBS10), three mutations, but no triallelism. *Eur J Hum Genet* **14**, 1195-203.

Le Douarin, N. M. and Dupin, E. (2003). Multipotentiality of the neural crest. *Curr Opin Genet Dev* **13**, 529-36.

Lei, Q., Jeong, Y., Misra, K., Li, S., Zelman, A. K., Epstein, D. J. and Matise, M. P. (2006). Wnt signaling inhibitors regulate the transcriptional response to morphogenetic Shh-Gli signaling in the neural tube. *Dev Cell* **11**, 325-37.

Leitch, C. C., Zaghloul, N. A., Davis, E. E., Stoetzel, C., Diaz-Font, A., Rix, S., Al-Fadhel, M., Lewis, R. A., Eyaid, W., Banin, E. et al. (2008). Hypomorphic mutations in syndromic encephalocele genes are associated with Bardet-Biedl syndrome. *Nat Genet* **40**, 443-8.

Leroux, M. R. (2007). Taking vesicular transport to the cilium. *Cell* **129**, 1041-3.

Li, G., Vega, R., Nelms, K., Gekakis, N., Goodnow, C., McNamara, P., Wu, H., Hong, N. A. and Glynne, R. (2007a). A role for Alström syndrome protein, alms1, in kidney ciliogenesis and cellular quiescence. *PLoS Genet* **3**, e8.

Li, J. B., Gerdes, J. M., Haycraft, C. J., Fan, Y., Teslovich, T. M., May-Simera, H., Li, H., Blacque, O. E., Li, L., Leitch, C. C. et al. (2004). Comparative genomics identifies a flagellar and basal body proteome that includes the BBS5 human disease gene. *Cell* **117**, 541-52.

Li, Y. X., Yang, H. T., Zdanowicz, M., Sicklick, J. K., Qi, Y., Camp, T. J. and Diehl, A. M. (2007b). Fetal alcohol exposure impairs Hedgehog cholesterol modification and signaling. *Lab Invest* **87**, 231-40.

Litingtung, Y., Dahn, R. D., Li, Y., Fallon, J. F. and Chiang, C. (2002). Shh and Gli3 are dispensable for limb skeleton formation but regulate digit number and identity. *Nature* **418**, 979-83.

Liu, A., Wang, B. and Niswander, L. A. (2005). Mouse intraflagellar transport proteins regulate both the activator and repressor functions of Gli transcription factors. *Development* **132**, 3103-11.

Liu, S., Lu, W., Obara, T., Kuida, S., Lehoczky, J., Dewar, K., Drummond, I. A. and Beier, D. R. (2002). A defect in a novel Nek-family kinase causes cystic kidney disease in the mouse and in zebrafish. *Development* **129**, 5839-46.

Lodish H., et al. (2002). Molecular Cell Biology (4th Edition) (Freeman).

Loos, R. J., and Bouchard, C. (2008). FTO: the first gene contributing to common forms of human obesity. *Obes. Rev.* **9**, 246-50.

Loos, R. J., Lindgren, C. M., Li, S., Wheeler, E., Zhao, J. H., Prokopenko, I., et al. (2008). Common variants near MC4R are associated with fat mass, weight and risk of obesity. *Nat. Genet.* **40**: 768-75.

Lorda-Sanchez, I., Ayuso, C. and Ibañez, A. (2000). Situs inversus and hirschsprung disease: two uncommon manifestations in Bardet-Biedl syndrome. *Am J Med Genet* **90**, 80-1.

Lorda-Sanchez, I., Ayuso, C., Sanz, R. and Ibañez, A. (2001). Does Bardet-Biedl syndrome have a characteristic face? *J Med Genet* **38**, E14.

Low, S. H., Vasanth, S., Larson, C. H., Mukherjee, S., Sharma, N., Kinter, M. T., Kane, M. E., Obara, T. and Weimbs, T. (2006). Polycystin-1, STAT6, and P100 function in a pathway that transduces ciliary mechanosensation and is activated in polycystic kidney disease. *Dev Cell* **10**, 57-69.

Lucker, B. F., Behal, R. H., Qin, H., Siron, L. C., Taggart, W. D., Rosenbaum, J. L. and Cole, D. G. (2005). Characterization of the intraflagellar transport complex B core: direct interaction of the IFT81 and IFT74/72 subunits. *J Biol Chem* **280**, 27688-96.

Lumsden, A. and Guthrie, S. (1991). Alternating patterns of cell surface properties and neural crest cell migration during segmentation of the chick hindbrain. *Development* **Suppl 2**, 9-15.

Mak, H. Y., Nelson, L. S., Basson, M., Johnson, C. D. and Ruvkun, G. (2006). Polygenic control of Caenorhabditis elegans fat storage. *Nat Genet* **38**, 363-8.

Marcucio, R. S., Cordero, D. R., Hu, D. and Helms, J. A. (2005). Molecular interactions coordinating the development of the forebrain and face. *Dev Biol* **284**, 48-61.

Marshall, J. D., Beck, S., Maffei, P. and Naggert, J. K. (2007). Alström syndrome. *Eur J Hum Genet* **15**, 1193-202.

Marshall, W. F. and Nonaka, S. (2006). Cilia: tuning in to the cell's antenna. *Curr Biol* **16**, R604-14.

Matthews, H. K., Marchant, L., Carmona-Fontaine, C., Kuriyama, S., Larraín, J., Holt, M. R., Parsons, M. and Mayor, R. (2008). Directional migration of neural crest cells in vivo is regulated by Syndecan-4/Rac1 and non-canonical Wnt signaling/RhoA. *Development* **135**, 1771-80.

May, S. R., Ashique, A. M., Karlen, M., Wang, B., Shen, Y., Zarbalis, K., Reiter, J., Ericson, J. and Peterson, A. S. (2005). Loss of the retrograde motor for IFT disrupts localization of Smo to cilia and prevents the expression of both activator and repressor functions of Gli. *Dev Biol* **287**, 378-89.

McGrath, J. and Brueckner, M. (2003). Cilia are at the heart of vertebrate left-right asymmetry. *Curr Opin Genet Dev* **13**, 385-92.

McGrath, J., Somlo, S., Makova, S., Tian, X. and Brueckner, M. (2003). Two populations of node monocilia initiate left-right asymmetry in the mouse. *Cell* **114**, 61-73.

Merscher, S., Funke, B., Epstein, J. A., Heyer, J., Puech, A., Lu, M. M., Xavier, R. J., Demay, M. B., Russell, R. G., Factor, S. et al. (2001). TBX1 is responsible for cardiovascular defects in velo-cardio-facial/DiGeorge syndrome. *Cell* **104**, 619-29.

Mollet, G., Salomon, R., Gribouval, O., Silbermann, F., Bacq, D., Landthaler, G., Milford, D., Nayir, A., Rizzoni, G., Antignac, C. et al. (2002). The gene mutated in juvenile nephronophthisis type 4 encodes a novel protein that interacts with nephrocystin. *Nat Genet* **32**, 300-5.

Moon, H. S., Jacobson, E. M., Khersonsky, S. M., Luzung, M. R., Walsh, D. P., Xiong, W., Lee, J. W., Parikh, P. B., Lam, J. C., Kang, T. W. et al. (2002). A novel microtubule destabilizing entity from orthogonal synthesis of triazine library and zebrafish embryo screening. *J Am Chem Soc* **124**, 11608-9.

Mykytyn, K., Braun, T., Carmi, R., Haider, N. B., Searby, C. C., Shastri, M., Beck, G., Wright, A. F., Iannaccone, A., Elbedour, K. et al. (2001). Identification of the gene that, when mutated, causes the human obesity syndrome BBS4. *Nat Genet* **28**, 188-91.

Mykytyn, K., Mullins, R. F., Andrews, M., Chiang, A. P., Swiderski, R. E., Yang, B., Braun, T., Casavant, T., Stone, E. M. and Sheffield, V. C. (2004). Bardet-Biedl syndrome type 4 (BBS4)-null mice implicate Bbs4 in flagella formation but not global cilia assembly. *Proc Natl Acad Sci USA* **101**, 8664-9.

Mykytyn, K., Nishimura, D. Y., Searby, C. C., Shastri, M., Yen, H. J., Beck, J. S., Braun, T., Streb, L. M., Cornier, A. S., Cox, G. F. et al. (2002). Identification of the gene (BBS1) most commonly involved in Bardet-Biedl syndrome, a complex human obesity syndrome. *Nat Genet* **31**, 435-8.

Nachury, M. V., Loktev, A. V., Zhang, Q., Westlake, C. J., Peränen, J., Merdes, A., Slusarski, D. C., Scheller, R. H., Bazan, J. F., Sheffield, V. C. et al. (2007). A core complex of BBS proteins cooperates with the GTPase Rab8 to promote ciliary membrane biogenesis. *Cell* **129**, 1201-13.

Nakane, T. and Biesecker, L. G. (2005). No evidence for triallelic inheritance of MKKS/BBS loci in Amish Mckusick-Kaufman syndrome. *Am J Med Genet A* **138**, 32-4.

Neuhauss, S. C., Solnica-Krezel, L., Schier, A. F., Zwartkruis, F., Stemple, D. L., Malicki, J., Abdelilah, S., Stainier, D. Y. and Driever, W. (1996). Mutations affecting craniofacial development in zebrafish. *Development* **123**, 357-67.

Nieto, M. A. (2001). The early steps of neural crest development. *Mech Dev* **105**, 27-35.

Nishimura, D. Y., Fath, M., Mullins, R. F., Searby, C., Andrews, M., Davis, R., Andorf, J. L., Mykytyn, K., Swiderski, R. E., Yang, B. et al. (2004). Bbs2-null mice have neurosensory deficits, a defect in social dominance, and retinopathy associated with mislocalization of rhodopsin. *Proc Natl Acad Sci USA* **101**, 16588-93.

Nishimura, D. Y., Searby, C. C., Carmi, R., Elbedour, K., Van Maldergem, L., Fulton, A. B., Lam, B. L., Powell, B. R., Swiderski, R. E., Bugge, K. E. et al. (2001). Positional cloning of a novel gene on chromosome 16q causing Bardet-Biedl syndrome (BBS2). *Hum Mol Genet* **10**, 865-74.

Nishimura, D. Y., Swiderski, R. E., Searby, C. C., Berg, E. M., Ferguson, A. L., Hennekam, R., Merin, S., Weleber, R. G., Biesecker, L. G., Stone, E. M. et al. (2005). Comparative genomics and gene expression analysis identifies BBS9, a new Bardet-Biedl syndrome gene. *Am J Hum Genet* **77**, 1021-33.

Nonaka, S., Shiratori, H., Saijoh, Y. and Hamada, H. (2002). Determination of left-right patterning of the mouse embryo by artificial nodal flow. *Nature* **418**, 96-9.

O'Dea, D., Parfrey, P. S., Harnett, J. D., Hefferton, D., Cramer, B. C. and Green, J. (1996). The importance of renal impairment in the natural history of Bardet-Biedl syndrome. *Am J Kidney Dis* **27**, 776-83.

Ocbina, P. J. and Anderson, K. V. (2008). Intraflagellar transport, cilia, and mammalian Hedgehog signaling: Analysis in mouse embryonic fibroblasts. *Dev Dyn* **237**, 2030-2038.

Oishi, I., Kawakami, Y., Raya, A., Callol-Massot, C. and Izpisúa Belmonte, J. C. (2006). Regulation of primary cilia formation and left-right patterning in zebrafish by a noncanonical Wnt signaling mediator, duboraya. *Nat Genet* **38**, 1316-22.

Olbrich, H., Fliegauf, M., Hoefele, J., Kispert, A., Otto, E., Volz, A., Wolf, M. T., Sasmaz, G., Trauer, U., Reinhardt, R. et al. (2003). Mutations in a novel gene, NPHP3, cause adolescent nephronophthisis, tapeto-retinal degeneration and hepatic fibrosis. *Nat Genet* **34**, 455-9.

Oro, A. E., Higgins, K. M., Hu, Z., Bonifas, J. M., Epstein, E. H. and Scott, M. P. (1997). Basal cell carcinomas in mice overexpressing sonic hedgehog. *Science* **276**, 817-21.

Otto, E. A., Loeys, B., Khanna, H., Hellemans, J., Sudbrak, R., Fan, S., Muerb, U., O'Toole, J. F., Helou, J., Attanasio, M. et al. (2005). Nephrocystin-5, a ciliary IQ domain protein, is mutated in Senior-Loken syndrome and interacts with RPGR and calmodulin. *Nat Genet* **37**, 282-8.

Otto, E. A., Schermer, B., Obara, T., O'Toole, J. F., Hiller, K. S., Mueller, A. M., Ruf, R. G., Hoefele, J., Beekmann, F., Landau, D. et al. (2003). Mutations in INVS encoding inversin cause nephronophthisis type 2, linking renal cystic disease to the function of primary cilia and left-right axis determination. *Nat Genet* **34**, 413-20.

Otto, E. A., Trapp, M. L., Schultheiss, U. T., Helou, J., Quarmby, L. M. and Hildebrandt, F. (2008). NEK8 mutations affect ciliary and centrosomal localization and may cause nephronophthisis. *J Am Soc Nephrol* **19**, 587-92.

Ou, G., Blacque, O. E., Snow, J. J., Leroux, M. R. and Scholey, J. M. (2005). Functional coordination of intraflagellar transport motors. *Nature* **436**, 583-7.

Ozgül, R. K., Satman, I., Collin, G. B., Hinman, E. G., Marshall, J. D., Kocaman, O., Tütüncü, Y., Yilmaz, T. and Naggert, J. K. (2007). Molecular analysis and long-term clinical evaluation of three siblings with Alström syndrome. *Clin Genet* **72**, 351-6.

Panizzi, J. R., Jessen, J. R., Drummond, I. A. and Solnica-Krezel, L. (2007). New functions for a vertebrate Rho guanine nucleotide exchange factor in ciliated epithelia. *Development* **134**, 921-31.

Park, T. J., Haigo, S. L. and Wallingford, J. B. (2006). Ciliogenesis defects in embryos lacking inturned or fuzzy function are associated with failure of planar cell polarity and Hedgehog signaling. *Nat Genet* **38**, 303-11.

Park, T. J., Mitchell, B. J., Abitua, P. B., Kintner, C. and Wallingford, J. B. (2008). Dishevelled controls apical docking and planar polarization of basal bodies in ciliated epithelial cells. *Nat Genet* **40**, 871-9.

Pazzaglia, S., Tanori, M., Mancuso, M., Gessi, M., Pasquali, E., Leonardi, S., Oliva, M. A., Rebessi, S., Di Majo, V., Covelli, V. et al. (2006). Two-hit model for progression of medulloblastoma preneoplasia in Patched heterozygous mice. *Oncogene* **25**, 5575-80.

Pepinsky, R. B., Zeng, C., Wen, D., Rayhorn, P., Baker, D. P., Williams, K. P., Bixler, S. A., Ambrose, C. M., Garber, E. A., Miatkowski, K. et al. (1998). Identification of a palmitic acid-modified form of human Sonic hedgehog. *J Biol Chem* **273**, 14037-45.

Perner, B., Englert, C. and Bollig, F. (2007). The Wilms tumor genes wt1a and wt1b control different steps during formation of the zebrafish pronephros. *Dev Biol* **309**, 87-96.

Perriton, C. L., Powles, N., Chiang, C., Maconochie, M. K. and Cohn, M. J. (2002). Sonic hedgehog signaling from the urethral epithelium controls external genital development. *Dev Biol* **247**, 26-46.

Peters, T., Ausmeier, K., Dildrop, R. and Rüther, U. (2002). The mouse Fused toes (Ft) mutation is the result of a 1.6-Mb deletion including the entire Iroquois B gene cluster. *Mamm Genome* **13**, 186-8.

Peters, T., Ausmeier, K. and Rüther, U. (1999). Cloning of Fatso (Fto), a novel gene deleted by the Fused toes (Ft) mouse mutation. *Mamm Genome* **10**, 983-6.

Peterson, R. T., Link, B. A., Dowling, J. E. and Schreiber, S. L. (2000). Small molecule developmental screens reveal the logic and timing of vertebrate development. *Proc Natl Acad Sci USA* **97**, 12965-9.

Peterson, R. T., Shaw, S. Y., Peterson, T. A., Milan, D. J., Zhong, T. P., Schreiber, S. L., MacRae, C. A. and Fishman, M. C. (2004). Chemical suppression of a genetic mutation in a zebrafish model of aortic coarctation. *Nat Biotechnol* **22**, 595-9.

Pingault, V., Bondurand, N., Kuhlbrodt, K., Goerich, D. E., Préhu, M. O., Puliti, A., Herbarth, B., Hermans-Borgmeyer, I., Legius, E., Matthijs, G. et al. (1998). SOX10 mutations in patients with Waardenburg-Hirschsprung disease. *Nat Genet* **18**, 171-3.

Radetti, G., Frick, R., Pasquino, B., Mengarda, G. and Savage, M. O. (1988). Hypothalamic-pituitary dysfunction and Hirschsprung's disease in the Bardet-Biedl syndrome. *Helvetica paediatrica acta* **43**, 249-52.

Rahmouni, K., Fath, M. A., Seo, S., Thedens, D. R., Berry, C. J., Weiss, R., Nishimura, D. Y. and Sheffield, V. C. (2008). Leptin resistance contributes to obesity and hypertension in mouse models of Bardet-Biedl syndrome. *J Clin Invest* **118**, 1458-67.

Rallu, M., Machold, R., Gaiano, N., Corbin, J. G., McMahon, A. P. and Fishell, G. (2002). Dorsoventral patterning is established in the telencephalon of mutants lacking both Gli3 and Hedgehog signaling. *Development* **129**, 4963-74.

Ramalho-Santos, M., Melton, D. A., McMahon, A. P. (2000). Hedgehog signals regulate multiple aspects of gastrointestinal development. *Development* **127**, 2763-72.

Read, A. P. and Newton, V. E. (1997). Waardenburg syndrome. *J Med Genet* **34**, 656-65.

Riley, B. B., Zhu, C., Janetopoulos, C. and Aufderheide, K. J. (1997). A critical period of ear development controlled by distinct populations of ciliated cells in the zebrafish. *Dev Biol* **191**, 191-201.

Rohatgi, R., Milenkovic, L. and Scott, M. P. (2007). Patched1 regulates hedgehog signaling at the primary cilium. *Science* **317**, 372-6.

Ross, A. J., May-Simera, H., Eichers, E. R., Kai, M., Hill, J., Jagger, D. J., Leitch, C. C., Chapple, J. P., Munro, P. M., Fisher, S. et al. (2005). Disruption of Bardet-Biedl syndrome ciliary proteins perturbs planar cell polarity in vertebrates. *Nat Genet* **37**, 1135-40.

Ruiz-Perez, V. L., Ide, S. E., Strom, T. M., Lorenz, B., Wilson, D., Woods, K., King, L., Francomano, C., Freisinger, P., Spranger, S. et al. (2000). Mutations in a new gene in Ellis-van Creveld syndrome and Weyers acrodental dysostosis. *Nat Genet* **24**, 283-6.

Rulifson, I. C., Karnik, S. K., Heiser, P. W., ten Berge, D., Chen, H., Gu, X., Taketo, M. M., Nusse, R., Hebrok, M. and Kim, S. K. (2007). Wnt signaling regulates pancreatic beta cell proliferation. *Proc Natl Acad Sci USA* **104**, 6247-52.

Saadi-Kheddouci, S., Berrebi, D., Romagnolo, B., Cluzeaud, F., Peuchmaur, M., Kahn, A., Vandewalle, A. and Perret, C. (2001). Early development of polycystic kidney disease in transgenic mice expressing an activated mutant of the beta-catenin gene. *Oncogene* **20**, 5972-81.

Saburi, S., Hester, I., Fischer, E., Pontoglio, M., Eremina, V., Gessler, M., Quaggin, S. E., Harrison, R., Mount, R. and McNeill, H. (2008). Loss of Fat4 disrupts PCP signaling and oriented cell division and leads to cystic kidney disease. *Nat Genet* **40**, 1010-5.

Saint-Jeannet, J. P., He, X., Varmus, H. E. and Dawid, I. B. (1997). Regulation of dorsal fate in the neuraxis by Wnt-1 and Wnt-3a. *Proc Natl Acad Sci USA* **94**, 13713-8.

Sanchez-Pulido, L. and Andrade-Navarro, M. A. (2007). The FTO (fat mass and obesity associated) gene codes for a novel member of the non-heme dioxygenase superfamily. *BMC Biochem* **8**, 23.

Santagati, F. and Rijli, F. M. (2003). Cranial neural crest and the building of the vertebrate head. *Nat Rev Neurosci* **4**, 806-18.

Sauka-Spengler, T. and Bronner-Fraser, M. (2008). A gene regulatory network orchestrates neural crest formation. *Nat Rev Mol Cell Biol* **9**, 557-68.

Sayer, J. A., Otto, E. A., O'Toole, J. F., Nurnberg, G., Kennedy, M. A., Becker, C., Hennies, H. C., Helou, J., Attanasio, M., Fausett, B. V. et al. (2006). The centrosomal protein nephrocystin-6 is mutated in Joubert syndrome and activates transcription factor ATF4. *Nat Genet* **38**, 674-81.

Schilling, T. F., Piotrowski, T., Grandel, H., Brand, M., Heisenberg, C. P., Jiang, Y. J., Beuchle, D., Hammerschmidt, M., Kane, D. A., Mullins, M. C. et al. (1996). Jaw and branchial arch mutants in zebrafish I: branchial arches. *Development* **123**, 329-44.

Schimmang, T., Lemaistre, M., Vortkamp, A. and Rüther, U. (1992). Expression of the zinc finger gene Gli3 is affected in the morphogenetic mouse mutant extra-toes (Xt). *Development* **116**, 799-804.

Scholey, J. M. and Anderson, K. V. (2006). Intraflagellar transport and cilium-based signaling. *Cell* **125**, 439-42.

Serra, A. L., Kistler, A. D., Poster, D., Struker, M., Wuthrich, R. P., Weishaupt, D., Tschrich, F. (2007). Clinical proof-of-concept trial to assess the therapeutic effect of sirolimus in patients with autosomal dominant polycystic kidney disease: SUISSE ADPKD study. *BMC Nephrol.* **8**:13.

Simons, M., Gloy, J., Ganner, A., Bullerkotte, A., Bashkurov, M., Krönig, C., Schermer, B., Benzing, T., Cabello, O. A., Jenny, A. et al. (2005). Inversin, the gene product mutated in nephronophthisis type II, functions as a molecular switch between Wnt signaling pathways. *Nat Genet* **37**, 537-43.

Simons, M. and Walz, G. (2006). Polycystic kidney disease: cell division without a c(l)ue? *Kidney Int* **70**, 854-64.

Sinha, S. and Chen, J. K. (2006). Purmorphamine activates the Hedgehog pathway by targeting Smoothened. *Nat Chem Biol* **2**, 29-30.

Shillingford, J. M., Murcia, N. S., Larson, C. H., Low S. H., Hedgepeth, R., Brown, N., Flask, C. A., Novick., A. C., Goldfarb, D. A., Kramer-Zucker, A., Walz, G., Piontek, K. B., Germino, G. G., Weimbs, T. (2006). The mTOR pathway is regulated by polycystin-1 , and its inhibition reverses renal cystogenesis in polycystic kidney disease. *Proc. Natl. Acad. Sci. USA* **103**(14), 5466-71.

Slavotinek, A. M., Stone, E. M., Mykytyn, K., Heckenlively, J. R., Green, J. S., Heon, E., Musarella, M. A., Parfrey, P. S., Sheffield, V. C. and Biesecker, L. G. (2000). Mutations in MKKS cause Bardet-Biedl syndrome. *Nat Genet* **26**, 15-6.

Smaoui, N., Chaabouni, M., Sergeev, Y. V., Kallel, H., Li, S., Mahfoudh, N., Maazoul, F., Kammoun, H., Gandoura, N., Bouaziz, A. et al. (2006). Screening of the eight BBS genes in Tunisian families: no evidence of triallelism. *Invest Ophthalmol Vis Sci* **47**, 3487-95.

Smith, U. M., Consugar, M., Tee, L. J., McKee, B. M., Maina, E. N., Whelan, S., Morgan, N. V., Goranson, E., Gissen, P., Lilliquist, S. et al. (2006). The transmembrane protein meckelin (MKS3) is mutated in Meckel-Gruber syndrome and the wpk rat. *Nat Genet* **38**, 191-6.

Sohara, E., Luo, Y., Zhang, J., Manning, D. K., Beier, D. R., Zhou, J. (2008). Nek8 regulates the expression and localisation of polycystin-1 and polycystin-2. *J. Am. Soc. Nephrol.* **19**, 469-76.

Stamataki, D., Ulloa, F., Tsoni, S. V., Mynett, A. and Briscoe, J. (2005). A gradient of Gli activity mediates graded Sonic Hedgehog signaling in the neural tube. *Genes Dev* **19**, 626-41.

Stoetzel, C., Laurier, V., Davis, E. E., Muller, J., Rix, S., Badano, J. L., Leitch, C. C., Salem, N., Chouery, E., Corbani, S. et al. (2006). BBS10

encodes a vertebrate-specific chaperonin-like protein and is a major BBS locus. *Nat Genet* **38**, 521-4.

Stoetzel, C., Muller, J., Laurier, V., Davis, E. E., Zaghloul, N. A., Vicaire, S., Jacquelin, C., Plewniak, F., Leitch, C. C., Sarda, P. et al. (2007). Identification of a novel BBS gene (BBS12) highlights the major role of a vertebrate-specific branch of chaperonin-related proteins in Bardet-Biedl syndrome. *Am J Hum Genet* **80**, 1-11.

Strähle, U., Lam, C. S., Ertzer, R. and Rastegar, S. (2004). Vertebrate floor-plate specification: variations on common themes. *Trends Genet* **20**, 155-62.

Stratigopoulos, G., Padilla, S. L., LeDuc, C. A., Watson, E., Hattersley, A. T., McCarthy, M. I., Zeltser, L. M., Chung, W. K. and Leibel, R. L. (2008). Regulation of Fto/Ftm gene expression in mice and humans. *Am J Physiol Regul Integr Comp Physiol* **294**, R1185-96.

Sullivan-Brown, J., Schottenfeld, J., Okabe, N., Hostetter, C. L., Serluca, F. C., Thiberge, S. Y. and Burdine, R. D. (2008). Zebrafish mutations affecting cilia motility share similar cystic phenotypes and suggest a mechanism of cyst formation that differs from pkd2 morphants. *Dev Biol* **314**, 261-75.

Sun, Z., Amsterdam, A., Pazour, G. J., Cole, D. G., Miller, M. S. and Hopkins, N. (2004). A genetic screen in zebrafish identifies cilia genes as a principal cause of cystic kidney. *Development* **131**, 4085-93.

Sun, Z. and Hopkins, N. (2001). vhnf1, the MODY5 and familial GCKD-associated gene, regulates regional specification of the zebrafish gut, pronephros, and hindbrain. *Genes Dev* **15**, 3217-29.

Sung, C. H. and Tai, A. W. (2000). Rhodopsin trafficking and its role in retinal dystrophies. *Int Rev Cytol* **195**, 215-67.

Svärd, J., Heby-Henricson, K., Henricson, K. H., Persson-Lek, M., Rozell, B., Lauth, M., Bergström, A., Ericson, J., Toftgård, R. and Teglund, S. (2006). Genetic elimination of Suppressor of fused reveals an essential repressor function in the mammalian Hedgehog signaling pathway. *Dev Cell* **10**, 187-97.

Tallila, J., Jakkula, E., Peltonen, L., Salonen, R. and Kestilä, M. (2008). Identification of CC2D2A as a Meckel syndrome gene adds an important piece to the ciliopathy puzzle. *Am J Hum Genet* **82**, 1361-7.

Tan, P. L., Barr, T., Inglis, P. N., Mitsuma, N., Huang, S. M., Garcia-Gonzalez, M. A., Bradley, B. A., Coforio, S., Albrecht, P. J., Watnick, T. et al. (2007). Loss of Bardet Biedl syndrome proteins causes defects in peripheral sensory innervation and function. *Proc Natl Acad Sci USA* **104**, 17524-9.

Tanaka, Y., Okada, Y. and Hirokawa, N. (2005). FGF-induced vesicular release of Sonic hedgehog and retinoic acid in leftward nodal flow is critical for left-right determination. *Nature* **435**, 172-7.

Tassabehji, M., Hammond, P., Karmiloff-Smith, A., Thompson, P., Thorgeirsson, S. S., Durkin, M. E., Popescu, N. C., Hutton, T., Metcalfe, K., Rucka, A. et al. (2005). GTF2IRD1 in craniofacial development of humans and mice. *Science* **310**, 1184-7.

Tayeh, M. K., Yen, H. J., Beck, J. S., Searby, C. C., Westfall, T. A., Griesbach, H., Sheffield, V. C. and Slusarski, D. C. (2008). Genetic interaction between Bardet-Biedl syndrome genes and implications for limb patterning. *Hum Mol Genet*.

Thiery, J. P. and Sleeman, J. P. (2006). Complex networks orchestrate epithelial-mesenchymal transitions. *Nat Rev Mol Cell Biol* **7**, 131-42.

Thomas, T., Kurihara, H., Yamagishi, H., Kurihara, Y., Yazaki, Y., Olson, E. N. and Srivastava, D. (1998). A signaling cascade involving endothelin-1, dHAND and msx1 regulates development of neural-crest-derived branchial arch mesenchyme. *Development* **125**, 3005-14.

Tobin, J. L. and Beales, P. L. (2007). Bardet-Biedl syndrome: beyond the cilium. *Pediatr Nephrol* **22**, 926-36.

Tobin, J. L. and Beales, P. L. (2008). Restoration of renal function in zebrafish models of ciliopathies. *Pediatr Nephrol*.

Tobin, J. L., Di Franco, M., Eichers, E., May-Simera, H., Garcia, M., Yan, J., Quinlan, R., Justice, M. J., Hennekam, R. C., Briscoe, J. et al. (2008). Inhibition of neural crest migration underlies craniofacial dysmorphology and Hirschsprung's disease in Bardet-Biedl syndrome. *Proc Natl Acad Sci USA* **105**, 6714-9.

Torres, V. E. (2004). Therapies to slow polycystic kidney disease. *Nephron Exp Nephrol* **98**, e1-7.

Tran, P. V., Haycraft, C. J., Besschetnova, T. Y., Turbe-Doan, A., Stottmann, R. W., Herron, B. J., Chesebro, A. L., Qiu, H., Scherz, P. J., Shah, J. V. et al. (2008). THM1 negatively modulates mouse sonic hedgehog signal transduction and affects retrograde intraflagellar transport in cilia. *Nat Genet* **40**, 403-10.

Tran, T. C., Sneed, B., Haider, J., Blavo, D., White, A., Aiyejorun, T., Baranowski, T. C., Rubinstein, A. L., Doan, T. N., Dingledine, R. et al. (2007). Automated, quantitative screening assay for antiangiogenic compounds using transgenic zebrafish. *Cancer Res* **67**, 11386-92.

Tschritter, O., Preissl, H., Yokoyama, Y., Machicao, F., Häring, H. U. and Fritsche, A. (2007). Variation in the FTO gene locus is associated with cerebrocortical insulin resistance in humans. *Diabetologia* **50**, 2602-3.

Ulloa, F., Itasaki, N. and Briscoe, J. (2007). Inhibitory Gli3 activity negatively regulates Wnt/beta-catenin signaling. *Curr Biol* **17**, 545-50.

Valente, E. M., Silhavy, J. L., Brancati, F., Barrano, G., Krishnaswami, S. R., Castori, M., Lancaster, M. A., Boltshauser, E., Boccone, L., Al-Gazali, L. et al. (2006). Mutations in CEP290, which encodes a centrosomal protein, cause pleiotropic forms of Joubert syndrome. *Nat Genet* **38**, 623-5.

van der Hoeven, F., Schimmang, T., Volkmann, A., Mattei, M. G., Kyewski, B. and Rüther, U. (1994). Programmed cell death is affected in the novel mouse mutant Fused toes (Ft). *Development* **120**, 2601-7.

van Rooijen, E., Giles, R. H., Voest, E. E., van Rooijen, C., Schulte-Merker, S. and van Eeden, F. J. (2008). LRRC50, a Conserved Ciliary Protein Implicated in Polycystic Kidney Disease. *J Am Soc Nephrol*.

Vierkotten, J., Dildrop, R., Peters, T., Wang, B. and Rüther, U. (2007). Ftm is a novel basal body protein of cilia involved in Shh signalling. *Development* **134**, 2569-77.

Wada, N., Javidan, Y., Nelson, S., Carney, T. J., Kelsh, R. N. and Schilling, T. F. (2005). Hedgehog signaling is required for cranial neural crest morphogenesis and chondrogenesis at the midline in the zebrafish skull. *Development* **132**, 3977-88.

Wåhlén, K., Sjölin, E. and Hoffstedt, J. (2008). The common rs9939609 gene variant of the fat mass- and obesity-associated gene FTO is related to fat cell lipolysis. *J Lipid Res* **49**, 607-11.

Wallace, K. N., Akhter, S., Smith, E. M., Lorent, K. and Pack, M. (2005). Intestinal growth and differentiation in zebrafish. *Mech Dev* **122**, 157-73.

Wang, W., Liu, X., Gelinas, D., Ciruna, B. and Sun, Y. (2007). A fully automated robotic system for microinjection of zebrafish embryos. *PLoS ONE* **2**, e862.

Watanabe, D., Saijoh, Y., Nonaka, S., Sasaki, G., Ikawa, Y., Yokoyama, T. and Hamada, H. (2003). The left-right determinant Inversin is a component of node monocilia and other 9+0 cilia. *Development* **130**, 1725-34.

Webber, W. A. and Lee, J. (1975). Fine structure of mammalian renal cilia. *Anat Rec* **182**, 339-43.

Wheatley, D. N. (2005). Landmarks in the first hundred years of primary (9+0) cilium research. *Cell Biol Int* **29**, 333-9.

Widelitz, R. (2005). Wnt signaling through canonical and non-canonical pathways: recent progress. *Growth Factors* **23**, 111-6.

Williams, C. L., Winkelbauer, M. E., Schafer, J. C., Michaud, E. J. and Yoder, B. K. (2008). Functional Redundancy of the B9 Proteins and Nephrocystins in Caenorhabditis elegans Ciliogenesis. *Mol Biol Cell* **19**, 2154-2168.

Wise, C. A., Chiang, L. C., Paznekas, W. A., Sharma, M., Musy, M. M., Ashley, J. A., Lovett, M. and Jabs, E. W. (1997). TCOF1 gene encodes a putative nucleolar phosphoprotein that exhibits mutations in Treacher Collins Syndrome throughout its coding region. *Proc Natl Acad Sci USA* **94**, 3110-5.

Wolf, M. T., Saunier, S., O'Toole, J. F., Wanner, N., Groshong, T., Attanasio, M., Salomon, R., Stallmach, T., Sayer, J. A., Waldherr, R. et al. (2007). Mutational analysis of the RPGRIP1L gene in patients with Joubert syndrome and nephronophthisis. *Kidney Int* **72**, 1520-6.

Wong, H. C., Bourdelas, A., Krauss, A., Lee, H. J., Shao, Y., Wu, D., Mlodzik, M., Shi, D. L. and Zheng, J. (2003). Direct binding of the PDZ domain of Dishevelled to a conserved internal sequence in the C-terminal region of Frizzled. *Mol Cell* **12**, 1251-60.

Wong, H. C., Mao, J., Nguyen, J. T., Srinivas, S., Zhang, W., Liu, B., Li, L., Wu, D. and Zheng, J. (2000). Structural basis of the recognition of the dishevelled DEP domain in the Wnt signaling pathway. *Nat Struct Biol* **7**, 1178-84.

Wu, X., Walker, J., Zhang, J., Ding, S. and Schultz, P. G. (2004). Purmorphamine induces osteogenesis by activation of the hedgehog signaling pathway. *Chem Biol* **11**, 1229-38.

Yamanaka, H., Moriguchi, T., Masuyama, N., Kusakabe, M., Hanafusa, H., Takada, R., Takada, S. and Nishida, E. (2002). JNK functions in the non-canonical Wnt pathway to regulate convergent extension movements in vertebrates. *EMBO Rep* **3**, 69-75.

Yoder, B. K. (2007). Role of primary cilia in the pathogenesis of polycystic kidney disease. *J Am Soc Nephrol* **18**, 1381-8.

Zeng, X., Goetz, J. A., Suber, L. M., Scott, W. J., Schreiner, C. M. and Robbins, D. J. (2001). A freely diffusible form of Sonic hedgehog mediates long-range signalling. *Nature* **411**, 716-20.

Zerres, K., Rudnik-Schöneborn, S. and Deget, F. (1993). Childhood onset autosomal dominant polycystic kidney disease in sibs: clinical picture and recurrence risk. German Working Group on Paediatric Nephrology (Arbeitsgemeinschaft für Pädiatrische Nephrologie. *J Med Genet* **30**, 583-8.

Zhang, X. M., Ramalho-Santos, M. and McMahon, A. P. (2001). Smoothened mutants reveal redundant roles for Shh and Ihh signaling including regulation of L/R symmetry by the mouse node. *Cell* **106**, 781-92.

Zhao, C. and Malicki, J. (2007). Genetic defects of pronephric cilia in zebrafish. *Mech Dev* **124**, 605-16.

Zweier, C., Albrecht, B., Mitulla, B., Behrens, R., Beese, M., Gillessen-Kaesbach, G., Rott, H. D. and Rauch, A. (2002). "Mowat-Wilson" syndrome with and without Hirschsprung disease is a distinct, recognizable multiple

congenital anomalies-mental retardation syndrome caused by mutations in the zinc finger homeo box 1B gene. *Am J Med Genet* **108**, 177-81.

Zweier, C., Thiel, C. T., Dufke, A., Crow, Y. J., Meinecke, P., Suri, M., Ala-Mello, S., Beemer, F., Bernasconi, S., Bianchi, P. et al. (2005). Clinical and mutational spectrum of Mowat-Wilson syndrome. *Eur J Med Genet* **48**, 97-111.